

Graduate School of  
Systemic Neurosciences

LMU Munich

An investigation into the human vestibular system  
with magnetic resonance imaging

Submitted by  
Theresa Marie Raiser



Dissertation der  
Graduate School of Systemic Neurosciences  
der Ludwig-Maximilians-Universität München

December 2019



Supervisor and  
First Reviewer:

Dr. Virginia Lee Flanagin

German Center for Vertigo and Balance Disorders (DSGZ)

Klinikum der Universität München, LMU, Munich

Second Reviewer:

Prof. Dr. Paul Taylor

External Reviewer:

Dr. Christopher Bockisch

Date of Submission:

December 12<sup>th</sup> 2019

Date of Defense:

May 20<sup>th</sup> 2020



# Contents

<i>Summary</i> .....	<i>I</i>
<i>Abbreviations</i> .....	<i>III</i>
<i>List of figures</i> .....	<i>V</i>
<b>1. General introduction</b> .....	<b>1</b>
<b>1.1 Anatomy and function of the vestibular system</b> .....	<b>3</b>
1.1.1 Peripheral vestibular system.....	3
1.1.1.1 Semicircular canals and otolith organs .....	3
1.1.1.2 Mechanoreceptive hair cells .....	6
1.1.1.3 Atlases of the inner ear .....	8
1.1.1.4 Afferent nerve fibers .....	8
1.1.2 Central vestibular areas .....	9
1.1.2.1 Vestibular nuclei of the brainstem.....	9
1.1.2.2 Cerebellar vestibular areas.....	11
1.1.2.3 Subcortical vestibular areas .....	11
1.1.2.4 Cortical vestibular areas .....	13
<b>1.2 Reflexive eye-movements as a window to the vestibular sense</b> .....	<b>16</b>
<b>1.3 Vestibular stimulation techniques</b> .....	<b>19</b>
1.3.1 Physical acceleration .....	19
1.3.2 Caloric irrigation .....	20
1.3.3 Galvanic vestibular stimulation .....	22
1.3.4 Magnetic vestibular stimulation .....	23
1.3.4.1 Influencing factors for the strength of the MVS effect .....	25
1.3.4.2 MVS as unimodal bilateral stimulation of the vestibular system .....	26
1.3.4.3 Effect of MVS onto the brain.....	26
<b>1.4 Aim of the thesis</b> .....	<b>27</b>

<b>2. Research chapter</b>	<b>29</b>
2.1 IE-Map: a human in-vivo atlas template of the inner ear	31
2.2 The human corticocortical vestibular connectome	67
2.3 Magnetic vestibular stimulation and its effect on brain networks	103
2.4 Pupil segmentation and gaze estimation using deep learning (DeepVOG)	151
<b>3. General discussion</b>	<b>165</b>
3.1 Summary of the main results	165
3.2 Main results in context	167
3.2.1 Structural insights into the human peripheral vestibular system	167
3.2.2 Organization of the human central corticocortical vestibular connectome	169
3.2.3 The magnetic field of the MRI and whether it affects the brain	170
3.2.4 (Cortical) laterality effects	171
3.2.5 Transient symptoms due to cortical lesions	172
3.2.6 Comparative neuroanatomy	173
3.3 Methodological considerations	174
3.3.1 Limitations due to spatial resolution and location precision	174
3.3.2 Other methodological limitations	176
3.4 Technical strengths	176
3.4.1 MRI	176
3.4.2 Eye-tracking improvements	177
3.4.3 Vestibular stimulation	178
3.5 Future work	179
3.5.1 The vestibular system and neighboring structures	179
3.5.2 Adding a third dimension to DeepVOG	180
3.5.3 Individual differences	180
3.5.4 Clinical and comparative studies	181
<b>References</b>	<b>184</b>
<b>Acknowledgements</b>	<b>197</b>
<b>List of publications</b>	<b>199</b>









## Summary

This thesis for receiving the doctorate PhD degree presents three projects about the vestibular system and one concerning eye-tracking analyses. Tracking the eye-movements elicited by the vestibulo-ocular reflex provide insights into vestibular function. Eye-tracking is therefore a major method used for investigating the vestibular system.

The first two projects present studies concerning the structure of the vestibular system measured with magnet resonance imaging (MRI). The first focused on the peripheral vestibular system, lying within the temporal bone. An atlas of the inner ear (IE-Map) was established using multiple non-invasive MRI sequences. This validated atlas comprises the three semicircular canals, their ampullae, the otolith organs (sacculae and utricle), and the cochlea (with scala tympani, scala vestibuli, cochlear cupula and cochlear duct), as well as their inner and outer dimensions. The IE-Map has the highest resolution and most accurate measurements of substructures of any inner ear atlas to date retrieved with non-invasive MRI. The IE-Map can be used as a widely applicable tool for future studies in neurology, neurosurgery and otorhinolaryngology.

The second structural project investigated the corticocortical connections of a priori localized vestibular regions. Structural and functional corticocortical vestibular connectomes (CVC) were derived from state-of-the-art multi-modal neuroimaging data. We derived their modules and common network measures and compared the structural CVC to findings previously reported in non-human primates (using gold standard tracer injections). Our results show that the modularity of the structural corticocortical vestibular connectome of humans is extremely robust. Comparisons with non-human primate data revealed substantial differences in the organization across the two species. The structural CVC was characterized by a strong connectivity within each hemisphere, whereas the functional connectome emphasized a substantial synchronicity for homotopic nodes. Overall a right laterality preference in vestibular processing could be observed from both functional and structural data.

The third project of this thesis investigated whether the resting state functional MRI BOLD signal or the functional connectivity is altered by the magnetic field of the MRI. Strong magnetic fields like the one in the MRI scanner elicit a nystagmus (eye-movements with a slow drift and a quick corrective movement) in complete darkness due to the Lorentz force that acts upon the

peripheral vestibular system. This phenomenon is known as the magnetic vestibular stimulation (MVS). It was not clear, whether the MVS effect occurs during functional MRI (fMRI) scanning and whether it affects the BOLD signal or the brain connectivity. In 88% of our participants we could detect the MVS induced nystagmus during resting state fMRI (rsfMRI) scanning. Not only horizontal semicircular canal orientation with respect to the magnetic field, but also vestibular sensitivity (as measured by means of caloric irrigation) seems to influence the strength of the MVS effect across participants. Comparing rsfMRI with and without visual fixation, functional connectivity only differed in visual occipital areas and cerebellar regions. The BOLD signal fluctuations were not related to the slow phase velocity over time. However, participants with greater horizontal slow phase velocity on average showed higher activation in vestibular, executive control and attention involved cortical areas.

The fourth project deals with improving eye-tracking analyses. As already mentioned, this step is very often of great importance when investigating the vestibular system. By making use of deep learning algorithms, a novel tool “DeepVOG” was developed. Eye-tracking in complete darkness for the MVS project resulted in eye-tracking videos with heterogeneous light conditions and a black rim in the field of view. Other already established eye-tracking analyses software failed estimating horizontal and vertical eye-position with a high confidence and low noise confound. DeepVOG was highly generalizable to other data sets. It results in pupil center localization, elliptical contour estimation and blink detection. For the MVS project we used the horizontal and vertical position of the pupil center as well as their confidence and blink detection.

With this thesis and its heterogeneous four projects, important aspects of the peripheral and central vestibular system in humans were discovered in-vivo. It also provides methodological advances that are important for future vestibular and oculomotor research.

## Abbreviations

---

CISS	constructive interference in steady state
CSv	cingulate sulcus visual
CVC	corticocortical vestibular connectome
DeepVOG	pupil segmentation and gaze estimation using deep learning
DMN	default mode network
DWI	diffusion weighted imaging
EH	eye-head (neurons)
EMI	electromagnetic induction
FEF	frontal eye field
fMRI	functional magnetic resonance imaging
GVS	galvanic vestibular stimulation
HIT	head impulse test
horSPV	horizontal slow phase velocity
hMST	human medial superior temporal area
hSCC	horizontal semicircular canal
IE-Map	atlas of the inner ear
LARP	left anterior and right posterior (functional SCC pair)
LHRH	left horizontal and right horizontal (functional SCC pair)
MHD	magnetohydrodynamic
MRI	magnetic resonance imaging
MRIQC	MRI Quality Control tool
MST(d)	(dorsal) medial superior temporal area
MVS	magnetic vestibular stimulation
PIVC	parietoinsular vestibular cortex
PVP	position-vestibular-pause (neurons)
RALP	right anterior and left posterior (functional SCC pair)
ROI	region of interest
rsfMRI	resting state functional magnetic resonance imaging
RSN	resting state network

---

---

SCC	semicircular canal
SMA	supplementary motor area
SNR	signal-to-noise ratio
SPV	slow phase velocity
TIV	total intracranial volume
VCR	vestibulo-collic reflex
vHIT	video head impulse test
VIP	ventral intraparietal area
VN	vestibular nuclei
VO	vestibular only (neurons)
VOG	video-oculography
VOR	vestibulo-ocular reflex
VPS	visual posterior sylvian area
VSR	vestibulo-spinal reflex

---

## List of figures

Figure 1. Schematic illustration of the three semicircular canals. ....	4
Figure 2. Schematic illustration of a hair cell. ....	4
Figure 3. Rendering of the inner ear .....	6
Figure 4. Vestibular cortical areas of the human brain .....	15
Figure 5. An exemplary caloric irrigation output. ....	21



## 1. General introduction

The ability to consciously experience sensory input enriches all aspects of our lives. We can enjoy the many facets of taste and fragrance of a good meal or lose ourselves in a concert or a painting. While people have a conscious representation of vision, audition, smell, and proprioception, the balance system has no direct conscious input, although it is a sense of its own just like the other modalities. What makes the sense of balance so different from our other senses?

The vestibular system is essential for our everyday life: our gaze and our posture are stabilized by the vestibular system, and, with the support of other sensory systems (e.g. vision, proprioception), moving objects can be distinguished from self-motion. In normal conditions we do not have access to the vestibular perception, but when the vestibular system is damaged, either in the periphery or in the central nervous system, people become well aware of its defect. Affected patients report vertigo, dizziness, oscillopsia, diplopia and/or nausea in an extent depending on the etiology, location and severity of the damage.

Although the vestibular system is a vital part of everyday life it remains poorly understood due to the following reasons. First of all, the inner ear is a very small structure embedded in the pars petrosa of the temporal bone making it very difficult to study. Second, the multisensory processing makes it very challenging to investigate the vestibular sense exclusively. In the living human, research tries to answer questions about the vestibular sense with magnet resonance imaging (MRI) which brings us to the third point: the MRI itself stimulates the vestibular system, but it is still not understood whether and how this affects the resting-state brain activity that has become one of the major workhorses for neurological and psychiatric research. Finally, the vestibular function is very often investigated indirectly through observing eye-movements. For removing one of the modalities, vision is often occluded (through closed eyes or with complete darkness). In complete darkness, video-oculography (VOG) is facing major challenges and resulting low quality VOG recordings need to be analyzed. Already established devices and software often fail to analyze these VOG recordings with a high accuracy.

Within this work, all of the above-mentioned challenges will be addressed. Hereby, it will focus on the healthy vestibular system and when applicable translation to the injured vestibular system will be made. To begin with, current knowledge about the anatomy and function of the peripheral and central vestibular system will be presented. Then the vestibulo-ocular reflex, one

of the fastest reflexes in the human system, will be described in detail as it offers good insights into the function of the vestibular peripheral system. Further, different techniques will be explained to stimulate the system of interest in clinical and research settings.

The research chapter of this PhD thesis is comprised of three manuscripts (first authorship) and one published paper (co-authorship) that will be presented in chapter 2. Research chapter. Imaging technologies have evolved over the past years, providing improved methodologies for characterizing and describing sensory systems in-vivo. The presented projects mainly used state-of-the-art imaging sequences in 3 T MRI. The first project presents a novel atlas of the labyrinth, the second introduces the first corticocortical vestibular connectome. In the third project, the influence of the magnet of the MRI onto the vestibular peripheral system and potentially also onto cortical networks is presented. It will be pointed out throughout this work, that spontaneous eye-movements can be a window for understanding or observing the function of the vestibular sense. We established a novel and freely available method for eye-tracking analyses using a deep learning approach. This published work is presented as the last project in the research chapter. A general discussion follows, which is ensured by the conclusion in the end (see chapter 3. General discussion and 4. Conclusion).

## **1.1 Anatomy and function of the vestibular system**

The vestibular system can be divided into a peripheral and a central component. The peripheral vestibular organ is part of the inner ear and sends vestibular information via nerve fibers to central structures. Not only brainstem and cerebellum, but also subcortical and cortical areas are known to receive vestibular input. Structures integrated in this bottom up processing will be described in detail in the following paragraphs.

### **1.1.1 Peripheral vestibular system**

#### **1.1.1.1 Semicircular canals and otolith organs**

The inner ear consists of three semicircular canals (SCC), the vestibule with the otolith organs, namely the utricle and saccule, and the cochlea. The semicircular canals and otolith organs respond to angular and linear accelerations, including gravity, whereas the cochlea contains the primary sensory cells involved in hearing. This peripheral vestibular and auditory system lies in the pars petrosa of the temporal bone. Since the focus of this thesis is the vestibular system, the cochlea will not be described in further detail. The inner ear with its substructures is visualized in Figure 3.

#### ***Semicircular canals***

The three SCC (horizontal/lateral, anterior, and posterior canals) are responsive to angular head acceleration in all three dimensions (i.e. pitch, yaw and roll). In proximity to the vestibule each SCC has one dilation, the ampulla. It contains the primary sensory neuroepithelium, i.e. the crista ampullaris, with mechanoreceptive hair cells. The crista is covered by the cupula, a gelatinous mass, which is deflected to the opposite direction of head movement. The hair cells in the canal of one side are depolarized, while those on the other side are hyperpolarized (Figure 1). For example, when the head turns to the left, rightward endolymphatic flow deflects the cupula in both horizontal SCC (hSCC). The left horizontal canal reacts with depolarization, and the firing rate of the relevant axons in the left vestibular nerve increases. In contrast, the cupula in the right horizontal canal is pushed to the same direction but reacts with hyperpolarization due to hair cell orientation, with a concomitant decrease in the firing rate of the related neurons (for details see chapter *1.1.1.2 Mechanoreceptive hair cells*).

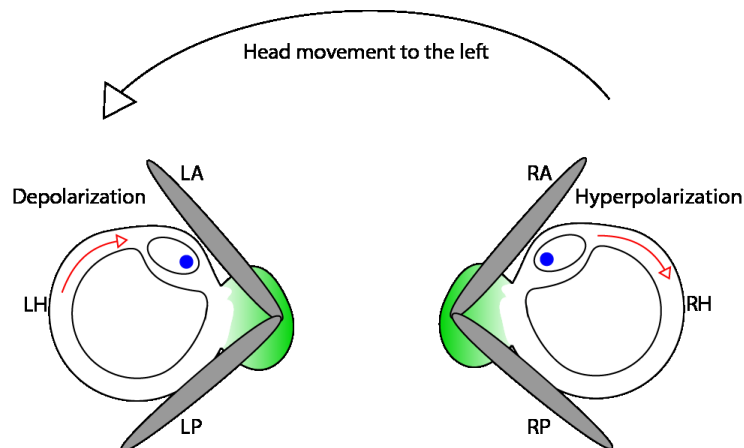


*Figure 1.* Schematic illustration of the three semicircular canals.

The left and the right semicircular canals (SCC) are shown from a superior view. With a head movement to the left, the endolymphatic fluid in the horizontal SCC (LH and RH) flows rightward (red arrow). Vertical SCC (LA, LP, RA, RP) are visualized in grey, utricle in green. Hair cell orientation of the horizontal SCCs' ampullae is depicted with the kinocilia being oriented towards the utricle (for simplification purposes indicated by the blue dot; for details see figure *Figure 2*). L = left, R = right, A = anterior, P = posterior, H = horizontal. The figure was generated with Adobe Illustrator CC 2017.

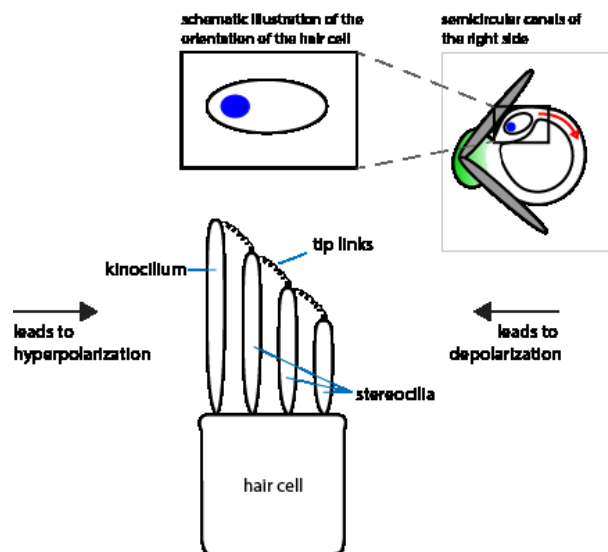


*Figure 2.* Schematic illustration of a hair cell.

The hair cell exists of several stereocilia and one longest kinocilium attached by tip links. The upper illustration is a simplification of hair cell orientation with the blue dot indicating the direction of kinocilium orientation. Arrows indicate movement direction that either leads to depolarization or hyperpolarization. The figure was generated with Adobe Illustrator CC 2017.

The canals of one side are approximately perpendicular to each other (Della Santina, Potyagaylo, Migliaccio, Minor, & Carey, 2005; Hashimoto, Naganuma, Tokumasu, Itoh, & Okamoto, 2005; Kim et al., 2015; Lee et al., 2013) so that a head movement in one plane causes activity in the SCCs in both the left and the right inner ear in functional pairs. The left and right horizontal (LHRH), left anterior and right posterior (LARP), and right anterior and left posterior SCC (RALP) canals are grouped together functionally (see Figure 1). If there is excitation of the SCC of one side of a functional pair, there will be inhibition of the other, and vice versa. It was assumed that the functional pairs were coplanar, that their predominant axis is in the same plane. The assumption of coplanarity was refuted only half a decade ago using MRI. MR images of 20 normal subjects revealed that the hSCCs of both sides have predominant axes that deviate  $15.1^\circ$  from another, planes of the LARP canals form a  $21.7^\circ$  angle and RALP canals a  $21.2^\circ$  angle (Kim et al., 2015).

Among all three SCC, the orientation of the hSCC is often of special interest as it is commonly stimulated with clinical routine techniques (see 1.3.1 Physical acceleration and 1.3.2 Caloric irrigation). Individual anatomical differences exist in the hSCC orientation with respect to Reid's plane (i.e. the locations of the infraorbital point and external auditory meatus, see Finby & Chynn (1982)). Using computer tomography, the angle of the (left) hSCC of 22 patients was found out to be  $19.9 \pm 7.0^\circ$  with respect to the x-y Reid's plane, generated by accessible manually determined skull landmarks (Della Santina et al., 2005). Despite this variation across subjects, Reid's plane is often used as an approximation for the orientation of the hSCC for simplification reasons (e.g. Boegle, Stephan, Ertl, Glasauer, & Dieterich, 2016). Nevertheless, in one of the studies within this thesis, the more accurate measurement of the actual hSCC orientation was considered (see 2.3 Magnetic vestibular stimulation and its effect on brain networks).

### ***Otolith organs***

The oval shaped otolith organs are comprised of the utricle and the saccule. Both respond to three-dimensional translational acceleration. Patches of otolithic sensory neuroepithelium, called maculae, are contained within each of the translational acceleration sensing organs. The macula is covered in a gelatinous mass with calcium carbonate particles embedded on the top, the so-called otoconia.

Translational accelerations (together with head tilt with respect to gravity) lead to inertial and shearing forces that then change the firing properties of the primary neuroepithelium. The utricle is oriented horizontally and primarily senses horizontal translational movement. The saccule is oriented perpendicular to the utricle and senses vertical translational movement (Babu, Schutt, & Bojrab, 2019).

Very importantly, the otolith organs sense gravity even in the absence of movement as the otoconia are pushing onto the macula with their weight. This makes the otolith organs a very interesting object of research in microgravity for instance (Hallgren et al., 2016).

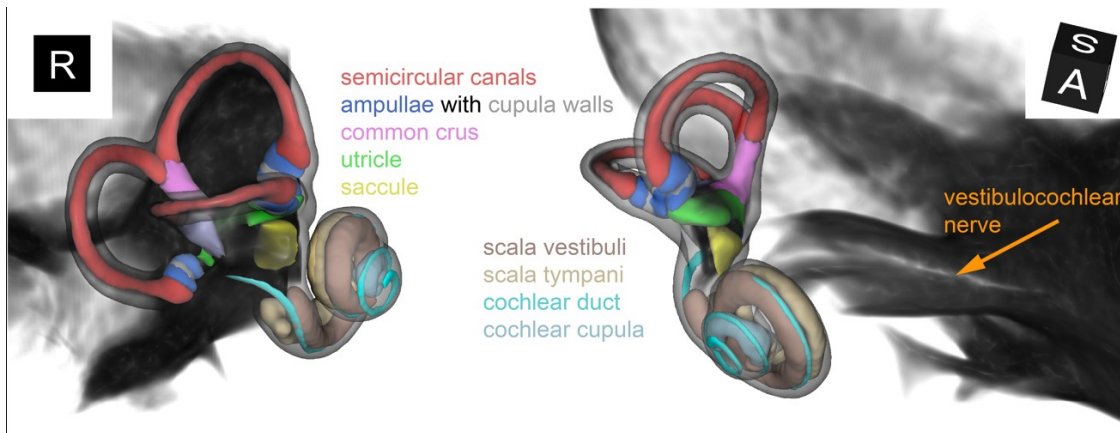


*Figure 3.* Rendering of the inner ear

Right inner ear and its segments (surface meshes) on the constructive interference in steady state (CISS) template volume rendering: IE-Map (Ahmadi, Raiser, Ruehl, Flanagan, & Eulenburg, 2019). From a right-lateral (left) and anterior-superior view (right). Black cubes in the corner of the illustrations indicate the exact orientation of the images: R = right, A = anterior, S = superior. Images were generated with 3D Slicer (Fedorov et al., 2012).

### 1.1.1.2 Mechanoreceptive hair cells

Vestibular sensation is based on the mechanoreceptive hair cells in the different organs of the vestibular system. Angular head acceleration leads to flow of the endolymphatic fluid in the SCC and translational head acceleration leads to inertial movement of the otoconia. These movements can lead to a deflection of the hair cells embedded in the crista ampullaris and the maculae respectively. On top of the hair cells there are stereocilia, rod like structures, that are ordered staircase like according to their height. After the longest stereocilia one kinocilium

follows. These cilia are interconnected through tip links at the top that can open or close ion channels through mechanically generated force (Barrett, Barman, Boitano, & Brooks, 2012). Figure 2 depicts the hair cell structures. When at rest, with no deflection of the cilia there is a spontaneous activity of the hair cells. During excitation the cilia bend towards the kinocilium and the tip links mechanically open channels for potassium influx. The resulting depolarization of the cell leads to additional opening of calcium channels at the base of the hair cells. Calcium influx prompts neurotransmitter release at the afferent nerve fibers and increased impulse frequency. With bending towards the smallest stereocilium the tip link tension is decreased which mechanically closes the channels at the top. In this state the cell hyperpolarizes, calcium channels are closed, and the impulse frequency is lowered.

The direction of flow that leads to excitation differs across the three SCC: while the horizontal SCC are excited with the endolymph flowing towards the ampulla, i.e. ampullopetal (see Figure 1), the vertical SCC (anterior and posterior) are excited with the endolymph flowing away from the ampulla, i.e. ampullofugal. In other words, the hair cells in the sensory epithelium of the ampullae of the horizontal SCC have a different directional tuning (kinocilia pointing away from the canal, towards the vestibule) compared to the vertical canals (kinocilia oriented towards the canal, away from the vestibule).

A similar pattern can be seen in the otoliths. Inertial drag and shearing forces lead to a movement of the otoconia and the gelatinous mass of the otolith system. This results in bending of the hair cells of the macula, and either in depolarization or hyperpolarization depending on the orientation of the hair cells. The otoliths' hair cells are arranged systematically. In both, the saccule and the utricle, the hair cells change their orientation along a line, the so-called striola, that runs approximately along the midline of the structure. In the utricle the kinocilia are oriented towards the striola. In the saccule, the kinocilia are oriented away from the it.

There are two types of hair cells that occur in all vestibular organs, namely type I and type II hair cells. Type I hair cells are found in the center of the crista ampullaris and the otolithic striolar zone, are flask-shaped and only present in amniotes (birds, reptiles and mammals). Type II hair cells are rather found in the periphery and extrastriola of the organs, they are cylindrical cells and exist in both non-amniotes (fish and amphibians) and amniotes (Eatock & Hurley, 2003). Therefore, type II hair cells are considered the evolutionarily older hair cell type (Liu, Koehler, Mikosz, Hashino, & Holt, 2016).

### **1.1.1.3 Atlases of the inner ear**

Atlases of the inner ear have been mainly created from ex-vivo 3D reconstructions of histological sections (e.g. Marianelli, Bassi Luciani, & Micera, 2012) or micro-CT studies (e.g. Gerber et al., 2017; Lee et al., 2013). All of them suffer from a low generalizability due to small sample sizes. Several works used geometric simplifications of substructures which might have led to overestimations or underestimations of the real size of the segments (Buckingham & Valvassori, 2001): cones were used as an approximation of the cochlea or spheres for the ampullae. Most published atlases are not openly available and are therefore not used by clinicians nor scientists. To overcome these obstacles, a novel morphologically unbiased and freely available atlas of the inner ear (IE-Map) is presented in chapter 2.1 IE-Map: a human in-vivo atlas template of the inner ear.

### **1.1.1.4 Afferent nerve fibers**

Afferent fiber units of the cranial nerve VIII (i.e. pars superior of the vestibulocochlear nerve) send information to the vestibular nuclei (see Figure 3). Horizontal and anterior SCC information as well as utricular information is sent via the superior division of the vestibular nerve (Hain, 2007). Saccular and posterior canal information is sent via the inferior division (Büttner-Ennever, 1999; Hain, 2007).

As with the primary sensory cells, there are two types of primary afferents that are distinguished due to their discharge regularity: regular and irregular afferents. Regular afferents preferentially send type II hair cell information upstream (Kathleen E. Cullen, 2012). Bouton fibers connect with bouton endings to these type II hair cells that are located in the periphery of the crista or macula. As the name suggests, regular afferents are characterized by a low variability in interspike intervals. The thicker, irregular afferents have, as the name suggests, a high variability in their interspike intervals and receive information from both hair cell types. First, calyx fibers innervate the centrally embedded type I hair cells with calyx endings. Second, dimorphic fibers innervate both type I hair cells with calyx endings and type II hair cells with bouton endings through irregular afferents (Cullen, 2012; Goldberg, 2000).

Because of the different dynamics of regular and irregular afferents, they are also thought to encode different aspects of self-motion information. Regular afferents encode information about the detailed time course of movements of the behaviorally significant frequency range (0-

20 Hz; Sadeghi, Chacron, Taylor, & Cullen, 2007). At low frequencies, like 0.5 Hz, regular and irregular afferents show similar gains. For information of higher frequencies, however, the irregular afferents outperform regular ones with higher gain (Kathleen E. Cullen, 2012; Sadeghi, Chacron, et al., 2007). Meaning, especially in higher frequency ranges, the irregular afferents encode changes in velocity and acceleration more quickly.

It is known by now that SCC afferents are most sensitive to the first derivative of rotational position independent of whether the head movement is active or passive: they are in phase with velocity of rotation (Sadeghi, Minor, & Cullen, 2007). The otolith organs, on the other hand, respond to the second derivative: besides gravity, the otolith afferents process linear acceleration (Angelaki & Dickman, 2000).

### **1.1.2 Central vestibular areas**

From the periphery, vestibular information is sent via the cranial nerve VIII to the ipsilateral vestibular nuclei (VN) in the brainstem and to the cerebellum (Ropper & Samuels, 2009). Subsequent higher order vestibular processing takes place in subcortical as well as cortical areas. The following paragraphs contain anatomical and functional descriptions of the most important infratentorial and supratentorial brain structures that are known to be involved in vestibular processing.

#### **1.1.2.1 Vestibular nuclei of the brainstem**

Besides some smaller vestibular nuclei in the brainstem (for further details see Barmack, 2003), the major VN receiving vestibular input are the medial, the lateral, the superior and the inferior vestibular nucleus (Khan & Chang, 2013; Tascioglu, 2005). The largest of those four nuclei, the medial vestibular nucleus, receives primarily hSCC input. The superior vestibular nucleus mainly receives input from the vertical SCC but also hSCC. The lateral vestibular nucleus is characterized by large cell bodies and receives primarily input from the otolith organs. The inferior vestibular nucleus largely receives otolith input as well. The VN of each side are connected via (inhibitory) commissure fibers and this crosstalk is not restricted to homotopic nuclei (Barmack, 2003).

Looking more closely at the vestibular processing of the VN there is much more convergence of SCC and otolithic input (Dickman & Angelaki, 2002; Highstein & Holstein, 2006). Horizontal SCC afferents project to the medial and superior vestibular nerve but also to the other two major VN

(Goldberg et al., 2012). Vertical SCC afferents send input primarily to the superior vestibular nucleus. The posterior SCC information projects to the lateral vestibular nucleus with frequent convergence of saccular information (Sato, Imagawa, Kushiro, Zakir, & Uchino, 2000). This is in line with previously mentioned convergence of saccular and posterior SCC information in the inferior division of the vestibular nerve (Büttner-Ennever, 1999; Hain, 2007). Utricular afferents terminate in all four vestibular nuclei (with a predominance for the inferior vestibular nucleus) as well as the abducens nucleus discovered in cats (Imagawa et al., 1995; Sato et al., 1996). Afferents of the feline saccule terminate mostly in the lateral and inferior and some in the superior vestibular nucleus. Few saccular afferents project to the reticular formation and the spinal trigeminal nucleus (Imagawa et al., 1998).

Considerable research has been carried out with head-restrained alert monkeys to gather further detailed knowledge on the neuronal level of VN (e.g. Boyle, Büttner, & Markert, 1985; Dickman & Angelaki, 2002; Waespe & Henn, 1977; Yakushin, Raphan, & Cohen, 2017). Studies have identified three neuron classes: (1) position-vestibular-pause (PVP) neurons, (2) vestibular-only (VO) neurons, and (3) eye-head (EH) neurons (Goldberg et al., 2012). PVP neurons stop firing (therefore the name position-vestibular-*pause*) during ipsilateral saccades or ipsilateral directed quick phases of vestibular nystagmus. Most of the PVP neurons can be found in the medial vestibular nucleus and are critical for the vestibulo-ocular reflex function (see chapter 1.2 Reflexive eye-movements as a window to the vestibular sense). VO neurons are unresponsive to eye-movements (e.g. saccades) but react to passive head motion (whole body rotation and translation). VO neurons are proposed to be involved in the vestibulo-collic reflex. EH neurons fire during smooth pursuit and during head movements when vestibulo-ocular reflex (VOR) is cancelled (Goldberg et al., 2012). EH neurons are also known as flocculus projecting neurons or floccular-target neurons due to their connections to the flocculus in the cerebellum (Langer, Fuchs, Scudder, & Chubb, 1985).

Besides the convergence of vestibular peripheral afferents (otolith and SCC) on this brainstem level there is also convergence of different modalities (visual input: Boyle et al., 1985; proprioceptive: Gdowski & McCrea, 2000; ocular motor: Sekirnjak & du Lac, 2006; visual motion: Waespe & Henn, 1977). The VN additionally receive input from several other brainstem, cerebellar and cortical areas. For higher order vestibular function these multimodal and multisensory interactions are essential. With the integration of visual, proprioceptive and vestibular cues as well as motor planning, humans are able to distinguish between active and

passive head movements and are able to control gaze and posture. The next paragraph will list the involved known cerebellar, subcortical and cortical regions.

#### **1.1.2.2 Cerebellar vestibular areas**

The cerebellum receives primary (from the vestibular afferents) and secondary (from the VN) vestibular input (Ango & Dos Reis, 2019; Langer et al., 1985). Thereby, it is believed that the cerebellum tunes both reflex and active movement (Manzoni, 2005).

Few cerebellar regions are reported to be involved in the sensory vestibular input processing. Primary afferents largely originate at the three SCC and end (as mossy fibers) in the ipsilateral nodulus and uvula (Balmer & Trussell, 2019; Barmack, 2003; Barmack & Yakhnitsa, 2013; Dow, 1936). Nodulus and ventral uvula have both been associated with the velocity storage (Angelaki & Hess, 1994). Secondary afferents end bilaterally in cerebellar regions, mainly uvula-nodulus and flocculus (Barmack, 2003). But also other deep cerebellar nuclei as for example the fastigial nucleus are reported to modulate and process both earth horizontal rotations and otolith-driven information (Shaikh, Ghasia, Dickman, & Angelaki, 2005). The Purkinje cells of the posterior cerebellar vermis on the other hand exclusively encode inertial motion (Yakusheva et al., 2007). Flocculus and ventral paraflocculus are both involved in gaze stabilization, and smooth pursuit and they keep compensatory eye movements plastic (Hain & Helminski, 2007; Ramos, Cal, Carmona, Weber, & Zuma E Maia, 2019).

Most of the studies claiming vestibular involvement of the cerebellum show that it processes and adjusts vestibular information according to different sensory inputs (mostly visual and/or vestibular). How exactly the cerebellum is involved in vestibular processing is far from understood and further investigations are needed. Technological improvement and future studies will help gain more knowledge about its vestibular involvement.

#### **1.1.2.3 Subcortical vestibular areas**

It is not easy to identify subcortical vestibular structures in-vivo with a high validity and confidence yet in human imaging studies. The signal-to-noise ratio (SNR) of MR images of deeper brain structures is lower than that of cortical regions since coil elements are furthest away from these brain structures. In addition, there are more motion artifacts due to pulsation in these areas, i.e. sub-voxel motion. Therefore, research on the human vestibular thalamus and other

subcortical structures are sparse. The studies that do attempt to identify human subcortical vestibular areas and their connections to cortical regions using MRI measurements suffer from poor MRI data quality in these deep brain structures. Therefore, these results should be treated with caution; we will focus on what is known from animal models instead.

The vestibular thalamic nuclei have been examined in non-human primates with single neuron recordings (Marlinski & McCrea, 2008), retrograde (Meng, May, Dickman, & Angelaki, 2007) and anterograde tracer injections (Lang, Büttner-Ennever, & Büttner, 1979). For instance, the ventroposterior and ventrolateral thalamic nuclei in primates were found to have vestibular sensitivity (Lang et al., 1979; Marlinski & McCrea, 2008). A retrograde tracer study revealed rotation and translation-sensitive cells in the dorsolateral thalamic region (Meng et al., 2007). A detailed description of the vestibular involvement of different thalamic nuclei can be found in previous work (e.g. Sherman, 2005; Wijesinghe, Protti, & Camp, 2015).

Similar to the thalamus, the hippocampus is a deep brain structure that is challenging to study in the living human brain. The hippocampus and parahippocampal cortex play an important role in navigation, for which vestibular input plays an important role. Place cells, grid cells, and head direction cells, that encode specific signals for navigation, have been found in the hippocampal and parahippocampal areas of rodents (Moser, Kropff, & Moser, 2008; Taube, 2007). A review of the literature showed that information from the SCC and otoliths are essential for the generation and stability of the head direction signal (Yoder & Taube, 2014). Some of these cells are reported to exist in humans as well; grid cells are present in the human entorhinal cortex (Doeller, Barry, & Burgess, 2010; Horner, Bisby, Zotow, Bush, & Burgess, 2016; Jacobs et al., 2013). Putative head direction cells are suggested to be present in the retrosplenial cortex and thalamus (Shine, Valdés-Herrera, Hegarty, & Wolbers, 2016). For further reading, please refer to detailed reviews about the hippocampus and its vestibular and navigational cell structures (e.g. Eichenbaum, 2017; Goodroe, Starnes, & Brown, 2018; Rowland, Roudi, Moser, & Moser, 2016; Yoder & Taube, 2014).

To date, MRI cannot overcome the obstacles given to accurately visualize these deeper brain structures in-vivo due to the sub-voxel motion (Terem et al., 2018). New methods and additional investigations will help us to fully understand the role of the human thalamus and hippocampus as part of vestibular sensory processing.

#### **1.1.2.4 Cortical vestibular areas**

In comparison to the subcortical structures, human cortical vestibular structures have been relatively well defined through animal studies and functional MRI (fMRI) studies of the human brain. Classical neuroscience has used experiments with unimodal sensory information to probe the sensory processing in primary sensory cortices (e.g. Hubel & Wiesel, 1959). In audition and vision as well as the motor and somatosensory system, unimodal stimulation is feasible and primary cortices are well understood. Cortical vestibular processing, on the other hand, is more difficult to understand, due to the large amount of multimodal and multisensory integration that occurs in already at the level of the primary vestibular nuclei.

##### ***Cortical vestibular areas in non-human primates***

Still a number of regions have been revealed that are important for cortical vestibular information processing. The parietoinsular vestibular cortex (PIVC) plays an essential role in higher order vestibular processing in non-human primates (Guldin, Akbarian, & Grüsser, 1992; Guldin & Grüsser, 1998). Rotational and translational vestibular stimulation excites neurons in the PIVC (Chen, DeAngelis, & Angelaki, 2010). Approximately 30% of PIVC neurons receive vestibular input and even more also respond to proprioceptive input (Hitier, Besnard, & Smith, 2014; Shinder & Taube, 2010). Further cortical brain areas involved in vestibular processing are the anterior parietal cortex of somatosensory area 2v and area 3aV (containing neurons responding to SCC afferents). Non-human primate area 3aNV, a subarea containing neck representations, receives vestibular input (Guldin & Grüsser, 1998). In the posterior parietal cortex, around 30% of neurons in the ventral intraparietal area (VIP) are responsive to rotations around the vertical axis (Bremmer, Klam, Duhamel, Ben Hamed, & Graf, 2002). Guldin and Grüsser (1998) reported that a marginal percentage of area 7 neurons responded to vestibular input. According to Guldin et al. (1992) most of the aforementioned cortical regions (PIVC, 3aV, Area 7) are unresponsive to otolith stimulation. Area 2v however is reported to receive otolith as well as SCC input (Büttner & Buettner, 1978). The (dorsal) medial superior temporal area (MST/MSTd) is another identified vestibular area often associated with self-motion (Fetsch, Wang, Gu, Deangelis, & Angelaki, 2007; Gu, Watkins, Angelaki, & DeAngelis, 2006). Further vestibular projections have been identified in the periarculate cortex (Ebata, Sugiuchi, Izawa, Shinomiya, & Shinoda, 2004).

### ***Human vestibular cortical areas***

All of the cortical vestibular areas identified in non-human primates have now been localized in humans as well. The human equivalent to the PIVC is considered to be the parietal operculum OP2 (Eickhoff, Weiss, Amunts, Fink, & Zilles, 2006; zu Eulenburg, Caspers, Roski, & Eickhoff, 2012). Damage in PIVC/OP2 leads to an impaired subjective vertical (Brandt, Dieterich, & Danek, 1994) indicating that OP2 is involved in vestibular processing. The human homologue area to area 7 is most likely the inferior parietal lobule, which has been shown to respond to head movements and changes in gaze direction (Petit & Beauchamp, 2003). Functional imaging in humans identified activity in cortical areas PIVC/OP2, area 3a, human area MST (hMST), the anterior and posterior cingulate, visual posterior sylvian area (VPS) and the frontal eye field (FEF) during vestibular stimulation via caloric irrigation (for details of the method see chapter 1.3.2 Caloric irrigation) (Fasold et al., 2002). Otolithic and galvanic vestibular stimulation revealed cingulate sulcus visual (CSv) activation (with electroencephalography: Ertl et al., 2017; with MRI: Smith, Wall, & Thilo, 2012). The lateral and medial premotor areas are closely connected with area OP2 and seem to also play a role in the vestibular cortical network (zu Eulenburg et al., 2012). Additionally, the vestibular system receives a large amount of feedback from, for instance, motor areas that constantly update and calibrate the vestibular signals.

The aforementioned regions are thought to make up the important cortical structures in human cortical vestibular processing, and have recently been brought together as a vestibular atlas containing each of the relevant regions as regions of interest (ROIs) (zu Eulenburg, Stephan, Dieterich, & Ruehl, 2018). This vestibular atlas (see Figure 4) was taken as the basis for the corticocortical vestibular connectome which is presented in chapter 2.2 The human corticocortical vestibular connectome, the second research project in this thesis.

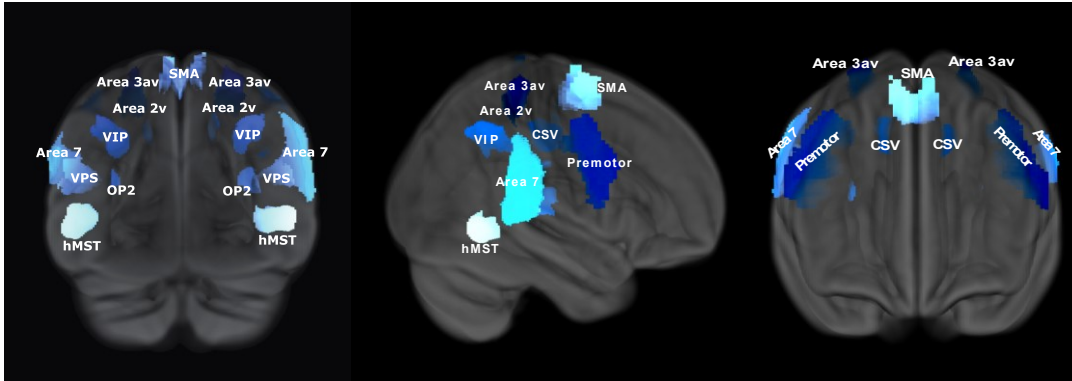


*Figure 4.* Vestibular cortical areas of the human brain

From a posterior, lateral and frontal view. Cortical areas involve: Area 2v, Area 3av, SMA = supplementary motor area, Premotor, CSV = cingulate sulcus visual, Area 7, VPS = visual posterior sylvian area, OP2, VIP = ventral intraparietal area, hMST = human medial superior temporal area. This atlas was visualized according to the vestibular regions reported by zu Eulenburg et al. (2018).

## 1.2 Reflexive eye-movements as a window to the vestibular sense

The requirement for clear vision is a stable image on the retina despite head movements. This is made possible with the vestibulo-ocular reflex (VOR). It is one of the fastest reflexes in primates as it has a latency of only 5-6 ms (Huterer & Cullen, 2002). The VOR was first described in 1933 by Lorente de Nò studying this reflex in rabbits (Nó, 1933). In our everyday life the VOR is beneficial and essential for gaze stabilization and corrects for the broad range of head movements (Huterer & Cullen, 2002).

Its pathway includes only three neurons. Under normal circumstances, a head rotation leads to movement of the endolymphatic fluid in the according SCC. The optimal and maximal excitation for the hSCC occurs for instance when the horizontal canal is aligned with the plane of head movement. The cupula is thereby deflected and the afferent fibers from the crista ampullaris send this information to the medial vestibular nucleus. PVP neurons are the major players amongst the vestibular nuclei neurons involved in the horizontal VOR. The PVP neurons send excitatory projections via the medial longitudinal fasciculus to the contralateral abducens motoneurons (i.e. extraocular motoneurons) and mediate the according compensatory eye-movement: the angular VOR. EH neurons with their floccular connections are involved in calibrating and adjusting the VOR gain (Hain & Helminski, 2007; Manzoni, 2005). This becomes very important due to changes in the environment (e.g. new glasses) or effects of aging. For vertical head rotations and the according compensatory eye-movement, the superior vestibular nucleus is involved in the pathway instead of the medial vestibular nucleus.

The gain of the VOR is defined as the ratio of eye velocity to head velocity. In the ideal case, eye velocity is equal to head velocity causing in a gain of 1. There are distance-related changes in VOR gain reported in primates (Chen-Huang & McCrea, 1999) indicating that there is constant modification of the VOR. The gain can be artificially altered through vestibular-visual mismatch stimuli to study adaptation mechanisms. For example, magnifying lenses (Demer, Goldberg, Jenkins, & Porter, 1987) or reversing prisms (Gonshor & Jones, 1976) let the environment appear larger or mirrored. The retinal slip and therefore eye-movements need to be bigger (magnifying lenses) or to the opposite direction (reversing prisms). After some initial time where gain is not ideal, adaptation takes place and VOR gain improves. Floccular input through EH neurons mediates this adaptation (reviewed in Cullen, 2008). Using incremental VOR adaptation, a frequency selection in VOR adaptation was found (Rinaudo, Schubert, Figtree, Todd, &

Migliaccio, 2019). In incremental VOR adaptation the vestibular-visual stimulus mismatch increases over time and leads to faster VOR gain adaptation than the classical methods (Rinaudo et al., 2019). For more detailed information about adaptation in VOR it is referred to the recent comprehensive review of Schubert and Migliaccio (2019).

If head movement exceeds a certain amplitude or duration, the eyes reach a limit in the complementary direction. Hence an eye-movement to a new start position (in head/body movement direction) is made and from there the compensatory eye-movement is further proceeded (Goldberg et al., 2012). This phenomenon is known as vestibular nystagmus. Nystagmus is characterized by a slow phase in one direction and a quick correcting phase into the opposite direction.

When this VOR pathway from the vestibular to the visual peripheral system is impaired, patients cannot stabilize their gaze. This gaze instability is called oscillopsia and is most severe during rapid head movements. Affected people have problems walking or driving due to the severely reduced VOR gain and are extremely impaired in their everyday-life (Halmagyi et al., 1990). Whether the VOR is functionally intact can be tested clinically with the head impulse test for instance (see chapter 1.3.1 Physical acceleration).

In clinical and scientific settings, the VOR is tested with head mounted eye-tracking systems. Some settings require the suppression of fixation to investigate the participants' spontaneous eye-movements. This can be achieved either with Frenzel glasses (Frenzel, 1956), occluded vision through endarkening glasses or complete darkness. When performing simultaneous VOG the latter two are the settings of choice in combination with infrared light cameras. However, in these special settings eye-tracking faces major challenges and most conventional eye-tracking devices fail to capture the pupil with a high precision due to dilated pupils or heterogenous illumination (Schnipke & Todd, 2000). Further, if the set-up requires to mount the eye-tracking camera very close to the eye (e.g. inside the MRI scanner) focusing can be a challenge. We therefore established a novel offline eye-tracking analysis method with the help of deep learning algorithms presented in chapter 2.4 Pupil segmentation and gaze estimation using deep learning (DeepVOG).

There are two other important physiological vestibular reflexes. First, the vestibulo-collic reflex (VCR) through which head and body postures are coordinated and maintained. This reflex compensates for the head-in-space or body in space velocity with movement of the head/body

in the opposite direction (Peterson, Bilotto, Goldberg, & Wilson, 1981; Wilson et al., 1995). The VCR is comprised of a more complex pathway than the VOR and is reviewed by Goldberg and Cullen (2011). The second important vestibular reflex is the vestibulo-spinal reflex (VSR). The VSR controls and modulates trunk and limb muscles in order to preserve balance and posture. It is based on many inputs from the vestibular periphery, visual system, brainstem and cerebellum (Khan & Chang, 2013). The lateral and medial vestibular nuclei and VO neurons are involved in the pathway of these reflexes (Boyle, Belton, & McCrea, 1996; Goldberg & Cullen, 2011; Khan & Chang, 2013). Adaptation can also be observed in these other vestibular reflexes: for instance the VSR has been reported to go through adaptation in astronauts (Minor, 1998).

### **1.3 Vestibular stimulation techniques**

Stimulating the vestibular system in an experimental environment requires a way to excite the vestibular system in a controlled manner. There are several ways to stimulate the vestibular system, the most common of these techniques involve: (1) physical, (2) thermal, (3) electrical and (4) magnetic stimulation. Most of these techniques aim for stimulation of the horizontal canal because this is the easiest part of the vestibular system to stimulate – in part because of its location. The otolith organs can be stimulated with vestibular evoked myogenic potentials (reviewed by Rosengren, Colebatch, Young, Govender, & Welgampola, 2019), but will not be covered in this thesis.

#### **1.3.1 Physical acceleration**

Two common ways to physically stimulate the vestibular system, in particular the semicircular canals are with the head impulse test (HIT) or stimulation with a rotational chair. The Halmagyi/head impulse test (Halmagyi & Curthoys, 1988) was refined through a video system for guaranteeing a more standardized and objective detection of potential corrective saccades, and termed video-HIT or vHIT (MacDougall, Weber, McGarvie, Halmagyi, & Curthoys, 2009). The readout from the vestibular system is the VOR (see chapter 1.2 Reflexive eye-movements as a window to the vestibular sense), which should be equal but in the opposite direction of the head movement to maintain a fixation point. The gain between the head motion and the reflexive eye-movement is computed, and values that are different from one are considered to be pathological.

The (v)HIT can be easily performed as a bedside test as it takes only little time, no instruments are required, and it is not invasive (Kheradmand & Zee, 2012). A study comparing three different vHIT devices reported mean vHIT gains values between 0.91 to 1.05 in normal participants (Janky, Patterson, Shepard, Thomas, & Honaker, 2017). With an impaired vestibular system, patients show corrective saccades during the head impulse test: unilateral vestibular hypofunction leads to a reduced VOG gain ( $< 1$ ) and corrective saccades when the head is moved quickly towards the affected side (Halmagyi et al., 1990; Ramos et al., 2019). For bilateral vestibulopathy these corrective saccades can be observed in both head directions leading to a lower gain (Ramos et al., 2019).

The second common way to physically test the SCC function is with a rotational chair. Just like the vHIT, it aims to measure the VOR with a physiologic stimulus, however in a slightly lower frequency range. Unlike the HIT not only the head but the whole body is moved passively. People are sitting in a chair that rotates along the center axis. Most commonly rotation is performed along the earth vertical axis and provides information about the hSCC function. Some devices can even rotate along all three axes allowing for testing of the VOR function of the vertical SCC (Dits, Houben, & van der Steen, 2013). Otolith function has been suggested to be measurable (along with the SCC function) with the axis of whole body rotation moved to the front or back, known as eccentric rotation (Takimoto, Imai, Okumura, Takeda, & Inohara, 2016). This measurement is mainly used in scientific settings as it requires more complicated hardware and the tests take a lot longer than vHIT.

### **1.3.2 Caloric irrigation**

Another test to objectify hSCC function is the caloric irrigation. This test stimulates the vestibular system at low frequencies and artificially, with no actual movement or acceleration of the head. This test is performed with water (alternatively air) applied unilaterally to the outer ear canal (for a standardized time of 30 seconds) with the participant lying in a supine 30° upward position. In this position, the hSCC is approximately perpendicular to the earth horizontal. Caloric irrigation stimulates the horizontal canal (as it is the closest canal to the outer ear canal) in the low frequency range (Perez & Rama-Lopez, 2003) which results in a physiological nystagmus that slowly increases in frequency, lasts for about two minutes and gradually diminishes. The slow phase velocity (SPV) of the nystagmus is the objective measurement for both ears in both conditions: warm and cold irrigation. *Figure 5* depicts the results of the caloric irrigation for one healthy participant.

One influencing factor for the strength and direction of the occurring nystagmus is the temperature of the water. Water below body temperature results in nystagmus with the quick phase away from the stimulated ear (i.e. stimulating the right ear results in a leftward quick phase), and water above body temperature leads to a quick phase of the nystagmus ipsilaterally to the stimulated ear. Another influencing factor is the head position with respect to gravity. The maximal response is obtained in a supine position with the hSCC forming a 90° angle with the earth horizontal (Behrman, 1942). At 100° there is an unexpected null point in the nystagmus

response (Coats & Smith, 1967). Not as expected with the hSCC being parallel to earth horizontal. This led to the idea that otoliths might modulate the caloric response (Coats & Smith, 1967). Another alternative explanation was that the temperature change in the hSCC leads to a change in neuronal fire rate (Hamid, 2005). Supporting this, monkeys with blocked SCC still showed a caloric induced nystagmus however in a lesser degree than before blocking the SCC (Paige, 1985).

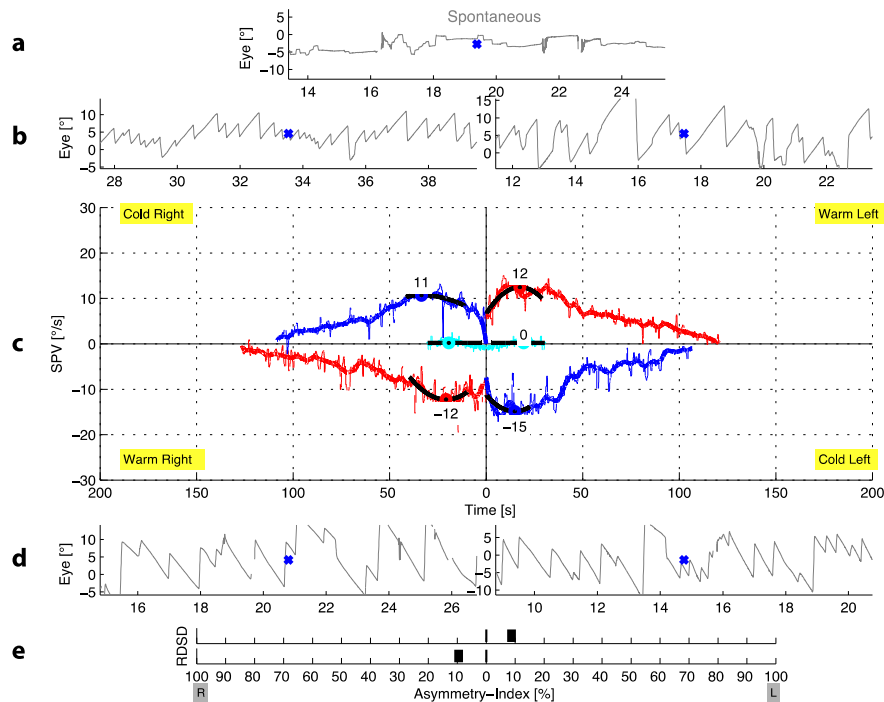


**Figure 5.** An exemplary caloric irrigation output.

Data visualized is the output from a participant of the MVS study. Panel a: excerpt of the spontaneous eye movements [in °]. Panel c: Spontaneous eye movements without stimulation are shown in cyan, warm water irrigation (44°C) depicted in red, cold water irrigation (30°C) depicted in blue. Values written close to the curves are the maximum SPV values recorded during each irrigation (positive values indicate rightward SPV, negative values leftward SPV). Panel b and d: excerpt of the quickest eye-movements during the measurement for both conditions and both sides. Panel e: asymmetry-Index. SPV = slow phase velocity; R = right, L = Left; RD = 'Richtungsdominanz' / direction dominance, SD = 'Seitendifferenz' / side difference.

The original hypothesized mechanism of caloric irrigation, presented in the early 20<sup>th</sup> century was that temperature changes the density of the endolymphatic fluid (Bárány, 1906). This convection theory claims that the density change due to warming of the lateral part of the

horizontal canal results in expansion of the endolymphatic fluid in this lateral part causing a deflection of the cupula (Jones, 1974; Wit, Spoelstra, & Segenhout, 1990).

The caloric test is an excellent measurement for peripheral vestibular function. Repeated testing however, revealed a large variability (Munro & Higson, 1996), and there is a temperature order effect with initial warm water causing larger differences (Noaksson, Schulin, Kovacovics, & Ledin, 1998). One main advantage with caloric irrigation is that the stimulation is unilateral and can therefore offer a better insight of laterality differences (i.e. asymmetry index). Caloric irrigation leads to more information about the vestibular sensitivity than the vHIT. Further it can be applied easily in a clinical setting and even in the MRI for investigating vestibular cortical areas for instance (Fasold et al., 2002).

### **1.3.3 Galvanic vestibular stimulation**

Another artificial vestibular stimulation technique is galvanic vestibular stimulation (GVS). Probing the human vestibular system with GVS is possible through modulated cathodal and anodal currents externally applied on the bony outcropping of mastoid bone behind the ear. GVS can either be applied unilaterally or bilaterally (Kim, 2013). Cathodal stimulation of one side and anodal inhibition of the other side leads to a realistic imitation of rotational head and/or body movement in roll plane (Schneider, Glasauer, & Dieterich, 2002).

GVS can activate sensory hair cells as well as vestibular afferent fibers as tested in the amphibian model (Gensberger et al., 2016). The exact mechanism of GVS in humans is still under debate. GVS predominantly affects irregular afferents due to their thicker diameter (Blair & Erlanger, 1933). It is unclear whether the stimulation is selective for SCC or otolith organs. Research suggested that mainly otolithic responses are perceived by the subject, i.e. tilt in roll plane (Bent, Bolton, & Macefield, 2006). However, with GVS in complete darkness a horizontal and torsional nystagmus is observed implying SCC activation (MacDougall, Brizuela, & Curthoys, 2003). Today, common opinion is a non-selective activation of vestibular organs as outlined in detail by Curthoys and MacDougall (2012).

Unfortunately, GVS does not only stimulate the vestibular system; the vagal nerve is stimulated as a side effect. At low stimulations frequencies, the results are changes in heart rate and blood pressure due to GVS blocked vasovagal responses in rats (Cohen et al., 2011; Cohen, Martinelli, Xiang, Raphan, & Yakushin, 2017). An increase in insulin secretion has been observed because

of the vagal stimulation making GVS a potential therapeutic option for diabetes (Sailesh, Archana, & Mukkadan, 2015; Sailesh & Mukkadan, 2014). As another side effect, subjects reported a metallic taste during GVS without nausea (Lobel, Kleine, Bihan, Leroy-Willig, & Berthoz, 1998) and increased saliva production (Wilkinson, Zubko, & Sakel, 2009) which is known to be a product of vagal stimulation (Ueda et al., 2016).

In humans currents up to 10mA have been used and electrodes are typically placed bilaterally on the mastoids (Aw, Todd, & Halmagyi, 2006). A variety of waveforms have been used: for example short current pulses (Phillips et al., 2015), sinusoidal stimuli (Bent et al., 2006), step stimuli (Wardman, Day, & Fitzpatrick, 2003), ramp stimuli (current building up) (Helmchen, Rother, Spliethoff, & Sprenger, 2019), and white noise GVS (Wuehr et al., 2018). GVS can also be applied inside the fMRI making it an excellent tool for understanding cortical vestibular function (e.g. Bense, Stephan, Yousry, Brandt, & Dieterich, 2001; review by Dlugaiczyk, Gensberger, & Straka, 2019).

#### **1.3.4 Magnetic vestibular stimulation**

Humans often report dizziness when they enter the bore of the MRI or when they are close to a strong magnet (Schenck, 1992; Weintraub, Khoury, & Cole, 2007). This dizziness can be explained by the electromagnetic induction (EMI) generated through a magnetic field and movement (of either the magnetic field or the conductor). Vestibular stimulation has additionally been described when humans are in a strong static magnetic field. This phenomenon has been explained by the magnetohydrodynamic (MHD) Lorentz force that acts upon the vestibular system (Roberts et al., 2011). This force is generated by the strong magnetic field in combination with flowing currents. These two factors are present when a human is in the MRI machine: 1. ionic currents created by the endolymphatic fluid in the inner ear and 2. a strong magnetic field of the MRI system. In the MRI the MHD mechanism and currents entering the utricular hair cells lead to a continuous deflection of the cupula in the ampullae: a constant acceleration is mimicked. This stimulation of the vestibular system can be measured indirectly using the physiological VOR (see 1.2 Reflexive eye-movements as a window to the vestibular sense) and resulting nystagmus. This phenomenon related to the static magnetic field is now known as magnetic vestibular stimulation (MVS).

In the pioneer work on the MVS effect, Roberts et al. (2011) measured eye-movements and changes in the magnetic field while participants were put in and out of the MRI bore without MRI data collection (no HF fields or fluctuating magnetic gradients). Complete darkness prevented fixation and potential suppression of eye movements. When entering the bore all participants showed a horizontal nystagmus that increased in amplitude of the SPV with increasing EMI. When the change in magnetic field returned to zero, but the static magnet remained, the SPV decreased, but not to zero. The SPV reached a stable plateau over the course of approximately 10 minutes in a static strong magnetic field. The horizontal nystagmus suggests that the horizontal SCC is predominantly stimulated. The authors interpreted this slow change to a stable SPV as an adaptation to the static magnetic field (Jareonsettasin et al., 2016; Roberts et al., 2011).

Additional work on the MVS effect has suggested that the Lorentz force also acts on the anterior semicircular canals (Ward et al., 2017; Ward, Roberts, Della Santina, Carey, & Zee, 2014). This has been demonstrated by exposing patients with unilateral labyrinth failure to MVS. These patients showed not only horizontal but also vertical components in their magnetically induced eye-movements (Ward et al., 2014). The direction of the vertical component was explained by Ward and colleagues with referring to Ewald's law of equilibrium (Ewald, 1882). Depending on the side of the damaged labyrinth patients showed either an upbeat or a downbeat nystagmus component elicited through the MVS (Ward et al., 2017). In healthy subjects the vertical component is canceled out through excitation of one and inhibition of the other vertical SCC. But if the vertical canals are not equally stimulated in the static magnetic field, for instance the head is tilted in roll plane, a vertical nystagmus should be observed (Roberts et al., 2011). Activation of the anterior SCC should also lead to torsional eye-movements and according to the laws of Ewald, they sum up which is observed in healthy subjects (Otero-Millan, Zee, Schubert, Roberts, & Ward, 2017; Ward et al., 2017).

Interestingly, recent findings suggest that intact utricles are necessary for a magnetic field induced nystagmus (Ward et al., 2018). By investigating mice with a mutation in the *Nox3* gene, which leads to an absence of otoconia in these animals but intact hair cells and synapses, they could specifically remove otolith function. None of the *Nox3* mice showed a magnetically induced nystagmus in any orientation (nose or tail first in horizontal canal aligned with earth horizontal; additionally, +10 degrees, and -10 degrees orientation), although the VOR itself was

unaffected. This is in line with the fact that the otoliths are thought to be the major factor contributing to the net ionic current that is necessary for the MVS effect (Ward et al., 2018). While participants report vertigo or some perception of rotation when entering the bore of the MRI machine, this sensation ceases after a short amount of time, although nystagmus persists. Ward et al. assumed that this nystagmus would eventually disappear after adaptation (2017). However, nystagmus in humans persists over a maximally reported period of 90 minutes (Roberts et al., 2011; Ward et al., 2017, 2014). Still, fluctuations are visible during the plateau phase of the SPV of the nystagmus that we will address in 2.3 Magnetic vestibular stimulation and its effect on brain networks.

#### **1.3.4.1 Influencing factors for the strength of the MVS effect**

The participant's head position is one factor that influences the magnitude of the occurring horizontal nystagmus during MVS. In general, the more the head of an individual is tilted backwards, the stronger the MVS effect (Roberts et al., 2011). Head pitch was measured with Reid's plane, which defines an unambiguous orientation of the human skull by defining a line that goes from the inferior margin of the orbit, or eye-socket, to the center of the external ear canal. A change in tilt, will change the relative orientation of the hSCC with respect to B<sub>0</sub>, which will lead to the strongest effect if these two are at right angles to one another.

Additionally, asymptomatic individual differences were recorded during MVS (Pawlak-Osinska et al., 2019; Roberts et al., 2011). Participants with the same head tilt angle with respect to B<sub>0</sub> showed large differences in the magnitude of the resulting SPV (Roberts et al., 2011). One explanation might be individual differences in the anatomical orientation of the hSCC with respect to Reid's plane (see section 1.1.1.1 *Semicircular canals and otolith organs*). This anatomical variability across subjects potentially influences the described variation in nystagmus strength.

The strength of the MVS effect scales with the strength of the magnetic field (Boegle et al., 2016; Roberts et al., 2011) an effect that could also be found in the strength of the resulting BOLD signal at rest (Boegle et al., 2016). The polarity of the magnetic field hereby determines the direction of the nystagmus.

#### **1.3.4.2 MVS as unimodal bilateral stimulation of the vestibular system**

Although the MVS is not a natural vestibular stimulation, it might be the only pure vestibular stimulation. Unimodal stimulation is crucial to detect primary sensory areas in the brain. In audition and vision as well as proprioception, unimodal stimulation is feasible and primary cortices are quite well defined. But with the vestibular sense things are more complicated. With common techniques vestibular stimulation, other sensory modalities are stimulated as a side effect (see chapter 1.3 Vestibular stimulation techniques). Besides the vestibular input, the rotary chair provides additional proprioceptive, during caloric irrigation a thermal stimulation through the water is present, and galvanic vestibular stimulation produces sensations on the skin under the electrodes (even with anesthetics). MVS seems to be the only pure and unimodal vestibular stimulation because no other sensory information is existent. It is a very unnatural stimulation, though, as it mimics a constant acceleration. A similar pattern of stimulation cannot be reached naturally over such long time.

#### **1.3.4.3 Effect of MVS onto the brain**

Little is known about whether and how the MVS effect influences the function of the brain. If it does, this could confound studies using fMRI, particularly resting state fMRI (rsfMRI). Boegle et al. (2016) investigated modulation in brain areas with the same scaling factor as the strength of the magnetic field in 1.5 and 3 Tesla MRI systems. They focused on the default mode network (DMN) since this resting state network (RSN) is often altered in patients with unilateral vestibular neuritis (Klingner, Volk, Brodoehl, Witte, & Guntinas-Lichius, 2014). Assuming a linearity of the Lorentz force, with increasing strength of the magnetic field there MVS increasingly modulated activation in the cerebellar vermis, the anterior cingulum and the calcarine sulcus (Boegle et al., 2016). The focus of the third research chapter 2.3 Magnetic vestibular stimulation and its effect on brain networks tries to answer the question whether MVS affects rsfMRI results.

## **1.4 Aim of the thesis**

Through improved technologies and methodologies, the human vestibular system can now be characterized in greater detail than ever before. This thesis aims first, to describe the human structural peripheral vestibular system in a non-biased way in a large sample size.

The second aim is to establish the first human corticocortical vestibular connectome through high resolution MRI measurements. This connectome is compared to non-human primate data. It gives insight into the architecture of the cortical vestibular network and reveals potential disadvantages of the method used.

Thirdly, the thesis aims to reveal the impact of magnetic vestibular stimulation on the brain through the MRI machine itself. The magnetic vestibular stimulation is the only “pure” vestibular stimulation without confounding stimulation of other modalities but also without sensory perception. The question remaining is whether the MVS effect is a confound for rsfMRI measurements. For achieving this, a novel eye-tracking analyses was developed since other programs failed to detect the pupil in complete darkness inside the MRI scanner, which forms the basis of the fourth and final research chapter in this thesis.



## 2. Research chapter

This PhD thesis consists of three detailed manuscripts (chapters 2.1, 2.2, and 2.3; all first authorship) and one peer-reviewed published paper (chapter 2.4; co-authorship):

A novel morphologically unbiased atlas of the peripheral inner ear is presented in the first subchapter (see 2.1 IE-Map: a human in-vivo atlas template of the inner ear). In the second subchapter, the first human corticocortical vestibular connectome is introduced including structural comparisons to non-human primates (see 2.2 The human corticocortical vestibular connectome).

Whether and how the magnetic field of the MRI affects brain activity and functional connectivity networks at rest is presented in the third subchapter (see 2.3 Magnetic vestibular stimulation and its effect on brain networks). As an excursion and prerequisite for the third study, an innovative eye-tracking analyses method was established and is presented in the last subchapter (2.4 Pupil segmentation and gaze estimation using deep learning (DeepVOG)).

The following paragraphs enclose each paper or manuscript with a preceding summary and explanation of author contributions.



## 2.1 IE-Map: a human in-vivo atlas template of the inner ear

Ahmadi, S.A.\* , **Raiser, T.M.\*** , Rühl, R.M., Flanagan, V.L., zu Eulenburg, P. (submitted).

\* Seyed-Ahmad Ahmad and Theresa Marie Raiser contributed equally to this work.

The article “IE-Map: A human in-vivo atlas template of the inner ear” was recently submitted for publication in the journal *Nature Scientific Reports*, with a preprint online version on medRxiv<sup>1</sup> uploaded in November 2019.

### Summary

IE-Map represents the first in-vivo morphologically unbiased atlas for the human inner ear (IE). It is a validated atlas comprised of all known neuroanatomical dimensions used to date in neuroimaging of the labyrinth and its auditory and vestibular organs from the largest dedicated cohort to date (126 inner ears). The atlas represents a unique multi-sequence structural MR imaging approach, achieving high-resolution (0.2mm) along the way completely non-invasively (hence without the use of a contrast agent or application of radiation), and through more accurate measurements of the substructures compared to any previously published works on the topic. With sharing all templates of the IE-Map as open-source material (github, neurovault) we provide this new, robust and widely applicable tool not only for imaging-based neuroscientific research in the future but as a starting point for a wide array of clinical applications (neurotology disease classifications, aging and plasticity of the peripheral auditory and vestibular system, vestibular implants, detection of neurodevelopmental disease, etc.).

### Author contributions

The following authors contributed to this work: Peter zu Eulenburg designed the study together with Seyed-Ahmad Ahmad and Theresa M. Raiser. Theresa M. Raiser and Ria M. Rühl collected the data under the supervision of Virginia L. Flanagan and Peter zu Eulenburg. Data analyses was done by Seyed-Ahmad Ahmad. Seyed-Ahmad Ahmad and Theresa M. Raiser wrote the paper as shared first authors with input from all listed authors.

---

<sup>1</sup> <https://www.medrxiv.org/content/10.1101/19011908v1>

# IE-Map: A novel in-vivo atlas template of the human inner ear

Seyed-Ahmad Ahmadi<sup>a,b,c,\*\*</sup>, Theresa Raiser<sup>a,d,\*\*</sup>, Ria Maxine Rühl<sup>a,c</sup>,  
Virginia L. Flanagin<sup>a,d</sup>, Peter zu Eulenburg<sup>a,d</sup>

<sup>a</sup>*German Center for Vertigo and Balance Disorders (DSGZ),  
Fraunhoferstr. 20, 82152 Planegg, Germany*

<sup>b</sup>*Faculty of Informatics, Technical University of Munich,  
Boltzmannstr. 3, 85748 Garching, Germany*

<sup>c</sup>*Department of Neurology, Klinikum der Universität München,  
Marchioninistr. 15, 81377 Munich, Germany*

<sup>d</sup>*Graduate School of Systemic Neurosciences, Ludwig-Maximilians-Universität München,  
Großhaderner Str. 2, 82152 Planegg, Germany*

---

## Abstract

Brain atlases and templates are core tools in scientific research with increasing importance also in clinical applications. Advances in neuroimaging now allowed us to expand the atlas domain to the vestibular and auditory organ, the inner ear. In this study, we present IE-Map, an in-vivo template and atlas of all known substructures of the human labyrinth derived from multi-modal high-resolution magnetic resonance imaging data in a non-invasive manner (no contrast agent or radiation). We reconstructed a common template from 126 inner ears (63 normal subjects) and annotated it with 94 established landmarks and semi-automatic segmentations. Quantitative substructure analysis revealed a correlation of labyrinth parameters with total intracranial volume. No effects of gender or laterality were found. We provide the validated templates, atlas segmentations, surface meshes and landmark annotations as open-access material, to provide neuroscience researchers and clinicians in neurology, neurosurgery, and otorhinolaryngology with a widely applicable tool for computational neuro-otology.

*Keywords:* neuro-otology, morphological template, atlas, inner ear,

---

\*Corresponding author: [aahmadi@med.lmu.de](mailto:aahmadi@med.lmu.de)

\*\*Seyed-Ahmad Ahmadi and Theresa Raiser contributed equally to this work.

## 1. Introduction

The pervasiveness of brain imaging techniques across many disciplines has increased the relevance of standardized templates of brain structures and developing atlases for the structural and functional substructures within these templates. Almost the entire human central nervous system has been mapped: various templates and atlases have charted out the human cortex, the subcortical nuclei, charting the thalamus and the cerebellum [1, 2, 3, 4] based on MRI. Recently, a dedicated neuroimaging template was also developed for the brain stem and spinal chord [5]. These templates provide a means to make group comparisons and to do quantitative assessments of individual patients, and as such have found applications in neurology [6, 7], in neurosurgery [8, 9] and in neuroscience [10]. In comparison, few works have proposed templates and corresponding atlases to chart the anatomy of sensory organs like the inner ear, and the few existing studies have focused on ex-vivo imaging using (micro-)CT, for comparative neuroanatomy in the field of anthropology.

The inner ear contains several important substructures [11, 12]: (1) The three semicircular canals with their ampullae that shelter the cupula containing the sensory hair cells, which detect head rotation. (2) The macular organs (utricle and saccule), which respond to translational head motion and convey the gravitational force vector [13]. Anatomically, the utricle and the saccule together form the vestibule. (3) The cochlea, which is a separate inner ear organ for hearing. The cochlea consists of the scala vestibuli, the scala tympani and the cochlear duct (with hair cells). These structures spiral  $2.57 \pm 0.28$  times from the base to the cochlear cupula, or apex of the cochlea [12]. Physiological and morphological alterations of the cochlea can result in hearing deficits or loss whereas affections of the semicircular canals or otoliths lead to vertigo and balance disorders [14, 15]. The shape of the labyrinth structures carries valuable functional and phylogenetic information about the inner ear over the course of

mammalian evolution [16]. Inner ear imaging aids neurological examination and neuroscientific analysis. A quantitative assessment of the inner ear organs often requires a preceding segmentation of the relevant target regions and a sub-parcellation into its key structures like the semicircular canals, vestibule and cochlea. As has been shown for brain images, segmentation with a template image and atlas is a versatile and robust tool for anatomic delineation [17]. Beyond deformable atlas segmentation, image templates and structural atlases are fundamental tools for statistical shape analysis [18, 8] and group-based image analysis [19].

Previous anatomical and morphological analyses of the inner have emphasised the cochlea and avoided the complex anatomy of the peripheral vestibular system. Models of the cochlea have been assessed for cross-species comparative neuroanatomy [16, 20, 21, 22], neuronavigation of cochlear electrode implantation and simulation [23, 24, 25], cochlear shape modeling and surgical trauma assessment [12]. In the field of anthropology, previous studies have investigated the inner ear through shape comparison of labyrinthine structures in ancient Egyptian mummies versus today [26], or in form and function of the mammalian inner ear across species [27].

The majority of these analyses were based on ex-vivo micro-CT as the imaging modality [28, 29], few also providing cyto-architecture scans based on synchrotron radiation [30] or ex-vivo ultra-high-field MRI [31]. A few studies have reported detailed measurements of the inner ear's membranous structures [32], and of the semicircular canals in particular, again based on ex-vivo micro-CT [33, 21] and multi-detector CT [34]. Recently, in-vivo visualization of the inner ear with MRI, either with [35, 36] or without Gadolinium-based contrast agents [37, 38, 39, 40, 41] has been used for the detection of endolymphatic hydrops [39] and for diagnosis of sensorineural hearing loss associated with inner ear lesions [42]. Furthermore, MRI sequences, such as *Constructive Interference in Steady State* (CISS) imaging, which have low susceptibility and a high contrast-to-noise ratio, have been used to image the inner ear for the detection of leakage of labyrinthine and cerebrospinal fluids [43].

The purpose of this study was to build a template and atlas of the human inner ear and its substructures, based on multiple non-invasive in-vivo MRI sequences. By harnessing the signal and contrast-to-noise advantages of multiple MRI sequences, all without invasive contrast agents or radiation, we believe the inner ear imaging procedures and corresponding template will have a widespread clinical applicability. We then demarcated the anatomical substructures of the inner ear by registering a previously available inner ear atlas, based on micro-CT, to our template. With this atlas, quantitative size and volume information of the inner ear substructures can be extracted for each individual and side. After validation of the template and atlas with the previous literature, we demonstrate the usability of the template and atlas by examining three questions about the population statistics of the inner ear. 1. Does head size, as measured by intracranial volume, influence labyrinth measurements? 2. Does gender have an effect in inner ear structure size? 3. Does ear laterality play a role in inner ear dimensions? In summary, we successfully created an inner ear template and atlas that can be applied to a wide range of MRI sequences. Our template and atlas are comprehensive, applicable, accessible, and generalizable, forming the basis for future non-invasive neuroimaging studies of the inner ear under the umbrella term computational neuro-otology.

## **2. Materials and Methods**

### *2.1. Subject cohort*

The template was created from a cohort of 63 healthy, right-handed subjects (32 female, 31 male, age:  $26 \pm 2.3$  years). To make the template and atlas representative and generally applicable to both left and right inner ears, left and right inner ears are treated independently, resulting in 126 inner ears in total that were used for template building. All subjects gave written informed consent regarding participation in this study. The local ethics committee of the Ludwig-Maximilians-Universität, Munich, approved the study in accordance with the latest revision of the Helsinki declaration from 2013.

## 2.2. MR imaging and pre-processing

We acquired multi-modal, isotropic 3D MRI data (whole-head T1- and T2-weighted at 0.75 mm, CISS measurement of the labyrinth at 0.5 mm isotropic) in a clinical 3T scanner with a 64-channel head/neck coil (Siemens Skyra, Erlangen, Germany). The high-resolution T1-weighted MPRAGE sequence was collected with GRAPPA in an interleaved mode and an acceleration factor 2 (TR 2060ms, TI 1040 ms, TE 2.17 ms, flip angle 12 deg., FoV 240 mm, slice thickness 0.75 mm, 256 slices, A-P phase encoding, echo spacing 7.9 ms, bandwidth 230Hz/Px, prescan normalized). A T2-SPACE sequence with varying flip angles (TR 3200 ms, TE 560 ms, FoV 240 mm, slice thickness 0.75 mm, 256 slices, A-P phase encoding direction, GRAPPA acceleration factor 2, echo spacing 4.06 ms, bandwidth 625Hz/Px, prescan normalized) was collected for an optimized contrast between tissue types for the atlas generation, to detect brain pathologies and achieve whole-head coregistration for all data. In addition, we acquired an optimised CISS sequence for labyrinthography (TR = 8.56 ms, TE = 3.91 ms, flip angle = 50 deg., FoV = 150 mm, slice thickness = 0.50 mm, right-left phase encoding direction, sequential multi-slice mode, tune up shimming, activation of head coil elements 5-7 and the cranial neck coil elements only, bandwidth 460Hz/pixel, the average of two repetitions was built, total time of acquisition 13:40 minutes) for achieving the best possible contrast and resolution for inner ear structures.

Head motion was controlled by a dedicated head fixation device (®Pearltec Crania Adult, Schlieren, Switzerland). All MRI image data underwent stringent quality assessment before inclusion in the study, using a state-of-the-art MRI quality control toolkit (MRIQC) [44]. As pre-processing, we performed a correction for MRI field inhomogeneity using the N4 bias correction algorithm [45]. Further, we performed a rigid intra-subject registration of T1 and CISS volumes to the T2 volume, before proceeding to template building. Intra-subject registration was performed using Advanced Normalization Tools (ANTs), with normalized mutual information for multi-modal alignment [19].

Total intracranial volume (TIV) as a potential covariate for head size was

obtained via segmentation of the T1-weighted image with the CAT12 toolbox (version 12.6 release 1450, <http://www.neuro.uni-jena.de/cat/>) of the Structural Brain Mapping group (Christian Gaser, Jena University Hospital, Jena, Germany), a toolbox implemented in SPM12 (v7487, Statistical Parametric Mapping, Institute of Neurology, London, UK).

### *2.3. Template building*

Template building was performed in three steps: 1) full-brain template building and annotation, 2) axial re-orientation of all subjects to the Reid’s axial plane, and 3) final inner ear template building. The template building method utilized in steps 1 and 3 is a state-of-the-art algorithm provided by the ANTs toolkit [19]. It is designed for computation of a geodesic mean template that optimally represents the average anatomic shape from a set of input volumes. Critically, all ANTs components are capable of multi-variate image registration, allowing us to fully leverage the multi-sequence appearance of the inner ear and its surrounding anatomy in T1, T2 and CISS MRI during template reconstruction. The high accuracy and robustness of ANTs registration and template normalization methods have been validated by demonstrating state-of-the-art performance in several internationally recognized medical image processing challenges [17, 46].

In the first step, we computed a full-brain template for our cohort using T1- and T2-weighted MRI sequences. For the full-brain template, CISS volumes had to be omitted since they were acquired only within a narrow axial field-of-view (FOV) centred around the inner ear region. In the full-brain template, we manually annotated four landmarks for identification of the Reid’s axial plane, i.e. the locations of the infraorbital point and external auditory meatus in the left and right hemisphere [47]. We further placed two landmarks at the locations of the left and right inner ear, for a consistent localization of the inner ears across all subjects. This procedure is illustrated in Fig. 1.

In the second step, we re-oriented source volumes to Reid’s standard plane. This was a necessary pre-processing step for the inner ear template building

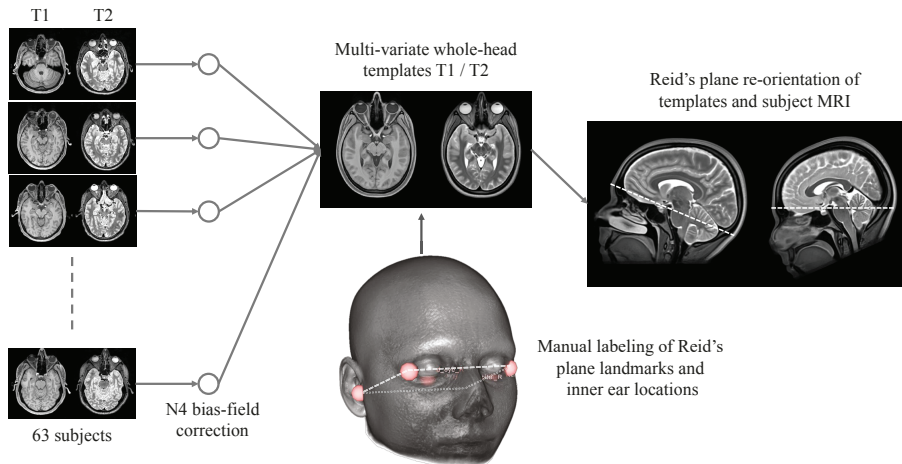


Figure 1: Full-brain template building and annotation, for re-orientation of the axial plane to Reid’s standard plane, and for localization of left/right inner ear region-of-interests (ROI). *(Print in colour.)*

(step 3), which took crops around the inner ear’s region-of-interest (ROI) as input. Pre-aligning these crops resulted in less out-of-border interpolation, i.e. less black margins and a better registration result at the ROI borders during template building. A side benefit of this step was that the lateral semicircular canal became approximately aligned with the axial plane, given the common assumption of coplanarity of the lateral semicircular canals with Reid’s standard plane [48, 49, 50]. The landmarks for Reid’s plane and inner ear FOV centres were transformed into the volumes of all input subjects beforehand, using a full-brain registration from template to individual spaces, followed by visual inspection for quality control. We then computed Reid’s plane parameters using least-squares fitting to the four landmarks, and re-oriented the axial plane in all volumes accordingly.

In the third step, we used the inner ear landmarks identified in step 2 to place region-of-interest (ROI) bounding boxes at the left and right inner ear. At these locations, the T2, CISS and T1 volumes were cropped ( $4 \times 4 \times 3$  cm) and resampled (0.2 mm isotropic, bi-cubic B-spline interpolation) with a ROI bounding

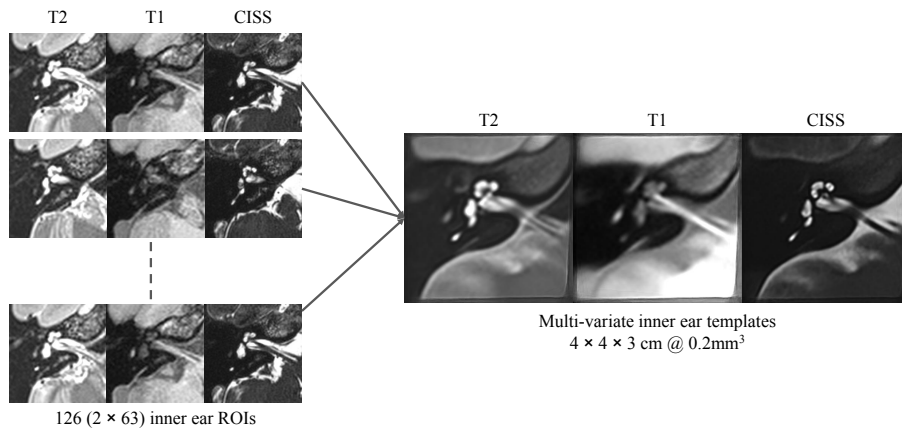


Figure 2: Inner ear template building input: three of 126 example multi-variate inputs (T2, T1, CISS) of the inner ear region are shown, centred, Reid’s plane aligned and cropped with a  $4 \times 4 \times 3$  cm ROI. The geodesic mean template is reconstructed and shown on the right side.

box that included all relevant inner ear structures as well as the vestibulo-cochlear nerve. As performed during pre-processing on the full brain volumes, we linearly registered the CISS and T1 crops to the T2 crop, to ensure a perfect alignment of fine structures of the inner ear across all MRI contrasts. Cropped volumes were centred and all left inner ears were mirrored with respect to the sagittal plane, to match the orientation of the right inner ear. This latter step ensured that the obtained template is unbiased with respect to afference laterality (sidedness) of the inner ear structures. The above steps resulted in 126 localized, multi-variate MRI volumes, oriented to Reid’s plane and hence roughly oriented with the lateral semicircular canal in the axial plane. These volumes served as input to the multi-variate template building algorithm, which computed three inner ear templates at an isotropic target resolution of 0.2 mm. The procedure and resulting template are illustrated in Fig. 2.

#### 2.4. Atlas annotation

The multi-sequence template was segmented into anatomic regions in order to obtain an atlas of the inner ear. Segmentations were obtained in parts by transferring fine-grained surface meshes of the semicircular canals, vestibule

and cochlea from *Ariadne*, a publicly available atlas and segmentation toolkit of the inner ear derived from ex-vivo micro-CT data [20]. From this toolbox, we leveraged micro-meter accurate surface meshes as delineations of inner ear structures, by registering them to our multi-variate MRI template.

Due to the lack of an accompanying micro-CT intensity volume in the *Ariadne* toolkit, we performed a volumetric registration and geometric transfer through alignment of the entire inner ear’s outer surface. For our T2 template volume, we computed the outer iso-surface of the inner ear at an optimal intensity threshold obtained by Otsu’s method [51], followed by manual removal of background structures that were obtained during thresholding. For the micro-CT data, we utilized the bony surface mesh provided in the *Ariadne* toolbox. Next, we voxelized both the T2 surface mesh and the micro-CT surface mesh of the inner ear at an isotropic resolution of 0.1 mm, and computed signed Euclidean distance transforms (SDT) for both meshes [52]. These SDT representations served as surrogate image volumes during deformable image registration, yielding a non-linear deformation field from *Ariadne* atlas space into our template space. All micro-CT surfaces including semicircular canals, vestibule, and cochlear ducts (i.e. scala vestibuli, scala tympani and cochlear duct) were then transferred onto our template volume and voxelized at the resolution of 0.2 mm. The resulting labelmap was manually post-processed, based on visual inspection, to ensure alignment of labels with the three intensity channels T2, T1 and CISS.

The cochlea regions were pre-segmented by intensity-based thresholding of the CISS template. The threshold was set to obtain a clear separation of the scala tympani and vestibuli. Both regions were refined manually using basic image processing operations such as connected components, and surface smoothing. The cochlear duct was transformed from the David micro-CT atlas [20] using the computed deformation fields.

The procedures described above were realized using various tools in the open-source software toolkits ANTs (deformable surface registration) [19], 3D Slicer (segment editor effects: threshold, connected components, paint, scis-

sors, margin) [53] and SimpleITK (Euclidean SDT computation with Signed-DanielssonDistanceMapImageFilter) [54].

Using landmark annotation in 3D Slicer [53], we further annotated multiple anatomic landmarks of the inner ear structures described in related literature. For the sake of reproducibility and annotation consistency, we placed all landmarks on the Otsu-threshold iso-surface of the T2 template volume. The landmark locations on the T2 iso-surface are visualized in detail in Fig. 3. Following guidelines and 3D visualizations in [33], we annotated the three semicircular canals regarding width and height, as well as inner widths and heights measured at three positions (Figure 3, panels A and B). We also followed instructions in [33] to compute the height and three width measures of the common crus. The height and width of the vestibule were described in [55]. The total inner ear length was described in [56] (Figure 3, panel C). The placement of landmarks for measurement of cochlea width, length and height was described in [57] (Figure 3, panel D). While cochlear height here was defined on an oblique 3D cut through the volume, earlier approaches defined cochlear height on the coronal plane [58, 59], which we also measured for comparison.

### 2.5. Statistical methods

First-order group statistics on inner ear dimensions and volumes were computed in terms of mean and standard deviation. Normality of variables throughout this work was tested using a Kolmogorov-Smirnov (KS) test with Lilliefors correction, at an alpha level of  $p < 0.05$  [60]. Comparisons of the semicircular canal dimensions between the left and right inner ear sides were performed using multiple paired statistical tests (t-test for normal distributed data, Mann-Whitney U test for non-normal distributions). We corrected p-values after multiple testing using the Benjamini-Hochberg False Discovery Rate (FDR) algorithm [61], results were considered as significant at a post-correction alpha level of  $p < 0.05$ . For the main general inner ear measures (total inner ear volume, total inner ear length, oblique cochlea height, and radii of anterior/posterior/lateral SCCs), we investigate a potential correlation with overall head size,

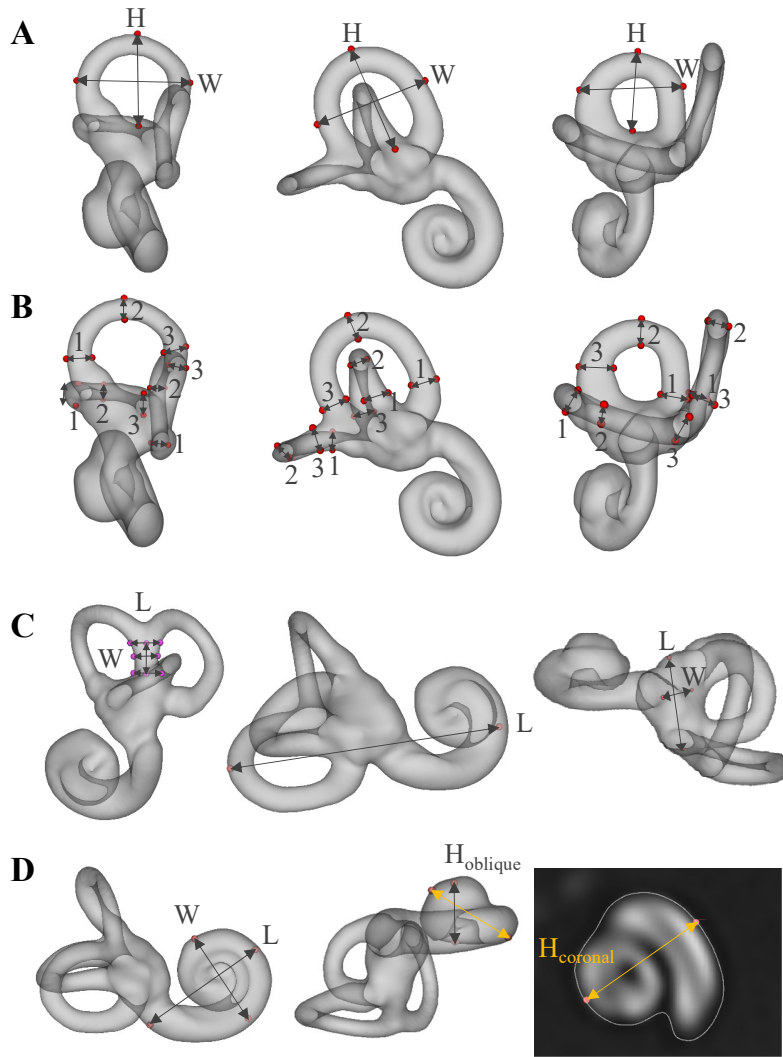


Figure 3: Inner ear landmark annotations in template space. Panel A: width and height of the anterior (left), posterior (middle) and lateral (right) semicircular canals. Panel B: inner widths and heights of semicircular canals, measured at three locations each (1-3). Panel C: height and three widths of the common crus (left), total inner ear length (middle), and vestibule length and width (right). Panel D: width, length and height of the cochlea. Cochlea height was tagged and measured using both the coronal plane approach (gold arrow) [58, 59], and the oblique plane (i.e. 3D) approach (grey arrow) [57]. H = height, W = width, L = length. *(Print in colour.)*

represented by TIV. Correlation is reported as Pearson’s correlation coefficient  $r$ , again at a significance level of  $p < 0.05$ . After clarification of the role of TIV, we tested gender effects, i.e. whether there was a significant difference between male and female cohort subgroups. These tests were performed on the two major inner ear measures, total inner ear volume, total inner ear length. To account for head size, we performed an Analysis of Covariance (ANCOVA), with TIV as the relevant covariate [62]. Statistical computation was performed using python implementations in `scipy.stats` [63], Pingouin [64] and `Statsmodels` [65], as well as MATLAB (The Mathworks Inc., MA, USA). Where available and applicable, we provide comparable values from literature that we are aware of, by referencing reported mean and standard deviation values.

### 3. Experiments and Results

#### 3.1. Inner ear template and atlas

The reconstruction of the T2- and T1-weighted MRI volumes into unbiased full-brain templates was successful. Using this template, the localization of both inner ears and the re-orientation of the axial slice to Reid’s standard plane could be executed for all subjects and inner ears without manual intervention. Subsequently, the reconstruction of the T2-, T1-weighted and CISS inner ear template volumes at 0.2 mm isotropic resolution was performed successfully using the ANTs toolkit.

Volume renderings can be seen in Fig. 4. The rendering transfer function was set as a linear ramp between the minimum and maximum voxel intensity for each template, no manual adjustments other than a shift of the centre intensity (T1: 1.2; T2: 1.5; CISS: 2.3) was necessary to achieve the visibility of inner ear structures as displayed. As noticeable from the rendering, the inner structures of semicircular canals, vestibule and cochlea are clearly visible and are morphologically correct. The volume rendering does not suffer from noise artefacts typical in single-subject volumes, which we attribute to the fact that the multi-variate templates on average have a 1.7 times higher signal-to-noise

MRI sequence	Template volumes	Individuals Mean	Individuals SD
T2	4.02	2.49	0.20
CISS	3.26	1.73	0.14
T1	3.13	1.85	0.28

Table 1: Signal-to-noise ratios in multi-variate MRI templates are on average 1.7 times higher than in individuals’ volumes, resulting in improved visibility of structural details. Rendering can be performed nearly free of noise (cf. Figure 4), and fine-grained structures like the separation of cochlear ducts become visible in templates that are sometimes not even clearly discernible in individual volumes (cf. Figure 4, panel E).

ratio (SNR) than the mean-SNR in single-subject volumes (see Table 1). SNR is approximated as the mean voxel intensity divided by the standard deviation of voxel intensities inside the inner ear ROI [66].

### 3.2. Cohort measurements and atlas validation

The characterization of the three semicircular canals (see Table 2) was compared to previously reported results using micro-CT in ex-vivo specimen [33]. In general, our atlas produces larger values than reported in literature, however, the error margin never exceeds the original image resolution of T1- and T2-weighted MRI (0.75 mm). Overall, the sub-voxel accurate distance measures demonstrate that the computed template has morphometric properties that are in line with previously ex-vivo micro-CT studies. The same applies to landmarks of the common crus (see Table 3) and the cochlea (see Table 4), which all corresponded to values in literature within a margin of less than 0.5 mm.

Inner ear volume measurements are also largely in line with related literature (see Table 5), with a notable difference of almost +50 mm<sup>3</sup> in total inner ear volume. Deviations from mean volumes reported in [67] can be attributed due to simplified geometric approximations made in that previous study. For example, authors in [67] modelled the ampullae as spheres with 2 mm diameter (i.e. 4.2 mm<sup>3</sup>; ours: 3.54/2.27/3.59 mm<sup>3</sup> for ant/post/lat ampulla), saccule as

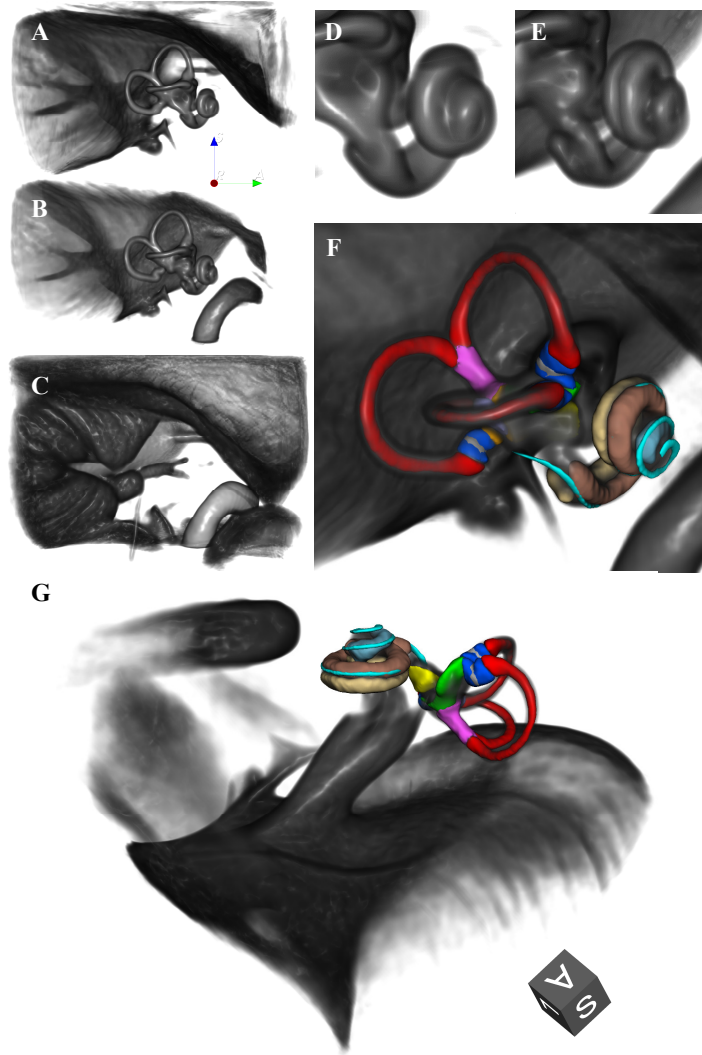


Figure 4: Volume renderings of inner ear templates and atlas (ROI size:  $4 \times 4 \times 3$  cm; resolution: 0.2 mm isotropic; viewpoint: right-lateral view onto right inner ear). Panels: A. T2 template; B. CISS template; C. T1 template; D. Closeup cochlea in T2 template; E. Closeup cochlea in CISS template, with a clear separation of scala tympani and vestibuli; F. Atlas surface meshes on CISS template volume rendering. G. Same as F, with a different perspective focussing on the vestibule. Colours and regions: red: semicircular canals; blue: ampullae; pink: common crus; grey: cupula walls; green: utricle; yellow: saccule; brown: scala vestibuli; beige: scala tympani; light blue: cochlear cupula; cyan: cochlear duct. (*Print in colour.*)

a hemisphere of 2 mm diameter (i.e. 2.1 mm<sup>3</sup>; ours: 2.6 mm<sup>3</sup>), utricle as an irregular oval averaging 1.35 mm in diameter and 5.5 mm in length (i.e. 7.9 mm<sup>3</sup>; ours: 8.8 mm<sup>3</sup>), and the cochlea as a cone with 8 mm diameter and 5 mm height (i.e. 83.8 mm<sup>3</sup>; ours: 94.4 mm<sup>3</sup>). Especially the larger volume measurements of the cochlea and the total inner ear region indicate an increased estimate of the inner ear region by our T2 iso-surface, by 11% and 12%, respectively.

### 3.3. Cohort analysis and statistics

As detailed in Table 2, paired univariate testing with multiple testing correction yielded no significant differences regarding sidedness in any of the semicircular canals measures (height, width, radius, as well as internal height and width measured at three distinct points from the distal to the common crus). We further investigated the major inner ear dimensions, i.e. total inner ear length, total inner ear volume, oblique cochlea height, and radii of the three semicircular canals. First, we found all these values to be normally distributed (KS-test with Lilliefors correction,  $p > 0.05$ ). Second, we investigated a possible correlation of selected inner ear measures with brain size measured by TIV. We found the total inner ear volume and length, as well as the radii of the anterior and posterior semicircular canals (SCC) to be moderately and significantly correlated with brain size, while the oblique cochlea height and the radius of the lateral SCC were not significantly correlated (cf. Figure 5). Third, we investigated a potential difference between male and female subjects in our cohort regarding the main and most robust inner ear measures, i.e. the total inner ear length and total inner ear volume. Since TIV was found to be a confounding variable for these measures, we performed an ANCOVA, correcting for TIV as a covariate. Our ANCOVA tests yielded no significant differences for the investigated inner ear measures (total inner ear length:  $p = 0.182$ ; total inner ear volume:  $p = 0.088$ ). In other words, after accounting for overall brain size, gender difference cannot explain residual differences in measured inner ear characteristics.

SCC	Dimension	Mean	SD	Mean [33]	SD [33]	$\Delta$ Mean	p-val L vs. R
Ant	Height	6.4	0.5	6.5	0.5	0.1	0.074
	Width	8.2	0.5	8.0	0.5	0.2	0.943
	Radius	3.7	0.2	3.6	0.2	0.1	0.088
	Internal width 1	1.8	0.1	1.2	0.2	0.6	0.995
	Internal width 2	1.4	0.2	0.9	0.2	0.5	0.779
	Internal width 3	1.6	0.2	1.2	0.1	0.4	*0.995
	Internal height 1	1.5	0.2	1.0	0.1	0.5	*0.571
	Internal height 2	1.3	0.2	0.7	0.1	0.6	0.943
Post	Internal height 3	1.6	0.2	0.9	0.1	0.7	0.327
	Height	7.0	0.6	6.7	0.6	0.3	0.921
	Width	7.7	0.6	7.7	0.5	0.0	0.695
	Radius	3.7	0.3	3.6	0.2	0.1	0.623
	Internal width 1	1.8	0.1	1.4	0.2	0.4	0.695
	Internal width 2	1.7	0.2	1.5	0.2	0.2	0.995
	Internal width 3	1.6	0.2	1.4	0.2	0.2	*0.995
	Internal height 1	1.4	0.1	1.0	0.1	0.4	0.779
Lat	Internal height 2	1.3	0.2	1.0	0.1	0.3	*0.995
	Internal height 3	1.4	0.2	0.9	0.1	0.5	*0.995
	Height	5.0	0.4	4.9	0.6	0.1	0.088
	Width	6.6	0.4	6.5	0.7	0.1	0.571
	Radius	2.9	0.2	2.9	0.3	0.0	0.088
	Internal width 1	1.8	0.2	2.1	0.3	0.3	*0.716
	Internal width 2	1.7	0.2	1.7	0.3	0.0	*0.995
	Internal width 3	2.2	0.1	1.7	0.2	0.5	0.164
Internal height 1	1.8	0.2	1.2	0.2	0.6	0.995	
Internal height 2	1.4	0.1	0.8	0.1	0.6	*0.954	
Internal height 3	1.7	0.1	1.2	0.3	0.5	*0.530	

Table 2: Dimensions of the anterior (Ant), posterior (Post) and lateral (Lat) semicircular canals (SCC). Unit: [mm]. \* indicates non-normal distribution (Kolmogorov-Smirnov test with Lilliefors correction,  $p < 0.05$ ).

	Mean	SD	Mean [33]	SD [33]	$\Delta$ Mean
Length	2.3	0.2	2.0	0.5	0.3
Width 1	2.2	0.2	1.6	0.3	0.6
Width 2	1.9	0.2	1.5	0.3	0.4
Width 3	2.3	0.2	1.9	0.4	0.4

Table 3: Dimensions of the common crus. Unit: [mm].

Distance	Mean (our)	SD (our)	Mean (lit.)	SD (lit.)	$\Delta$ Mean	Reference
Cochlea height coronal	5.58	0.26	5.31	0.52	0.27	[58]
	5.58	0.26	5.11	0.30	0.47	[59]
Cochlea height oblique	3.56	0.22	3.59	0.12	0.03	[57]
Cochlea length	8.92	0.34	9.32	0.53	0.40	[68]
	8.92	0.34	8.84	0.29	0.08	[57]
Cochlea width	6.78	0.31	6.30	0.38	0.48	[57]
Vestibule length	5.39	0.26	5.45	0.54	0.06	[55]
Vestibule width	3.08	0.17	3.20	0.39	0.12	[55]
Inner ear length total	17.59	0.76	17.13	0.64	0.45	[56]

Table 4: Cochlear and other inner ear measurements. Unit: [mm].

Region	Mean	SD	Mean (lit.)	SD (lit.)	$\Delta$ Mean	Reference
Ampulla (ant)	3.54	0.43	4.20	n.r.	0.66	[67]
Ampulla (post)	2.27	0.27	4.20	n.r.	1.93	[67]
Ampulla (lat)	3.49	0.45	4.20	n.r.	0.71	[67]
Sacculae	2.58	0.41	2.10 / 2.10	n.r.	0.48	[67, 69]
Utriculae	8.78	1.12	7.90 / 8.20	n.r.	0.88 / 0.58	[67, 69]
Cochlea	94.42	9.41	83.80	n.r.	10.62	[67]
Inner ear total	269.34	24.67	221.47	24.29	47.87	[56]

Table 5: Inner ear volumes. Unit:  $[\text{mm}^3]$ . (n.r. = not reported)

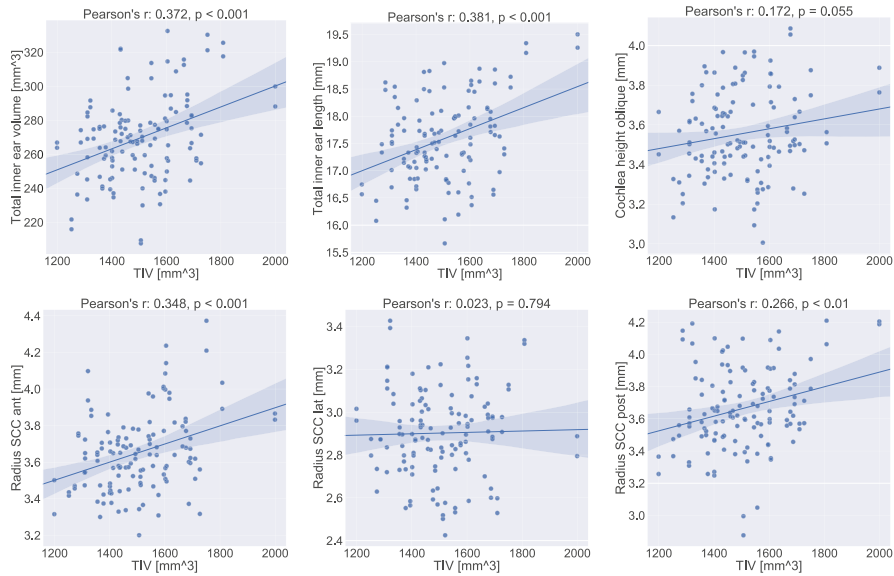


Figure 5: Correlation plots for inner ear measurements with total intracranial volume (TIV). Linear correlation values (Pearson’s  $r$ ) and corresponding  $p$ -values are indicated in the subplot titles. The 95% confidence interval for the regression estimate is drawn as a translucent band around the regression line. Total inner ear volume and length, as well as the radii of the anterior and posterior semicircular canals (SCC) are linearly correlated with head size. The oblique cochlea height might well be while the radius of the lateral SCC appears to not be correlated at all with TIV. The results indicate the importance of TIV for future quantitative assessments between cohorts.

#### 4. Discussion

In this work, we presented a human inner ear atlas derived from multi-sequence magnetic resonance imaging in-vivo and non-invasively. To the best of our knowledge, this is the first time a multi-sequence MRI template-atlas-combination of the human labyrinth covering vestibular and auditory structures has been proposed, and the first time its has been constructed from a sizable cohort (>50 subjects). The segmentation and annotation of templates in our work benefitted predominantly from the SNR of the source whole-head T2 images in combination with the high spatial resolution of the CISS sequence. The data analyses resulted in an inner ear atlas uniquely depicting the vestibule (including utricle and saccule), the three semicircular canals and their ampullae, and the cochlea with its three ducts (scala vestibuli, scala tympani and cochlear duct) as well as the cochlear cupula. The TIV was found to be a relevant covariate for measurements of the labyrinth and its substructures. After controlling for TIV as a covariate, no gender or laterality effects were found.

Analogous to the volumetric measures, our reported landmark distances were very much in line with the published literature. We were able to reproduce these landmarks and the distances in-between mainly with the help of detailed illustrations of landmark locations with high-quality 3D visualizations in several works [33, 57], which we followed closely in our work, and which are presented in a similar fashion for comparison purposes in Fig. 3. Earlier descriptions of landmark placement were often based on 2D volume planes, which can be more difficult to understand and reproduce. For example, the cochlear height was previously defined either in the coronal image plane [59, 58], or using an oblique volume cut through the centre of the cochlear basal turn and the cochlear apex [57]. While the former depends on the orientation of the inner ear anatomy with respect to the coronal plane, the latter is uniquely defined in 3D space. Consequently, our measurements of the former has a larger  $\Delta$ Mean from measurements reported in either [59] or [58], while the measurement of the latter is almost identical to the ones in [57]. A further improvement without going to

higher MRI field strengths is difficult to achieve without a significantly higher voxel resolution in the source material. In any case, an exact replication of reported values in literature is not relevant at this point because i) we relied on a young healthy cohort, while several other works we compared to included pathologies [59, 58, 70] ii) we relied on a single-rater placement of landmarks, and neither we nor related works considered intra- or inter-rater variability on these localizations, and iii) it is not clear yet whether and to what degree distance measures in MRI can be identical to micro-CT.

Overall, no other publicly available template or atlas of the inner ear has assembled and published a comprehensive list of inner ear landmarks for distance measurements. It should be noted that the literature-oriented landmark annotation in our work was time-consuming and non-trivial. By publicly providing these landmarks along with our templates and segmentations, we hope to provide a reproducible and consistent basis for such measurements in future studies as well as to pave the road for population-based standard values. Recently, another inner ear MRI template was presented, albeit including the application of Gadolinium contrast agent and with a less extensive quantitative assessment of template morphology, without investigation of potential confounds, and with separate (i.e. biased) templates for the left and right ear [71]. In comparison, we created an unbiased template and atlas, with detailed labels for sub-structures of the semicircular duct system, vestibule and cochlea. These were obtained through manual labelling and registration of an atlas from micro-CT [20]. We validated the template and atlas by performing a morphometric analysis of the semicircular canals, vestibule and cochlea, and by comparing anatomical measurements to established measures from literature.

It is important to note that the multi-sequence intensity templates provide a lot of flexibility for usage of this atlas. Future studies based on T1-, T2-weighted data and CISS-sequences can directly utilize the provided templates through intra-modal atlas registration (in a single- or multi-variate approach). Other structural MRI sequences (with or without contrast), MRI paradigms (e.g. diffusion-weighted MRI) or even other modalities (e.g. CT, micro-CT)

can still register and utilize the atlas through multi-modal image similarity functions (e.g. normalized mutual information).

Our atlas deviates slightly from the related literature, in particular regarding volumetric measures. For example, the overall inner ear volume appears to be marginally over-estimated. This may be due to partial volume effects and signal blurring after template building. Other volumetric measures like the ampullae look to be slightly under-estimated compared to the literature. This is likely due to simplified geometric assumptions for anatomic shapes made by the authors in the previous work [67], e.g. a sphere for the ampullae. These simplifications were probably helpful in this pioneering study, which approximated 3D volumes through 2D cross-cuts but should be dropped in the long run at higher resolutions to reach anatomical ground truth. Materials like our 3D templates and surface meshes should allow for more accurate volumetric and thus more realistic measurements. Overall, it is remarkable in our opinion that the outer surface of the inner ear in the T2-weighted template (i.e. the Otsu-threshold iso-surface) seems to very accurately represent the outer surface of bony structures as measured by micro-CT, a result that was not expected prior to the conductance of this study. This result in return then also justifies the surface-based co-registration of the bony surface mesh from Ariadne to our T2 iso-surface, in order to transfer internal surface meshes into our template.

*Implications.* Our atlas can be applied for localization, segmentation and sub-parcellations of the entire human inner ear for clinical and scientific questions. With co-registration to the template, individual differences can be detected (e.g. of the anatomical structures itself or with respect to deviations from Reid’s plane). The atlas may also be helpful for surgical planning of implanting the electrodes of cochlear or vestibular implants. Even though malformations were not used to build our atlas, image-based registration is often robust enough to compensate for a wide range of deformations, such that we expect the material to be useful for in-vivo detection and comparison of morphological abnormalities of the inner ear structures as well.

*Limitations.* Despite the high isotropic voxel resolution of 0.2 mm in our final template, our results still do not resolve every fine detail of the inner ear, especially not of the auditory aspects. We were able to visualize the three major parts of the cochlea (the scala vestibuli, the scala tympani and the cochlear duct), but the results were still insufficient for e.g. a visualization of the organ of corti that lies inside the cochlear duct and houses the hair cells. The same holds true for the structure inside the ampullae: the cupulae. These structures are not ossified and it is far more complex to detect them with 3T MRI contrasts due to the tissue type, achievable isotropic resolution, and mitigating head motion during data acquisition. In this context, it seems feasible and realistic to achieve improvements to the resolution of a high-resolution T2-SPACE with coverage of the temporal bone alone and the CISS sequence in the target range of 0.4mm. It should further be noted as a limitation that the cohort’s mean age was 26 +/- 2.3 years, i.e. after development of a fully formed adult human skull. Changes due to age cannot be addressed within our cohort. However, we would not expect a change in bony structures in elderly patients with hearing or vestibular problems. Typically, a degeneration of soft tissue like hair cells in the organ of corti or the cochlear nerve lead to age related hearing loss. Further inner ear malformations reported previously [70] are not represented by our atlas, since we only investigated MRI images of normal subjects. Nonetheless, as noted, malformations may well be detectable as significant structural deviations, through co-registration and overlay on our template on a subject-basis.

*Future Work.* There are several ways in which the proposed inner ear atlas can be extended. First, the atlas can be augmented with additionally labelled regions nearby. The auditory and the two vestibular nerves appear as separable structures in the templates and are hence of particular interest, but were out of scope for this inaugural study. Once these nerves are included, the facial nerve can as well be segmented as it runs in close proximity of the vestibule. Similar to the inner ear micro-CT atlas [20] used in this work, other micro-CT atlases as in [29] can help in identifying and accurately delineating nerves, vas-

culature and bones in our template space. For nerves, the T1-weighted template could become more relevant than in this study. In T1, nerve structures are not only visible (compared to the rest of the inner ear structures), but they have a complementary, hyper-intense appearance, while appearing hypo-intense in the T2 and CISS templates (see Figure 4, panel C). Adding the angles of the semicircular canals towards each other on a single-subject basis and analysing the coplanarity of functional pairs [72], together with the orientation of the eye muscles can further increase the clinical relevance of our IE-Map atlas. Another next step is to develop an automatic segmentation method for prospective validation and application of the templates and atlas. In initial registration experiments, we have verified that segmentation of new subjects is possible using pair-wise single- and multi-variate image registration methods, again provided by ANTs [19]. A fully automatic segmentation method would require the tool-chaining of left and right inner ear localization, template displacement, and local deformation to the inner ear structures of test subjects. The implementation and validation of such a toolkit is also left for future work. A further exciting avenue for improvement stems from the multi-modal fusion of our in-vivo template with micro-CT volumes from multiple subjects. In-vivo MRI may never resolve a similarly fine-grained structural information as micro-CT, but we have demonstrated the feasibility of geometric fusion through multi-variate image registration and surface alignment. Eventually, this could allow for the construction of probabilistic label maps in micro-meter resolution, within the unbiased geometry of our template space.

## 5. Conclusion

In this work, we presented a comprehensive human inner ear atlas and three unbiased templates. Data were acquired in-vivo in a completely non-invasive approach from the largest dedicated cohort for vestibular substructures to date. Semimanual segmentation allowed for successful quantitative assessment of all relevant vestibular and auditory substructures of the inner ear and landmark-

based annotation. Total intracranial volume was found to be a confounding covariate with inner ear measurements. We found no differences in inner ear measurements with respect to gender or ear. Due to the absence of laterality effects, a single unified multi-variate template and atlas was published. It is our hope and aim that template and atlas can find application in numerous domains and disciplines studying neurootological health and disease. Potential applications include inner ear localization, segmentation and sub-parcellation, to quantitatively assess peripheral vestibular and auditory anatomy in group comparisons as well as over the course of longitudinal studies. By providing the templates, atlas segmentation, surface meshes and landmark annotations freely and publicly, we hope to provide clinicians and researchers in neurology, neuroscience and otorhinolaryngology with a new tool and robust basis as a starting point for computational neuro-otology grounded in neuroimaging.

### **Data availability**

The atlas material in this repository can be downloaded and used for non-commercial purposes from our public github repository under the URL:

<https://github.com/pydsgz/IEMap>.

### **Acknowledgements**

The study was supported by the German Federal Ministry of Education and Research (BMBF) in connection with the foundation of the German Center for Vertigo and Balance Disorders (DSGZ) (grant number 01 EO 0901), and a stipend of the Graduate School of Systemic Neurosciences (DFG-GSC 82/3) to Theresa Raiser. We thank Paul Taylor for critical input and feedback.

### **References**

- [1] A. C. Evans, A. L. Janke, D. L. Collins, S. Baillet, Brain templates and atlases, *Neuroimage* 62 (2) (2012) 911–922. doi:10.1016/j.neuroimage.2012.01.024.

- [2] S. Ewert, P. Plettig, N. Li, M. M. Chakravarty, D. L. Collins, T. M. Herrington, A. A. Kühn, A. Horn, Toward defining deep brain stimulation targets in mni space: a subcortical atlas based on multimodal mri, histology and structural connectivity, *Neuroimage* 170 (2018) 271–282. doi:[10.1016/j.neuroimage.2017.05.015](https://doi.org/10.1016/j.neuroimage.2017.05.015).
- [3] T. E. Behrens, H. Johansen-Berg, M. Woolrich, S. Smith, C. Wheeler-Kingshott, P. Boulby, G. Barker, E. Sillery, K. Sheehan, O. Ciccarelli, et al., Non-invasive mapping of connections between human thalamus and cortex using diffusion imaging, *Nature neuroscience* 6 (7) (2003) 750. doi:[10.1038/nn1075](https://doi.org/10.1038/nn1075).
- [4] J. Diedrichsen, J. H. Balsters, J. Flavell, E. Cussans, N. Ramnani, A probabilistic mr atlas of the human cerebellum, *Neuroimage* 46 (1) (2009) 39–46. doi:[10.1016/j.neuroimage.2009.01.045](https://doi.org/10.1016/j.neuroimage.2009.01.045).
- [5] B. De Leener, V. S. Fonov, D. L. Collins, V. Callot, N. Stikov, J. Cohen-Adad, Pam50: unbiased multimodal template of the brainstem and spinal cord aligned with the icbm152 space, *Neuroimage* 165 (2018) 170–179. doi:[10.1016/j.neuroimage.2017.10.041](https://doi.org/10.1016/j.neuroimage.2017.10.041).
- [6] M. Milchenko, S. A. Norris, K. Poston, M. C. Campbell, M. Ushe, J. S. Perlmutter, A. Z. Snyder, 7T MRI subthalamic nucleus atlas for use with 3T MRI, *Journal of Medical Imaging* 5 (01) (2018) 1. doi:[10.1117/1.jmi.5.1.015002](https://doi.org/10.1117/1.jmi.5.1.015002).
- [7] M. C. Keuken, P.-L. Bazin, L. Crown, J. Hootsmans, A. Laufer, C. Müller-Axt, R. Sier, E. J. van der Putten, A. Schäfer, R. Turner, B. U. Forstmann, Quantifying inter-individual anatomical variability in the subcortex using 7T structural MRI, *NeuroImage* 94 (2014) 40–46. doi:[10.1016/j.neuroimage.2014.03.032](https://doi.org/10.1016/j.neuroimage.2014.03.032).
- [8] J. H. Noble, R. F. Labadie, O. Majdani, B. M. Dawant, Automatic segmentation of intracochlear anatomy in conventional ct, *IEEE Transactions*

- on Biomedical Engineering 58 (9) (2011) 2625–2632. doi:10.1109/TBME.2011.2160262.
- [9] F. A. Reda, T. R. McRackan, R. F. Labadie, B. M. Dawant, J. H. Noble, Automatic segmentation of intra-cochlear anatomy in post-implantation ct of unilateral cochlear implant recipients, Medical Image Analysis 18 (3) (2014) 605–615. doi:10.1016/j.media.2014.02.001.
- [10] G. Grabner, A. L. Janke, M. M. Budge, D. Smith, J. Pruessner, D. L. Collins, Symmetric atlasing and model based segmentation: an application to the hippocampus in older adults, Med Image Comput Comput Assist Interv Int Conf Med Image Comput Comput Assist Interv 9 (2006) 58–66. doi:10.1007/11866763\_8.
- [11] J. M. Goldberg, V. J. Wilson, D. E. Angelaki, K. E. Cullen, J. Buttner-Ennever, K. Fukushima, The vestibular system: a sixth sense, Oxford University Press, 2012.
- [12] T. Demarcy, C. Vandersteen, N. Guevara, C. Raffaelli, D. Gnansia, N. Ayache, H. Delingette, Automated analysis of human cochlea shape variability from segmented micro-ct images, Computerized Medical Imaging and Graphics 59 (2017) 1–12. doi:10.1016/j.compmedimag.2017.04.002.
- [13] T. Brandt, Vertigo: Its Multisensory Syndromes, Springer London, 1991. doi:10.1007/978-1-4471-3342-1.
- [14] L. Sennaroğlu, M. D. Bajin, Classification and current management of inner ear malformations, Balkan medical journal 34 (5) (2017) 397–411.
- [15] M. Strupp, T. Brandt, Peripheral vestibular disorders, Current opinion in Neurology 26 (1) (2013) 81–89.
- [16] P. Gunz, M. Ramsier, M. Kuhrig, J.-J. Hublin, F. Spoor, The mammalian bony labyrinth reconsidered, introducing a comprehensive geometric morphometric approach, Journal of Anatomy 220 (6) (2012) 529–543. doi:10.1111/j.1469-7580.2012.01493.x.

- [17] A. Klein, J. Andersson, B. A. Ardekani, J. Ashburner, B. Avants, M. C. Chiang, G. E. Christensen, D. L. Collins, J. Gee, P. Hellier, J. H. Song, M. Jenkinson, C. Lepage, D. Rueckert, P. Thompson, T. Vercauteren, R. P. Woods, J. J. Mann, V. R. Parsey, Evaluation of 14 nonlinear deformation algorithms applied to human brain MRI registration, *NeuroImage* 46 (3) (2009) 786–802. doi:[10.1016/j.neuroimage.2008.12.037](https://doi.org/10.1016/j.neuroimage.2008.12.037).
- [18] T. Heimann, H.-p. Meinzer, Statistical shape models for 3d medical image segmentation : A review, *Medical Image Analysis* 13 (4) (2009) 543–563. doi:[10.1016/j.media.2009.05.004](https://doi.org/10.1016/j.media.2009.05.004).
- [19] B. B. Avants, P. Yushkevich, J. Pluta, D. Minkoff, M. Korczykowski, J. Detre, J. C. Gee, The optimal template effect in hippocampus studies of diseased populations, *NeuroImage* 49 (3) (2010) 2457–2466. doi:[10.1016/j.neuroimage.2009.09.062](https://doi.org/10.1016/j.neuroimage.2009.09.062).
- [20] R. David, A. Stoessel, A. Berthoz, F. Spoor, D. Bennequin, Assessing morphology and function of the semicircular duct system: Introducing new in-situ visualization and software toolbox, *Scientific Reports* 6 (32772). doi:[10.1038/srep32772](https://doi.org/10.1038/srep32772).
- [21] R. Glueckert, L. Johnson Chacko, D. Schmidbauer, T. Potrusil, E. J. Pechriggl, R. Hoermann, E. Brenner, A. Reka, A. Schrott-Fischer, S. Handschuh, Visualization of the Membranous Labyrinth and Nerve Fiber Pathways in Human and Animal Inner Ears Using MicroCT Imaging, *Frontiers in Neuroscience* 12 (2018) 501. doi:[10.3389/fnins.2018.00501](https://doi.org/10.3389/fnins.2018.00501).
- [22] A. V. Schweizer, R. Lebrun, L. A. Wilson, L. Costeur, T. Schmelzle, M. R. Sánchez-Villagra, Size variation under domestication: Conservatism in the inner ear shape of wolves, dogs and dingoes, *Scientific reports* 7 (1) (2017) 13330.
- [23] A. Postnov, A. Zarowski, D. N. Clerck, F. Vanpoucke, F. E. Offeciers, V. D. Dyck, S. Peeters, High resolution micro-`{ct}` scanning as an in-

- novatory tool for evaluation of the surgical positioning of cochlear implant electrodes, *Acta Oto-Laryngologica* 126 (5) (2006) 467–474. doi:  
[10.1080/00016480500437377](https://doi.org/10.1080/00016480500437377).
- [24] H. M. Kjer, J. Fagertun, S. Vera, M. A. González Ballester, R. R. Paulsen, Shape modelling of the inner ear from micro-ct data, in: *Proceedings of Symposium on Statistical Shape Models & Applications, Shape 2014*, 2014, p. 21, poster presentation.
- [25] N. Gerber, M. Reyes, L. Barazzetti, H. M. Kjer, S. Vera, M. Stauber, P. Mistrik, M. Ceresa, N. Mangado, W. Wimmer, T. Stark, R. R. Paulsen, S. Weber, M. Caversaccio, M. A. G. Ballester, A multiscale imaging and modelling dataset of the human inner ear, *Scientific Data* 4 (2017) 170132. doi:  
[10.1038/sdata.2017.132](https://doi.org/10.1038/sdata.2017.132).
- [26] C. Schmidt, J. Harbort, R. Knecht, U. Grzyska, A. Muenschler, C. V. Dalchow, [Measurement and comparison of labyrinthine structures with the digital volume tomography: ancient Egyptian mummies' versus today's temporal bones](#), *European Archives of Oto-Rhino-Laryngology* 270 (3) (2013) 831–840. doi:  
[10.1007/s00405-012-2047-y](https://doi.org/10.1007/s00405-012-2047-y).  
URL <http://link.springer.com/10.1007/s00405-012-2047-y>
- [27] E. G. Ekdale, [Form and function of the mammalian inner ear](#), *Journal of Anatomy* 228 (2) (2016) 324–337. doi:  
[10.1111/joa.12308](https://doi.org/10.1111/joa.12308).  
URL <http://doi.wiley.com/10.1111/joa.12308>
- [28] T. van den Boogert, M. van Hoof, S. Handschuh, R. Glueckert, N. Guinand, J.-P. Guyot, H. Kingma, A. Perez-Fornos, B. Seppen, L. Johnson Chacko, A. Schrott-Fischer, R. van de Berg, [Optimization of 3d-Visualization of Micro-Anatomical Structures of the Human Inner Ear in Osmium Tetroxide Contrast Enhanced Micro-CT Scans](#), *Frontiers in Neuroanatomy* 12 (2018) 41. doi:  
[10.3389/fnana.2018.00041](https://doi.org/10.3389/fnana.2018.00041).  
URL <https://www.frontiersin.org/article/10.3389/fnana.2018.00041/full>

- [29] R. Gupta, S. H. Bartling, S. K. Basu, W. R. Ross, H. Becker, A. Pfoh, T. Brady, H. D. Curtin, Experimental flat-panel high-spatial-resolution volume ct of the temporal bone, *American journal of neuroradiology* 25 (8) (2004) 1417–1424.
- [30] J. S. Iyer, N. Zhu, S. Gasilov, H. M. Ladak, S. K. Agrawal, K. M. Stankovic, Visualizing the 3d cytoarchitecture of the human cochlea in an intact temporal bone using synchrotron radiation phase contrast imaging, *Biomedical Optics Express* 9 (8) (2018) 3757. doi:10.1364/boe.9.003757.
- [31] D. S. Thylur, R. E. Jacobs, J. L. Go, A. W. Toga, J. K. Niparko, Ultra-high-field magnetic resonance imaging of the human inner ear at 11.7 tesla, *Otology & neurotology: official publication of the American Otological Society, American Neurotology Society [and] European Academy of Otology and Neurotology* 38 (1) (2017) 133.
- [32] H. Uzun, I. S. Curthoys, >. S. Jones, [A new approach to visualizing the membranous structures of the inner ear – high resolution X-ray micro-tomography](#), *Acta Oto-Laryngologica* 127 (6) (2007) 568–573. doi:10.1080/00016480600951509.  
URL <http://www.tandfonline.com/doi/full/10.1080/00016480600951509>
- [33] J.-Y. Lee, K.-J. Shin, J.-N. Kim, J.-Y. Yoo, W.-C. Song, K.-S. Koh, A morphometric study of the semicircular canals using micro-ct images in three-dimensional reconstruction, *The Anatomical Record* 296 (5) (2013) 834–839.
- [34] W. Daocai, W. Qing, W. Ximing, H. Jingzhen, L. Cheng, M. Xiangxing, Size of the semicircular canals measured by multidetector computed tomography in different age groups, *Journal of Computer Assisted Tomography* 38 (2) (2014) 196–199. doi:10.1097/rct.0b013e3182aaf21c.
- [35] R. Lingam, S. Connor, J. Casselman, T. Beale, *Mri in otology: applications*

- in cholesteatoma and ménière's disease, *Clinical Radiology* 73 (1) (2018) 35–44. doi:10.1016/j.crad.2017.09.002.
- [36] S. Naganawa, T. Nakashima, Visualization of endolymphatic hydrops with mr imaging in patients with ménière's disease and related pathologies: current status of its methods and clinical significance, *Japanese Journal of Radiology* 32 (4) (2014) 191–204. doi:10.1007/s11604-014-0290-4.
- [37] J. H. Keller, B. E. Hirsch, R. S. Marovich, B. F. Branstetter IV, Detection of endolymphatic hydrops using traditional mr imaging sequences, *American journal of otolaryngology* 38 (4) (2017) 442–446. doi:10.1016/j.amjoto.2017.01.038.
- [38] M. Van der Jagt, W. Brink, M. Versluis, S. Steens, J. Briaire, A. Webb, J. Frijns, B. Verbist, Visualization of human inner ear anatomy with high-resolution mr imaging at 7t: initial clinical assessment, *American Journal of Neuroradiology* 36 (2) (2015) 378–383. doi:10.3174/ajnr.A4084.
- [39] E. L. van den Burg, M. van Hoof, A. Postma, A. M. L. Janssen, R. J. Stokroos, H. Kingma, R. van de Berg, An exploratory study to detect meniere's disease in conventional mri scans using radiomics, *Frontiers in neurology* 7 (2016) 190. doi:10.3389/fneur.2016.00190.
- [40] F. G. Gonçalves, L. L. F. do Amaral, Constructive interference in steady state imaging in the central nervous system, *European Neurological Review* 6 (2011) 138–42. doi:10.17925/ENR.2011.06.02.138.
- [41] H. Inui, T. Sakamoto, T. Ito, T. Kitahara, Volumetric measurements of the inner ear in patients with meniere's disease using three-dimensional magnetic resonance imaging, *Acta oto-laryngologica* 136 (9) (2016) 888–893. doi:10.3109/00016489.2016.1168940.
- [42] J. Cho, H. Cheon, J. H. Park, H.-J. Lee, H.-J. Kim, H. G. Choi, J.-W. Koo, S. K. Hong, Sudden sensorineural hearing loss associated with inner ear lesions detected by magnetic resonance imaging, *PLOS ONE* 12 (10)

(2017) e0186038. doi:10.1371/journal.pone.0186038.

URL <http://dx.plos.org/10.1371/journal.pone.0186038>

- [43] D. Hingwala, S. Chatterjee, C. Kesavadas, B. Thomas, T. R. Kapilamoorthy, Applications of 3d ciss sequence for problem solving in neuroimaging, *The Indian journal of radiology & imaging* 21 (2) (2011) 90. doi:10.4103/0971-3026.82283.
- [44] O. Esteban, D. Birman, M. Schaer, O. O. Koyejo, R. A. Poldrack, K. J. Gorgolewski, Mriqc: Advancing the automatic prediction of image quality in mri from unseen sites, *PloS one* 12 (9) (2017) e0184661. doi:10.1371/journal.pone.0184661.
- [45] N. J. Tustison, B. B. Avants, P. A. Cook, Y. Zheng, A. Egan, P. A. Yushkevich, J. C. Gee, N4itk: Improved n3 bias correction, *IEEE Transactions on Medical Imaging* 29 (6) (2010) 1310–1320. doi:10.1109/TMI.2010.2046908.
- [46] B. H. Menze, A. Jakab, S. Bauer, J. Kalpathy-Cramer, K. Farahani, J. Kirby, Y. Burren, N. Porz, J. Slotboom, R. Wiest, L. Lanczi, E. Gerstner, M. A. Weber, T. Arbel, B. B. Avants, N. Ayache, P. Buendia, D. L. Collins, N. Cordier, J. J. Corso, A. Criminisi, T. Das, H. Delingette, C. Demiralp, C. R. Durst, M. Dojat, S. Doyle, J. Festa, F. Forbes, E. Geremia, B. Glocker, P. Golland, X. Guo, A. Hamamci, K. M. Iftekharuddin, R. Jena, N. M. John, E. Konukoglu, D. Lashkari, J. A. Mariz, R. Meier, S. Pereira, D. Precup, S. J. Price, T. R. Raviv, S. M. Reza, M. Ryan, D. Sarikaya, L. Schwartz, H. C. Shin, J. Shotton, C. A. Silva, N. Sousa, N. K. Subbanna, G. Szekely, T. J. Taylor, O. M. Thomas, N. J. Tustison, G. Unal, F. Vasseur, M. Wintermark, D. H. Ye, L. Zhao, B. Zhao, D. Zikic, M. Prastawa, M. Reyes, K. Van Leemput, The multimodal brain tumor image segmentation benchmark (brats), *IEEE Transactions on Medical Imaging* 34 (10) (2015) 1993–2024. doi:10.1109/TMI.2014.2377694.
- [47] N. Finby, K.-Y. Chynn, Cranial computerized tomography: Technique and

- anatomy, in: *Manual of Cranial Computerized Tomography*, S. Karger {AG}, 1982, pp. 15–29. doi:10.1159/000406259.
- [48] C. C. Della Santina, V. Potyagaylo, A. A. Migliaccio, L. B. Minor, J. P. Carey, Orientation of human semicircular canals measured by three-dimensional multiplanar ct reconstruction, *Journal of the Association for Research in Otolaryngology* 6 (3) (2005) 191–206. doi:10.1007/s10162-005-0003-x.
- [49] R. Blanks, I. Curthoys, C. Markham, Planar relationships of the semicircular canals in man, *Acta oto-laryngologica* 80 (1-6) (1975) 185–196. doi:10.3109/00016487509121318.
- [50] S. Hashimoto, H. Naganuma, K. Tokumasu, A. Itoh, M. Okamoto, Three-dimensional reconstruction of the human semicircular canals and measurement of each membranous canal plane defined by reid’s stereotactic coordinates, *Annals of Otology, Rhinology & Laryngology* 114 (12) (2005) 934–938. doi:10.1177/000348940511401207.
- [51] N. Otsu, A threshold selection method from gray level histograms, *IEEE Transactions on Systems, Man, and Cybernetics* 9 (1) (1979) 62–66. doi:10.1109/TSMC.1979.4310076.
- [52] P.-E. Danielsson, Euclidean distance mapping, *Computer Graphics and Image Processing* 14 (3) (1980) 227–248. doi:10.1016/0146-664X(80)90054-4.
- [53] A. Fedorov, R. Beichel, J. Kalpathy-Cramer, J. Finet, J. C. Fillion-Robin, S. Pujol, C. Bauer, D. Jennings, F. Fennessy, M. Sonka, J. Buatti, S. Aylward, V. J. Miller, S. Pieper, R. Kikinis, 3d slicer as an image computing platform for the quantitative imaging network, *Magnetic Resonance Imaging* 30 (9) (2012) 1323–1341. doi:10.1016/j.mri.2012.05.001.
- [54] B. C. Lowekamp, D. T. Chen, L. Ibáñez, D. Blezek, The design of sim-

- pleitk, *Frontiers in neuroinformatics* 7 (2013) 45. doi:[10.3389/fninf.2013.00045](https://doi.org/10.3389/fninf.2013.00045).
- [55] E. M. Sugihara, A. L. Marinica, N. D. Vandjelovic, B. M. Kelley, S. S. Sana, N. E. Starkey, S. C. Babu, Mastoid and Inner Ear Measurements in Patients With Meniere's Disease, *Otology & Neurotology* 38 (10) (2017) 1484–1489. doi:[10.1097/MAO.0000000000001576](https://doi.org/10.1097/MAO.0000000000001576).
- [56] M. T. Teixido, G. Kirkilas, P. Seymour, K. Sem, A. Iaia, O. Sabra, H. Isildak, Normative Inner Ear Volumetric Measurements:, *The Journal of Craniofacial Surgery* 26 (1) (2015) 251–254. doi:[10.1097/SCS.0000000000001204](https://doi.org/10.1097/SCS.0000000000001204).
- [57] Y.-K. Liu, C.-L. Qi, J. Tang, M.-L. Jiang, L. Du, Z.-H. Li, S.-H. Tan, A.-Z. Tang, The diagnostic value of measurement of cochlear length and height in temporal bone CT multiplanar reconstruction of inner ear malformation, *Acta Oto-Laryngologica* 137 (2) (2017) 119–126. doi:[10.1080/00016489.2016.1221132](https://doi.org/10.1080/00016489.2016.1221132).
- [58] D. Purcell, J. Johnson, N. Fischbein, A. K. Lalwani, Establishment of normative cochlear and vestibular measurements to aid in the diagnosis of inner ear malformations, *Otolaryngology—Head and Neck Surgery* 128 (1) (2003) 78–87. doi:[10.1067/mhn.2003.51](https://doi.org/10.1067/mhn.2003.51).
- [59] H. Shim, J.-E. Shin, J. Chung, K.-S. Lee, Inner ear anomalies in cochlear implantees: Importance of radiologic measurements in the classification, *Otology and Neurotology* 27 (6) (2006) 831–837. doi:[10.1097/01.mao.0000227902.47483.ef](https://doi.org/10.1097/01.mao.0000227902.47483.ef).
- [60] H. W. Lilliefors, *On the Kolmogorov-Smirnov Test for Normality with Mean and Variance Unknown*, *Journal of the American Statistical Association* 62 (318) (1967) 399–402. doi:[10.1080/01621459.1967.10482916](https://doi.org/10.1080/01621459.1967.10482916).  
URL <http://www.tandfonline.com/doi/abs/10.1080/01621459.1967.10482916>

- [61] Y. Benjamini, Y. Hochberg, Controlling the false discovery rate: a practical and powerful approach to multiple testing, *Journal of the Royal statistical society: series B (Methodological)* 57 (1) (1995) 289–300. doi:<http://dx.doi.org/10.2307/2346101>.
- [62] L. M. O'Brien, D. A. Ziegler, C. K. Deutsch, J. A. Frazier, M. R. Herbert, J. J. Locascio, [Statistical adjustments for brain size in volumetric neuroimaging studies: Some practical implications in methods](#), *Psychiatry Research: Neuroimaging* 193 (2) (2011) 113–122. doi:[10.1016/j.psychresns.2011.01.007](https://doi.org/10.1016/j.psychresns.2011.01.007).  
URL <https://linkinghub.elsevier.com/retrieve/pii/S0925492711000357>
- [63] E. Jones, T. Oliphant, P. Peterson, et al., *Scipy: Open source scientific tools for python*[Online; accessed 06. Dec. 2017].
- [64] R. Vallat, *Pingouin: Statistics in python*, *The Journal of Open Source Software* 3 (31) (2018) 1026.
- [65] S. Seabold, J. Perktold, *Statsmodels: Econometric and statistical modeling with python*, in: *9th Python in Science Conference*, 2010.
- [66] M. Mahesh, [The Essential Physics of Medical Imaging, Third Edition.](#), *Medical Physics* 40 (7) (2013) 077301. doi:[10.1118/1.4811156](https://doi.org/10.1118/1.4811156).  
URL <http://doi.wiley.com/10.1118/1.4811156>
- [67] R. A. Buckingham, G. E. Valvassori, *Inner Ear Fluid Volumes and the Resolving Power of Magnetic Resonance Imaging: Can it Differentiate Endolymphatic Structures?*, *Annals of Otology, Rhinology & Laryngology* 110 (2) (2001) 113–117. doi:[10.1177/000348940111000204](https://doi.org/10.1177/000348940111000204).
- [68] B. Escudé, C. James, O. Deguine, N. Cochard, E. Eter, B. Fraysse, *The Size of the Cochlea and Predictions of Insertion Depth Angles for Cochlear Implant Electrodes*, *Audiology and Neurotology* 11 (1) (2006) 27–33. doi:[10.1159/000095611](https://doi.org/10.1159/000095611).

- [69] M. Igarashi, T. O-Uchi, H. Isago, W. K. Wright, Utricular and Saccular Volumetry in Human Temporal Bones, *Acta Oto-Laryngologica* 95 (1-4) (1983) 75–80. [doi:10.3109/00016488309130918](https://doi.org/10.3109/00016488309130918).
- [70] A. Dhanasingh, A. Dietz, C. Jolly, P. Roland, Human inner-ear malformation types captured in 3d, *The journal of international advanced otology* 15 (1) (2019) 77.
- [71] V. Kirsch, F. Nejatbakhsheshfahani, S.-A. Ahmadi, M. Dieterich, B. Ertl-Wagner, [A probabilistic atlas of the human inner ear’s bony labyrinth enables reliable atlas-based segmentation of the total fluid space](#), *Journal of Neurology* 266 (S1) (2019) 52–61. [doi:10.1007/s00415-019-09488-6](https://doi.org/10.1007/s00415-019-09488-6).  
URL <http://link.springer.com/10.1007/s00415-019-09488-6>
- [72] D.-K. Kim, D.-R. Kim, S. H. Jeong, G. J. Kim, K.-H. Chang, B.-C. Jun, [Analysis of the coplanarity of functional pairs of semicircular canals using three-dimensional images reconstructed from temporal bone magnetic resonance imaging](#), *The Journal of Laryngology & Otology* 129 (5) (2015) 430–434. [doi:10.1017/S0022215115000201](https://doi.org/10.1017/S0022215115000201).  
URL [https://www.cambridge.org/core/product/identifier/S0022215115000201/type/journal\\_article](https://www.cambridge.org/core/product/identifier/S0022215115000201/type/journal_article)

## 2.2 The human corticocortical vestibular connectome

**Raiser, T.**, Duering, M., Flanagin, V. L., van Ombergen, A., and zu Eulenburg, P. (under review and revision).

The article “The human corticocortical vestibular connectome” was recently submitted for publication in *NeuroImage* and is currently under review and revision.

### Summary

In this second chapter, the first established human corticocortical vestibular connectome is presented. With our work, we aim to robustly delineate and characterize the entire human corticocortical vestibular network. Through the mapping of recently localized vestibular regions of interest, we derived structural and functional corticocortical connectomes from state-of-the-art 3T multi-modal neuroimaging data, investigated their modules and common network measures, and compared the human structural connectome to respective findings previously reported in non-human primates (using gold standard tracer injections). Our results show that the modularity of the structural corticocortical vestibular connectome of humans is extremely robust. Comparisons with non-human primate data revealed substantial differences in the organization across the two species. The structural vestibular connectome seems to be characterized by very intrahemispheric connectivity indices whereas the functional one emphasizes a substantial synchronicity for homotopic nodes. Overall a laterality preference in vestibular processing could be observed from the functional and structural data alike for the right hemisphere confirming earlier works from lesion data that suggested such a predominant processing for the vestibular system.

### Author contributions

The following authors contributed to this work: Peter zu Eulenburg designed the study. Angeliqve von Ombergen collected the data under the supervision of Peter zu Eulenburg. Data analyses were performed by Theresa M. Raiser, Marco Duering and Peter zu Eulenburg. Data visualization and data analyses were done by Theresa M. Raiser and discussed with Virginia Flanagin. Theresa M. Raiser wrote the paper with guidance from Peter zu Eulenburg and input from all listed authors.

# The human corticocortical vestibular connectome

Theresa Raiser<sup>a,b</sup>, Marco Duering<sup>b,c,e</sup>, Virginia L. Flanagan<sup>a,b</sup>, Angelique van Ombergen<sup>a,f</sup>, Ria Maxine Rühl<sup>a,d</sup>, Peter zu Eulenburg<sup>a,b</sup>

<sup>a</sup>*German Center for Vertigo and Balance Disorders (DSGZ),  
Fraunhoferstr. 20, 82152 Planegg, Germany*

<sup>b</sup>*Graduate School of Systemic Neurosciences, Ludwig-Maximilians-Universität Munich,  
Großhaderner Str. 2, 82152 Planegg, Germany*

<sup>c</sup>*Institute for Stroke and Dementia Research, Ludwig-Maximilians-Universität Munich,  
Feodor-Lynen-Straße 17, 81377 Munich*

<sup>d</sup>*Department of Neurology, Klinikum der Universität München,  
Marchioninstr. 15, 81377 Munich, Germany*

<sup>e</sup>*Munich Cluster for Systems Neurology (SyNergy),  
Marchioninstr. 15, 81377 Munich, Germany*

<sup>f</sup>*Department of Translational Neurosciences, Faculty of Medicine and Health Sciences,  
University of Antwerp, Universiteitsplein 1, 2610 Antwerpen, Belgium*

---

## Abstract

**Background.** Little is known about the cortical organization of human vestibular information processing. There is no established primary vestibular cortex - regions receiving vestibular input are rather spread throughout the cortex. The aim of this study is to describe this network, the human corticocortical vestibular connectome, and compare it to previously published results in non-human primates.

**Methods.** We collected high-resolution multi-shell diffusion-weighted (DWI) and state-of-the-art resting-state functional MR images of 29 right-handed normal subjects. Ten vestibular cortical regions per hemisphere were predefined and applied as regions of interest. Four different structural corticocortical vestibular connectomes accounting for established constraints were investigated. The analyses included the investigation of common network measures and hemispheric differences for functional and structural connectivity patterns alike. In addition, the results of the structural vestibular connectome were compared to findings reported in non-human primates with respect to tracer injections.

---

\*Corresponding author: [peter.zu.eulenburg@med.uni-muenchen.de](mailto:peter.zu.eulenburg@med.uni-muenchen.de)

Results. All structural connectomes independent of the applied constraints showed a recurring subdivision into identical three submodules. The structural human connectome was characterized by a predominantly intrahemispheric connectivity, whereas the functional pattern highlighted a strong synchronicity for all homotopic nodes. A significant laterality preference towards the right hemisphere can be observed throughout the analyses: (1) with larger nodes, (2) stronger connectivity values structurally and functionally, and (3) a higher functional relevance. Comparisons with non-human primate data revealed substantial differences in the organization across the two species.

Conclusion. The vestibular sense is an ancient system from an evolutionary perspective and as such our analysis delineated a remarkably stable organization. Differences found between primate species may be attributed to phylogeny as well as methodological differences. With our work we solidified evidence for lateralization within the corticocortical vestibular network. Our results might explain why cortical lesions in humans do not lead to persistent vestibular symptoms. For this redundant structural routing throughout the network and high-degree functional synchronicity may buffer connectivity and reestablish network integrity quickly in case of injury.

*Keywords:* functional connectome, structural connectome, vestibular system, comparative connectomics

---

**Highlights:**

- robust modularity of the structural corticocortical vestibular connectome (CVC)
- fundamental differences in the organization of the CVC across humans and macaques
- structural CVC is characterized by a substantial intrahemispheric connectivity
- functional CVC is characterized by a strong synchronicity for homotopic nodes
- laterality preference in vestibular processing for the right hemisphere

**1. Introduction**

With the evolution of methods like functional MRI and diffusion-weighted imaging, we are able to build a model of the connections within the human brain from a functional and structural point of view. The concept of a connectome was introduced by Sporns, Tononi, and Kotter [1]. In the past years it has become a research target to build a detailed human connectome for answering questions in neuroscience [2]. Here, disease connectomics [3] and comparative connectomics (e.g. [4, 5]) have lately gained attention for investigating differences and common substrates within and among species. In this study we aimed to comprehensively characterize the vestibular corticocortical structural and functional connectome of the human brain. Besides whole brain connectomes, researchers work on connectomes of subnetworks of several species on various scales. On a cellular level (microscale nm to  $\mu\text{m}$ ; mesoscale  $\mu\text{m}$  to mm), mostly performed in rats and monkeys, researchers use injected tracers for identifying (long) interneuronal connections. These invasive methods can resolve

directionality. On a macroscale level, diffusion weighted imaging is used as an indirect and non-invasive measurement of fiber orientations. This method is widely used for researching the human brain and cannot detect retrograde or anterograde directionality. Mapping the entire human brain on a cellular level in the living organism is facing major technical challenges and is not (yet) realizable in comparison to other species (e.g. mouse connectome, [6]). Different sensory connectomes have been characterized over the past years. In non-human primate research visual areas have been defined, connectomes constructed and compared across species [7, 8, 9]. Further auditory [10], pain [11], and olfactory [12] connectomes have been established for instance. Independent of the modality or methods used, it is first of all essential to define the cortical areas of the specific (sensory) network or to choose an appropriate parcellation of the brain. In contrast to the auditory or visual system, where unimodal stimulation is feasible, manifold confounders hampered the definition of the vestibular cortical network [13]. In the macaque, some pure vestibular interconnected cortical areas have been identified with tracer injections [14] and human homologue areas have been identified, too [15, 16, 17, 18]. Hemispheric lateralization has been observed in several networks like language [19] and the auditory system [10]. With regard to the vestibular system, Dieterich et al. [20] found a correlation with handedness and vestibular dominance of the ipsilateral hemisphere. Lesions in the right hemisphere seem to cause vestibular symptoms more often than lesions in the left hemisphere [21] and symptoms persist longer (e.g. [22]). Very recently it has been shown that functional lateralization of certain tasks or states correlates negatively with the corpus callosum probability of the connection [23]. In our current study we aimed for a corticocortical vestibular connectome on a macroscale with non-invasive diffusion weighted imaging (DWI) and state-of-the-art functional connectivity from resting-state data. The human corticocortical vestibular connectome was to be compared to the tracer-based structural connectome in non-human primates. We also wanted to characterize our vestibular network with respect to common network measures. Last but not least a goal of this study was to investigate if there is a lateralization of

the structural and/or functional vestibular corticocortical connectome and the role of commissural connections via the corpus callosum. Central disorders can lead to vestibular deficits in the acute stage, but no chronic central vestibular disorder with persisting vertigo symptoms exists [24]. Therefore, we aimed to analyze the robustness of the corticocortical vestibular connectome and derive its vulnerability to cortical node lesions with an additional focus on hemispheric laterality from our results.

## 2. Materials and methods

We recruited 29 right-handed participants (age range: 20.5 - 36.7 years, mean age:  $27.4 \pm 4.3$  years, 16 female). All participants gave their written informed consent and were paid for participation. The local ethics committee of the Ludwig-Maximilians-Universität, Munich, approved the study in accordance with the latest revision of the Helsinki declaration from 2008. The imaging data were acquired on a clinical 3T MRI scanner (SKYRA Siemens, Erlangen, Germany) with a 64-channel head/neck coil. During all scans, participants wore ear plugs and a dedicated head fixation device to limit head motion artifacts during structural and functional imaging (®Pearltec Crania adult, Schlieren, Switzerland). A high-resolution T1-weighted image was acquired for each subject at the start of the study (TR= 2060 ms, TE= 2.17 ms, flip angle = 12 deg., FoV= 240mm, 320x320 matrix, 0.75mm isotropic voxel resolution, A-P phase encoding, GRAPPA 2). Multi-shell diffusion weighted images were obtained for three shells of (1) $b= 1000$  s/mm<sup>2</sup>, (2) $b= 1750$  s/mm<sup>2</sup>, and (3) $b= 2500$  s/mm<sup>2</sup> at a 1.75mm isotropic spatial resolution. Ten non-diffusion and 150 directions encoding scans were obtained with the following parameters: acquisition matrix 128x128, 72 slices, TR= 3800ms, TE= 104.8ms, FoV= 224x224 mm, slice thickness= 1.75 mm, multi-band factor 3 [25]. Reverse phase encoding in a subsequent otherwise identical second run was applied to minimize susceptibility-induced distortions during post-processing. Resting state fMRI images were obtained during which participants had their eyes open fixating a

dot straight ahead. Here, eye movements were recorded (with the MRC camera built into MRI compatible binocular goggles; NordicNeuroLab, Bergen, Norway). The images (589 volumes) with whole-brain coverage (2.5mm isotropic resolution) were acquired in an interleaved slice order with multiband acceleration factor 6 (TR = 700 ms, TE = 33 ms, flip angle = 45 deg., FoV = 210 mm, matrix size = 84x84, slice thickness 2.5mm, anterior-posterior phase encoding direction, prescan normalized).

### *2.1. Vestibular Node Definition*

Defining robust, biologically motivated regions of interest is essential for an accurate connectome. In this study we targeted the vestibular cortical network. Ten cortical regions known in primates for vestibular processing were motivated from a large group study using whole-nerve galvanic vestibular stimulation for each hemisphere [18] and used as regions-of-interest consisting of Area 2v, Area 3av, premotor area, cingulate sulcus visual (CSv), ventral intraparietal area (VIP), OP2, Area 7, visual posterior sylvian area (VPS), supplementary motor area (SMA) and human medial superior temporal area (hMST) (a detailed list of the nodes with size and coordinates can be found in Supplement S1). For each subject we took the T1 to DWI co-registered image and created a deformation field (T1 to Montreal Neurological Institute (MNI) space) using the CAT12 toolbox (version: r1432; <http://www.neuro.uni-jena.de/cat/index.html>) in SPM12 (version: 7487). An inverse of the spatial deformation field was applied onto the atlas to generate an atlas on single subject level. We then created an intercept between a binarized grey matter mask (from the 5TT image; grey matter >0.1) and the atlas on single subject level to guarantee anatomical correctness with respect to tissue boundaries.

### *2.2. Description of the vestibular cortical regions*

The vestibular atlas in MNI space is visualized in Figure 1. The volume of the nodes varied across the established vestibular atlas. Additionally, on average the right vestibular nodes were 23% larger than the respective left nodes ( $t(9)=2.27$ ,

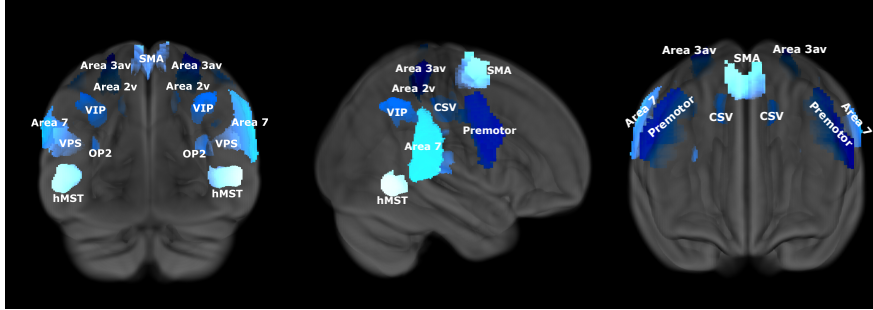


Figure 1: Vestibular cortical regions. Bilaterally: Area 2v, Area 3av, Premotor, CSV, VIP, OP2, Area 7, VPS, SMA and hMST (in dorsal, right medial and frontal view).

$p < 0.05$ ). We therefore constrained the connectome not only for stream length as advised by Betzel, Griffa, Hagmann, and Mišić [26] but also corrected for the inverse node volume of the nodes.

### 2.3. Structural Connectivity Analyses

#### 2.3.1. Diffusion weighted data preprocessing and analysis

The DW images were visually inspected in all three orthogonal views and no severe artifacts were revealed, i.e. no signal dropout and no gross geometric distortions could be seen. Preprocessing was performed using MRtrix3 (<http://www.mrtrix.org/>; version: 3.0\_rc3; Brain Research Institute, Melbourne, Australia), the FMRIB Software Library (FSL) [27], and Advanced normalization tools (ANTs) [28]. Preprocessing steps involved denoising (MRtrix 'dwi denoise'), Gibbs artefact removal (MRtrix 'mrdegibbs'), correcting for eddy currents, motion and susceptibility-induced distortions (FSL topup and eddy) and intensity bias corrections (ANTs 'N4biascorrection'). MRtrix3 was further used for constrained spherical-deconvolution (CSD) and anatomically-constrained whole brain probabilistic tractography [29, 30, 31]. T1 images were registered to the DW images using ANTs [28]. Segmentation was obtained through generating five-tissue-type (5TT) images (consisting of: grey matter, white matter, CSF, subcortical grey matter, lesions). In none of the participants

lesions were detected through the segmentation. The anatomically informed response function was then estimated from the data using the dhollander option [32]. Fiber orientation distributions (FOD) were estimated from the data with a spherical deconvolution followed by a multi-tissue informed log-domain intensity normalization. With the anatomically-constrained tractography (ACT) [33] ten million streamlines ( $=10^7$  streamlines with a maximum length of 250 mm and a FOD amplitude cutoff of 0.06) were generated. The 5TT anatomical information in this step results in biologically greater accuracy [33]. For visual inspection a subset of  $10^5$  streamlines was generated for each subject and overlaid on the 5TT images to check for correctness. For the tractography we used gray and white matter interface cropped streamlines, the backtrack option and determined the seed points dynamically with the help of the white matter norm mask. ACT was used in combination with spherical deconvolution informed filtering of tractograms (SIFT2) to further improve the biological accuracy of streamlines [33, 34, 35].

### 2.3.2. Establishment of a structural corticocortical vestibular connectome (sCVC)

By means of combining the delineated 10 million streamlines and the above described vestibular atlas, we constructed corticocortical vestibular connectomes for each subject. Using the calculated weightings after SIFT2 filtering, we created symmetric, undirected structural connectivity matrices of all cerebral nodes with a diagonal set to zero. Betzel et al. [26] recently pointed out that correcting for the length of the streamline outperforms other more conventional approaches of establishing connectomes. When not correcting for the distance between nodes, short-range connections are typically overestimated and local and global network statistics are not preserved [26]. Further it also seemed important to correct for node volume as nodes were quite different in size. We generated an unscaled version of the connectome as well as a streamline length scaled, an inverse node volume scaled and a scaled combined connectome. Focus of our analyses is the structural scaled combined connectome. The three additional structural connectomes were established to see whether the modularity

of the network is stable across the differing constraints.

#### *2.4. Establishment of a functional corticocortical vestibular connectome (fCVC)*

A functional connectivity analyses was performed with the rsfMRI data using CONN toolbox (version 18b; [36]; <http://www.nitrc.org/projects/conn>) for Matlab (version 2019a). Movement parameters, quality control timeseries and scrubbing regressors were employed by the CONN Toolbox as first level covariates. For denoising we used the following nuisance regressors' time series to lessen their impact: white matter (WM) and cerebrospinal fluid (CSF) confounds were considered with their first five principal components each. Furthermore, six principal temporal components of the movement parameters (three translation and three rotation parameters) as well as their six derivatives were employed. Images were denoised with a temporal band-pass filter (0.008-0.09 Hz). The ROI-to-ROI analysis resulted in the functional weighted connectivity matrices with Fisher-transformed correlation coefficients. The results are thresholded at  $p < 0.05$  FDR corrected (two-sided) together with 1000 permutations for non-parametric thresholding. This fCVC was used for detecting a stable number of modules within the network. For the subsequent network analyses, we set any negative correlation values to zero [37, 38].

#### *2.5. Brain Connectivity Analyses*

##### *2.5.1. Network Modularity*

The weighted undirected networks were all ordered by applying the community Louvain algorithm [39] of the brain connectivity toolbox (BCT, version 2017-15-01; [38]) iteratively onto the mean matrices of the four different scaled versions of the structural connectome as well as the functional connectome. With looping over several gamma values (ranging from 0 to 2.5) we detected a stable number of modules. The connectomes on single subject level were ordered accordingly. As we are not comparing two groups, we normalized the data for each subject to make the connectomes comparable to each other. The presence of a normal distribution of certain network measures was tested with

the Anderson Darling test and then pairwise t-tests were performed to precisely test for significant differences between the right and the left hemispheres.

#### *2.5.2. Network measures*

Characteristics of a network are typically described by a combination of network measures. The following steps were only applied onto the structural stream length and inverse node volume scaled connectome (for reasons described above), as well as the functional connectome.

#### *2.5.3. Clustering coefficient and path length*

We generated random networks from the existing matrices to be able to detect whether our structural connectome follows a small world character. According to the pioneer work of Watts and Strogatz [40], a small world network is characterized by the ratio between path length  $L$  of a network and the path length  $L_r$  of a random network being equal or bigger than 1. Additionally, the ratio of the clustering coefficient  $C$  of a network and  $C_r$  of a random network is greater than 1. The generated random networks were identical in the degree and strength distributions of the input matrix [37].

#### *2.5.4. Degree and betweenness centrality*

For hubs the network measures often comprise degree centrality (DC) and betweenness centrality (BC), and can be combined with vulnerability. For every node we calculated the DC using the BCT after applying different thresholds onto the connectome (from 0 to 1 in 0.1 steps). Putting thresholds on the matrices lowers the likelihood of false positive and false negative connections [41]. The area underneath the curve (AUC) of the degree centrality was calculated for each node with jackknife resampling of all subjects. To further investigate the homotopic organization of the brain, we performed a pair-wise t-test of the AUC values for left and right brain regions. For each node we further calculated the mean BC. For BC we calculated the AUC as described for DC.

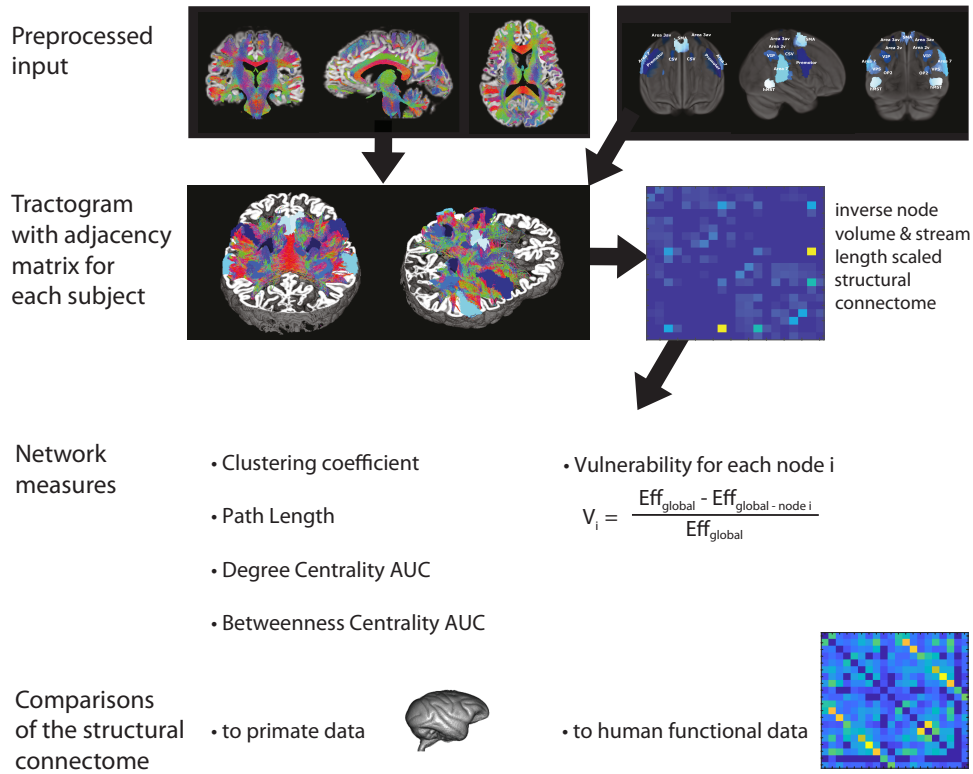


Figure 2: Visualization of parts of the pipeline analyses. The tractogram as well as the adjacency matrices of the connectome were generated with MRtrix3 (detailed pipeline commands can be found in the supplement). Visualized is data of one representative subject. The functional data were generated with the CONN toolbox. The brain connectivity toolbox was used for generating network measures. AUC = Area under the curve.

#### *2.5.5. Local and Global Efficiency and Vulnerability*

Further, the local and global efficiency was calculated for each node using the BCT. To investigate the resilience of the network communication, we measured the vulnerability as described in Iturria-Medina, Sotero, Canales-Rodriguez, Aleman-Gomez, and Melie-Garcia [42]. The vulnerability  $V_i$  was calculated for each node  $i$  by subtracting the global efficiency without node  $i$  from the global efficiency, and then dividing it by the global efficiency. As vulnerability values can be both negative and positive and can change sign when applying different thresholds, we calculated the vulnerability for the adjacency matrices without applying thresholds and calculating the AUC. Positive  $V_i$  values give rise to how important node  $i$  is for the global efficiency and removing node  $i$  harms the network efficiency. Negative values on the other hand indicate that the node is reducing the global efficiency. Values around 0 denote that the global efficiency does not change when node  $i$  is damaged or removed from the network.

#### *2.6. Comparison with primate data*

We compared our human structural scaled combined connectome to the connections reported in non-human primates of the homotopic vestibular ROIs. We took the mean values of the homotopic human nodes that led to a mean 10x10 structural connectome without hemispheric information. The connections between the analogous ROIs in primates were all generated via tracer projections [14], whereas our results originate from noninvasive imaging methods. Hence, we applied a filtering normalized threshold of 0.2 on our structural connectome to eliminate spurious connections. We considered connections with values between 0.6 and 1 as densely connected and values ranging from 0.2 to 0.6 as moderately dense connected. As we cannot detect directionality with our measures, we also extracted the non-human primate data without directionality from the literature. In non-human primates the connections were only reported as groups of either densely or moderately dense connected nodes. For the densely connected nodes, we chose a value of 0.8 and for the moderately dense connections a value of 0.4 for visualization purposes. Within the scope of the non-human primate

tracer studies the majority but not all known cortical vestibular nodes have been investigated to date (e.g. periarculate cortex, VIP) leaving us with eight out of ten nodes and its connections to compare descriptively. Area 3av was separated into Area 3aHv and Area 3aNV in the primate study but was combined to one region in our analysis.

### 3. Results

#### 3.1. Characteristics of the structural CVC

A stable subdivision into three modules were generated consistently across all structural corticocortical vestibular connectomes (sCVC): (1) the left ROIs: Area 2v, 3av, IPS3, OP2, 7, VPS, hMST, (2) the right ROIs: Area 2v, 3av, IPS3, OP2, 7, VPS, hMST, and (3) bilaterally the premotor cortex, CSV and SMA (for the following gamma values: unscaled  $0.59 \leq \textit{gamma} \leq 1.1$ ; inverse node volume scaled  $0.31 \leq \textit{gamma} \leq 0.9$ ; stream length scaled  $0.88 \leq \textit{gamma} \leq 1.05$ ; combined  $0.59 \leq \textit{gamma} \leq 1.1$ ; Figure 3). In all four connectomes the second module with right hemispheric nodes reveals higher intensities than the first module with the respective left hemispheric nodes. Hemispheric differences are addressed in a separate section below. Volume correction is obvious when comparing the inverse volume scaled connectome to the unscaled version. Connections between Area 2v and 3av gain weight as the nodes are relatively small in size and we corrected for the inverse of the node volume. Relatively large nodes' (e.g. premotor) connectivity values do not change drastically with inverse node volume correction. Further, the influence of correcting for the stream length is evident when comparing all four differently constrained connectomes. For example, Area VPS and Area 7 are in very close proximity in the brain and receive a highly dense connection attributed in those connectomes, which do not correct for stream length (i.e. unscaled and inverse node volume scaled). The same holds true for Area 2v and Area 3av. Stream length correction did not affect longer connections (e.g. Premotor – hMST) as much as shorter ones. The premotor regions are overall densely connected within the according hemi-

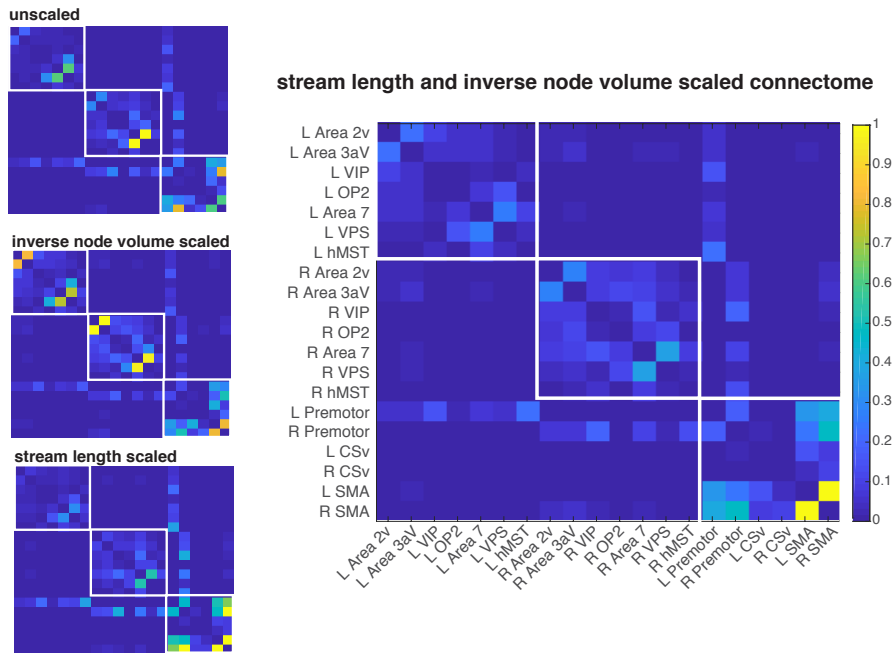


Figure 3: Mean normalized structural matrices in community Louvain order: the unscaled, the inverse node volume scaled, and the stream length scaled connectome are listed on the left. The combined scaled connectome is shown bigger on the right. Higher values depict greater connectivity between regions. R corresponds to nodes in right hemisphere, L to the ones in the left hemisphere. Order of the node labels is identical for all four connectomes. White frames indicate stable modules assigned by the community Louvain algorithm.

sphere and are highly connected with each other, as well as with the SMA of both hemispheres. Right and left SMA are densely interconnected and after correcting for stream length, SMA is ranked the most densely connected node of the network.

### 3.2. Homotopic organization of the network

Structurally we compared our results of the streamline strength and inverse node volume scaled connectome to connections reported in primates [14]. We identified overlap and differences in connections between the vestibular nodes in human and non-human primates (Figure 4). Unfortunately, we could not

compare all connections of the vestibular nodes as two of the vestibular defined nodes (IPS3/VIP and periarculate/SMA) were not reported in the tracer study of Guldin and Grusser [14]. On the one hand, we found some similarities between the two species in the vestibular structural connectomes. Two connections with very high density described in the human sCVC are also reported to be densely connected in primates: Area 2v – Area 3av, and VPS – Area 7. A rather moderately dense connection in humans of VPS and OP2 (0.33) is reported as a dense connection in primates (VPS-PIVC). On the other hand, there is quite some difference in the reported connections. A moderate connection between hMST and the human premotor cortex (0.45), as well as hMST and Area 7 (0.23) are not reported in primates. A dense connection of MST and VPS in primates is not observable in the thresholded human connectogram. Further the densely connected PIVC in primates with several regions (VC, Area 6, Area 3av, Area 2v, VPS and Area 7) are mostly absent in the human equivalent OP2 (except a moderately dense connection to Area 3av (0.21) and to VPS (0.32)).

### 3.3. Hemispheric differences

We proceeded by comparing the left and right hemispheric node values of the human streamline strength and inverse node volume scaled connectome. The sum of the unthresholded intrahemispheric connections for each node was calculated for each hemisphere across subjects. The connectivity density values followed a normal distribution and were significantly larger for the right hemisphere compared to the left ( $t(9) = 3.0, p < 0.05$ ). Pair-wise t-tests of left and right hemispheric AUC DC with jackknife resampled data was narrowly missing conventional significance for the inverse node volume and stream length scaled connectome ( $t(9) = 2.22, p = 0.0536$ ). For the AUC BC there was no hemispheric difference for the structural connectome. The structural vulnerability failed significance when comparing hemispheres.

### 3.4. Network measures

Premotor and SMA areas are characterized by relatively high vulnerability values for the network (between 0.13 and 0.2) in comparison to the vulnerability

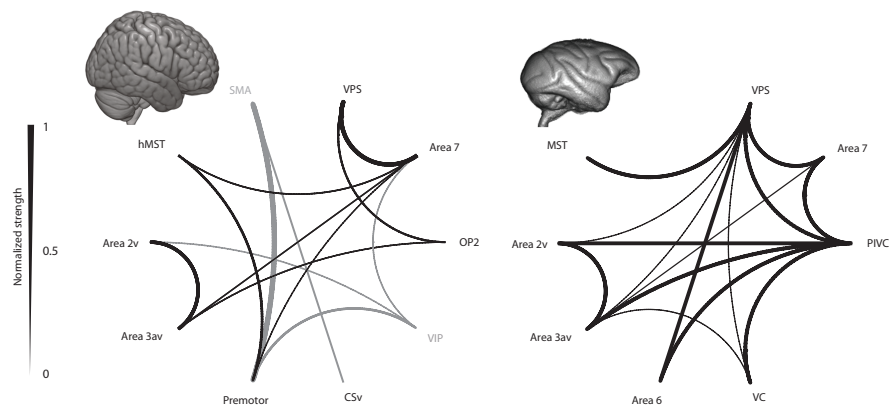


Figure 4: Connectograms: (left) mean values across hemispheres of the normalized and weighted structural stream length and inverse node volume scaled connectome of humans with a threshold at 0.2, grey color indicates that a homologous region/connection was not taken into account in primates; human brain template in MNI space 3Drendered with MRIcroGL; (right) primate dense (thicker lines) and moderate dense (thinner lines) projections (right) between the respective homologous nodes reported by Guldin and Grusser (1998); image of the macaque brain was acquired from the INIA19 Primate Brain Atlas; brain pictures are not scaled according to their relative size.

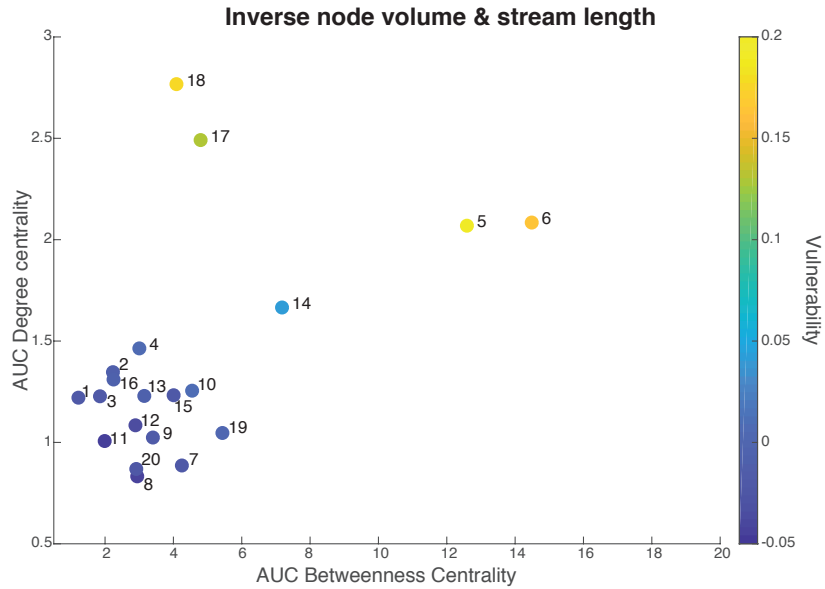


Figure 5: Network measures for the stream length and inverse node volume scaled structural connectome. Color code visualizes the vulnerability of each node. Odd numbers are assigned to left hemispheric nodes, even numbers to right hemispheric nodes (1-2: Area 2v, 3-4: Area 3av, 5-6: Premotor, 7-8: CSv, 9-10: VIP, 11-12: OP2, 13-14: Area 7, 15-16: VPS, 17-18: SMA and 19-20: hMST).

values of the rest of the nodes that accumulate around 0 (Figure 5). Even though the SMA (node 17 and 18) displays a lower AUC BC than the premotor areas (node 5 and 6), the vulnerability is comparably high (between 0.1 and 0.2). Premotor and SMA areas are characterized by a relatively high AUC DC in both hemispheres. The premotor areas are additionally characterized by a high AUC BC.

The remaining nodes cluster with relatively low centrality (AUC DC 0.75-1.5, AUC BC 1.5-6) and low vulnerability values around 0 and none of the nodes show lower values than -0.05 for the vulnerability. The path length  $L$  of the structural combined scaled connectome was 4.16 whereas the one of the random network  $L_r$  was 0.14. Hence, the ratio  $L/L_r$  was much greater than 1. The ratio of the clustering coefficient  $C/C_r$  was 1.1.

### 3.5. Characteristics of the functional CVC

The functional connectome was divided into seven stable modules for  $1.41 \leq \gamma \leq 1.68$  with the iteratively performed community Louvain algorithm. Modules consist of bilateral (1) Area2v and Area 3aV, (2) Premotor Area, (3) CSv and VIP, (4) OP2, (5) Area 7, (6) VPS, and (7) SMA and hMST (Figure 6). We observed higher correlation coefficients for the right hemisphere compared to the left ( $t(9) = 4.66$ ,  $p < 0.01$ ). Investigating centrality measures a clustering of nodes is visible in the upper right corner of the graph (AUC DC between 3.9 and 5.9; AUC BC between 7.1 and 14.3). Both SMA regions (17 & 18) are spatially separated from this cluster with lower AUC DC and AUC BC values (see Figure 6). For the functional connectome AUC DC was significantly higher for the right hemisphere ( $t(9) = 3.16$ ,  $p < 0.05$ ). For the AUC BC there was no hemispheric difference. The higher the AUC DC and the higher the AUC BC, the higher the vulnerability of the nodes. Functional vulnerability was significantly higher for the right hemisphere ( $t(9) = 3.64$ ,  $p < 0.01$ ). Right hemispheric areas VIP and VPS show the highest vulnerability in the functional network. Mean path length  $L_f$  of the fCVC was 0.29 and the one of the random network  $L_{fr}$  0.01. The ratio  $L_f/L_{fr}$  showed a 29fold larger path length for fCVC. The mean clustering coefficient ratio came to 1.1.

## 4. Discussion

The current results provide novel insights into the corticocortical organization of vestibular information processing in the human brain. We investigated the structural corticocortical vestibular connectome in humans across all established constraints (i.e. unscaled, streamline length scaled, inverse node volume scaled and a scaled combined connectome). We then compared the structural vestibular connectome with tracer-based findings in non-human primates. We discovered clear differences between the human and non-human primate vestibular structural connections. Finally, our structural and functional connectivity

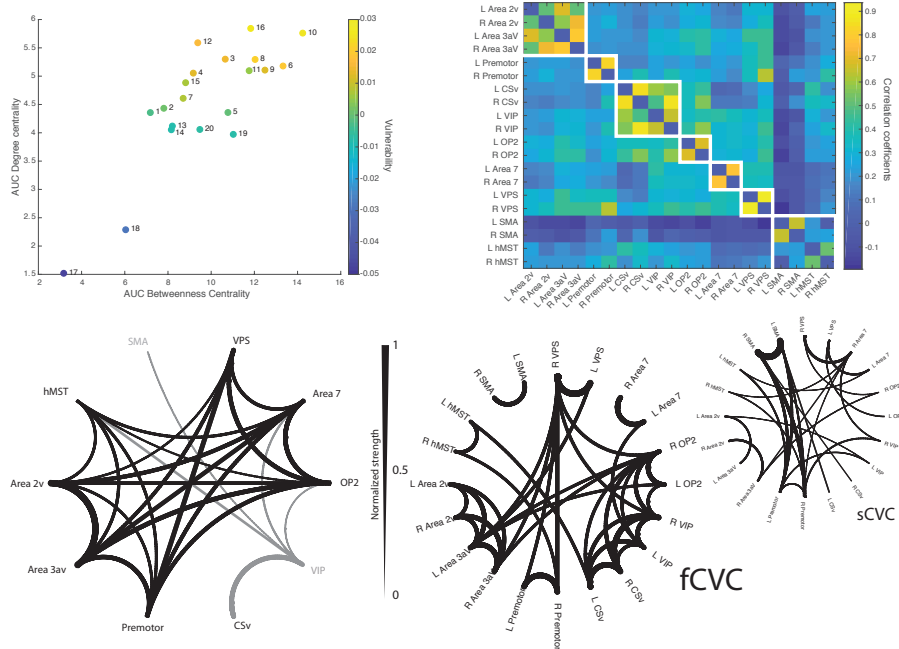


Figure 6: (upper left) Network measures AUC Degree centrality, AUC betweenness centrality and vulnerability for all nodes of the functional network. Odd numbers are assigned to left hemispheric nodes, even numbers to right hemispheric nodes (1-2: Area 2v, 3-4: Area 3av, 5-6: Premotor, 7-8: CSv, 9-10: VIP, 11-12: OP2, 13-14: Area 7, 15-16: VPS, 17-18: SMA and 19-20: hMST); (upper right) Mean matrix of the functional community Louvain ordered connectome. Color of the matrix corresponds to the clustering coefficients between nodes. For further analyses negative values were set to zero. (lower left) Connectogram of the functional connectome thresholded at 0.2, grey color indicates that a homologous primate region/connection was not considered; (lower middle) connectogram of the fCVC with hemispheric information and a threshold at 0.4. For comparison reasons the sCVC connectogram with hemispheric information is shown on the lower right thresholded at 0.1. R corresponds to right hemisphere nodes, L to the left hemisphere nodes.

findings might explain why cerebral stroke patients present with only with transient vertigo.

#### *4.1. Robust modularity of the cortical vestibular network across constraints*

Independent of the constraints and scaling that were put on the structural connectomes, we consistently found three modules with identical composition. These modules were found irrespective of correcting or not correcting for stream length or node volume. The first two modules are homogenous for both hemispheres. These findings underpin the stability and robustness of the CVC connectome. Neither of the constraints resulted in a different separation of modules.

#### *4.2. The corticocortical vestibular connectome in human and non-human primates*

We quantified the density of the connections between our predefined ROIs and compared them to previously reported connections in the macaque brain [14]. Directly neighboring regions of interest are shown to be (densely) connected in both species (Area2v - Area3av, OP2/PIVC - VPS, VPS - Area7). We additionally found clear differences between the two species' connectomes. In the macaque brain, the PIVC is densely connected within the vestibular network. Surprisingly, dense structural connections of the pendant human OP2 region with other vestibular regions of interest are scarce. Yet, human area OP2 is functionally very well interconnected with other vestibular regions. Interestingly, the whole functional connectogram of humans shares more similarities with the macaques structural connectogram than the structural connectome of humans (this might be due to the different methods used, see below). Functionally, OP2 is in high synchronicity with Area2v, Area 3av, the Premotor Regions, VPS and Area 7. All these connections are detectable in the structural connections of the monkey's pendant regions. The same holds true for the area VPS. However, even within the same species, structural connection not always resolves in functional connectivity and vice versa. Consequently, one has to be cautious with interpretations and comparisons of structure and function.

While the clear differences between the structural connectomes of humans and macaques might be due to the investigation of two different species, they might as well arise due to the different methods used to obtain the structural connectomes. Unfortunately, DWI-based tractography cannot detect the underlying anatomical connectivity on a micro scale and can only give us an estimation of the fiber orientation. In general, we have to be careful with the interpretation of streamlines as we cannot detect orientations of all fibers as resolution is too poor [43]. Fibers can be fanning, branching, crossing, or twisting. The method of DWI-based tractography is limited due to the detection of false-positive and false-negative connections. With better resolution the chance of multiple orientations of fibers within one voxel decreases, but it still cannot depict the cellular organization. Besides that, conclusions about retrograde or anterograde directionality cannot be drawn with DWI and a graph theoretical method [3]. Hence at the moment we are still lacking appropriate in vivo methods for quantifying and comparing connections within the human brain and across species. With the tracer studies, on the other hand, not all possible connections between the regions might have been studied. There is only a limited number of injections possible per animal and it is time-consuming work. Within our pool of regions two regions SMA and VIP were not reported in the macaques' connectome by Guldin and Grusser [14]. With our comparison we face two problems: we are not comparing the same species nor same methodologies. More work is needed to compare in vivo MRI and tracer injections within the same species across species to potentially overcome this obstacle as already pointed out by van den Heuvel et al. [5]. Limits of DWI in direct comparison with tracer injections are discussed elsewhere [44, 45].

#### *4.3. Characterization of the vestibular connectome by network measures*

Network measures further characterize the corticocortical vestibular connectome. Despite the clustering coefficient ratio  $C/C_r$  being 1.1, path length is (almost) 30fold larger than the one of random networks for both the structural and the functional connectome. According to pioneer work in the field of graph

theory in brain networks this is not optimally in line with small world properties. In a small world network, the ratio  $L/L_r$  should be bigger but close to one [46, 40]. Hence, we suggest that the vestibular corticocortical network has only a tendency toward a small world character. However, the presented network size seems too small for exploring small worldness, hubs or rich clubs. Future studies could include more sensory modalities and their corticocortical networks. Naturally, the vestibular network is communicating with the visual and proprioceptive networks and it is important to investigate their brain connectivity patterns during rest and vestibular stimulations. Our main goal of this work was to characterize the vestibular network itself without comparing it to other sensory subnetworks. But with a bigger network, the likelihood of identifying subnetworks is greater.

#### 4.4. *Structural vs. functional CVC*

If DWI-based tractography can actually give us a good assessment of the streamline fiber orientations, we hypothesize that the central vestibular information flow in humans works bottom-up through projection and association fibers without many structural commissural connections and information flow between the hemispheres. Structurally a greater intrahemispheric connectivity is observable. Two modules consisting of seven brain regions were found in both hemispheres (Area 2v, 3av, IPS3, OP2, 7, VPS and hMST). All ten homotopic nodes of the left and the right hemisphere are in high functional synchronicity in humans despite lacking the structural connection in almost all cases (except premotor and SMA regions). This can be witnessed in the hemisphere specific connectograms and the modularity profiles. Therefore, we hypothesize that vestibular information flow might spread bottom-up from either the brainstem or thalamic regions creating a high synchronicity in the homotopic cortical nodes.

#### 4.5. *Cerebral laterality in the CVC*

Our results suggest that there is a right-sided dominance. Firstly, we observed this in the volume of the homotopic regions. Secondly, across all four

structural, as well as the functional connectomes, the connections were significantly stronger in the right hemisphere compared to the left. Thirdly, functional vulnerability and the functional AUC DC were significantly higher for the right hemisphere. Karolis et al. [23] recently investigated the functional lateralization in combination with structural corpus callosum connectivity across four different axes including communication, emotion, perception/action and decision. The vestibular network was not part of the laterality profile. Our results might help to close this gap: Within our vestibular network only two brain structures, premotor and SMA, were presented with interhemispheric connections via the corpus callosum and there seems to be a lateralization to the right. These results are in line with the reported results of Karolis et al. [23] tested with other sensory modalities.

#### *4.6. Remission of central vestibular symptoms due to cortical lesions*

In about 5% of patients with dizziness, imbalance or vertigo symptoms an acute ischemic stroke is diagnosed [47]. With lesions in one node or one connection of the vestibular network patients can suffer from vertigo in the acute stage prior and shortly after stroke (see review [24]). Chronic central vestibular disorders however do not exist. That was the motivation for us to investigate the degree of vulnerability within the cortical vestibular network. Across our delineated connectomes we found characteristics, that might at least partly explain the generally transient nature of vestibular symptoms following a cerebral stroke. Hereto, the high degree of preexisting intrahemispheric structural connectivity might help to overcome lesion-associated symptoms occurring from stroke or other etiologies. In the acute state, functional synchronicity might be reduced between homotopic regions leading to vertigo. But we infer from our results that depending on which edge or node is damaged, this information flow can be quickly rebuilt through an alternative route. The structural corticocortical network with the detected modules forms a good basis for this on a corticocortical level. Our findings with respect to functional vulnerability being significantly higher in right hemispheric nodes are in line with previously

reported higher prevalence of vestibular symptoms due to right hemispheric lesions [21]. Further, Abe and colleagues reported longer rehabilitation time in the Pusher Syndrome (a disorder of postural balance that manifests as a pushing away toward the contralesional side in unilateral stroke) following right hemispheric lesions [22]. Whether there is a general difference in remission of vestibular symptoms depending on the lesion site needs to be further investigated by comparing vulnerability profiles of the nodes with lesion mapping and vestibular symptom status.

#### *4.7. Methodological considerations*

We want to emphasize the quality of our generated dataset as we did not only include a reasonable number of subjects, but also guaranteed a state-of-the-art DWI data quality. DWI data quality benefitted from three shells (b-values of 1000, 1750 & 2500  $s/mm^2$ ) and 150 directions certainly improved the sensitivity of the fiber orientation [43]. Some previous studies of the vestibular system using single shell DWI data on bias-field prone scanners at lower resolutions than ours make ambitious statements about corticothalamic or even brain stem-cortex connections within the vestibular network (e.g. [48, 49]). We fear that the investigators were neglecting limitations of the signal-quality of their data and the applied analytical methods. It is due to the awareness of the still prevalent profound limitations of DWI for deeper brain structures that we completely refrained from investigating any subcortical connectivity patterns.

## **Conclusion**

With the present work, we described and characterized the corticocortical vestibular network. Modularity of the human structural corticocortical vestibular connectome is extremely robust. There are substantial differences and little overlap for the vestibular connectome of humans and monkeys leaving abundant room for future research. The human structural corticocortical vestibular connectome features a stronger intrahemispheric connectivity whereas

the resting-state derived corticocortical vestibular connectome emphasizes a substantial synchronicity of homotopic nodes. A laterality preference for the right hemisphere was observable in vestibular processing for the functional and structural analysis alike (stronger connectivity values, larger anatomical nodes, higher functional vulnerability in the right cerebral cortex). There are obviously still many steps pending to fully understand the cortical vestibular organization and its embedding in and contribution to the whole-brain network. We are optimistic that our results and subsequent characterizations of the vestibular and adjacent subnetworks will help us understand the vestibular system in health and disease.

### **Author contributions**

PzE designed the study. AVO and RMR carried out the experiment (recruiting participants, MRI data collection). Data analyses were done by TR, MD, and PzE. Visualizations were generated by TR with input from VLF and PzE. TR wrote the manuscript with input from all authors. The authors declare that they have no conflict of interest.

### **Acknowledgement**

We thank all participants for taking part in the experiment. Further, we thank Mathias Hübner for his technical MRI facility assistance, Judita Huber and Alex Knorr for methodological discussions.

### **Funding**

This work was supported by the Federal Ministry of Education and Research (BMBF 01 EO 0901) and a stipend of the Graduate School of Systemic Neurosciences grant DFG-GSC 82/3 (to TR), a research fellowship (11U6414N and 11U6416N) and a research grant to stay abroad (V400717N) by the Research Foundation Flanders/FWO (to AVO), an Amelia Earhart fellowship by Zonta International (to AVO) and BELSPO Prodex (to AVO).

## References

- [1] O. Sporns, G. Tononi, R. Kotter, [The human connectome: A structural description of the human brain](#), *PLoS Comput Biol* 1 (4) (2005) e42. doi: [10.1371/journal.pcbi.0010042](https://doi.org/10.1371/journal.pcbi.0010042).  
URL <https://www.ncbi.nlm.nih.gov/pubmed/16201007>
- [2] D. C. Van Essen, S. M. Smith, D. M. Barch, T. E. Behrens, E. Yacoub, K. Ugurbil, W. U.-M. H. Consortium, [The wu-minn human connectome project: an overview](#), *Neuroimage* 80 (2013) 62–79. doi: [10.1016/j.neuroimage.2013.05.041](https://doi.org/10.1016/j.neuroimage.2013.05.041).  
URL [https://www.ncbi.nlm.nih.gov/pubmed/23684880https://ac.els-cdn.com/S1053811913005351/1-s2.0-S1053811913005351-main.pdf?\\_tid=7e7520df-66ff-46bc-9bdd-e73864d33de4&acdnat=1550148081\\_f1b5777d0b641d42de02b73c34fb778b](https://www.ncbi.nlm.nih.gov/pubmed/23684880https://ac.els-cdn.com/S1053811913005351/1-s2.0-S1053811913005351-main.pdf?_tid=7e7520df-66ff-46bc-9bdd-e73864d33de4&acdnat=1550148081_f1b5777d0b641d42de02b73c34fb778b)
- [3] P. Klauser, S. Whittle, J. G. Simmons, M. L. Byrne, L. K. Mundy, G. C. Patton, A. Fornito, N. B. Allen, [Reduced frontal white matter volume in children with early onset of adrenarache](#), *Psychoneuroendocrinology* 52 (2015) 111–8. doi: [10.1016/j.psyneuen.2014.10.020](https://doi.org/10.1016/j.psyneuen.2014.10.020).  
URL <https://www.ncbi.nlm.nih.gov/pubmed/25459897>
- [4] A. Goulas, M. Bastiani, G. Bezgin, H. B. Uylings, A. Roebroek, P. Stiers, [Comparative analysis of the macroscale structural connectivity in the macaque and human brain](#), *PLoS Comput Biol* 10 (3) (2014) e1003529. doi: [10.1371/journal.pcbi.1003529](https://doi.org/10.1371/journal.pcbi.1003529).  
URL <https://www.ncbi.nlm.nih.gov/pubmed/24676052https://www.ncbi.nlm.nih.gov/pmc/articles/PMC3967942/pdf/pcb.1003529.pdf>
- [5] M. P. van den Heuvel, E. T. Bullmore, O. Sporns, [Comparative connectomics](#), *Trends Cogn Sci* 20 (5) (2016) 345–361. doi: [10.1016/j.tics.2016.03.001](https://doi.org/10.1016/j.tics.2016.03.001).  
URL <https://www.ncbi.nlm.nih.gov/pubmed/27026480>

- [6] S. W. Oh, J. A. Harris, L. Ng, B. Winslow, N. Cain, S. Mihalas, Q. Wang, C. Lau, L. Kuan, A. M. Henry, M. T. Mortrud, B. Ouellette, T. N. Nguyen, S. A. Sorensen, C. R. Slaughterbeck, W. Wakeman, Y. Li, D. Feng, A. Ho, E. Nicholas, K. E. Hirokawa, P. Bohn, K. M. Joines, H. Peng, M. J. Hawrylycz, J. W. Phillips, J. G. Hohmann, P. Wahnoutka, C. R. Gerfen, C. Koch, A. Bernard, C. Dang, A. R. Jones, H. Zeng, [A mesoscale connectome of the mouse brain](#), *Nature* 508 (7495) (2014) 207–14. doi: [10.1038/nature13186](https://doi.org/10.1038/nature13186).  
URL <https://www.ncbi.nlm.nih.gov/pubmed/24695228><https://www.nature.com/articles/nature13186.pdf>
- [7] G. A. Orban, D. Van Essen, W. Vanduffel, [Comparative mapping of higher visual areas in monkeys and humans](#), *Trends Cogn Sci* 8 (7) (2004) 315–24. doi: [10.1016/j.tics.2004.05.009](https://doi.org/10.1016/j.tics.2004.05.009).  
URL <https://www.ncbi.nlm.nih.gov/pubmed/15242691>
- [8] M. G. Rosa, R. Tweedale, [Brain maps, great and small: lessons from comparative studies of primate visual cortical organization](#), *Philos Trans R Soc Lond B Biol Sci* 360 (1456) (2005) 665–91. doi: [10.1098/rstb.2005.1626](https://doi.org/10.1098/rstb.2005.1626).  
URL <https://www.ncbi.nlm.nih.gov/pubmed/15937007><https://www.ncbi.nlm.nih.gov/pmc/articles/PMC1874231/pdf/rstb20051626.pdf>
- [9] Q. X. Wang, O. Sporns, A. Burkhalter, [Network analysis of corticocortical connections reveals ventral and dorsal processing streams in mouse visual cortex](#), *Journal of Neuroscience* 32 (13) (2012) 4386–4399. doi: [10.1523/Jneurosci.6063-11.2012](https://doi.org/10.1523/Jneurosci.6063-11.2012).  
URL <http://www.jneurosci.org/content/jneuro/32/13/4386.full.pdf>
- [10] B. Misic, R. F. Betzel, A. Griffa, M. A. de Reus, Y. He, X. N. Zuo, M. P. van den Heuvel, P. Hagmann, O. Sporns, R. J. Zatorre, [Network-based asymmetry of the human auditory system](#), *Cereb Cortex* 28 (7) (2018) 2655–2664. doi: [10.1093/cercor/bhy101](https://doi.org/10.1093/cercor/bhy101).

- URL <https://www.ncbi.nlm.nih.gov/pubmed/29722805><https://www.ncbi.nlm.nih.gov/pmc/articles/PMC5998951/pdf/bhy101.pdf>
- [11] A. Kucyi, K. D. Davis, *The dynamic pain connectome*, Trends Neurosci 38 (2) (2015) 86–95. doi:10.1016/j.tins.2014.11.006.  
URL <https://www.ncbi.nlm.nih.gov/pubmed/25541287>
- [12] D. Milardi, A. Cacciola, A. Calamuneri, M. F. Ghilardi, F. Caminiti, F. Cascio, V. Andronaco, G. Anastasi, E. Mormina, A. Arrigo, D. Bruschetta, A. Quartarone, *The olfactory system revealed: Non-invasive mapping by using constrained spherical deconvolution tractography in healthy humans*, Front Neuroanat 11 (2017) 32. doi:10.3389/fnana.2017.00032.  
URL <https://www.ncbi.nlm.nih.gov/pubmed/28443000>
- [13] R. M. Ruehl, T. Stephan, M. Dieterich, P. zu Eulenburg, *Towards a human vestibular cortex – manifold confounders hamper the delineation of vestibular responses in functional neuroimaging*, Clinical Neurophysiology 128 (10) (2017) e331–e332. doi:<https://doi.org/10.1016/j.clinph.2017.06.090>.
- [14] W. O. Guldin, O. J. Grusser, *Is there a vestibular cortex?*, Trends Neurosci 21 (6) (1998) 254–9.  
URL <https://www.ncbi.nlm.nih.gov/pubmed/9641538><https://www.sciencedirect.com/science/article/pii/S0166223697012113?via%3Dihub>
- [15] C. Lopez, O. Blanke, F. W. Mast, *The human vestibular cortex revealed by coordinate-based activation likelihood estimation meta-analysis*, Neuroscience 212 (2012) 159–79. doi:10.1016/j.neuroscience.2012.03.028.  
URL <https://www.ncbi.nlm.nih.gov/pubmed/22516007>
- [16] P. zu Eulenburg, S. Caspers, C. Roski, S. B. Eickhoff, *Meta-analytical definition and functional connectivity of the human vestibular cortex*, Neuroimage 60 (1) (2012) 162–9. doi:10.1016/j.neuroimage.2011.12.032.  
URL <https://www.ncbi.nlm.nih.gov/pubmed/22209784>

- [17] P. zu Eulenburg, W. Muller-Forell, M. Dieterich, [On the recall of vestibular sensations](#), *Brain Struct Funct* 218 (1) (2013) 255–67. doi:10.1007/s00429-012-0399-0.  
URL <https://www.ncbi.nlm.nih.gov/pubmed/22367249><https://link.springer.com/article/10.1007%2Fs00429-012-0399-0>
- [18] P. zu Eulenburg, T. Stephan, M. Dieterich, R. M. Ruehl, The human vestibular cortex, in: 30th Bárány Society meeting, 2018.
- [19] S. Knecht, M. Deppe, B. Drager, L. Bobe, H. Lohmann, E. Ringelstein, H. Henningsen, [Language lateralization in healthy right-handers](#), *Brain* 123 ( Pt 1) (2000) 74–81. doi:10.1093/brain/123.1.74.  
URL <https://www.ncbi.nlm.nih.gov/pubmed/10611122>
- [20] M. Dieterich, S. Bense, S. Lutz, A. Drzezga, T. Stephan, P. Bartenstein, T. Brandt, [Dominance for vestibular cortical function in the non-dominant hemisphere](#), *Cereb Cortex* 13 (9) (2003) 994–1007. doi:10.1093/cercor/13.9.994.  
URL <https://www.ncbi.nlm.nih.gov/pubmed/12902399>
- [21] S. Eguchi, G. Hirose, M. Miaki, [Vestibular symptoms in acute hemispheric strokes](#), *J Neurology* doi:10.1007/s00415-019-09342-9.  
URL <https://www.ncbi.nlm.nih.gov/pubmed/31037419><https://link.springer.com/content/pdf/10.1007%2Fs00415-019-09342-9.pdf>
- [22] H. Abe, T. Kondo, Y. Oouchida, Y. Suzukamo, S. Fujiwara, S. Izumi, [Prevalence and length of recovery of pusher syndrome based on cerebral hemispheric lesion side in patients with acute stroke](#), *Stroke* 43 (6) (2012) 1654–6. doi:10.1161/STROKEAHA.111.638379.  
URL <https://www.ncbi.nlm.nih.gov/pubmed/22382159>
- [23] V. R. Karolis, M. Corbetta, M. Thiebaut de Schotten, [The architecture of functional lateralisation and its relationship to callosal connectivity in the human brain](#), *Nat Commun* 10 (1) (2019) 1417.

[doi:10.1038/s41467-019-09344-1](https://doi.org/10.1038/s41467-019-09344-1).

URL [https://www.ncbi.nlm.nih.gov/pubmed/30926845https://www.ncbi.nlm.nih.gov/pmc/articles/PMC6441088/pdf/41467\\_2019\\_Article\\_9344.pdf](https://www.ncbi.nlm.nih.gov/pubmed/30926845https://www.ncbi.nlm.nih.gov/pmc/articles/PMC6441088/pdf/41467_2019_Article_9344.pdf)

- [24] T. Brandt, M. Dieterich, [The dizzy patient: don't forget disorders of the central vestibular system](#), *Nat Rev Neurol* 13 (6) (2017) 352–362. [doi:10.1038/nrneurol.2017.58](https://doi.org/10.1038/nrneurol.2017.58).  
URL <https://www.ncbi.nlm.nih.gov/pubmed/28429801>
- [25] D. A. Feinberg, S. Moeller, S. M. Smith, E. Auerbach, S. Ramanna, M. Gunther, M. F. Glasser, K. L. Miller, K. Ugurbil, E. Yacoub, [Multiplexed echo planar imaging for sub-second whole brain fmri and fast diffusion imaging](#), *PLoS One* 5 (12) (2010) e15710. [doi:10.1371/journal.pone.0015710](https://doi.org/10.1371/journal.pone.0015710).  
URL <https://www.ncbi.nlm.nih.gov/pubmed/21187930https://www.ncbi.nlm.nih.gov/pmc/articles/PMC3004955/pdf/pone.0015710.pdf>
- [26] R. F. Betzel, A. Griffa, P. Hagmann, B. Mišić, [Distance-dependent consensus thresholds for generating group-representative structural brain networks](#), *Network Neuroscience* 3 (2) (2019) 475–496. [doi:10.1162/netn\\_a\\_00075](https://doi.org/10.1162/netn_a_00075).
- [27] M. Jenkinson, C. F. Beckmann, T. E. Behrens, M. W. Woolrich, S. M. Smith, [Fsl](#), *Neuroimage* 62 (2) (2012) 782–90. [doi:10.1016/j.neuroimage.2011.09.015](https://doi.org/10.1016/j.neuroimage.2011.09.015).  
URL <https://www.ncbi.nlm.nih.gov/pubmed/21979382>
- [28] B. Avants, N. Tustison, G. Song, [Advanced normalization tools](#), *ants* 1.0, Sourceforge. Jun.
- [29] J. D. Tournier, F. Calamante, A. Connelly, [Robust determination of the fibre orientation distribution in diffusion mri: non-negativity constrained super-resolved spherical deconvolution](#), *Neuroimage* 35 (4) (2007) 1459–72.

[doi:10.1016/j.neuroimage.2007.02.016](https://doi.org/10.1016/j.neuroimage.2007.02.016).

URL <https://www.ncbi.nlm.nih.gov/pubmed/17379540>

- [30] J. D. Tournier, F. Calamante, A. Connelly, [Mrtrix: Diffusion tractography in crossing fiber regions](#), *International Journal of Imaging Systems and Technology* 22 (1) (2012) 53–66. [doi:10.1002/ima.22005](https://doi.org/10.1002/ima.22005).

URL [http:https://doi.org/10.1002/ima.22005https://onlinelibrary.wiley.com/doi/pdf/10.1002/ima.22005](http://https://doi.org/10.1002/ima.22005https://onlinelibrary.wiley.com/doi/pdf/10.1002/ima.22005)

- [31] J. D. Tournier, R. Smith, D. Raffelt, R. Tabbara, T. Dhollander, M. Pietsch, D. Christiaens, B. Jeurissen, C. H. Yeh, A. Connelly, [Mrtrix3: A fast, flexible and open software framework for medical image processing and visualisation](#), *Neuroimage* (2019) 116137[doi:10.1016/j.neuroimage.2019.116137](https://doi.org/10.1016/j.neuroimage.2019.116137).

URL <https://www.ncbi.nlm.nih.gov/pubmed/31473352>

- [32] T. Dhollander, D. Raffelt, A. Connelly, [Unsupervised 3-tissue response function estimation from single-shell or multi-shell diffusion mr data without a co-registered t1 image](#), *ISMRM Workshop on Breaking the Barriers of Diffusion MRI*.

- [33] R. E. Smith, J. D. Tournier, F. Calamante, A. Connelly, [Anatomically-constrained tractography: improved diffusion mri streamlines tractography through effective use of anatomical information](#), *Neuroimage* 62 (3) (2012) 1924–38. [doi:10.1016/j.neuroimage.2012.06.005](https://doi.org/10.1016/j.neuroimage.2012.06.005).

URL <https://www.ncbi.nlm.nih.gov/pubmed/22705374>

- [34] R. E. Smith, J. D. Tournier, F. Calamante, A. Connelly, [Sift: Spherical-deconvolution informed filtering of tractograms](#), *Neuroimage* 67 (2013) 298–312. [doi:10.1016/j.neuroimage.2012.11.049](https://doi.org/10.1016/j.neuroimage.2012.11.049).

URL [https://www.ncbi.nlm.nih.gov/pubmed/23238430https://ac.els-cdn.com/S1053811912011615/1-s2.0-S1053811912011615-main.pdf?\\_tid=e760d98f-363f-4ac5-95fc-1c57533b4175&acdnat=1549981741\\_0c897f5a21e524782f584956b52ed84d](https://www.ncbi.nlm.nih.gov/pubmed/23238430https://ac.els-cdn.com/S1053811912011615/1-s2.0-S1053811912011615-main.pdf?_tid=e760d98f-363f-4ac5-95fc-1c57533b4175&acdnat=1549981741_0c897f5a21e524782f584956b52ed84d)

- [35] R. E. Smith, J. D. Tournier, F. Calamante, A. Connelly, [Sift2: Enabling dense quantitative assessment of brain white matter connectivity using streamlines tractography](#), *Neuroimage* 119 (2015) 338–51. doi:10.1016/j.neuroimage.2015.06.092.  
URL <https://www.ncbi.nlm.nih.gov/pubmed/26163802>
- [36] S. Whitfield-Gabrieli, A. Nieto-Castanon, [Conn: a functional connectivity toolbox for correlated and anticorrelated brain networks](#), *Brain Connect* 2 (3) (2012) 125–41. doi:10.1089/brain.2012.0073.  
URL <https://www.ncbi.nlm.nih.gov/pubmed/22642651>
- [37] M. Rubinov, O. Sporns, [Weight-conserving characterization of complex functional brain networks](#), *Neuroimage* 56 (4) (2011) 2068–79. doi:10.1016/j.neuroimage.2011.03.069.  
URL <https://www.ncbi.nlm.nih.gov/pubmed/21459148>
- [38] M. Rubinov, O. Sporns, [Complex network measures of brain connectivity: uses and interpretations](#), *Neuroimage* 52 (3) (2010) 1059–69. doi:10.1016/j.neuroimage.2009.10.003.  
URL <https://www.ncbi.nlm.nih.gov/pubmed/19819337>
- [39] V. D. Blondel, J.-L. Guillaume, R. Lambiotte, E. Lefebvre, [Fast unfolding of communities in large networks](#), *Journal of Statistical Mechanics: Theory and Experiment* 2008 (10) (2008) P10008. doi:10.1088/1742-5468/2008/10/p10008.  
URL <http://dx.doi.org/10.1088/1742-5468/2008/10/P10008https://iopscience.iop.org/article/10.1088/1742-5468/2008/10/P10008/pdf>
- [40] D. J. Watts, S. H. Strogatz, [Collective dynamics of 'small-world' networks](#), *Nature* 393 (6684) (1998) 440–2. doi:10.1038/30918.  
URL <https://www.ncbi.nlm.nih.gov/pubmed/9623998https://www.nature.com/articles/30918.pdf>

- [41] M. A. de Reus, M. P. van den Heuvel, [Estimating false positives and negatives in brain networks](#), *Neuroimage* 70 (2013) 402–9. doi:10.1016/j.neuroimage.2012.12.066.  
URL <https://www.ncbi.nlm.nih.gov/pubmed/23296185>
- [42] Y. Iturria-Medina, R. C. Sotero, E. J. Canales-Rodriguez, Y. Aleman-Gomez, L. Melie-Garcia, [Studying the human brain anatomical network via diffusion-weighted mri and graph theory](#), *Neuroimage* 40 (3) (2008) 1064–76. doi:10.1016/j.neuroimage.2007.10.060.  
URL <https://www.ncbi.nlm.nih.gov/pubmed/18272400>
- [43] D. K. Jones, T. R. Knosche, R. Turner, [White matter integrity, fiber count, and other fallacies: the do’s and don’ts of diffusion mri](#), *Neuroimage* 73 (2013) 239–54. doi:10.1016/j.neuroimage.2012.06.081.  
URL [https://www.ncbi.nlm.nih.gov/pubmed/22846632https://acels-cdn.com/S1053811912007306/1-s2.0-S1053811912007306-main.pdf?\\_tid=131a2283-edb5-46df-a383-1019a3ec664c&acdnat=1549981704\\_ccdaabe221b5306e57db67f619dd616f](https://www.ncbi.nlm.nih.gov/pubmed/22846632https://acels-cdn.com/S1053811912007306/1-s2.0-S1053811912007306-main.pdf?_tid=131a2283-edb5-46df-a383-1019a3ec664c&acdnat=1549981704_ccdaabe221b5306e57db67f619dd616f)
- [44] C. J. Donahue, S. N. Sotiropoulos, S. Jbabdi, M. Hernandez-Fernandez, T. E. Behrens, T. B. Dyrby, T. Coalson, H. Kennedy, K. Knoblauch, D. C. Van Essen, M. F. Glasser, [Using diffusion tractography to predict cortical connection strength and distance: A quantitative comparison with tracers in the monkey](#), *J Neurosci* 36 (25) (2016) 6758–70. doi:10.1523/JNEUROSCI.0493-16.2016.  
URL <https://www.ncbi.nlm.nih.gov/pubmed/27335406https://www.ncbi.nlm.nih.gov/pmc/articles/PMC4916250/pdf/zns6758.pdf>
- [45] C. Reveley, A. K. Seth, C. Pierpaoli, A. C. Silva, D. Yu, R. C. Saunders, D. A. Leopold, F. Q. Ye, [Superficial white matter fiber systems impede detection of long-range cortical connections in diffusion mr tractography](#), *Proc Natl Acad Sci U S A* 112 (21) (2015) E2820–8. doi:10.1073/pnas.

1418198112.

URL <https://www.ncbi.nlm.nih.gov/pubmed/25964365>

- [46] E. Bullmore, O. Sporns, [Complex brain networks: graph theoretical analysis of structural and functional systems](#), *Nat Rev Neurosci* 10 (3) (2009) 186–98. doi:10.1038/nrn2575.

URL <https://www.ncbi.nlm.nih.gov/pubmed/19190637><https://www.nature.com/articles/nrn2575.pdf>

- [47] Y. Kim, M. Faysel, C. Balucani, D. Yu, N. Gilles, S. R. Levine, [Ischemic stroke predictors in patients presenting with dizziness, imbalance, and vertigo](#), *J Stroke Cerebrovasc Dis* 27 (12) (2018) 3419–3424. doi:10.1016/j.jstrokecerebrovasdis.2018.08.002.

URL <https://www.ncbi.nlm.nih.gov/pubmed/30206000>

- [48] V. Kirsch, D. Keeser, T. Hergenroeder, O. Erat, B. Ertl-Wagner, T. Brandt, M. Dieterich, [Structural and functional connectivity mapping of the vestibular circuitry from human brainstem to cortex](#), *Brain Struct Funct* 221 (3) (2016) 1291–308. doi:10.1007/s00429-014-0971-x.

URL <https://www.ncbi.nlm.nih.gov/pubmed/25552315><https://link.springer.com/content/pdf/10.1007%2Fs00429-014-0971-x.pdf>

- [49] A. M. Wirth, S. M. Frank, M. W. Greenlee, A. L. Beer, [White matter connectivity of the visual-vestibular cortex examined by diffusion-weighted imaging](#), *Brain Connect* 8 (4) (2018) 235–244. doi:10.1089/brain.2017.0544.

URL <https://www.ncbi.nlm.nih.gov/pubmed/29571264>

## Supplementary material

Table S1: List of nodes of the corticocortical vestibular network, its volume and the coordinates of the center of mass in MNI space.

Node	Assigned Area	Volume (in in mm <sup>3</sup> )	MNI-coordinates (x;y;z)
1	Left Area2v	416	-23;-39;61
2	Right Area2v	569	28;-39;61
3	Left Area3aV	1142	-23;-37;61
4	Right Area3aV	1265	27;-36;67
5	Left Area6/ Premotor	5608	-44;-9;51
6	Right Area6/ Premotor	8808	47;7;36
7	Left CSv/ VC	1789	-10;-17;41
8	Right CSv/ VC	1795	12;-24;43
9	Left VIP/ IPS3	1298	-29;-51;42
10	Right VIP/ IPS3	2182	34;-50;44
11	Left OP2/ PIVC	988	-39;-30;20
12	Right OP2/ PIVC	1375	37;-31;19
13	Left PF/ Area7	1775	-58;-35;25
14	Right PF/ Area7	3640	64;-33;20
15	Left PFcm/ VPS	2447	-46;-34;21
16	Right PFcm/ VPS	2594	54;-33;23
17	Left Periarculate/ SMA	1752	-8;-8;65
18	Right Periarculate/ SMA	2592	4;1;60
19	Left hMST	2513	-52;-60;3
20	Right hMST	2398	53;-58;2

## 2.3 Magnetic vestibular stimulation and its effect on brain networks

Raiser, T. M. \*, Ahmadi, S. A. \*, Flanagin, V. L. (in preparation)

\* Theresa M. Raiser and Seyed-Ahmad Ahmadi contributed equally to this work

### Summary

The project “Magnetic vestibular stimulation and its effect on brain networks” investigates whether the magnetic field of the MRI machine is influencing brain activity or functional connectivity of normal participants. In 33 participants we investigated vestibular sensitivity, cortical activation patterns due to galvanic vestibular stimulation, rsfMRI activity and connectivity in complete darkness in relation with video-oculography parameters (n=29) as well as rsfMRI with fixation. In summary, on a group level, the MVS effect does not influence cortical network activity nor connectivity in a 3T MRI scanner. Our data suggests, that there is a high variance across participants onto the MVS effect, in line with previously reported results (Roberts et al., 2011). This might reflect an intersubjective sensitivity to the MVS stimulation and it is still unclear which individual factor is influencing this. With our results it is clear that the orientation of the horizontal semicircular canal is not the only underlying cause. Vestibular sensitivity is varying across participants (measured with caloric irrigation) and is explaining some of the variance in the observed MVS effect in our data set.

### Author contributions

The following authors contributed to this work: Virginia L. Flanagin designed the study. Theresa M. Raiser collected the data under the supervision of Virginia L. Flanagin. Seyed-Ahmad Ahmadi provided the horizontal and vertical components of the eye-tracking data. Further eye-tracking analyses were performed by Virginia L. Flanagin. Seyed-Ahmad Ahmadi provided canal orientations with respect to the magnetic field and with respect to Reid’s plane. MRI data analyses were done by Theresa M. Raiser and Virginia L. Flanagin. Theresa M. Raiser wrote the manuscript with guidance of Virginia L. Flanagin and input from all authors.

# Magnetic vestibular stimulation and its effects on brain activity

Theresa M. Raiser<sup>†,a,d</sup>, Seyed-Ahmad Ahmadi<sup>†,a,b,c</sup>, Virginia L. Flanagan<sup>\*a,d</sup>

<sup>a</sup>*German Center for Vertigo and Balance Disorders (DSGZ),  
Fraunhoferstr. 20, 82152 Planegg, Germany*

<sup>b</sup>*Faculty of Informatics, Technical University of Munich,  
Boltzmannstr. 3, 85748 Garching, Germany*

<sup>c</sup>*Department of Neurology, Klinikum der Universität München,  
Marchioninistr. 15, 81377 Munich, Germany*

<sup>d</sup>*Graduate School of Systemic Neurosciences, Ludwig-Maximilians-Universität München,  
Großhaderner Str. 2, 82152 Planegg, Germany*

---

## Abstract

About a decade ago the magnetic vestibular stimulation (MVS) has been described. Strong magnetic fields like the one in the MRI scanner elicit nystagmus eye-movements in complete darkness due to the Lorentz force that acts upon the peripheral vestibular system. To date it is not clear, whether the MVS effect affects the BOLD signal or the brain connectivity.

We investigated the MVS effect in 33 healthy right-handed participants via videooculography (VOG) in a 3T MRI. Parallel to VOG we collected resting state fMRI (rsfMRI) data in two conditions: in complete darkness and with a fixation task (i.e. nystagmus suppression). For increasing the likelihood of nystagmus, participants were lying in the scanner with a neck extension (head tilted backwards). Further, vestibular sensitivity measurements (video head impulse test and caloric irrigation) and questionnaires about physical activity and motion sickness have been conducted.

In 88% of our participants we could detect a MVS induced nystagmus during rsfMRI scanning. The variability of the MVS effect could not be exclusively explained by the horizontal semicircular canal orientation with respect to the

---

\*Corresponding author: [vflanagin@lrz.uni-muenchen.de](mailto:vflanagin@lrz.uni-muenchen.de)

† T.M. Raiser and S.-A. Ahmadi contributed equally to this work.

magnetic field. Caloric irrigation as a measurement of vestibular sensitivity additionally explains part of the variance observed in the MVS effect. BOLD fluctuations did not correlate significantly with slow phase velocity (SPV) over time. Participants with higher mean horizontal SPV however, showed higher activation in vestibular, executive control and attention regions. Comparing the two rsfMRI conditions, functional connectivity did not change apart from the visual occipital areas and cerebellar regions. Main effect of the horizontal slow phase velocity correlated with higher connectivity in the sensorimotor network of the rsfMRI session in complete darkness.

Not only horizontal semicircular canal orientation with respect to the magnetic field, but also vestibular sensitivity (measured with caloric irrigation) influence the strength of the MVS effect across participants. Whether other vestibule measurements (e.g. utricle) are contributing to the variability in the MVS effect remains unclear.

*Keywords:* MVS, vestibular stimulation, horizontal canal, rsfMRI

---

## 1. Introduction

For many years we try to understand how the brain functions, which brain regions are responsible for which processes, how we perceive, etc. and developed methods to investigate neural mechanisms and solve neuroscientific questions. One method of focus here is resting state functional magnetic resonance imaging (rsfMRI). During rsfMRI the person lying in the scanner is instructed to do nothing in particular, is not trained to perform any task, but asked to not fall asleep. The signal of rsfMRI contains low frequency fluctuations and their origin is not fully understood yet. Recent studies claim that some eye parameters like dilation or movement confound the signal. In this paper we try to solve whether a stimulation of the vestibular system by the MRI scanner itself might contribute to these fluctuations. This stimulation is known as magnetic vestibular stimulation (MVS).

### *1.1. Fluctuations of resting state BOLD fMRI signal*

RsfMRI is one standard method to solve functional neuroscientific questions about the human brain. However, there is no standardized condition in rsfMRI. It is performed in one of the following combinations: either eyes are closed or open, either with or without fixation, in an enlightened or completely darkened room. Over the past years rsfMRI gained popularity due to its ease in acquisition in contrast to task functional MRI (fMRI). Further for performing rsfMRI there exists no specific presuppositions for the participant or patient, meaning you can easily study brains of children, people with low intelligence, patients with disorders of consciousness etc..

The activity of neurons of the brain consists of both high and low frequency spectral power distributions. Studying task fMRI, low frequencies are considered background noise and the high frequencies are in focus. The background noise in task fMRI is considered the main signal in rsfMRI. During rest the BOLD signal contains spontaneous low-frequency fluctuations ranging from 0.01 - 0.08 Hz [1, 2]. This constant background activity can be split into several spatially separated, functional networks that are known as the resting state networks (RSN): e.g. default mode network (DMN), sensorimotor network, salience, visual, and auditory network, etc. [3].

All reasons for the fluctuations in rsfMRI have yet to be clarified. Besides the neural there are also non-neural contributions. In the following paragraph we aim to address (potential) influencing factors and artifacts before we investigate whether the magnet of the MRI counts as one of the factors. First of all, physiological parameters influence the signal. At 3T fMRI experiments respiratory and cardiac related noise have been reported to account for 1/3 of the total physiological noise in gray matter [4, 5]. Fortunately, the cardiovascular (0.6 – 1.2 Hz) and respiratory signal frequencies (0.1 – 0.5 Hz) can be separated from the BOLD since they are in a slightly faster frequency range [1]. Removing the physiological confounding noise is significantly improving both fMRI and rsfMRI data quality [4]. Further, eye-tracking can be used to study the relationship of eye specific parameters (e.g. eye movements and pupillometry) with

the signal. Fransson et al. [6] detected slow fluctuations in the DMN to be in line with slow eye movement fluctuations during passive visual fixation. Pupil dilations have been linked to the resting state fluctuations, especially in the buildup of DMN activity and suppression in the sensorimotor network activity [7]. Schneider et al. [8] reported pupil dilations to correlate with activity of the salience network. Eye movement recordings were also done with closed eyes: Ramot et al. [9] recorded spontaneous electro-ocular activity and demonstrated a link between amplitude and velocity of the eye movements and the BOLD fluctuations in occipital and parietal cortices. Eye-tracking can additionally be a good measurement of wakefulness of the participant. Not only can we observe whether eyes are open or whether the pupil is dilated, but also whether eye parameters change with decreasing wakefulness. With measures of EEG activity Regen et al. [10] identified a high correlation of pupillary unrest with sleepiness. During sleep there is a higher whole brain fluctuation compared to the awake stage [11]. So sleep is affecting the signal but the extracted RSN are reported to stay relatively stable through different sleep stages. RSN can still be identified and the integrity of the DMN is comprised, however the frontal and posterior areas of the DMN are for example less correlated with reduced consciousness caused by sleep [12, 13]. In the meantime, right and left parietal regions have an increased correlation during deep sleep [12]. For more information about functional and effective connectivity during sleep, we refer to a comprehensive review by Klimova [14].

Concerning the MRI itself we further consider technical factors for causing fluctuations in the rsfMRI signal. There are high frequency oscillations in the MRI when obtaining images. During rsfMRI we focus on the low fluctuations though. However, one indirectly influencing factor might be the magnetic field. The magnetic field is nearly homogeneous in the middle of the bore, but it can lead to some physiological fluctuations in humans described in the next paragraph.

### *1.2. The magnetic vestibular stimulation*

Roberts et al. [15] reported not long ago that the magnetic field of the MRI machine is stimulating the vestibular system. This can indirectly be measured by observing eye movements in complete darkness. Through the strong magnetic field and currents within the inner ear a force (i.e. Lorentz force) acts upon the vestibular organ. Through the created deflection of the cupula in the inner ear the vestibulo ocular reflex is elicited, and eye movements can be recorded. The eye movements are characterized by a slow (mostly horizontal) movement in one and a quick phase in the opposite direction, and are called nystagmus.

Influencing factors to the strength and the direction of the occurring nystagmus are (1) polarity of the magnetic field of the MRI scanner, (2) field strength, (3) orientation of the head with respect to the magnetic field, and (4) it has been hypothesized that individual anatomical differences might be an influencing factor [15, 16]. With a change in polarity the direction of the eye-movement reverses. Some MRI systems therefore elicit a rightward nystagmus and others a leftward nystagmus. With increasing field strength of the MRI the MVS effect increases [15, 16]. Further the orientation (along the pitch plane) is essential for the direction and the strength of the effect [15]: with the head tilted backwards horizontal nystagmus occurs in one direction. With a head position where the chin is close to the chest the nystagmus direction reverses with a null position in between. This null position varies across participants and might indicate that individual anatomical differences might be the underlying cause here. Further with a head tilt in roll plane, vertical and torsional components of the nystagmus occur as the Lorentz force affects the vertical semicircular canals [17, 18].

Once in a certain position in the MRI scanner and after some adaptation time, there are still fluctuations within the nystagmus strength, i.e. variation in slow phase velocity across time. Our aim is to relate the fluctuations of these eye movements to the rsfMRI signal and reveal a potential additional explanation for the rsfMRI fluctuations. It is of course essential for the data quality and research results to separate non-neuronal from neuronal signal contributions for allowing valid statements.

## 2. Methods

### 2.1. Participants

Thirty-six right-handed participants (mean age:  $28.1 \pm 3.97$  years, 19 female) were initially recruited for the study. Only participants without any neurological condition were recruited. None of the participants had ever been diagnosed with vertigo. None of the participants showed signs of ocular misalignment, as measured via the cover test (see section 2.2.2 paragraph Orthoptic testing). Prior to analysis, two participants were excluded due to excessive head motion during MRI data acquisition (see section 2.4.1 and figure S1), and one additional participant was excluded because of missing eye-tracking calibration, resulting in 33 participants that were included in the analyses (mean age:  $28.4 \pm 3.99$  years, 18 female). The local ethics committee in Munich approved the study and all participants gave their written informed consent in accordance with the declaration of Helsinki (ethics approval 366-16; declaration of Helsinki amended by the 64th WMA General Assembly, Fortaleza, Brazil, October 2013). Of those 33 participants, an additional four participants were excluded from those analyses involving eye-tracking information, because they did not show spontaneous nystagmus during data acquisition ( $n= 29$ , mean age:  $28.5 \pm 4.0$  years, 17 female).

### 2.2. Procedure Day 1

The experiment was performed over two days, with no more than 12 days in between. On the first day, we gave participants questionnaires and vestibular diagnostic testing. Participants were required to meet the following criteria in order to participate in the MRI experiment on day 2. Only right-handed healthy individuals between 20 and 40 years of age have been recruited. Exclusion criteria were any neurological disease, especially if they have ever been diagnosed with vertigo as well as generally acknowledged contraindications to MRI (claustrophobia, metal implants, etc.). None of the participants that were initially recruited were excluded at this point. The details of the individual tests are explained below.

### *2.2.1. Questionnaires*

To investigate the vestibular sensitivity two questionnaires have been performed: the Motion Sickness Susceptibility Questionnaire Short-form (MSSQ-Short) [19] for investigating the likelihood of kinetosis, and the Global Physical Activity Questionnaire (GPAQ) [20] to interrogate participants about their exercise level. Handedness was documented with a subset of 10 questions [21] out of the original 20 question handedness inventory [22].

### *2.2.2. Orthoptic testing*

We tested ocular dominance and the absence of strabismus in each participant at the beginning of the first day, since video-oculographic (VOG) measures were so critical to the study. To test for ocular misalignment, the cover test was performed on both eyes. None of the participants showed a shift in fixation of the uncovered nor the covered eye. A variation of the Miles test [23] was used to assess ocular dominance. Participants stretched out their arms as far away from their bodies as possible and formed a small triangle with both hands through which they focused on a mark on the wall that was completely within the boundaries of the triangle. The mark was 3.5m away from the participant. Participants were then instructed to close one eye followed by the other eye. The eye through which they still could sight the object was defined as their dominant eye. For consistency of our results, eye-tracking was performed with the participants' dominant eye.

### *2.2.3. Vestibular diagnostic testing*

After orthoptic testing, vestibular diagnostic testing was performed. To test the sensitivity of the peripheral vestibular system we used the video-based head impulse test (vHIT) and caloric thermal irrigation. Physiological data was based on VOG using the EyeSeeCam eye-tracking system and accompanying software [24]. The Halmagyi/head impulse test [25] was refined by [26] through a video system for guaranteeing a more standardized and objective detection of corrective saccades. For the vHIT a five-point calibration was performed. Then

participants were instructed to fixate a point at 3.5m distance. Participants' head position was kept at an approximately 30 degrees downward pitch during performance of the vHIT to increase the mean gain. The gain for left and right as well as the respective median gain  $\pm$  one standard deviation (0-100 ms) were recorded. Deficiencies detected by this test can indicate a peripheral vestibular lesion. Caloric thermal irrigation was used to test the sensitivity of the left and right peripheral vestibular system separately. The caloric irrigation test was first described by Robert Bárány and is done in clinical settings since the late 1800s [27, 28]. The caloric irrigation is clinically used to detect vestibular deficiencies like the acute peripheral vestibulopathy. After another five-point calibration, participants were placed on a chair in a supine position at 30 degrees upright from earth horizontal. Like this, the horizontal canal is perpendicular to earth horizontal and hence maximally stimulated in this position. Spontaneous eye movements were recorded with occluded vision due to the special darkened glasses used for this test that allowed eye-tracking with infrared lights. After this baseline, the thermal irrigation was performed. The procedure was done with 44°C and 30°C water at both sides successively (right warm, left warm, left cold, right cold). Water was rinsing into the outer ear canal for 30 seconds and eye-movements of the dominant eye were recorded for 100 seconds after stimulation. The output parameters were the slow-phase velocity (SPV) for each side and condition (in °/s). We calculated the absolute value out of the four thermal irrigation conditions plus the spontaneous SPV without water irrigation for each participant.

### *2.3. Procedure Day 2*

On the second day, participants performed two MRI sessions: in the first session, we positioned the participants heads with a maximal chin-upwards tilt (see figure 1), to maximize the likelihood of MVS-based nystagmus in all participants, with a rightward SPV direction. Galvanic vestibular stimulation was performed after topical anesthetic (Emla <sup>®</sup> creme, AstraZeneca, Wedel, Germany; 5 g for each side, active substances: 25 mg Lidocain and 25 mg Prilocain) was applied

to the skin of the mastoid bone and surrounding areas and left to soak for at least 45 minutes. During this time, the first MRI session was performed (for exact sequences see chapter 2.3.1 MRI data acquisition). Participants then left the MRI room, the anesthetic crème was removed and the galvanic electrodes were placed behind the ears with electrode gel (see chapter 2.3.2 Galvanic vestibular stimulation for details). We placed the participants back into the MRI machine for the second session with the head in a neutral tilt position for the remaining structural MRI as well as the GVS fMRI scans.

### 2.3.1. MRI data acquisition

We performed imaging on a 3 Tesla MRI scanner (SKYRA Siemens, Erlangen, Germany), with a compatible 64-channel head and neck coil. During all scans participants wore the Pearltec Crania Pad to minimize head motion artifacts (MRI / CT Pearltec Crania Pad). There were three functional sessions: rsfMRI in darkness (rsDark), rsfMRI with visual fixation (rsFix) and fMRI with galvanic vestibular stimulation (GVS) in complete darkness. Each of the whole brain EPI sequences contain 460 volumes and were acquired in an interleaved order and a multiband acceleration factor of 8 (TR = 828 ms, TE = 38 ms, flip angle = 45 deg., FoV = 212 mm, matrix size = 106, phase sampling = 100%, 2 mm isotropic voxel size, anterior-posterior phase encoding direction). The order of the resting state sessions was randomized. fMRI with GVS always took place after the resting state sessions as an anesthetic crème (necessary for performing painless GVS) was soaking in during the first scans. Both resting state runs, rsDark and rsFix, were performed with the subjects' head tilted backwards to increase the likelihood for MVS stimulation and nystagmus (in rsDark). During GVS-fMRI subjects were lying in a comfortable supine position with a neutral tilt position. During all fMRI sessions we recorded heart rate at 400Hz sampling rate via four EKG electrodes. In addition to the functional images, a high-resolution T1 weighted MPrage sequence was collected with GRAPPA, interleaved mode and an acceleration factor of 2 (TR = 2400 ms, TE = 2.17 ms, flip angle = 12 deg., FoV = 240 mm, slice thickness = 0.75

mm, A-P phase encoding). A T2-SPACE sequence with varying flip angles (TR = 3200 ms, TE = 560 ms, FoV = 240 mm, slice thickness = 0.75 mm, A-P phase encoding direction, GRAPPA acceleration factor PE = 2) was collected to exclude neurological pathologies in the brain. Finally, we performed a constructive interference in steady state (CISS; TR = 8.56 ms, TE = 3.91 ms, flip angle = 50 deg., FoV = 150 mm, slice thickness = 0.50 mm, right-left phase encoding direction, sequential multi-slice mode) in order to determine the exact orientation of the horizontal semicircular canal with respect to Reid's plane and B0.

### *2.3.2. Galvanic vestibular stimulation*

For descriptive reasons and for further analyses not reported within this work, bimastoidal GVS [29] was performed using rubber electrodes (surface of 24 X 16 mm) with conductive gel and handmade cables. Synchronized timing of fMRI data acquisition and GVS was coordinated from the control room via optical cables. Controlled by own programs written in Matlab a 2.5mA sinusoidal stimulus with a frequency of 0.9Hz and duration of 9 seconds elicited naturalistic vestibular sensations. After each stimulation a varying pause of 22-26 scans followed and the cycle of stimulation was repeated 15 times. During the GVS conditions, participants had their eyes open in complete darkness.

### *2.3.3. Orientation of the horizontal semicircular canal*

Instead of relying on Reid's base line or Reid's plane, an external landmark-based reference frame for defining the orientation of the human head in space, we chose to directly measure the orientation of the inner ear with respect to B0. The horizontal semicircular canal (hSCC) lies approximately parallel to Reid's plane with a degree of individual variability [30]. A direct measure of the hSCC orientation based on high-resolution MRI images, is important for understanding the variability in the MVS effect [15]. To this end, we collected T1 and T2 images, as well as a CISS sequence, with 0.5 mm resolution, specifically located over both inner ears.

We were interested in the orientation of the hSCC during resting state imaging. During this imaging session, with a neck extension to maximize the MVS effect, the T1 image was also acquired. The CISS sequence was coregistered rigidly to the T2 and T1 images. The T1 DICOM images were converted to Nifti format using 3D Slicer (Version 4.10.1 r27931 [31]). After conversion, the world coordinate system in 3D slicer represented the scanner coordinates, with the z-axis in alignment with the B0 field. The T1 and T2 images were brain extracted using FSL bet [32]. The T1 image was then rigidly co-registered to the T2 image with a normalized mutual information loss function using SPM12 (Version v7487) in Matlab (R2018b Version 9.5.0.944444). To robustly account for the high differences in neck extension between the T1 and T2 scans, the magnitude of separation and the number of iterations were increased to [30 20 10 4 2 1] (values in mm). All other parameters were left as default.

We only analyzed the orientation of the hSCC (not the vertical SCC). First, the hSCC was localized using our custom whole-head and inner ear templates within IE-Map [33], which was registered to subject data using the Advanced Normalization Toolkit (ANTs) [34]. Part of IE-Map are 21 landmarks which indicate anatomical keypoints of the hSCC (e.g. the mid- and endpoints, inner and outer width and height etc.). We extracted the orientation of the hSCC plane by performing a least-squares fit to these landmarks, i.e. we computed a PCA to generate the three components that explain the variance of the given landmarks' spatial distribution. The smallest of these three eigenvectors indicates the normal vector to the hSCC plane. The center of the hSCC was defined as the average 3D location of all hSCC landmarks from IE-Map. Similar to the hSCC, we calculated the Reid's plane orientation of each subject. Using the whole-head template in IE-Map and ANTs deformable image registration, we located the left and right infraorbital and external auditory meatus points [35], followed by a least-squares identification of the plane normal, analogous to the hSCC plane. The resulting plane orientations are illustrated in Figure 1.

For head tilt in roll direction, we added the two values for the left and the right hSCC. We assume a symmetric orientation for this step. A perfectly

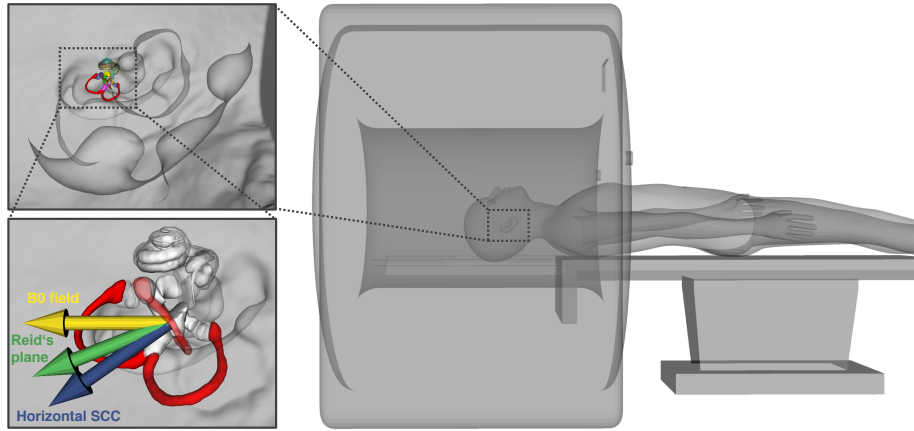


Figure 1: Overview of angles considered in our study. Right panel: During rsfMRI acquisition, subjects were lying with a neck extension, to maximize the MVS effect. For simplification reasons, the head coil as well as the mounted goggles for eye-tracking and visual stimulation are not visualized. Left top panel: Using IE-Map, we were able to localize the inner ear and accurately segment the fine-grained structures, including the hSCC. Left bottom panel: Detailed zoom on the normals of the hSCC (red) and Reid’s plane (blue), compared to the B0 field (yellow), and angle differences between them. In the left two panels, the surface rendering of the head and inner ear structures, as well as the inner ear orientations and plane normal directions are illustrated physically accurately, computed for one subject in our study (P19). There is a notable difference between the normals of Reid’s plane and the hSCC.

straight aligned head in y-axis would result in a zero misalignment. Head roll tilt to the right results in positive and head roll tilt to the left in negative values. Values for head tilt in yaw plane can not be extracted from the analyses performed.

#### 2.3.4. VOG during MRI

During functional MRI, we recorded the participants’ eye movements with the MRC camera built into MRI compatible binocular goggles (NordicNeuroLab (NNL), Bergen, Norway). Two infrared lights installed in the device guaranteed good sight of the participants’ dominant eye (the right eye in 25 out of 33 participants). We monitored the participant’s dominant eye at a sample rate of 60Hz (RGB24 320x240) using the NNL EyeTracking camera and collected

the data with the ViewPoint EyeTracker software (Version 2.9.5.117) from Arrington Systems (Scottsdale, USA). Before the rsfMRI, a 5 point calibration (central point plus four additional points on the vertical and horizontal axes with  $8.5^\circ$  distance) was presented via the binocular goggles and the eye movements were recorded with ViewPoint. The calibration matrix was determined by the EyeSeeCam software [24].

Since the commercial algorithms for pupil detection failed to detect the pupil center in our VOG data in darkness, we created a custom deep learning network with a manually labelled training set for detecting the pupil center. The resulting network represents an intermediate step of the final DeepVOG framework that was published in [36]. The network returned x- and y-coordinates (in pixels) for the center of the pupil for each frame, along with a confidence value for the detection. After training, the network performed localizations on an independent test set with a high accuracy and precision (localization error:  $3.7 \pm 0.7$  pixels). Once the pupil center data were available, blinks were removed and the data were smoothed [37, 38]. An example frame with labeled pupil center can be seen in Figure 3.

VOG data in pixels were transformed into angular velocity (in  $^\circ/\text{s}$ ), based on the five point calibration. The resulting x and y positional information were then analysed for nystagmus in a three-step procedure in Matlab (R2018b Version 9.5.0.944444). In the first step, fast eye-movements were detected in an iterative way, according to [39]. Eye velocity was computed by upsampling, filtering and 2-point differentiation. This 2D eye velocity was then separated into fast and slow components via a three step iterative algorithm. Fast eye-movements were detected if the velocity exceeded a threshold that decreased with each iteration. The threshold was set to 1.5 times the standard deviation (SD) of the eye-velocity for each participant separately, half the SD and  $2^\circ/\text{s}$ . The beginning and end of each fast phase were defined as the time points before and after peak velocity when the velocity vector either became zero or deviated by more than  $90^\circ$  from its direction at peak velocity. The slow phase velocity was then estimated by linearly interpolating over the fast phases, and then low

pass filtering (2, 5, and 8 Hz were used in the three iterative steps). At the end of this step, the eye trace was separated into fast and slow phases.

In the second step, the quick-phase direction was manually determined by selecting well-defined individual nystagmus events with the characteristic alternating slow drift (slow phase) and fast resetting movement (quick phase) in the videos of the eyes and in an interactive graph of the x and y eye position. All quick eye movements that were within 30 degrees of this direction were considered potential nystagmus quick-phases. If the slow phase preceding these quick phases were approximately opposite in direction ( $\pm 15$  degrees) then the event was considered a nystagmus. Finally, eye-movement traces from each participant were visually inspected, with fast eye-movements and nystagmus events labeled differently, and could be interactively corrected if a nystagmus was falsely labeled or vice versa.

The following values were then calculated for each participant from the labeled nystagmus events in complete darkness. The peak slow-phase velocity (peakSPV) was the magnitude of the vector describing the average slow phase eye velocity in 2D. This was additionally decomposed into the horizontal and vertical components (horSPV and verSPV respectively). The average 2D direction of quick phases in degrees was also extracted for each participant (QPdir). These values were used for between-subject comparisons. In addition, we created five regressors for the fMRI analysis based on the time course of the VOG data. The x- and y- eye position and eye-velocity over time, the slow-phase velocity (SPV) over time, and the confidence of the pupil-tracking were used. All time courses except the confidence values were convolved with the hemodynamic response function (HRF) from SPM [40], with the `spm_get_bf` and `conv` functions and all of the regressors were linearly down-sampled to the first slice acquisition timepoint (`inperp1`).

Four participants were removed from the time course related VOG analyses as they did not show a nystagmus at all.

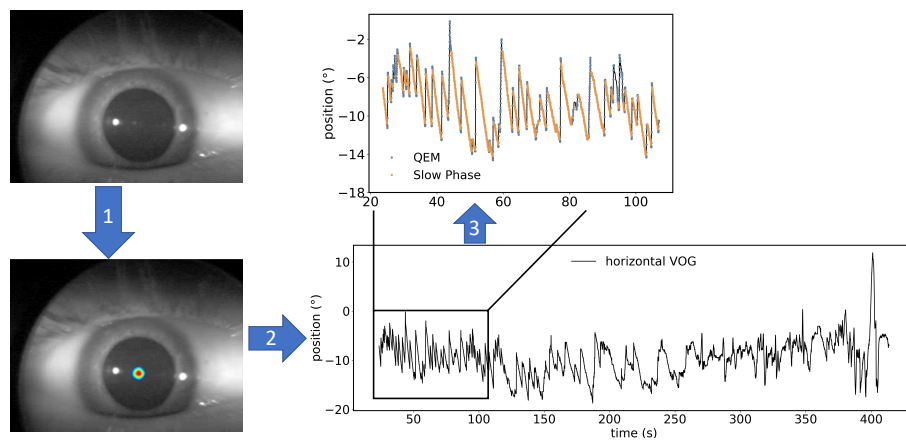


Figure 2: The VOG analysis. This graphic illustrates the steps of the analysis (blue arrows). Step 1: the DeepVOG algorithm detected the pupil in each video frame, creating a heatmap (lower eye picture) for the most likely location of the pupil center (in red). Step 2: using a 5-point calibration, the pupil center in image pixels per frame was converted into x and y positional information in degrees visual angle. Plotted here is the horizontal eye-position for the participant shown on the left during resting-state dark. Step 3: Nystagmus detection. In the final step, the nystagmus events were detected via detecting quick eye-movements (blue) and then in a semi-automated manner detecting the nystagmus-related eye movements, and then using the slow-phase (orange) to calculate the slow-phase velocity (SPV).

## 2.4. MRI analyses

### 2.4.1. Quality control and preprocessing

Prior to data analysis, we ran the MRI Quality Control tool (MRIQC, Version 0.9.6) [41] to exclude any data sets with low quality data. Due to excessive motion any participant with a grey matter SNRd value [42] lower than 1.5 times the 25th percentile was excluded from further analyses. Two participants were excluded at this step (see supplementary figure S1).

Analyses were performed in Matlab (version R2018a). To improve the starting point for the preprocessing algorithms, we ensured the origin was set to the anterior commissure in all data. The origin of the T1 weighted images was set using the predefined script, `nii_setOrigin12x.m`, and manually for the functional images. Preprocessing was done using SPM 12 (version v7219, Statistical Parametric Mapping Software, Wellcome Department of Imaging Neuroscience, London, UK, <http://www.fil.ion.ucl.ac.uk/spm>). If not indicated at each preprocessing step parameters were kept default. Voxel displacement maps (vdm) were calculated using the phase and magnitude images of the gradient field map (short TE 4.92, long TE 7.38, with a mask brain, blip direction = -1, total EPI read out time 66.78, non-EPI based field map, unwarping method: Mark3D, field map was coregistered to the EPI, the T1 was chosen for anatomical comparison and was matched to the distortion corrected EPIs). By using the generated vdm-file, images were realigned and unwarped, and coregistered to the anatomical T1 scan. After segmentation of the anatomical scan (saving bias corrected images and forwarding the deformation), both the coregistered functional and the bias-corrected T1 weighted data have been normalized to MNI space (functional: 2mm isotropic, anatomical: 1mm isotropic). The smoothing kernel was set to 6mm isotropic for the functional images. Denoising of the functional data was performed with the CONN Toolbox (version18a [www.conn-toolbox.org](http://www.conn-toolbox.org)) for Matlab (version 2018a). We used the following nuisance regressors' time series to prevent their impact: white matter (WM) and cerebrospinal fluid (CSF) confounds were taken into account with their first 10 principal components each.

Further, 6 physiological noise confounds consisting of heart beat PCA temporal components (generated by PhysIO toolbox), and the 6 PCA temporal components of the movement parameters (3 translation and 3 rotation parameters) as well as their 6 derivatives were considered. Images were denoised with a band-pass temporal filter (0.008-0.09 Hz).

To generate the regressors of EKG we used the PhysIO Toolbox [43] for Matlab (Mathworks, version 2018a). Breathing curves were not integrated as clipping effects occurred in approximately 50 % of all cases. In one participant and one condition the physiological data could not be collected for technical reasons and was therefore replaced by a matrix of zeros.

#### *2.4.2. Analyses of rsfMRI and GVS in complete darkness*

The preprocessed and denoised data of the rsDark and GVS session were fed into SPM12. Cardiac and movement parameters were added to the first level analysis. VOG regressors were added in the rsDARK condition as well. High pass filter was set to 512 and the masking threshold to minus infinity. For rsDark we defined contrasts on the first level for the slow phase velocity (SPV) over time of the nystagmus. For the second level we investigated positive and negative contrasts for the second level covariate horizontal SPV (horSPV). In the model we additionally added peak SPV, vertical SPV (vertSPV), the quick phase direction (QPdir) and the head tilt in roll plane as nuisance regressors. For the GVS session, we only investigated the positive contrast for the stimuli. We report brain regions with an uncorrected peak level of  $p < 0.001$  and a cluster size  $> 28$  voxels ( $> 43$  voxels for GVS). We chose this threshold due to the cluster significance of  $p < 0.05$  without correcting for clusters in our analyses.

#### *2.4.3. Connectivity analyses*

We further performed a group independent component analysis (Group-ICA) with the CONN Toolbox (version18a [www.conn-toolbox.org](http://www.conn-toolbox.org)) for Matlab (version 2018a). First, we compared the rsDark session to the rsFix session in all 33 participants. Second, we analyzed the relation of rsDark connectivity with the

VOG regressors (see section 2.3.4). Only 29 participants could be analyzed at this step (see section 2.3.4). At the group level, we added MSSQ score, GPAQ score (without rest), caloric absolute values, peak slow phase velocity (peak-SPV), horizontal and vertical component of the SPV (horSPV and vertSPV), quick phase direction (QPdir), and the tilt of the hSCC in roll and pitch plane as covariates of interest.

The following steps were performed for both analyses. EKG and movement parameters were fed into the CONN Toolbox as covariates. Age, gender, MSSQ score, GPAQ score without resting period, caloric irrigation results were added as covariates. For the second analysis (with only rsfMRI in complete darkness) the VOG regressors (see section 2.3.4) and hSCC tilt (see section 2.3.3) were additionally added as covariates for the between-subject effects. Voxel to voxel analysis was performed with a group-ICA consisting of 20 components and a default dimensionality reduction of 64. Two noise components identified via visual inspection have been excluded from further analyses. The following most common ICA spatial components were identified via spatial correlation between the components and CONN's default networks files, as well as visual inspection of the group-level maps: default mode network, salience, sensorimotor, visual networks, and cerebellar network.

### 3. Results

Seventy-five percent of our right handed participants were right-eye-dominant. The demographics of the participants as well as the results of the questionnaires are listed in table S1. None of the participants showed neurological pathology in their brain verified by visual inspection of the T2-SPACE images. The VOG data were collected in such a way that an online eye-video was visible to the experimenters, we had a reliable measurement of participants' wakefulness during all functional MRI runs. Previous research suggests that approximately 30 percent of participants fall asleep during rsfMRI within 4 minutes and participants are more likely to stay awake during fixation than with eyes-closed or without

fixation [44]. In our experiment, less than 1% of participants fell asleep after three minutes, and less than 20% were asleep after five minutes in the rsDark condition with eyes open, as measured with the VOG video data. In the rsFix and GVS conditions, none of our participants fell asleep in the seven minutes of data collection.

### 3.1. Does MVS occur during functional MRI imaging?

Although human subjects show MVS effect in a strong static magnetic field in complete darkness, it was possible that the additional magnetic and electrical activity that occur when the MRI machine is in use, cancel out the MVS effect in humans. We found consistent MVS activity, as measured by spontaneous nystagmus, while the MRI machine was collecting functional MRI data. Out of the 33 participants analysed, only four of these participants did not show any measurable MVS-induced nystagmus (Figure 3).

### 3.2. Intersubject variability in MVS effects

The magnitude of the MVS effect is thought to be measured by the amplitude of the horSPV. If the proposed mechanism is correct, the strength of the SPV will increase with an increasing tilt of the head in pitch because the plane of the hSCC more perpendicular to the magnetic field, thereby increasing the Lorentz force within the canal. This has been shown within individuals at different head pitch orientations, but the variability between participants in the null-point, the head angle at which the SPV is zero, has been too high to see an effect [15]. Here we could for the first time measure the tilt of the hSCC directly via MRI, in each of our participants. We additionally measured vestibular sensitivity through diagnostic testing and behavioral questionnaire, summarized in table S2. The hSCC orientation with respect to B0 was strongly correlated with the orientation of Reid's plane with respect to B0, but there was quite some variability across our sample (Figure 3). Angles between the two planes ranged from -22.6 to 7.5 degrees (mean angle:  $-8.4 \pm 6.1$  deg.). A multiple linear regression ( $F[2,28] = 60.55$ ,  $p = 6.78 \times 10^{-11}$ ) revealed that larger MVS effects (measured by horSPV)

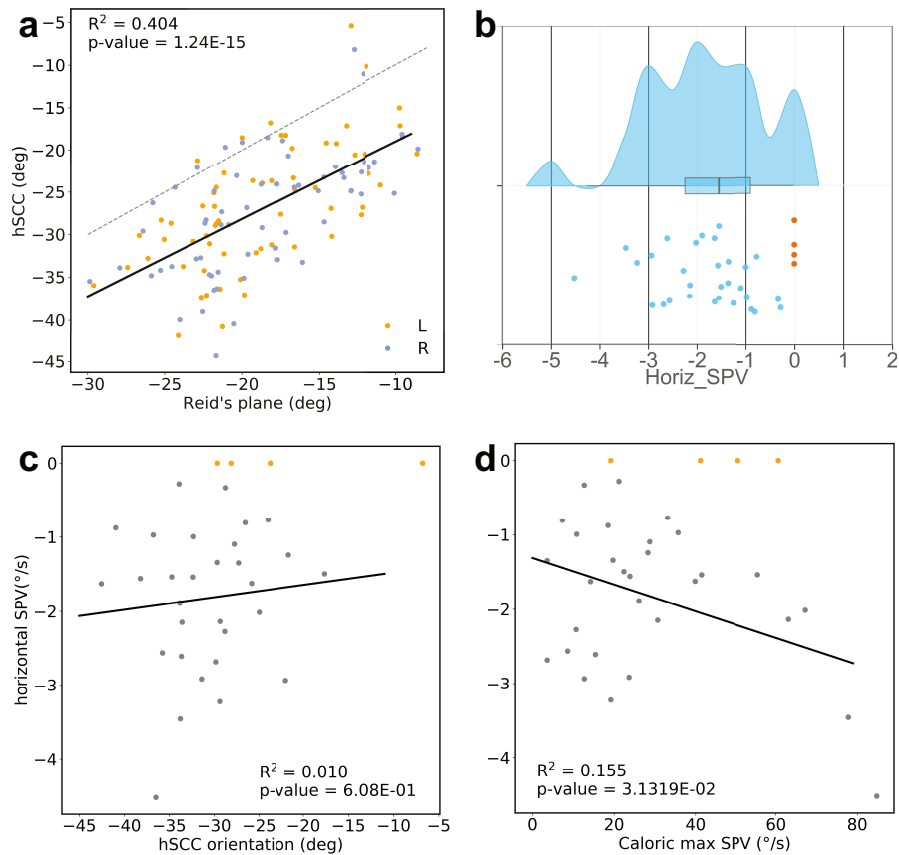


Figure 3: Physiological effects on SPV during MVS. a) The relationship between Reid's plane and the hSCC as seen by the tilt with respect to B0. There is a strong relationship between the orientation of the hSCC and Reid's plane, however there is a stronger variability in the orientation of the hSCC. No systematic differences were seen between the left and the right ear. The equality line is the dashed gray line. A few hSCC lie above this line. b) the distribution of SPV across the participants measured. The four orange data points show the 4 participants that did not have a measurable SPV. These participants are also represented in orange in c) and d). c) The orientation of the hSCC has a weak effect on the SPV. d) The vestibular sensitivity as measured by caloric irrigation also affects the strength of the MVS effect, measured with the SPV during MVS.

was related to larger head extension (larger deviations between hSCC and B0,  $t = 4.521$   $p = 0.000$ ) and the magnitude of the caloric response ( $t = -2.388$ ,  $p = 0.024$ ) (Figure 3). No other factors measured contributed to the variability in horSPV.

### 3.3. SPM analyses of GVS and rsDark

To prob the vestibular system and look at the brain regions recruited for vestibular processing, we measured brain activity during GVS stimulation. We observed an activation pattern, visualized in Figure 4, similar to the one that has been found in a meta-analysis of the vestibular system [45]. Activation was found bilaterally in the insular and opercular cortex (OP), middle superior temporal area (MST), inferior frontal gyri (IFG), superior parietal lobules (SPL), cerebellar regions VIIb, the left cingulate sulcus visual (CSv), and the right frontal pole (FP).

We then tested whether SPV correlated with brain activity during rsDark. We found no voxels with a significant average correlation between SPV and brain activity over the resting-state interval across participants. However, the subjects differed in the strength of the MVS effect. So we investigated whether the horizontal component of the SPV correlates with the cortical activation between groups. Here we find distributed activity in the cortex and cerebellum (Figure 5) in the right premotor cortex, right frontal orbital cortex, bilateral lateral occipital cortex, superior frontal gyri, SPL, pars opercularis of the IFG (i.e. Broca 44), and the cerebellar vermis and left cerebellar region VIIb. Significant results are listed in table S3 of the supplement.

### 3.4. Contrasting connectivity: rsDark vs. rsFix

Although we found no main relationship between resting-state brain activity and the MVS effect, it is possible that a connectivity analysis revealed differences in activity. To this end we compared the network connectivity between the rsfMRI session in complete darkness to the one with fixation, calculated with an ICA analysis. We found significant connectivity differences between rsDark



Figure 4: Activation pattern for the sinusoidal GVS stimulus with eyes open in complete darkness. Operculum (OP), middle superior temporal area (MST), inferior frontal gyri (IFG), superior parietal lobules (SPL), cerebellar regions VIIb (VIIb), cingulate sulcus visual (CSv), frontal pole (FP). Images were generated with FSLeyes with the provided MNI template with a resolution of 0.5mm in neurological view.

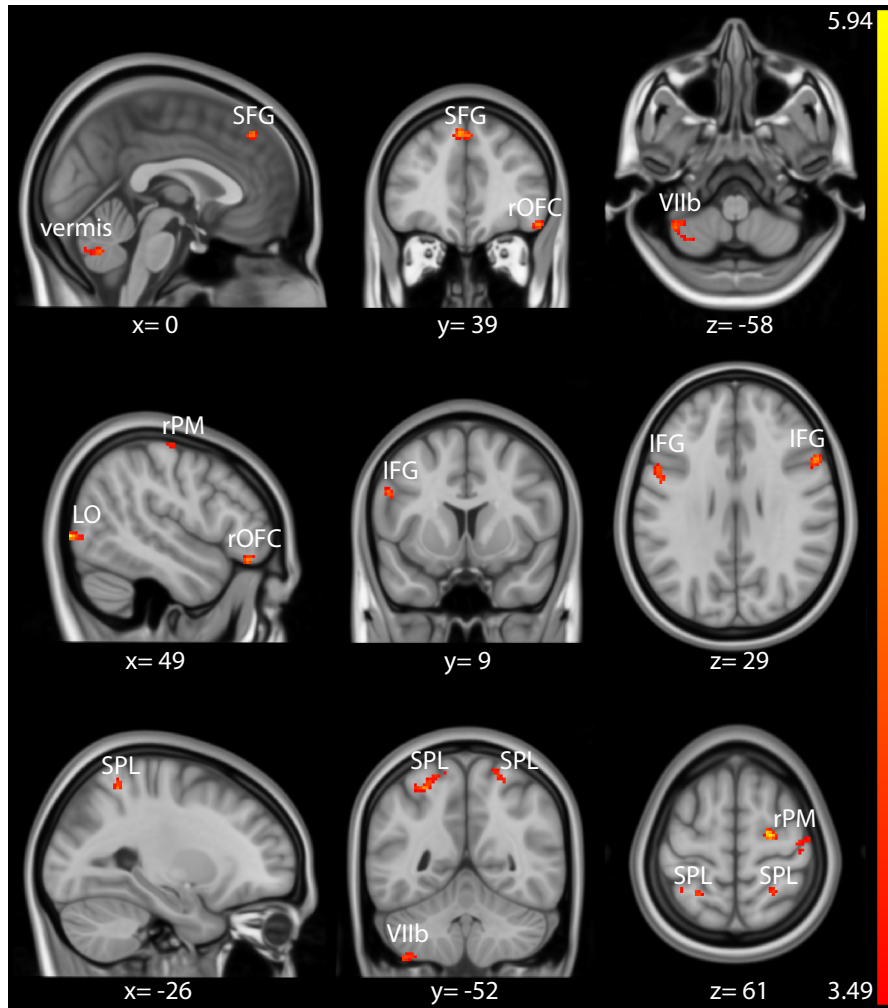


Figure 5: Correlation between rsfMRI activity in complete darkness and horizontal SPV (with contrasting SPV over time on the first level). Right premotor cortex (rPM), right frontal orbital cortex (rOFC), bilateral lateral occipital cortex (LO), superior frontal gyri (SFG), superior parietal lobules (SPL), pars opercularis of the inferior frontal gyrus (IFG; i.e. Broca 44), and the cerebellar vermis and left cerebellar region VIIb. Images were generated with FSLEyes with the provided MNI template with a resolution of 0.5mm in neurological view.

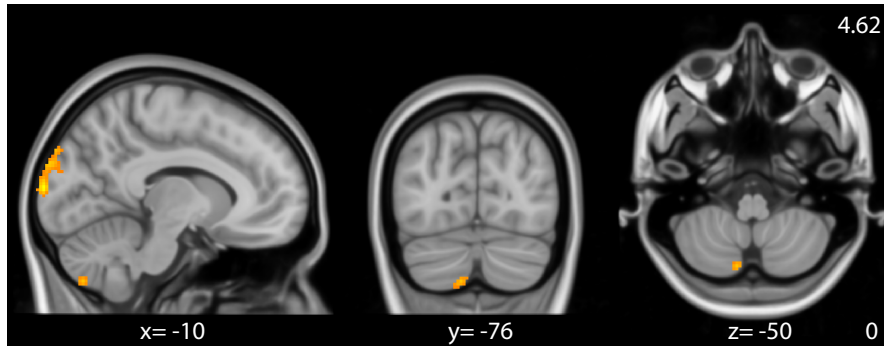


Figure 6: Contrasting the connectivity of rs dark >rs fix; F contrasts; Images were generated with FSLeyes with the provided MNI template with a resolution of 0.5mm in neurological view.

and rsFix ( $F(18,576)=2.4$ ; two-sided) in the visual cortices, namely bilateral occipital pole and bilateral lateral occipital cortex, and in the left cerebellar VIIb region (see figure 6 and table 1 for details).

The specific effects were then tested for five resting-state networks (RSN), separately: the default mode network (DMN), the salience network, the visual network, the sensorimotor network and the cerebellar network. These are reported at a significance level of  $t(32)= 3.37$ , in table 2. The DMN showed significantly larger connectivity in bilateral precentral gyrus and smaller left precentral and postcentral gyrus left connectivity in rsDark compared to rs-Fix. The main effect of the salience network revealed higher left occipital pole (positive, dark>fix) connectivity. Main effect of the visual network showed higher connectivity in right lateral occipital cortex (inferior division) and bilateral cuneal cortex. There was no main effect in the sensorimotor network nor the cerebellum.

### 3.5. Connectivity of rsDark

Finally, we correlated the connectivity measures of the resting state session in complete darkness (rsDark) between subjects with the MVS and vestibular parameters measured, to see to what degree the resting-state networks are

Table 1: F-contrast across all ICA components contrasting the rsfMRI session in complete darkness to the one with fixation; two-sided;  $F(18,576)=2.4$ ; L = left, R = right, Coordinates are reported in MNI space (x,y,z)

brain region	coordinate (in mm)	size (voxel)	p-FDR
occipital pole L	-10,-102,12	334	<0.001
occipital pole R	18,-94,20	66	<0.005
lateral occipital cortex L	-26,-64,54	40	<0.05
lateral occipital cortex R	46,-66,0	63	<0.05
cerebellum L	-10,-76,-50	29	<0.05

Table 2: Main effects of resting state networks (RSN) of interest comparing both rsfMRI conditions: darkness (rsDark) and fixation (rsFix), one-sided,  $t(32)= 3.37$ ,  $t(32)= 3.37$ . R = right, L = left, comp. = component, DMN = Default Mode Network. Coordinates are reported in MNI space (x,y,z).

brain region	coordinate (in mm)	size (voxel)	p-FDR	positive in condition	comp. RSN
precentral gyrus L	-60,-4,26	57	<0.05	rsDark	DMN
precentral gyrus R	62,8,14	108	<0.005	rsDark	DMN
pre- and postcentral gyrus L	-46,-14,52	97	<0.005	rsFix	DMN
occipital pole L	-8,-104,14	77	<0.05	rsDark	salience
lateral occipital cortex R	38,-72,6	118	<0.001	rsDark	visual
precuneal cortex	16,-76,32	156	<0.001	rsDark	visual

Table 3: Main effect of the GPAQ score onto the connectivity of the rsDark condition

brain region	coordinate (MNI space)	size (voxel)	p-FDR
inferior temporal gyrus L	-48,-66,-22	63	<0.05
inferior temporal gyrus R	42,-46,-30	62	<0.05
precentral gyrus L	-44,4,30	60	<0.05
precuneus	4,-66,40	51	<0.05

related to vestibular sensitivity, activity levels and the strength of the MVS effect. The global physical activity questionnaire was the only covariate that showed a significant effect on the connectivity in rsDark ( $t(27)=3.42$ ; see table 3). With greater GPAQ scores, less connectivity was revealed in the inferior temporal gyri, the precuneus and the left precentral gyrus. We did not find significant main effects on connectivity of the remaining covariates of the second level analyses (these being MSSQ score, caloric absolute values, peakSPV, horSPV, vertSPV, QPdir, and the head tilt in roll or pitch plane). Specifically, the measures of the MVS effect did not correlate with brain connectivity.

Investigating horSPV influence on the five RSN of interest, we only found significant changes in connectivity in the sensorimotor network: higher horSPV is associated with higher functional connectivity in the right inferior frontal gyrus ( $t(27)=3.42$ ,  $p<0.05$  FDR, 60 voxels, peak:  $x=50$ ,  $y=18$ ,  $z=38$ ).

#### 4. Discussion

The presented study investigated whether magnetic vestibular stimulation (MVS), which occurs within an MRI machine when it is not creating an image, is also present during MRI scanning and whether the MVS effect also effects brain activity or functional connectivity at rest. To test for overlap between cortical vestibular processing regions and brain activity that is related to the MVS effect, we also had subjects experience galvanic vestibular stimulation during fMRI. In 88% of participants we found a clear MVS effect shown via

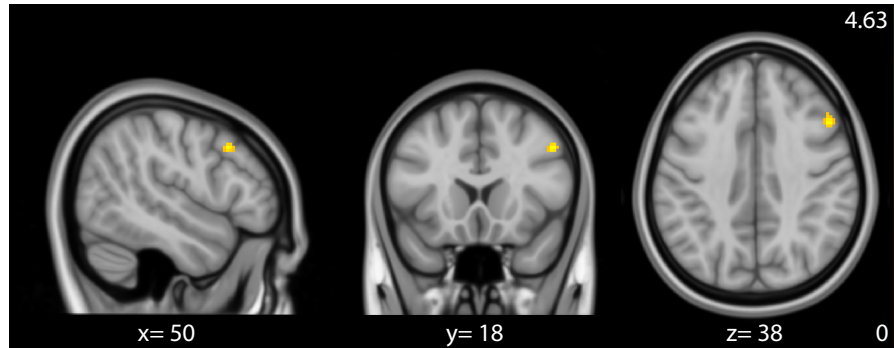


Figure 7: Main effect of the horizontal SPV onto the connectivity in the sensorimotor network of the rsfMRI session. Images were generated with FSLeyes with the provided MNI template with a resolution of 0.5mm in neurological view.

a horizontal nystagmus with a rightward slow phase velocity (SPV), measured with the head tilted back in a 3T MRI machine. Unlike previous studies [15, 16] we did not measure the resulting SPV at different head positions within participants. Therefore it is possible that the head position in the remaining 12% of participants was such that the MVS effect was small. Alternatively, individuals vary in the ability to see into the infrared spectrum. The infrared illumination for the VOG camera may have been visible to these participants, providing them with visual information to fixate with thereby suppressing the MVS effect.

One average, across the participants we measured, the MVS effect influences neither cortical network activity nor connectivity. Our data confirms previous reports that the MVS effect has a high degree of between-subject variability [15]. We show that this variability is due to the variability in the orientation of the hSCC with respect to Reid’s plane, which was measured in the previous studies ([46, 15]), as well as the variation in vestibular sensitivity between individuals. We used the peak SPV during caloric irrigation as a measure of vestibular sensitivity. Previous results show that the time constants for nystagmus obtained via caloric irrigation match those calculated with MVS ([47], providing additional support for the hypothesis that MVS is due to a Lorentz

force. Caloric irrigation has limited explanatory power, since the results are dependent on multiple factors and when the same participants are measured a second time, the results can vary greatly ([28]).

#### *4.1. Do individual differences explain the variation in SPV across participants?*

We did find the MVS effect measured via VOG during rsDark. However, in contrast to Roberts et al. [15] in our study not all participants' VOG data showed a nystagmus during the rsfMRI session in complete darkness even though we tried to maximize its likelihood through the head tilt. In contrast to previous studies [16], we did not use Reid's plane as a regressor for the rsfMRI analyses but the actual orientation of the horizontal semicircular canal (hSCC). Even though there is a strong correlation between hSCC orientation and Reid's plane in our data set (see figure 3), there is to be a bigger variability in hSCC orientation (with respect to Reid's plane) across participants than previously reported [30]. Della Santina and colleagues [30] investigated anatomical differences of the hSCC orientation in relation to Reid's plane: 22 participants were examined with computer tomography and the (left) hSCC was found out to be located  $19.9 \pm 7.0^\circ$  with respect to the x-y Reid's plane, generated by accessible skull landmarks. Therefore, in our view, it is worth while to measure the orientation of hSCC with respect to B0; the additional information makes a large difference when studying the MVS effect.

Despite removing the additional anatomical variance, the variation in SPV across participants could not solely be explained by the physical orientation of the hSCC with respect to B0. Adding the individual sensitivity for vestibular stimuli (with caloric irrigation) improved our model and explained further variance in our data. During caloric irrigation the density of the endolymph is thought to change with the change in temperature ([28]), suggesting that additional physical or physiological parameters of the semicircular canals may influence the MVS effect. Possible parameters include the diameter of the hSCC duct, the orientation of the cupula inside the ampulla, or the concentration of potassium/ ionic currents in the endolymphatic fluid. The vestibule, especially

the utricle and its dimensions should be examined in the future as animal data suggests that the structure of the utricle affects MVS [48].

#### *4.2. Can we detect the SPV fluctuations in the BOLD activity?*

The primary goal of this study was test whether the MVS induced nystagmus [15] has a similar time course as the BOLD rsfMRI fluctuations in healthy participants and whether functional connectivity is changing depending on the strength of the effect. On average across the participants we measured, the SPV over time did not correlate with brain activity. This suggests that MVS has no clear influence on brain activity inside a 3T MRI. However, the high variability in the amount of MVS effect in our participants could also lead to this effect. More studies that select participants with a high vestibular sensitivity would help to elucidate this result.

This is supported by the between-subject findings. The horizontal SPV (hor-SPV) was found to be correlated with cortical and cerebellar brain regions. Very interesting are the patterns in the cerebellum: an activation in the vermis as well as in the left lobe of the cerebellum. Cerebellar vermis activation could be a direct influence of primary vestibular input from the vestibular afferents sending information from the hSCC [49, 50]. Cortically, we could detect coactivation of regions involved in vestibular processing, executive control and attention. Hence, participants that were more sensitive to the MVS effect might show a higher BOLD response in these regions. Previous studies using PET and caloric irrigation show primarily visual and parietal vestibular activity [51], which we could not confirm with this study, but which could still be due to the different stimulation paradigms.

#### *4.3. Differences in connectivity between MVS effect (rsDark) and nystagmus suppression (rsFix)*

Contrasting the functional connectivity of the rsfMRI session in complete darkness to the one with a fixation cross, the only significant difference has been observed in the occipital cortex and the left cerebellum. Our data did

not show a change in any of the cortical resting state networks apart from the visual. The latter was expected due to the visual stimulus (i.e. complete darkness vs. fixation cross), although the connectivity was higher in rsDark than in rsFix. Areas of the visual cortex in non-human primates increase their activity in response to saccades ([52]. A similar mechanism could cause increased visual cortex connectivity here. The left cerebellar (VIIb) functional connectivity is significantly different between the two sessions. There is not only higher activation associated with horSPV (see section 4.2), but also significantly different connectivity in the left cerebellar region VIIb. The same holds true for the right inferior frontal gyrus in the rsDark condition. It would be very interesting to see, whether our results can be replicated in a mirrored fashion with MRI systems that have opposite polarity (e.g. a Philips MRI).

#### 4.4. Methodological considerations

Although we instructed participants to tilt their head back and supported their neck with a triangular cushion we observe a large variation of head position across participants which might be due to the head coil itself. The 64-channel head coil is rather narrow and depending on the head size some participants can tilt their head further back than others. In some cases, we had to compromise to still be able to track the participants' eye movements with the coil mounted goggles.

Unfortunately, we only measured the MVS effect in each participant with one head orientation. The previously reported individual range of SPV due to different orientations, could therefore not be investigated.

Considering the connectivity in our work, increasing the number of ICA components for a higher model order decomposition might resolve in more stable components and better results. Future studies might take this into account.

## 5. Future Directions and Conclusion

The MVS effect occurred during scanning in 88% of our participants. We can not explain the variability of the MVS effect (measured by SPV of the

nystagmus) by the canal orientation with respect to the magnetic field alone. Other anatomical mechanisms might be responsible, such as the diameter of the hSCC duct or the exact orientation of the cupula inside the ampulla of the hSCC, the concentration of the ionic currents or utricle parameters. Further, intersubjective sensitivity to vestibular stimulation varies. Caloric irrigation as a measure of individual vestibular sensitivity additionally explained parts of the variance seen in MVS effect. Future studies investigating the MVS effect should consider these factors. Connectivity studies should further investigate the cerebellar and attentional networks in greater detail.

### **Author contributions**

VLF designed the study. TMR carried out the experiment (recruiting participants, vestibular sensitivity tests and fMRI and MRI data collection). SAA analyzed the horizontal and vertical components of the eye-tracking data through a deep learning algorithm. SAA provided the canal orientation within the magnetic B0 field. Data analyses were done by TMR and VLF. TR wrote the manuscript with input from all authors.

### **Acknowledgements**

We thank all participants for taking part in the experiment. Further, we wish to thank Mathias Hübner for his technical MRI facility assistance, Hans Hintermaier for sewing material for a completely darkened MRI room, Thomas Stephan for providing the GVS stimulus, Stanislavs Bardins and Thomas Eggert for useful advice concerning the eye-tracking data, and Peter zu Eulenburg for fruitful discussions about the project.

### **Funding**

The study was supported by the German Federal Ministry of Education and Research (BMBF) in connection with the foundation of the German Center for Vertigo and Balance Disorders (DSGZ) (grant number 01 EO 0901), and a stipend of the Graduate School of Systemic Neurosciences (DFG-GSC 82/3; TMR: Oct. 2015 - Jan. 2016; Mar. 2018 - Sept. 2018).

### **Conflict of Interest**

The authors declare no competing financial interests.

## References

- [1] D. Cordes, V. M. Haughton, K. Arfanakis, J. D. Carew, P. A. Turski, C. H. Moritz, M. A. Quigley, M. E. Meyerand, Frequencies contributing to functional connectivity in the cerebral cortex in “resting-state” data, *American Journal of Neuroradiology* 22 (7) (2001) 1326–1333.
- [2] J.-C. Kim, S. Kyeong, Reliable new measures capturing low-frequency fluctuations from resting-state functional mri, *NeuroReport* 29 (3) (2018) 197–202. [doi:10.1097/WNR.0000000000000951](https://doi.org/10.1097/WNR.0000000000000951).
- [3] J. S. Damoiseaux, S. Rombouts, F. Barkhof, P. Scheltens, C. J. Stam, S. M. Smith, C. F. Beckmann, Consistent resting-state networks across healthy subjects, *Proceedings of the national academy of sciences* 103 (37) (2006) 13848–13853.
- [4] R. M. Birn, J. B. Diamond, M. A. Smith, P. A. Bandettini, Separating respiratory-variation-related fluctuations from neuronal-activity-related fluctuations in fmri, *Neuroimage* 31 (4) (2006) 1536–1548. [doi:10.1016/j.neuroimage.2006.02.048](https://doi.org/10.1016/j.neuroimage.2006.02.048).
- [5] G. Krüger, G. H. Glover, Physiological noise in oxygenation-sensitive magnetic resonance imaging, *Magnetic Resonance in Medicine: An Official Journal of the International Society for Magnetic Resonance in Medicine* 46 (4) (2001) 631–637.
- [6] P. Fransson, P. Flodin, G. Ö. Seimyr, T. Pansell, Slow fluctuations in eye position and resting-state functional magnetic resonance imaging brain activity during visual fixation, *European Journal of Neuroscience* 40 (12) (2014) 3828–3835. [doi:10.1111/ejn.12745](https://doi.org/10.1111/ejn.12745).
- [7] D. Yellin, A. Berkovich-Ohana, R. Malach, Coupling between pupil fluctuations and resting-state fmri uncovers a slow build-up of antagonistic responses in the human cortex, *NeuroImage* 106 (2015) 414–427. [doi:10.1016/j.neuroimage.2014.11.034](https://doi.org/10.1016/j.neuroimage.2014.11.034).

- [8] M. Schneider, P. Hathway, L. Leuchs, P. G. Sämann, M. Czisch, V. I. Spoormaker, Spontaneous pupil dilations during the resting state are associated with activation of the salience network, *NeuroImage* 139 (2016) 189–201. doi:[10.1016/j.neuroimage.2016.06.011](https://doi.org/10.1016/j.neuroimage.2016.06.011).
- [9] M. Ramot, M. Wilf, H. Goldberg, T. Weiss, L. Y. Deouell, R. Malach, Coupling between spontaneous (resting state) fmri fluctuations and human oculo-motor activity, *Neuroimage* 58 (1) (2011) 213–225. doi:[10.1016/j.neuroimage.2011.06.015](https://doi.org/10.1016/j.neuroimage.2011.06.015).
- [10] F. Regen, H. Dorn, H. Danker-Hopfe, Association between pupillary unrest index and waking electroencephalogram activity in sleep-deprived healthy adults, *Sleep medicine* 14 (9) (2013) 902–912.
- [11] M. Fukunaga, S. G. Horovitz, P. van Gelderen, J. A. de Zwart, J. M. Jansma, V. N. Ikonomidou, R. Chu, R. H. Deckers, D. A. Leopold, J. H. Duyn, Large-amplitude, spatially correlated fluctuations in bold fmri signals during extended rest and early sleep stages, *Magnetic resonance imaging* 24 (8) (2006) 979–992. doi:[10.1016/j.mri.2006.04.018](https://doi.org/10.1016/j.mri.2006.04.018).
- [12] S. G. Horovitz, A. R. Braun, W. S. Carr, D. Picchioni, T. J. Balkin, M. Fukunaga, J. H. Duyn, Decoupling of the brain’s default mode network during deep sleep, *Proceedings of the National Academy of Sciences* 106 (27) (2009) 11376–11381. doi:[10.1073/pnas.0901435106](https://doi.org/10.1073/pnas.0901435106).
- [13] L. J. Larson-Prior, J. M. Zempel, T. S. Nolan, F. W. Prior, A. Z. Snyder, M. E. Raichle, Cortical network functional connectivity in the descent to sleep, *Proceedings of the National Academy of Sciences* 106 (11) (2009) 4489–4494.
- [14] M. Klimova, What is lost during dreamless sleep: the relationship between neural connectivity patterns and consciousness, *Journal of European Psychology Students* 5 (3).

- [15] D. C. Roberts, V. Marcelli, J. S. Gillen, J. P. Carey, C. C. Della Santina, D. S. Zee, Mri magnetic field stimulates rotational sensors of the brain, *Current Biology* 21 (19) (2011) 1635–1640. doi:10.1016/j.cub.2011.08.029.
- [16] R. Boegle, T. Stephan, M. Ertl, S. Glasauer, M. Dieterich, Magnetic vestibular stimulation modulates default mode network fluctuations, *Neuroimage* 127 (2016) 409–421. doi:10.1016/j.neuroimage.2015.11.065.
- [17] J. Otero-Millan, D. S. Zee, M. C. Schubert, D. C. Roberts, B. K. Ward, Three-dimensional eye movement recordings during magnetic vestibular stimulation, *Journal of neurology* 264 (1) (2017) 7–12. doi:10.1007/s00415-017-8420-4.
- [18] B. K. Ward, J. Otero-Millan, P. Jareonsettasin, M. C. Schubert, D. C. Roberts, D. S. Zee, Magnetic vestibular stimulation (mvs) as a technique for understanding the normal and diseased labyrinth, *Frontiers in neurology* 8 (2017) 122. doi:10.3389/fneur.2017.00122.
- [19] J. F. Golding, Motion sickness susceptibility questionnaire revised and its relationship to other forms of sickness, *Brain research bulletin* 47 (5) (1998) 507–516.
- [20] W. H. Organization, WHO STEPS Surveillance Manual: the WHO STEP-wise Approach to Chronic Disease Risk Factor Surveillance, 2005.
- [21] D. Salmaso, A. M. Longoni, Problems in the assessment of hand preference, *Cortex* 21 (4) (1985) 533–549.
- [22] R. C. Oldfield, The assessment and analysis of handedness: the edinburgh inventory, *Neuropsychologia* 9 (1) (1971) 97–113.
- [23] W. R. Miles, Ocular dominance in human adults, *The journal of general psychology* 3 (3) (1930) 412–430. doi:10.1080/00221309.1930.9918218.

- [24] E. Schneider, T. Villgrattner, J. Vockeroth, K. Bartl, S. Kohlbecher, S. Bardins, H. Ulbrich, T. Brandt, Eyesecam: an eye movement-driven head camera for the examination of natural visual exploration, *Annals of the New York Academy of Sciences* 1164 (1) (2009) 461–467. doi:[10.1111/j.1749-6632.2009.03858.x](https://doi.org/10.1111/j.1749-6632.2009.03858.x).
- [25] G. M. Halmagyi, I. S. Curthoys, A clinical sign of canal paresis, *Archives of neurology* 45 (7) (1988) 737–739.
- [26] H. MacDougall, K. Weber, L. McGarvie, G. Halmagyi, I. Curthoys, The video head impulse test: diagnostic accuracy in peripheral vestibulopathy, *Neurology* 73 (14) (2009) 1134–1141. doi:[10.1212/WNL.0b013e3181bacf85](https://doi.org/10.1212/WNL.0b013e3181bacf85).
- [27] R. Bárány, *Physiologie und Pathologie des Bogengangsapparates beim Menschen: klinische Studien*, Deuticke Wien, 1907.
- [28] N. Shepard, G. Jacobson, The caloric irrigation test, in: *Handbook of clinical neurology*, Vol. 137, Elsevier, 2016, pp. 119–131. doi:[10.1016/B978-0-444-63437-5.00009-1](https://doi.org/10.1016/B978-0-444-63437-5.00009-1).
- [29] C. A. M. Cyran, R. Boegle, T. Stephan, M. Dieterich, S. Glasauer, Age-related decline in functional connectivity of the vestibular cortical network, *Brain Structure and Function* 221 (3) (2016) 1443–1463. doi:[10.1007/s00429-014-0983-6](https://doi.org/10.1007/s00429-014-0983-6).
- [30] C. C. Della Santina, V. Potyagaylo, A. A. Migliaccio, L. B. Minor, J. P. Carey, Orientation of human semicircular canals measured by three-dimensional multiplanar ct reconstruction, *Journal of the Association for Research in Otolaryngology* 6 (3) (2005) 191–206.
- [31] A. Fedorov, R. Beichel, J. Kalpathy-Cramer, J. Finet, J. C. Fillion-Robin, S. Pujol, C. Bauer, D. Jennings, F. Fennessy, M. Sonka, J. Buatti, S. Aylward, J. V. Miller, S. Pieper, R. Kikinis, 3d Slicer as an image computing

- platform for the Quantitative Imaging Network, *Magnetic Resonance Imaging* 30 (9) (2012) 1323–1341. doi:10.1016/j.mri.2012.05.001.
- [32] S. M. Smith, Fast robust automated brain extraction, *Human Brain Mapping* 17 (3) (2002) 143–155. doi:10.1002/hbm.10062.
- [33] S.-A. Ahmadi, T. Raiser, R. M. Ruehl, V. Flanagin, P. z. Eulenburg, *Ie-map: A novel in-vivo atlas template of the human inner ear*, medRxivdoi: t.b.a.  
URL <https://www.medrxiv.org/2019/011908>
- [34] B. B. Avants, N. J. Tustison, M. Stauffer, G. Song, B. Wu, J. C. Gee, The Insight ToolKit image registration framework., *Frontiers in neuroinformatics* 8 (April) (2014) 44. doi:10.3389/fninf.2014.00044.
- [35] N. Finby, K.-Y. Chynn, Cranial computerized tomography: Technique and anatomy, in: *Manual of Cranial Computerized Tomography*, S. Karger {AG}, 1982, pp. 15–29. doi:10.1159/000406259.
- [36] Y.-H. Yiu, M. Aboulatta, T. Raiser, L. Ophey, V. L. Flanagin, P. zu Eulenburg, S.-A. Ahmadi, Deepvog: Open-source pupil segmentation and gaze estimation in neuroscience using deep learning, *Journal of neuroscience methods*.
- [37] D. Garcia, Robust smoothing of gridded data in one and higher dimensions with missing values, *Computational Statistics & Data Analysis* 54 (4) (2010) 1167–1178. doi:10.1016/j.csda.2009.09.020.
- [38] D. Garcia, A fast all-in-one method for automated post-processing of piv data, *Experiments in fluids* 50 (5) (2011) 1247–1259.
- [39] J. Ladda, T. Eggert, S. Glasauer, A. Straube, *Velocity scaling of cue-induced smooth pursuit acceleration obeys constraints of natural motion*, *Experimental Brain Research* 182 (3) (2007) 343–356. doi:10.1007/s00221-007-0988-y.  
URL <https://doi.org/10.1007/s00221-007-0988-y>

- [40] G. H. Glover, Deconvolution of impulse response in event-related bold fmri, *Neuroimage* 9 (4) (1999) 416–429.
- [41] O. Esteban, D. Birman, M. Schaer, O. O. Koyejo, R. A. Poldrack, K. J. Gorgolewski, Mriqc: Advancing the automatic prediction of image quality in mri from unseen sites, *PloS one* 12 (9) (2017) e0184661. doi:[10.1371/journal.pone.0184661](https://doi.org/10.1371/journal.pone.0184661).
- [42] O. Dietrich, J. G. Raya, S. B. Reeder, M. F. Reiser, S. O. Schoenberg, Measurement of signal-to-noise ratios in mr images: influence of multi-channel coils, parallel imaging, and reconstruction filters, *Journal of Magnetic Resonance Imaging: An Official Journal of the International Society for Magnetic Resonance in Medicine* 26 (2) (2007) 375–385. doi:[10.1002/jmri.20969](https://doi.org/10.1002/jmri.20969).
- [43] L. Kasper, S. Bollmann, A. O. Diaconescu, C. Hutton, J. Heinzle, S. Iglesias, T. U. Hauser, M. Sebold, Z.-M. Manjaly, K. P. Pruessmann, et al., The physio toolbox for modeling physiological noise in fmri data, *Journal of neuroscience methods* 276 (2017) 56–72. doi:[10.1016/j.jneumeth.2016.10.019](https://doi.org/10.1016/j.jneumeth.2016.10.019).
- [44] E. Tagliazucchi, H. Laufs, Decoding wakefulness levels from typical fmri resting-state data reveals reliable drifts between wakefulness and sleep, *Neuron* 82 (3) (2014) 695–708. doi:[10.1016/j.neuron.2014.03.020](https://doi.org/10.1016/j.neuron.2014.03.020).
- [45] P. zu Eulenburg, S. Caspers, C. Roski, S. Eickhoff, [Meta-analytical definition and functional connectivity of the human vestibular cortex](#), *NeuroImage* 60 (1) (2012) 162 – 169. doi:<https://doi.org/10.1016/j.neuroimage.2011.12.032>.  
URL <http://www.sciencedirect.com/science/article/pii/S1053811911014340>
- [46] B. K. Ward, D. C. Roberts, C. C. Della Santina, J. P. Carey, D. S. Zee, Magnetic vestibular stimulation in subjects with unilateral labyrinthine

- disorders, *Frontiers in neurology* 5 (2014) 28. doi:[10.3389/fneur.2014.00028](https://doi.org/10.3389/fneur.2014.00028).
- [47] P. M. Glover, Y. Li, A. Antunes, O. S. Mian, B. L. Day, A dynamic model of the eye nystagmus response to high magnetic fields, *Physics in Medicine and Biology* 59 (3) (2014) 631–645. doi:[10.1088/0031-9155/59/3/631](https://doi.org/10.1088/0031-9155/59/3/631).
- [48] B. K. Ward, Y. H. Lee, D. C. Roberts, E. Naylor, A. A. Migliaccio, C. C. Della Santina, Mouse magnetic-field nystagmus in strong static magnetic fields is dependent on the presence of nox3, *Otology & Neurotology* 39 (10) (2018) e1150–e1159. doi:[10.1097/MAO.0000000000002024](https://doi.org/10.1097/MAO.0000000000002024).
- [49] F. Ango, R. Dos Reis, Sensing how to balance, *eLife* 8.
- [50] T. Langer, A. Fuchs, C. Scudder, M. Chubb, Afferents to the flocculus of the cerebellum in the rhesus macaque as revealed by retrograde transport of horseradish peroxidase, *Journal of Comparative Neurology* 235 (1) (1985) 1–25.
- [51] A. Deutschländer, S. Bense, T. Stephan, M. Schwaiger, T. Brandt, M. Dieterich, [Sensory system interactions during simultaneous vestibular and visual stimulation in pet](#), *Human Brain Mapping* 16 (2) (2002) 92–103. arXiv:<https://onlinelibrary.wiley.com/doi/pdf/10.1002/hbm.10030>, doi:[10.1002/hbm.10030](https://doi.org/10.1002/hbm.10030).  
URL <https://onlinelibrary.wiley.com/doi/abs/10.1002/hbm.10030>
- [52] T. Moore, A. S. Tolia, P. H. Schiller, [Visual representations during saccadic eye movements](#), *Proceedings of the National Academy of Sciences* 95 (15) (1998) 8981–8984. arXiv:<https://www.pnas.org/content/95/15/8981.full.pdf>, doi:[10.1073/pnas.95.15.8981](https://doi.org/10.1073/pnas.95.15.8981).  
URL <https://www.pnas.org/content/95/15/8981>

## Supplementary Material

Table S1: Demographics of participants and questionnaires. LQ = laterality quotient for handedness, positive LQ (in %) is indicating right handedness. m = male, eye = dominant eye, r= right, GPAQ = Global Physical Activity Questionnaire Score (in minutes per week), GPAQ- = GPAQ score without rest, GPAQ+ = GPAQ score with rest; MSSQ = Motion Sickness Susceptibility Questionnaire Short-form (total score).

ID	age (in yrs.)	gender (m=0)	LQ	eye (1=r)	GPAQ-	GPAQ+	MSSQ
P01	28	0	100	1	2480	7520	13.5
P02	28	1	100	1	2480	6680	0
P03	25	1	100	2	4200	7560	28
P04	23	1	100	2	1240	7120	10
P05	30	0	67	1	3840	7200	10
P06	34	0	100	2	2640	6000	3
P07	33	0	100	1	4680	8040	16
P08	27	1	100	2	2400	5760	2
P09	28	1	100	1	2640	6210	13
P10	39	1	27	1	3840	6990	8
P11	27	0	60	1	1920	4440	15
P12	23	0	100	1	480	6780	6.375
P13	26	1	100	1	3180	6120	2.125
P14	30	1	100	1	1080	5280	13.93
P15	32	1	100	1	20520	21150	15
P17	24	0	100	1	720	4920	7
P18	25	1	100	1	2800	6580	36
P19	35	0	100	1	40	6340	0
P21	30	0	82	1	3600	6540	3
P22	27	1	100	1	1620	3510	29
P23	31	1	100	2	2160	5940	11
P24	26	0	82	2	960	3900	0

Table S1: Demographics of participants and questionnaires. LQ = laterality quotient for handedness, positive LQ (in %) is indicating right handedness. m = male, eye = dominant eye, r= right, GPAQ = Global Physical Activity Questionnaire Score (in minutes per week), GPAQ- = GPAQ score without rest, GPAQ+ = GPAQ score with rest; MSSQ = Motion Sickness Susceptibility Questionnaire Short-form (total score).

ID	age (in yrs.)	gender (m=0)	LQ	eye (1=r)	GPAQ-	GPAQ+	MSSQ
P25	25	1	100	1	2280	4380	15.75
P26	30	0	100	1	6120	9480	4
P28	22	1	100	1	1680	4620	11.875
P29	23	1	100	1	720	6600	12.86
P30	25	1	100	2	5400	9600	35.1
P31	33	0	100	1	3000	7200	0
P32	29	1	100	1	2160	4680	9.625
P33	29	0	100	1	2880	6660	25.5
P34	29	1	100	2	1560	5340	3
P35	26	0	100	1	3480	4740	19.93
P36	34	0	100	1	1800	3900	6.6

Table S2: Vestibular sensitivity measures. abs. = absolute values, vHIT = video head-impulse test, R = right, L = left

ID	Caloric abs. (in °/s)	vHIT gain R	vHIT gain L
P01	14.2	1.05	0.82
P02	55.45	0.95	0.94
P03	33.1	1.11	1.03
P04	63.1	1.01	1.04
P05	21.2	0.95	0.95
P06	41.5	1.03	0.96
P07	26.1	0.95	0.87
P08	28.74	1.1	1.05
P09	50.6	0.98	1.02
P10	77.8	1.28	1.12
P11	84.8	1.05	0.81
P12	60.6	1.19	1.11
P13	22.4	1.18	0.96
P14	8.6	0.91	0.92
P15	23.9	1.19	0.88
P17	23.7	1.18	1.03
P18	12.7	1.03	0.94
P19	18.5	1.06	1
P21	30.7	1.1	1.01
P22	3.6	1.16	1.02
P23	35.7	1.25	1.04
P24	7.3	1.14	0.96
P25	10.8	0.97	0.92
P26	19.7	0.96	0.81
P28	28.3	1	0.87
P29	12.7	1.06	1.09

Table S2: Vestibular sensitivity measures. abs. = absolute values, vHIT = video head-impulse test, R = right, L = left

ID	Caloric abs. (in °/s)	vHIT gain R	vHIT gain L
P30	67.2	1.1	0.94
P31	41.2	1.09	1
P32	39.9	1.17	1.12
P33	19.2	1.01	0.85
P34	15.4	1.08	0.83
P35	19.2	0.95	0.88
P36	3.6	1.15	1.13

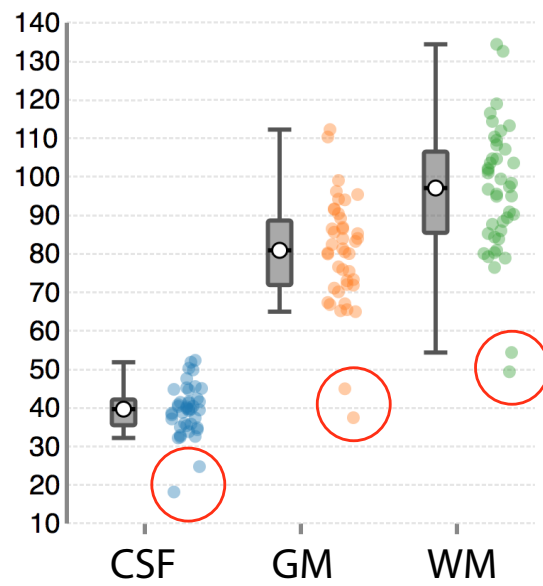


Figure S1: Dietrich's SNR (SNRd) for cerebro spinal fluid (csf) grey matter (gm) and white matter (wm) of the structural T1 images. Each dot represents one participant. The red circles mark two outliers for each tissue type. The lower dot of the outliers in each tissue type represents one participant, the upper one another participant. These two participants were removed from further analyses.

Table S3: Results of the second level analyses of the resting state fMRI data in complete darkness for positive correlation with horizontal slow phase velocity over time. Reported are the significant uncorrected peak-level ( $p < 0.001$ ) results with a cluster threshold of 28 voxels. Only significant results are reported

cluster-level		peak-level		
K	p uncorr	T	[x;y;z] in mm	brain region
110	0.001	5.939	[30;-6;52]	right premotor cortex
		5.739	[24;-12;60]	
72	0.004	5.913	[-4;36;46]	left superior frontal gyrus
35	0.031	5.871	[50;-84;0]	right lateral occipital cortex
				inferior division
31	0.041	5.532	[-36;-76;12]	left lateral occipital cortex
				visual cortex V5
82	0.002	5.029	[-28;-52;56]	left superior parietal lobule
		4.207	[-12;-50;66]	
		3.927	[-20;-50;64]	
43	0.019	4.960	[12;-6;78]	right premotor cortex
		4.030	[6;-12;78]	
43	0.019	4.948	[50;36;-16]	right frontal orbital cortex
		3.973	[56;32;-12]	
42	0.020	4.825	[54;16;28]	right Broca44/45
				inferior frontal gyrus pars opercularis
52	0.011	4.643	[-42;-50;-60]	left cerebellum VIIb
		3.818	[-32;-62;-58]	left cerebellum VIIb
41	0.021	4.637	[2;-66;-34]	Vermis VIIIa
		4.127	[2;-74;-32]	

Table S3: Results of the second level analyses of the resting state fMRI data in complete darkness for positive correlation with horizontal slow phase velocity over time. Reported are the significant uncorrected peak-level ( $p < 0.001$ ) results with a cluster threshold of 28 voxels. Only significant results are reported

cluster-level		peak-level		
K	p uncorr	T	[x;y;z] in mm	brain region
				left Broca 44
47	0.015	4.568	[-52;8;30]	inferior frontal gyrus pars opercularis
		4.149	[-48;2;26]	
35	0.031	4.395	[22;-50;64]	right superior parietal lobule
28	0.050	3.816	[44;-16;62]	right premotor cortex



## 2.4 Pupil segmentation and gaze estimation using deep learning (DeepVOG)

Yiu, YH, Aboulatta, M., **Raiser, T.**, Ophey, L., Flanagin, V.L., zu Eulenburg, P., Ahmadi, S.A. (2019). *Journal of Neuroscience Methods*, 324.

The article “DeepVOG: Open-source Pupil Segmentation and Gaze Estimation in Neuroscience using Deep Learning” was published in the *Journal of Neuroscience Methods*, 324, Copyright Elsevier in August 2019 (with a pre-online version in June 2019) and is reprinted here (no written permission is required by Elsevier).

### Summary

This fourth project of the thesis entitled “DeepVOG: Open-source Pupil Segmentation and Gaze Estimation in Neuroscience using Deep Learning” represents an important basis for the eye-tracking analyses reported in the previous chapter. Eye-tracking in complete darkness resulted in eye-tracking videos with heterogeneous light conditions and a black rim in the field of view. Other already established eye-tracking analyses software failed estimating horizontal and vertical eye-position with a high confidence and low noise confound. Hence, we established a deep learning network that can be generalized to other data sets. It results in pupil center localization, elliptical contour estimation and blink detection. For the magnetic vestibular stimulation project reported in the previous chapter we used the horizontal and vertical position of the pupil center as well as their confidence and blink detection. These were eye-tracking parameters in a pre-version of the final Deep-VOG published paper.

### Author contributions

The following authors contributed to this work: Seyed-Ahmad Ahmadi designed the study. Theresa M. Raiser and Leoni Ophey collected the data under the supervision of Virginia L. Flanagin and Peter zu Eulenburg. Data tagging was performed by all authors. Yuk-Hoi Yiu and Moustafa Aboulatta performed the deep learning network analyses under the supervision of Seyed-Ahmad Ahmadi. Yuk-Hoi Yiu wrote the paper with input from all authors.

Contents lists available at [ScienceDirect](https://www.sciencedirect.com)

Journal of Neuroscience Methods

journal homepage: [www.elsevier.com/locate/jneumeth](http://www.elsevier.com/locate/jneumeth)

## DeepVOG: Open-source pupil segmentation and gaze estimation in neuroscience using deep learning



Yuk-Hoi Yiu<sup>a</sup>, Moustafa Aboulatta<sup>b</sup>, Theresa Raiser<sup>a,d</sup>, Leoni Ophey<sup>a</sup>, Virginia L. Flanagan<sup>a</sup>, Peter zu Eulenburg<sup>a,c</sup>, Seyed-Ahmad Ahmadi<sup>a,\*</sup>

<sup>a</sup> German Center for Vertigo and Balance Disorders (DSGZ), Feodor-Lynen-Str. 19, 81377 Munich, Germany

<sup>b</sup> Faculty of Informatics, Technical University of Munich, Boltzmannstr. 3, 85748 Garching, Germany

<sup>c</sup> Department of Neurology, Klinikum der Universität München, Marchioninistr. 15, 81377 Munich, Germany

<sup>d</sup> Graduate School of Systemic Neurosciences, Ludwig-Maximilians Universität München, Großhadern Str. 2, 82152 Planegg, Germany

### ARTICLE INFO

#### Keywords:

Video oculography  
Pupil segmentation  
Gaze estimation  
blink detection  
Deep learning  
Convolutional neural networks

### ABSTRACT

**Background:** A prerequisite for many eye tracking and video-oculography (VOG) methods is an accurate localization of the pupil. Several existing techniques face challenges in images with artifacts and under naturalistic low-light conditions, e.g. with highly dilated pupils.

**New method:** For the first time, we propose to use a fully convolutional neural network (FCNN) for segmentation of the whole pupil area, trained on 3946 VOG images hand-annotated at our institute. We integrate the FCNN into DeepVOG, along with an established method for gaze estimation from elliptical pupil contours, which we improve upon by considering our FCNN's segmentation confidence measure.

**Results:** The FCNN output simultaneously enables us to perform pupil center localization, elliptical contour estimation and blink detection, all with a single network and with an assigned confidence value, at framerates above 130 Hz on commercial workstations with GPU acceleration. Pupil centre coordinates can be estimated with a median accuracy of around 1.0 pixel, and gaze estimation is accurate to within 0.5 degrees. The FCNN is able to robustly segment the pupil in a wide array of datasets that were not used for training.

**Comparison with existing methods:** We validate our method against gold standard eye images that were artificially rendered, as well as hand-annotated VOG data from a gold-standard clinical system (EyeSeeCam) at our institute.

**Conclusions:** Our proposed FCNN-based pupil segmentation framework is accurate, robust and generalizes well to new VOG datasets. We provide our code and pre-trained FCNN model open-source and for free under [www.github.com/pydsgz/DeepVOG](http://www.github.com/pydsgz/DeepVOG).

## 1. Introduction

Many disciplines in clinical neurology and neuroscience benefit from the analysis of eye motion and gaze direction, which both rely on accurate pupil detection and localization as a prerequisite step. Over the years, eye tracking techniques have been contributing to the advancement of research within these areas. Examples include the analysis of attentional processes in psychology (Rehder and Hoffman, 2005) or smooth pursuit assessment in patients with degenerative cerebellar lesions (Moschner et al., 1999). One important area of application for eye tracking is vestibular research, where measurements of the vestibulo-ocular reflex (VOR) and nystagmus behavior are essential in the diagnostic pathway of balance disorders (Ben Slama et al., 2017).

Beyond neuroscientific applications, eye-tracking was also utilized by autonomous driving industry for driver fatigue detection (Hornig et al., 2004). Other than that, the trajectories and velocities of eye movements over a viewing task can serve as individual biometric signature for identification purpose (Bednarik et al., 2005; Liang et al., 2012). In consumer-behaviour research, eye-tracking has been used to study the dynamics and locations of consumers' attention deployment on promoted products in order to improve the design of advertisement (Lohse, 1997; Reutskaja et al., 2011). It is clear that pupil detection and tracking techniques build a fundamental block for eye movement analysis, enabling advancement in neuroscientific research, clinical assessment and real life applications.

Despite their importance, robust, replicable and accurate eye

\* Corresponding author.

E-mail address: [ahmad.ahmadi@med.uni-muenchen.de](mailto:ahmad.ahmadi@med.uni-muenchen.de) (S.-A. Ahmadi).

<https://doi.org/10.1016/j.jneumeth.2019.05.016>

Received 28 February 2019; Received in revised form 28 May 2019; Accepted 28 May 2019

Available online 06 June 2019

0165-0270/© 2019 The Authors. Published by Elsevier B.V. This is an open access article under the CC BY license (<http://creativecommons.org/licenses/by/4.0/>).

tracking and gaze estimation remain challenging under naturalistic low-light conditions. Most of the gaze estimation approaches, such as Pupil-Centre-Corneal-Reflection (PCCR) tracking (Guestrin and Eizenman, 2006) and geometric approaches based on eye shapes (Krafka et al., 2016; Chen and Ji, 2008; Yamazoe et al., 2008; Yang and Saniie, 2016; Ishikawa et al., 2004) depend on inferring gaze information from the pupil's location and shape in the image. However, the pupil is not always clearly visible to the camera. As summarized in (Schnipke and Todd, 2000), the pupil appearance can suffer from occlusion due to half-open eyelids or eyelashes, from reflection of external light sources on the cornea or glasses, from contact lenses or from low illumination, low contrast, camera defocusing or motion blur. All these artifacts pose challenges to pupil detection, and eye tracking algorithms which were not specifically designed with these artifacts in mind, may fail or give unreliable results under these circumstances.

In medical image analysis and computer vision, dramatic improvements in dealing with such artifacts have been achieved in recent years due to the introduction and rapid advancement of deep learning, specifically convolutional neural networks (CNN). An important distinction to hand-designed algorithms is that a CNN can achieve robust pupil segmentation, by automatically learning a sequence of image processing steps which are necessary to optimally compensate for all image artifacts which were encountered during training.

### 1.1. Related work

Conventional gaze estimation is often based on the Pupil-Centre-Corneal-Reflection (PCCR) method (Guestrin and Eizenman, 2006), which requires accurate localization of the pupil centre and glints, i.e. corneal reflections. Localization algorithms for the pupil and glints are often based on image processing heuristics such as adaptive intensity thresholding, followed by ray-based ellipse fitting (Li et al., 2005), morphological operators for contour detection (Fuhl et al., 2015a), circular filter matching (Fuhl et al., 2015b), Haar-like feature detection and clustering (Świrski et al., 2012), or radial symmetry detection (Kumar et al., 2009). It is important to note that most of these approaches assume the pupil to be the darkest region of the image (Fuhl et al., 2015a), which is susceptible to different illumination conditions and may require manual tuning of threshold parameters (Satriya et al., 2016; Kumar et al., 2009; Santini et al., 2017). Previous to our approach, several deep-learning based pupil detection approaches have been proposed to improve the robustness to artifacts by learning hierarchical image patterns with CNNs. PupilNet (Fuhl et al., 2016) locates the pupil centre position with two cascaded CNNs for coarse-to-fine localization. In Chinsatit and Saitoh (2017), another CNN cascade first classifies the eye states of “open”, “half-open” and “closed”, before applying specialized CNNs to estimate the pupil centre coordinates, based on the eye state. However, current CNN approaches output only the pupil centre coordinates, which alone are not enough to determine the gaze direction without calibration or additional information from corneal reflection. Some studies focus on end-to-end training of a CNN, directly mapping the input space of eye images to the gaze results (Krafka et al., 2016; Naqvi et al., 2018), but they are confined to applications in specific environment, such as estimating gaze regions on the car windscreen (Naqvi et al., 2018) or mobile device monitors (Krafka et al., 2016), which are not suitable for clinical measurement of angular eye movement.

### 1.2. Contribution

In this work, we propose DeepVOG, a framework for video-oculography based on deep neural networks. As its core component, we propose to use a fully convolutional neural network (FCNN) for segmentation of the complete pupil instead of only localizing its center.

The segmentation output simultaneously enables us to perform pupil center localization, elliptical contour estimation and blink detection, all with a single network, and with an assigned confidence value. We train our network on a dataset of approximately four thousand eye images acquired during video-oculography experiments at our institute, and hand-labeled by human raters who outlined the elliptical pupil contour. Though trained on data from our institute, we demonstrate that the FCNN can generalize well to pupil segmentation in multiple datasets from other camera hardware and pupil tracking setups. On consumer-level hardware, we demonstrate our approach to infer pupil segmentations at a rate of more than 100 Hz. Beyond pupil segmentation, we re-implement a published and validated method for horizontal and vertical gaze estimation and integrate it as an optional module into our framework (Świrski and Dodgson, 2013). We show that the integration of gaze estimation is seamless, given that our FCNN approach provides elliptical pupil outline estimates. We further show that by considering ellipse confidence measures from our FCNN output, the accuracy of the gaze estimation algorithm can be increased. Our implementation is fully Python-based and provided open-source for free usage in academic and commercial solutions. Our code, pre-trained pupil segmentation network and documentation can be found under: [www.github.com/pydsgz](http://www.github.com/pydsgz).

## 2. Materials and methods

### 2.1. Datasets

For this study, we acquired three datasets at the German Center for Vertigo and Balance Disorders, two for training validation of the pupil segmentation network and one for validation of the gaze estimation. Training sequences were acquired in a challenging environment, i.e. inside a MRI scanner, during a neuroscientific experiment setup involving VOG and simultaneous functional MRI (fMRI) assessment. Both training datasets were collected on a cohort of healthy young adults. Training dataset A was acquired from 35 subjects (16 male, 19 female, age  $28.1 \pm 4.0$  years) in a fully darkened MRI scanner room. Training dataset B was acquired from 27 subjects (8 male, 19 female, age  $25.5 \pm 3.7$  years) in a scanner room with normal illumination. For MRI-compatible recording, we utilized a commercial VOG system (NNL EyeTracking Camera, NordicNeuroLab AS, Bergen, Norway), yielding VOG videos at a  $320 \times 240$  pixel resolution and a framerate of 60 Hz. Both datasets A and B contained video sections with challenging pupil appearance, leading to high dropout rates of eye tracking and mis-localizations of the pupil center with two commercial eye tracking software solutions (ViewPoint EyeTracker, Arrington Research, Arizona, USA; EyeSeeCam, EyeSeeTec GmbH, F + 1/4rstenfeldbruck, Germany). Typical example images from both datasets are shown in Fig. 1. Pupil detection failures occur e.g. due to highly dilated pupils in dark environments, dark circular borders from ocular mount gaps, heterogeneous illumination and pupil occlusion from ocular borders, eyelids and eyelashes.

For network training, we randomly sampled 3946 eye image frames from both datasets (training set A: 1539 frames, training set B: 2416 frames). Five human raters segmented the pupil in all images (one rater per image), using a custom labeling tool implemented in Python, by manual placement of at least five points on the visible part of the pupil boundary, followed by least-squares fitting of an ellipse to the boundary points.

Validation of the pupil segmentation performance was done on the test images from datasets A (959 frames) and B (1043 frames), i.e. images that were not seen by the network during training. In order to test the generalization capability of our network to entirely novel eye appearances, we tested its pupil detection performance on previously unseen third-party data, including Delhi Iris Database (Delhi) (Kumar and Passi, 2010), Labelled Pupil in the Wild (LPW) (Tonsen et al., 2015) and Multimedia-University Iris (MMU Iris)

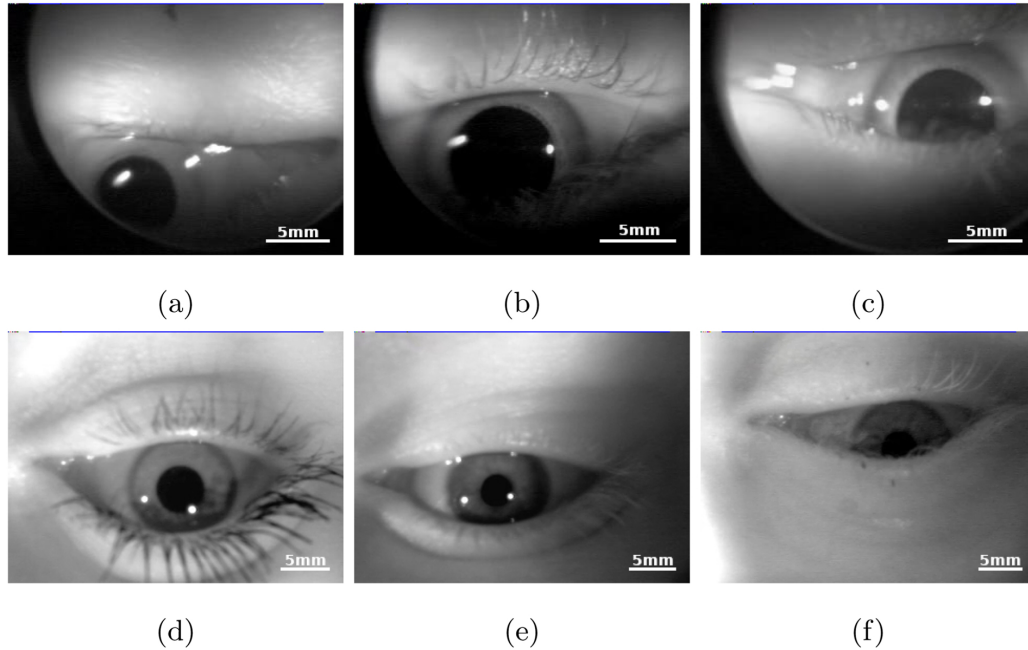


**Fig. 1.** Examples of input eye images in training dataset A (a, b, c) and dataset B (d, e, f). Observations and artifacts include: (a, b) pupil merging with dark background from ocular edge, (b) motion blur, (c) eyelid occlusion, (d) clear pupils with glint reflection, (e) inhomogeneous illumination, (f) half occluded pupil with dark iris. All images have a resolution of  $320 \times 240$  in pixel.

**Table 1**

(a) Difference between predicted and manually labelled pupil regions, measured in terms of median values (inter-quartile range) of Dice's coefficient, Euclidean distance between pupil centers, and Hausdorff distance between pupil contours. Results on different datasets (blink images excluded for datasets A and B) are shown. Notably, the DeepVOG network was only trained on datasets A and B, but is able to generalize with high pupil segmentation accuracy to the five other datasets. (b) Blink detection rate analyzed on dataset A and B. Pupil ellipses with confidence  $< 0.96$  were classified as blink.

(a)			
Datasets	Dice's coefficient	Euclidean distance (px)	Hausdorff distance (px)
Dataset A & B (1892)	0.966 (0.948–0.976)	1.0 (0.6–1.6)	2.8 (2.0–4.0)
Dataset C (323)	0.97 (0.958–0.978)	0.9 (0.6–1.3)	2.8 (2.0–3.2)
Delhi (763)	0.978 (0.971–0.983)	0.8 (0.5–1.2)	2.8 (2.0–3.0)
LPW (466)	0.938 (0.914–0.957)	0.9 (0.6–1.4)	3.2 (2.2–4.0)
MMU Iris (167)	0.958 (0.947–0.968)	1.0 (0.6–1.4)	2.2 (2.1–3.0)
Blender (361)	0.965 (0.901–0.982)	1.8 (1.3–2.4)	3.6 (2.0–8.2)
(b)			
Datasets	Accuracy (%)	Sensitivity (%)	Specificity (%)
Dataset A & B (2002)	0.93	0.94	0.93

(Multimedia-University, 2019). Furthermore, we acquired one more set of video sequence data (Dataset C) at our institute, for the quantitative validation of gaze estimation (see below). LPW and MMU Iris were provided with labels of pupil centre coordinates in their images, which enables quantitative analysis on our network's performance of localizing pupil centers. To quantitatively validate the segmentation accuracy on the other unlabelled datasets, we labeled pupils in a small subset of each dataset (cf. Table 1a). As a pre-processing step, all images or video frames with different resolution were resized to  $320 \times 240$  in pixel for the analysis.

Dataset C, the validation set for gaze estimation, was acquired from 9 healthy subjects (5 male, 4 female, age  $33.8 \pm 5.9$  years), in the neuro-ophthalmological examination laboratory of the German Center for Vertigo and Balance Disorders. The setup included a commercial

system for clinical video oculography (EyeSeeTec GmbH,<sup>1</sup> F+1/4rstenfeldbruck, Germany; video resolution  $320 \times 240$  pixels, 120 Hz framerate). To calibrate each subject's gaze, a gold standard calibration was performed using a projector-assisted five-point calibration paradigm ( $8.5^\circ$  horizontal and vertical gaze extent). For 3D eye model fitting using our framework, each subject additionally performed two projector-free, unassisted calibrations with three trials each (for details, see Section 2.5). To validate the accuracy of gaze estimates, each subject underwent an oculomotoric examination comprising four clinical tests: saccade test, fixation nystagmus, smooth pursuit and optokinetic nystagmus. We then compare gaze estimates from our framework to

<sup>1</sup> [www.eyeseecam.com](http://www.eyeseecam.com).

estimates from the clinical gold standard calibration and system.

### 2.2. Pupil segmentation network

The general structure of deep CNNs features stacked convolutional image filters and other signal processing layers (e.g. for image re-sampling), arranged in a sequence of processing layers (LeCun et al., 2015). These filters are trained towards optimally fulfilling a defined goal given an input image, in this study the robust segmentation of pupils, despite challenging appearance. Initially, i.e. before training, these filters extract meaningless information from images and fail to achieve the segmentation task. During training, the network is repeatedly presented with different pupil images and corresponding human pupil segmentations as a gold standard, including highly challenging examples. By means of back-propagation of the residual segmentation error through the network (LeCun et al., 2015), the filters in the network weights gradually get adapted to compensate for artifacts and iteratively make better and better estimates for the optimal pupil area.

### 2.3. CNN architecture and pupil segmentation

Numerous architectures for medical image segmentation have been proposed to date, and surveys like (Litjens et al., 2017) provide a good entrypoint into this fast growing field. A well-established architecture is the U-Net (Ronneberger et al., 2015), which has shown to be adaptable to many segmentation problems in various medical imaging modalities. For this work, we adapt a basic U-Net architecture for pupil segmentation in 2D greyscale images. A U-Net consists of multiple layers of feature extraction, which are arranged in a down-sampling path on the left side and an up-sampling path on the right side. Horizontal skip connections relay high-resolution image features from the down-sampling path into the up-sampling path, in order to preserve high-frequency image features and achieve a sharp segmentation output.

Our architecture is depicted in Fig. 2. Compared to the original U-Net, we previously proposed several architectural changes as V-Net (Milletari et al., 2016), which we partly adopt in this work as well. At each stage of the up- and down-sampling path, we utilize a convolutional layer with  $10 \times 10$  filters which outputs feature maps with the same size of the input by appropriate padding. The down-sampling path reduces the size of the feature maps and increases the size of receptive fields of convolutional filters at each stage, such that more complex features in a larger context can be extracted. Compared to (Ronneberger et al., 2015), which performs down- and up-sampling

through pooling operations, we utilize strided convolution ( $2 \times 2$  filter kernel size, stride 2) for downsampling and transposed convolution (Noh et al., 2015) for upsampling, which is more memory efficient (Springenberg et al., 2014; Milletari et al., 2016) and able to learn optimal down-/up-sampling filters.

The final output layer has two output maps for pupil and background, with the same size as the input layer ( $320 \times 240$  pixels). We employ a softmax layer (Litjens et al., 2017) to perform smooth maximum activation across regions. The prediction yields a probabilistic output, to which we can fit an elliptical contour representing the pupil center and eccentricity of the boundary. To determine the contour points for ellipse fitting, we incorporate a simple post-processing on the network's probabilistic prediction of the pupil foreground: the prediction posterior is thresholded at a probability of  $p > 0.5$ , denoised through morphological closing (Soille, 2003), and the largest connected component is extracted to reject small false positive regions (cf. Fig. 3c). For both pupil area and center, a detection confidence value can be determined by computing the average prediction confidence within the detected pupil area. Finally, a blink can be detected if this confidence falls under a pre-defined threshold.

The pupil fitting procedure, including probabilistic network output, post-processing and ellipse fitting, is depicted in Fig. 3. Importantly, compared to previous approaches (Fuhl et al., 2016; Chinsatit and Saitoh, 2017; Krafa et al., 2016; Naqvi et al., 2018), our fully convolutional approach does not require a cascade of several CNNs to achieve the pupil detection, neither are we restricted to pure center localization. Pupil segmentation, center estimation and blink detection can be performed with a single FCNN, and outputs are assigned with confidence values which can be further utilized for gaze estimation and VOG evaluation.

### 2.4. Augmentation

To make the network more robust to expectable variations in camera pose and eye appearance, we artificially enhance the training dataset through random augmentation of image-segmentation pairs. During training, we apply random rotation within the range of  $\pm 40^\circ$ . Images were further randomly translated in the range of  $\pm 20\%$  of height and width. We also applied random zooming by a factor of 0.2 and random flipping in horizontal and vertical direction.

### 2.5. Gaze estimation

As derived by Świrski and Dodgson (2013), it is possible to

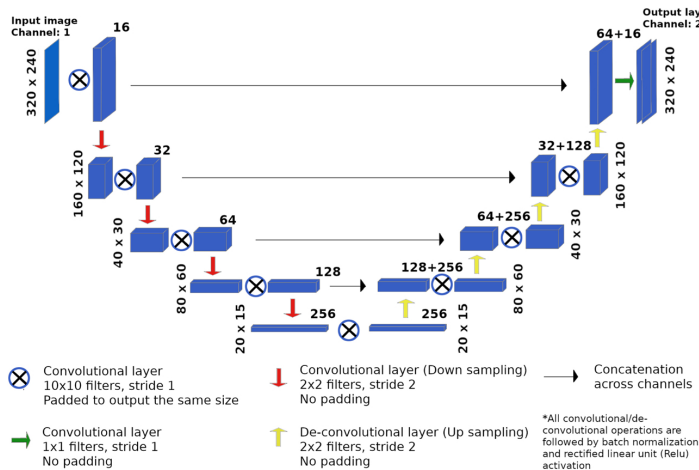
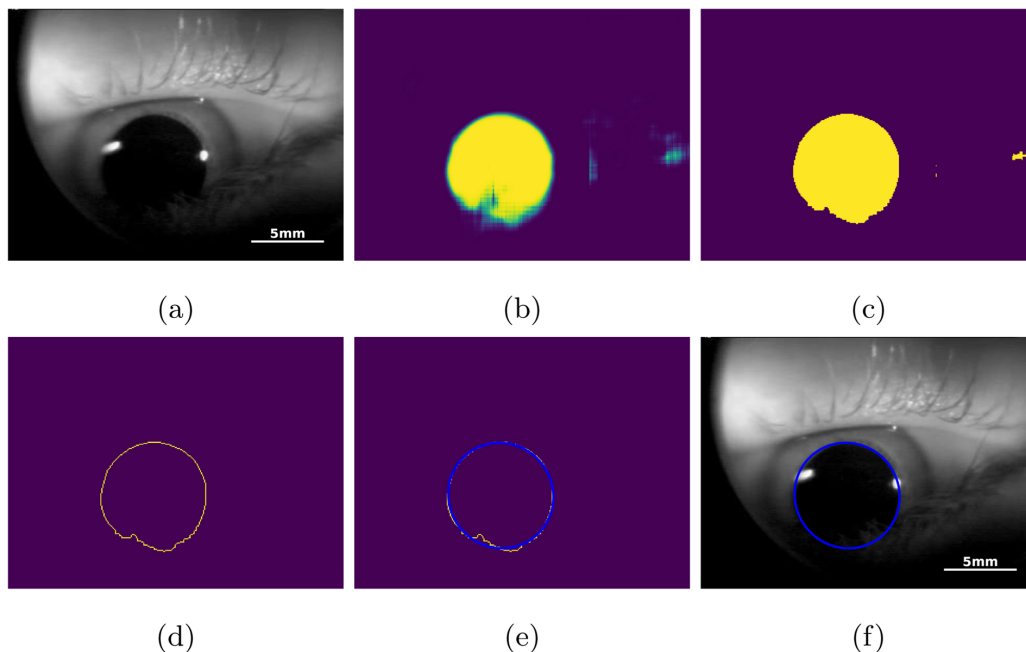


Fig. 2. Architecture of the fully convolutional neural network (FCNN) for pupil detection, inspired by U-Net (Ronneberger et al., 2015) and V-Net (Milletari et al., 2016). The network takes a single eye image as input, and produces an image-sized output with pixel-wise estimates for the pupil area. The network consists of a sequence of convolutional image filters which robustly extract features to distinguish the pupil from the background. The numbers on the top-right corner of the feature maps represent the number of filter channels. Several down-sampling operations allow the network to localize and segment the pupil at multiple image resolutions. In the up-sampling path, the low-resolution image representation gets inflated back to the original size, while reconstructing the location and shape of the pupil. Horizontal skip connections preserve high-frequency image information and sharp edges throughout the down-/up-sampling operations. During training, all image filters are tuned towards optimally compensating for image artifacts encountered in the training set.



**Fig. 3.** Procedure of fitting an ellipse to a probability map of segmented pupil area. (a) Original input image. (b) Probabilistic pupil prediction output from the network. (c) Binarization of the output with threshold 0.5 and morphological closing for filling in small gaps. (d) Isolation of largest connected area, and extraction of perimeter points of the area. (e) Fitted ellipse (blue line) from perimeter points. (f) Fitted pupil contour on the input image. (For interpretation of the references to color in this figure legend, the reader is referred to the web version of this article.)

reconstruct a 3D model of the eyeball and perform gaze estimation, purely based on a set of estimated 2D pupil ellipses from a video sequence, and without further fixation-based or projector-assisted calibration. Using the fitted 3D model, estimates of horizontal and vertical gaze angles can then be derived in each frame of a newly recorded VOG video, using the location and eccentricity of pupil ellipses. The reconstruction of the 3D eye model is based on the un-projection algorithm by Safaee-Rad et al. (1992). Its extension to gaze estimation is described in detail in Świrski and Dodgson (2013). Notably, it is assumed that the eyeball is of spherical shape and the pupil is a perfect circular disk (with varying radius) on the sphere surface, whose projections onto the camera's image plane form the 2D ellipse shapes. For a detailed derivation of the eye model fitting theory and algorithm, we refer the reader to (Świrski and Dodgson, 2013). Likewise, our Python-based re-implementation of the method with documentation can be found in our public code repository. Here, we want to emphasize that this “self-calibration” method can be very well complemented by our FCNN model, since it directly outputs a full segmentation of the pupil and elliptical pupil outlines. In particular, we can make the 3D eye model fitting more robust and gaze estimates more accurate by incorporating the confidence estimates of our FCNN into the fitting procedure. To this end, we extend the original formulae (6) and (9) in (Świrski and Dodgson, 2013) by incorporating a confidence factor  $\alpha_i$  for each image frame (and elliptical pupil estimate) that is considered during 3D model fitting and gaze estimation. Our confidence-weighted fitting formulae for the 3D eyeball center  $C$  and radius  $R$  can be denoted as:

$$\alpha_i = \begin{cases} 0, & \text{confidence}_i < \theta \\ 1, & \text{confidence}_i > \theta' \end{cases} \quad (1)$$

$$\hat{C} = \left( \sum_i \alpha_i (\mathbf{I} - \hat{\mathbf{n}}_i \hat{\mathbf{n}}_i^T) \right)^{-1} \left( \sum_i \alpha_i (\mathbf{I} - \hat{\mathbf{n}}_i \hat{\mathbf{n}}_i^T) \hat{\mathbf{p}}_i \right) \quad (2)$$

$$R = \frac{1}{\sum_i \alpha_i} \left( \sum_i \alpha_i \| \mathbf{p}'_i - C \| \right) \quad (3)$$

Here, following the notation of (Świrski and Dodgson, 2013),  $\hat{C}$  denotes the projection of the eyeball center to the 2D image plane, in which all projected pupil normals  $\hat{\mathbf{n}}_i$  have to intersect, given projected pupil centres  $\hat{\mathbf{p}}_i$  estimated by the FCNN. The symbol  $\mathbf{p}'_i$  is the intersection between  $\hat{\mathbf{p}}_i$  and the parameterized line  $(C + \mathbf{n}t)$ , as illustrated in Fig. 4b.

To fit the 3D eyeball model, the camera needs to be fixed with respect to the participant's head and eye, while the participant performs some form of eye motion that yields sufficiently many image frames with pupils of elliptical appearance. This can be achieved with different unassisted calibration paradigms. In this study, we fit and compare the 3D eyeball model based on three such calibration paradigms. The motivation is to assess the robustness of gaze estimation against different calibration methods and to discuss the requirements of a correct model fitting protocol which maximizes the estimation performance. The first paradigm is “Free-looking”. Here, participants need to keep their head fixed, while freely and smoothly looking all around the periphery of their visual field, thus yielding highly elliptical pupil appearances. The second is inspired by “CalibMe”, a recently proposed unassisted calibration approach for eye tracking, proposed by Santini et al. (2017). Here, participants select a stationary marker in their visual field and move their heads around it in a circular motion, while keeping her gaze fixed at the selected marker. The third one is “narrow-ranged”, a projector-assisted calibration approach that is commonly utilized in clinical eye-tracking systems and experiments. At our clinical center, participants focus their gaze on five sequentially presented fixation points

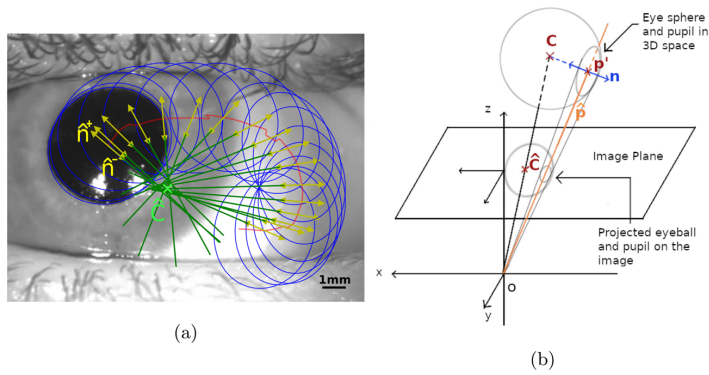


**Fig. 4.** Gaze estimation procedure, as adopted from Świrski and Dodgson (2013). Given a set of FCNN-based pupil segmentations in the camera image frame, the method reconstructs a 3D eyeball geometry that optimally explains the observed elliptic pupil projections. (a) Estimation of projected eye sphere centre  $\hat{C}$ . Gaze normals (yellow arrows,  $\hat{n}^+$  pointing outward and  $\hat{n}^-$  pointing towards  $\hat{C}$ ) intersect in  $\hat{C}$ , its location is approximated in a least-squares fashion. (b) Estimation of eye sphere radius  $R$ . The orange line denotes the possible candidates of pupil centres ( $\hat{p}$ ) after unprojection, which intersects with the parameterized line ( $C + nt$ ) at  $p'$ . The difference vector between  $p'$  and  $C$  gives information about eye radius  $R$ , and after the fitting stage, gaze direction  $n'$  (not shown here). For details, see (Świrski and Dodgson, 2013) and our documented open-source implementation. (For interpretation of the references to color in this figure legend, the reader is referred to the web version of this article.)

located at the screen's centre in both horizontal and vertical direction at  $\pm 8.5^\circ$ . We investigate whether unassisted calibration is feasible under these circumstances, which is particularly relevant towards a retrospective evaluation of datasets in which large-range gaze angles were not yet considered during the calibration protocol.

### 3. Results

#### 3.1. CNN-based pupil detection results

##### 3.1.1. Robustness

Our network successfully segmented the pupil areas in images under difficult conditions such as occlusion from eyelid or eyelashes, specular reflections, non-homogeneous illumination and naturalistic low-light, leading to highly dilated pupils. Several examples are illustrated in

Fig. 5. It is also robust to glint reflection, motion blur, camera de-focusing, and even to the appearance of unexpected dark edges from off-center ocular placement (see Fig. 5f), which is not a consistent feature throughout the dataset.

##### 3.1.2. Network validation

We tested the performance of DeepVOG on the testing images of datasets A and B, which were similar to the training images but had not been seen by the network during the training process. The accuracy of pupil center detection is measured by the Euclidean distance (unit: pixel) between the predicted and manually labelled pupil centers. The accuracy of pupil area segmentation is computed by the Dice overlap coefficient and Hausdorff distance. The Dice coefficient computes the overlap between predicted and manually labelled areas of the pupil (range [0...1], with 1.0 indicating perfect overlap), while the Hausdorff

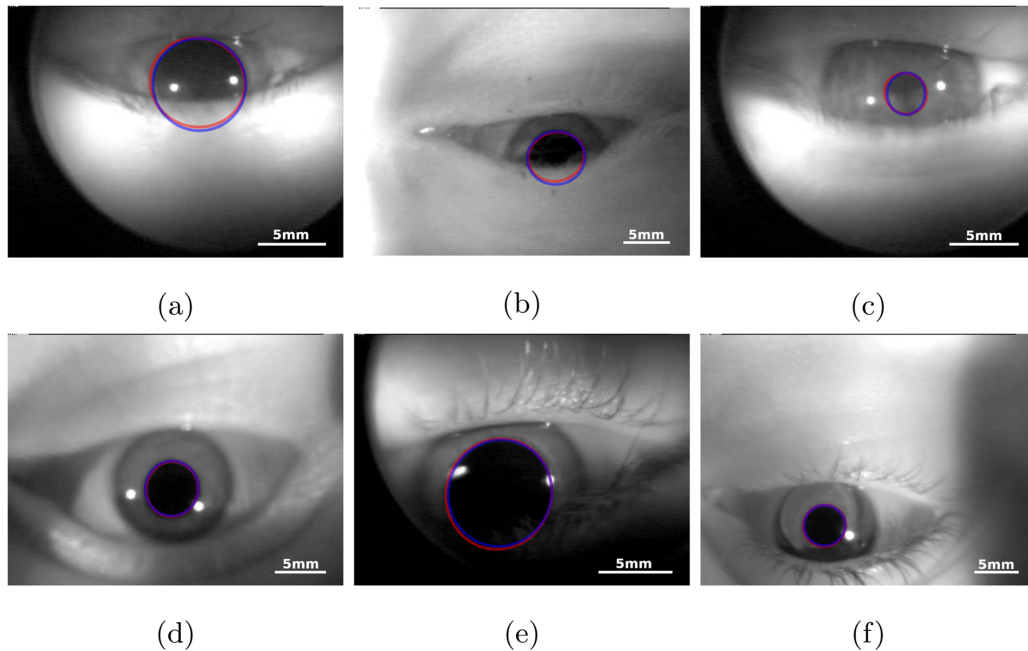


**Fig. 5.** Pupil detection results under different difficult or noisy conditions. Red lines are pupil ellipses manually labeled by human raters. Blue lines are pupil ellipses fitted to the FCNN segmentations in DeepVOG. The resolution of images are  $320 \times 240$  in pixel. (a, b) Eyelid occlusion and dilated pupils. (c) Eyelashes occlusion. (d) Camera de-focusing. (e) Motion blur and dark edge. (f) Contact lenses and non-homogeneous illumination. (For interpretation of the references to color in this figure legend, the reader is referred to the web version of this article.)

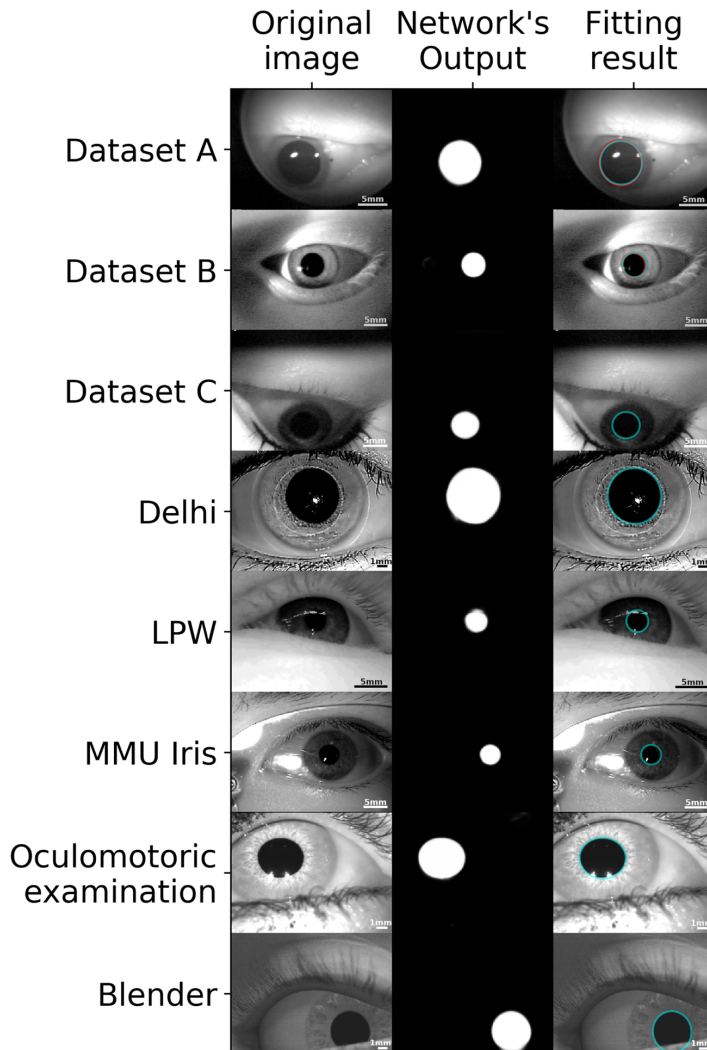


**Fig. 6.** Generalization capability of the FCNN pupil segmentation in DeepVOG. Examples of eye images ( $320 \times 240$  in pixel) from all datasets in this study. Left column: the original image used as an input to the network. Middle: the output of the network as a probability map of the pupil area. Right: the ellipse fitting result based on the network's output. Light blue contours denote the fitted ellipse by our model and red contours denote the manually fitted ellipse (shown only in datasets A and B). It is noteworthy that even though the FCNN was only trained on images from datasets A and B, the segmentation maps in all other datasets represent the pupil accurately and with a high confidence. (For interpretation of the references to color in this figure legend, the reader is referred to the web version of this article.)

distance (unit: [pixel]) measures the maximum pupil contour distance between prediction and manual labeling. Overall, the FCNN in DeepVOG achieved a high accuracy in pupil tracking on the 2002 unseen images of datasets A and B (see Table 1a). The median Euclidean distance was 1.0 pixel (IQR: 0.6–1.6 pixels), which is visually difficult to discern in a  $320 \times 240$  image. The Dice coefficient (median = 0.966) and Hausdorff distance (median = 2.8 pixels) further suggest that not only the pupil centre, but the entire segmented pupil areas were highly similar to the manually labelled ground truths.

### 3.1.3. Generalizability to other datasets

Test images from datasets A and B were similar to training images. To test whether the network can generalize to images from other completely novel datasets, we utilized a wide variety of datasets including dataset C, Delhi, LPW, MMU Iris and artificially rendered eye images using Blender. Fig. 6 shows an example image and segmentation result for each of these datasets. Although images from Delhi, MMU Iris and LPW differ significantly with the training datasets A and B in terms of their illuminance, contrast, camera angles, shadows and reflection,

our network was still able to segment a perfect pupil shape. Particularly in Fig. 6, the segmentation results are still robust against low pupil-boundary contrast in dataset C and LPW, contact lenses in Delhi and glasses in MMU Iris. On the other hand, there are a few failure cases in novel datasets if the surrounding of the pupil is shadowed and comparably dark (cf. Fig. 7). Regarding quantitative measures in Table 1a, the performance of pupil centre detection on the third-party datasets LPW (median of Euclidean distance = 0.9 pixels) and MMU Iris (median of Euclidean distance = 1.0 pixel) is on par with results on datasets A and B, which our network was trained on. The accuracy of pupil segmentation remains high on Dataset C and Delhi, as indicated by the decent quantitative results of Dice's coefficient, Euclidean distance and Hausdorff distance. This demonstrates a robust detection of pupil centres in unseen datasets, without much decrease of accuracy.

Among the datasets above, we tested the performance of DeepVOG on artificially rendered eye images which we generated with a VOG simulation (Świrski and Dodgson, 2014) in the 3D modeling software “Blender”, as well as on oculomotoric examination data from our clinical center (for details, see Sections 3.2 and 3.3). Here, a remarkable

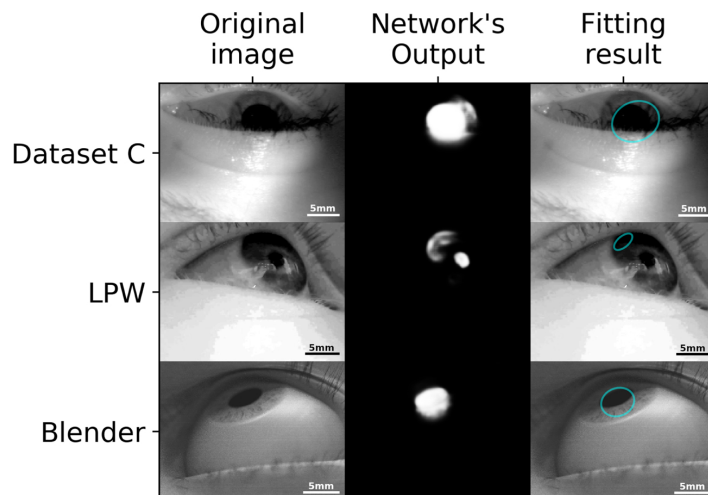


Fig. 7. Examples of failed pupil segmentation results (320 × 240 in pixel). The light blue contour denotes the fitted ellipse by our model. (For interpretation of the references to color in this figure legend, the reader is referred to the web version of this article.)

accuracy can also be observed for both datasets, which adds to the impression that DeepVOG can generalize to new data distributions to a great extent.

### 3.1.4. Blink detection

To realize blink detection, we utilize the fact that when the FCNN is uncertain about the classification, it will yield a lower confidence estimate, which we calculate as the average confidence of the output pixel values within the fitted ellipse area. Here we analyze how reliable this confidence indicator is in identifying blinks. Table 1b shows that a straightforward confidence thresholding is able to classify blinks with high accuracy, sensitivity and specificity on dataset A and B where image frames with during blinks ( $n = 110$ ) had also been manually labelled.

### 3.1.5. Inference speed

The FCNN forward-pass and inference speed is important with respect to real-time measurement of eye positions, as well as efficient offline data analysis. We tested the forward inference speed of DeepVOG network on a consumer-level workstation with a Nvidia GTX 1080 Ti graphics processing unit (GPU). The results show that DeepVOG runs at a 30 Hz detection rate if segmentations are inferred frame-by-frame (corresponding to 17 ms latency). If segmentations are computed in batches of 32 frames (i.e. 533 ms latency), inference can reach a framerate of more than 130 Hz (see Fig. 8), demonstrating the potential of fast offline data inference, and real-time pupil detection

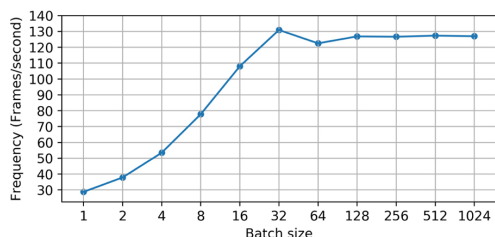


Fig. 8. Prediction speed: Forward inference frequency (in frames per second) of the FCNN in DeepVOG, with various input batch sizes at test time. At a batch size and latency of 32 frames, the FCNN can segment pupils at a rate of more than 130 Hz.

above 100 Hz and with latencies well below one second.

### 3.2. Gaze estimation on artificial data

Using the 3D modeling software “Blender”, we generated artificial gold standard eye images and gaze directions using a dedicated VOG simulation (Świrski and Dodgson, 2014). DeepVOG performed the pupil centre detection on Blender’s dataset with high accuracy, as indicated by small Euclidean distances between the predicted centres and simulation ground-truths (Table 2). Further, our model can estimate gaze directions with very small angular errors at a median of around 0.5°. We further investigated the effect of using only confident pupil segmentations predicted by the network for 3D eye model fitting. If we filter out gaze estimation results based on low-confidence network’s outputs, the median of angular errors is reduced by around 0.13° and its upper-quartile by 0.2°–0.4°. Fig. 9 visualizes the comparison between the predicted and ground-truth pupil centre coordinates. The visualization demonstrates a highly accurate performance on Blender images for both pupil centre detection and gaze estimation, except at the top left corner where the pupil shape becomes highly elliptical or barely visible from the camera angle (example shown in Fig. 7). With confidence thresholding, these relatively inaccurate predictions can be identified and optionally omitted (cf. Fig. 9c and d).

### 3.3. Gaze estimation on clinical data

#### 3.3.1. Accuracy and precision

We evaluated the gaze estimation accuracy of the DeepVOG framework, given three calibration paradigms (Free-looking, CalibMe and narrow-ranged calibration), using the oculomotoric examination videos

Table 2

Median (inter-quartile range) of absolute angular errors for horizontal and vertical eye movements, as well as Euclidean distance between predictions and simulation ground-truth. Confident prediction includes only data with pupil segmentation confidence > 0.96 while normal prediction includes all data.

Prediction type	Absolute horizontal angular errors (°)	Absolute vertical angular errors (°)	Euclidean distance (px)
Normal	0.61 (0.24–1.29)	0.51 (0.26–1.01)	1.78 (1.36–2.42)
Confident	0.45 (0.20–1.02)	0.38 (0.22–0.66)	1.56 (1.22–1.99)

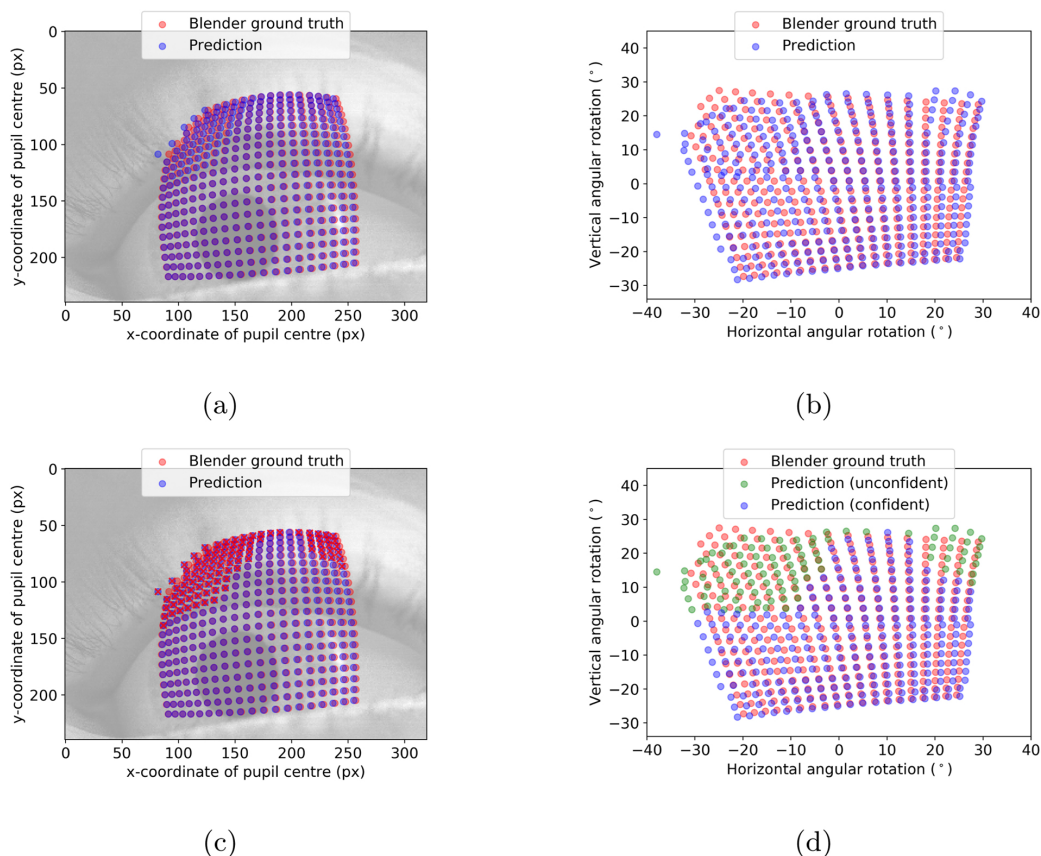


**Fig. 9.** Results of DeepVOG gaze estimations compared to gold-standard artificial eye images rendered with a VOG simulation (Świrski and Dodgson, 2014) in the 3D modeling software Blender. (a) Predicted pupil centre positions (blue dots) by the FCNN on images rendered by Blender, overlaid on ground-truth centre positions (red dots). (b) Predicted gaze directions by DeepVOG (blue dots) on rendered images, overlaid on ground-truth gaze directions (red dots). (c) Same figure as a, but with unconfident pupil detections crossed out (confidence < 0.96). (d) Same figure as b, but with the unconfident gaze estimation points shown as green dots. (For interpretation of the references to color in this figure legend, the reader is referred to the web version of this article.)

of 9 participants (Dataset C, cf. Section 2.1). Each examination was repeated for 3 trials to assess the repeatability of each calibration paradigm. Our gaze estimation results were validated against the results of the clinical gold standard system (EyeSeeTec). An example of gaze estimation results for the oculomotor examination video sequence is shown in Fig. 10. The median angular errors range between  $0.3^\circ$  and  $0.6^\circ$  (Table 3a), which demonstrates an accurate detection of eye angular movement. This also implies that the FCNN in DeepVOG is able to generalize well to this novel dataset of oculomotoric examination videos, given that the correctness of gaze estimation is substantially determined by the success of pupil area segmentation.

### 3.3.2. Robustness to self-calibration paradigm

All three self-calibration paradigms in this study enabled sub-degree performance of angular eye movement tracking, demonstrating the robustness to all three calibration paradigms. Nonetheless, there are differences. The Free-looking and CalibMe paradigms produced less angular errors than the narrow-ranged paradigm, as indicated in the accumulative distributions of angular errors (Fig. 11a and b). Importantly, in Świrski's and Dodgson's model (Świrski and Dodgson, 2013), the 3D eyeball parameters are more accurately fitted if a large range of pupil motion and elliptical appearances is covered. Here, the free-looking and CalibMe paradigms provide observations from a wider

distribution of gaze angles, while the narrow-ranged paradigm gives only small gaze angles at five distinct directions, which is not diverse enough for estimating an accurate 3D eyeball model. Consequently, this leads to larger angular deviations.

### 3.3.3. Repeatability

To assess the repeatability of 3D eye model fitting, we computed the intra-class correlation coefficient (ICC) across the measurements of three trials of each calibration paradigm (Table 2b), using ICC's two-way mixed effect, single-measures and absolute agreement model, i.e. ICC(A,1). Results revealed that the gaze predictions from the three trials achieved an excellent ( $ICC > 0.9$ , (Koo and Li, 2016)) reliability on their absolute agreement. The high reliability of measurement implies that DeepVOG can produce consistent and repeatable results across several experiment trials. Again, the Free-looking and CalibMe calibrations lead to similar ICC values, which are higher than if only Narrow-ranged gaze angles are used during 3D eye model fitting.

## 4. Discussion

In this manuscript, we describe DeepVOG, a novel eye-tracking framework that uses fully convolutional neural networks to perform pupil segmentation. It outputs pupil centers, pupil areas, elliptical

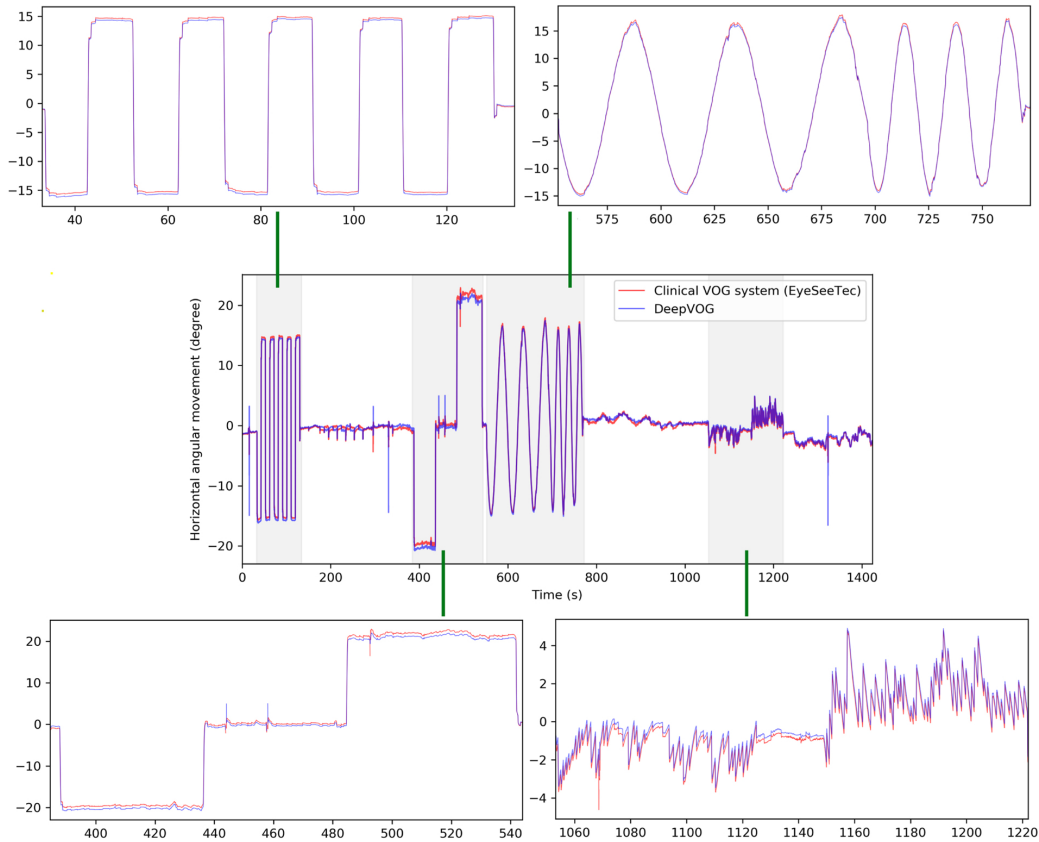


**Fig. 10.** Example gaze estimation results on an oculomotor examination video sequence (Dataset C). The blue line represents the estimations from DeepVOG and the red line from the gold-standard clinical VOG setup and eye tracking system (EyeSeeCam, EyeSeeTec GmbH, F + 1/4rstenfeldbruck, Germany). The oculomotor examination comprises measurement of saccades, fixation nystagmus, smooth pursuit and optokinetic nystagmus (shaded regions, from left to right). (For interpretation of the references to color in this figure legend, the reader is referred to the web version of this article.)

**Table 3**

(a) Absolute horizontal and vertical angular errors (in  $^{\circ}$ ), across calibration paradigms (Free-looking, CalibMe and Clinical standard) and three trials. (b) Intra-class correlation coefficient (ICC) as a measure for the repeatability of DeepVOG method under each calibration paradigm.

(a)			
	1st Trial	2nd Trial	3rd Trial
	Free-looking	Free-looking	Free-looking
Horizontal	0.364 (0.187–0.691)	0.383 (0.211–0.763)	0.404 (0.209–0.837)
Vertical	0.54 (0.2–1.223)	0.477 (0.191–1.116)	0.476 (0.189–1.16)
	CalibMe	CalibMe	CalibMe
Horizontal	0.309 (0.158–0.557)	0.329 (0.165–0.717)	0.315 (0.158–0.574)
Vertical	0.569 (0.22–1.144)	0.591 (0.235–1.213)	0.565 (0.22–1.167)
	Narrow-ranged	Narrow-ranged	Narrow-ranged
Horizontal	0.472 (0.191–1.209)	0.547 (0.208–1.464)	0.604 (0.235–1.512)
Vertical	0.561 (0.248–1.172)	0.59 (0.255–1.21)	0.567 (0.258–1.212)
(b)			
Intra-class correlation coefficient	Free-looking	CalibMe	Narrow-ranged
Horizontal	0.996	0.998	0.980
Vertical	0.996	0.998	0.958

contour estimates and blink events, as well as a measure of confidence for these values. In addition, gaze direction is estimated using an established method for 3D spherical eyeball model fitting, which we improve upon by incorporating confidence estimates from our network. Our results show our FCNN-based pupil segmentation, center localization and blink detection to be highly accurate and robust. Likewise, FCNN-based elliptical pupil contours are accurate enough to be directly used for robust, accurate and repeatable gaze estimation, which we validated with a clinical gold standard VOG system.

#### 4.1. Utility of DeepVOG

Traditionally, and in most related works, hand-engineered steps such as thresholding, edge detection and rejection were used to segment the pupil area in images. Instead, we utilize a deep-learning model to autonomously learn the optimal image filters and segmentation rules from training data. The trained FCNN model yields robust pupil fitting results even in noisy, underexposed and artifact-ridden images. Though trained on hand-annotated data from our institute, we demonstrated a high level of generalizability to new datasets from various eye tracking setups, which is why we hope that DeepVOG can be readily used by other research labs in the community. It should be emphasized that DeepVOG can segment a pupil's shape robustly from low-contrast images with heterogenous illuminance and highly dilated pupils. This makes it particularly useful in low-light environments such as darkened

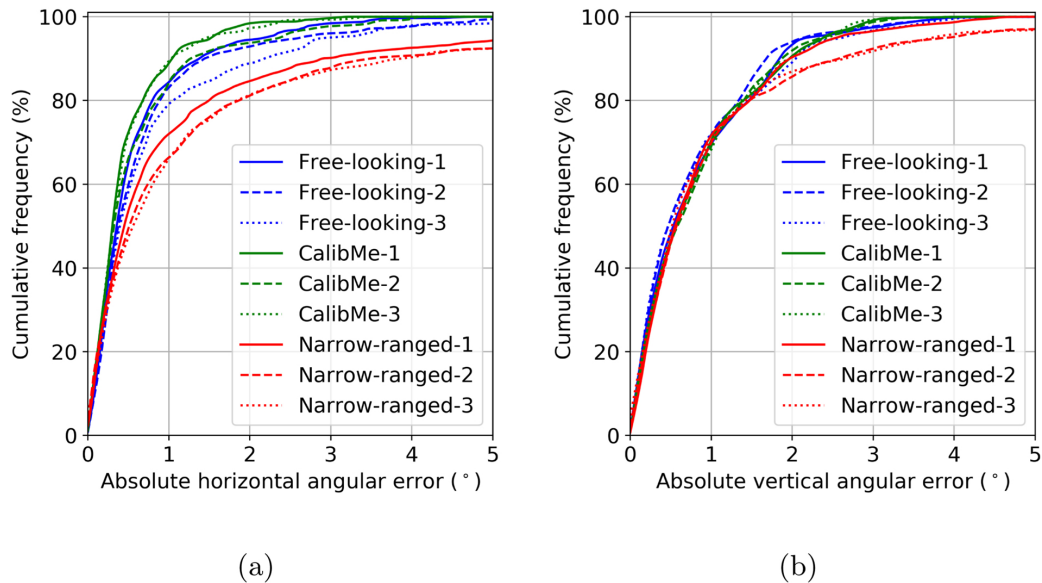


Fig. 11. Cumulative frequency plots for absolute (a) horizontal and (b) vertical angular errors, for three calibration paradigms (free-looking, CalibMe and narrow-ranged, represented by blue, green and red line respectively). To assess repeatability, each paradigm was repeated three times, represented by solid, dashed and dotted lines, respectively. (For interpretation of the references to color in this figure legend, the reader is referred to the web version of this article.)

MRI scanner rooms, a scenario for which we had difficulties performing eye tracking using established solutions. The unique feature of pupil region segmentation separates DeepVOG from previously proposed CNN-based approaches that only infer pupil centre coordinates (Fuhl et al., 2016; Chinsatit and Saitoh, 2017). This not only allows gaze inference based on pupil shape, but also enables other applications in neuroscientific research. For example, a change in pupil size is an automatic response to affective stimuli and an objective measure for emotional arousal (Bradley et al., 2008). The pupil segmentation may then aid or even replace the extra measurements of skin conductance and heart rate in some studies of emotion. Additionally, the output as a probability map informs the user about the confidence of the segmentation, which gives valuable information on data reliability, interpretation and blink detection.

The pupil ellipse estimates and confidence estimates from our FCNN lay the foundation for accurate gaze estimation with median angular errors of around  $0.5^\circ$ , as compared to RMSE of  $1.6^\circ$  in the original study of (Świrski and Dodgson, 2013), and  $0.59^\circ$  in EyeRecToo (Santini et al., 2017), one of the best-performing, recently proposed methods. We further show that if the network's confidence output is considered for 3D model fitting and gaze estimation, the accuracy can be further improved to angular errors around  $0.38^\circ$ – $0.45^\circ$ . Such accuracy could improve the validity of results in eye-tracking based experiments, for example, clinical assessment of vestibular and ocular motor disorders as well as visual attention studies in cognitive neuroscience. Further, DeepVOG demonstrates a high repeatability given multiple trials of two unassisted calibration paradigms, making it a stable tool for gaze data acquisition. Naturally, a projector-assisted, fixation-based calibration routine as in the neuro-ophthalmological examination laboratory of our clinical center can further improve the accuracy of gaze estimates. However, if such a procedure is impossible, for example due to hardware constraints, or in patients with fixation problems, the investigated unassisted calibration and gaze estimations in DeepVOG might be a very interesting option. Finally, we highlight the accessibility of DeepVOG as an open-source software, which does not depend on corneal reflections or stimulus-based calibrations, leaving a head-mounted low-cost camera as the only required equipment.

#### 4.2. Limitations and future work

Even though DeepVOG's FCNN-based pupil segmentation can generalize well to unseen datasets, mis-segmentations still do occur (cf. Fig. 7). In particular, if videos are recorded from a longer distance, thus containing other facial features such as eyebrows or the nose, DeepVOG is likely to fail, since it did not encounter such images during training. Further, if DeepVOG is used for gaze estimation, our experiments demonstrated that a narrow-angle calibration yields inferior accuracy during unassisted calibration. Hence, study conductors should make sure that study participants cover a sufficiently wide angular range of gaze directions (e.g. larger than  $20^\circ$ ), to achieve highly elliptical pupil shapes ideally in the entire visual periphery. A fundamental limitation of the gaze estimation method which we employ in DeepVOG is the assumption of a spherical eye model, as proposed by Świrski and Dodgson (2013). Several improvements can be made here, since the real pupil is not exactly circular, and elliptical shapes are distorted by light refraction through the cornea. To this end, in a very recent work by Dierkes et al. (2018) and Pupil Labs Research (Pupil Labs GmbH, Berlin, Germany), the Le Grand eye model (Le Grand, 1968) was employed instead, which assumes the eye to consist of two intersecting spheres, i.e. the eyeball and the cornea. The non-elliptical appearance of pupils caused by corneal refraction leads to reported gaze estimation errors similar to those observed in our experiments (cf. Fig. 9d). An improved 3D eye model fitting loss function and algorithm were proposed (Dierkes et al., 2018), which could help in further improving gaze estimates in future work. Further, DeepVOG is not applicable in eye tracking setups where no video can be recorded and provided as input to the algorithm as a video file or as a real-time video stream. Certain eye tracking systems, especially those operating at high frequencies around 1 kHz (e.g. EyeLink 1000, SR Research, Ottawa, Canada), commonly process eye tracking data internally and do not provide an interface to high-quality video data in real-time and at a high framerate.

#### 4.3. Conclusion

DeepVOG is a software solution for gaze estimation in neurological

and neuroscientific experiments. It incorporates a novel pupil localization and segmentation approach based on a deep fully convolutional neural network. Pupil segmentation and gaze estimates are accurate, robust, fast and repeatable, under a wide range of eye appearances. We have made DeepVOG's pupil segmentation and gaze estimation components open-source and provide it to the community as freely available software modules for standalone video-oculography, or incorporation into already existing frameworks.

In future work, we aim to incorporate a large number of images from third-party public eye datasets into training of the DeepVOG FCNN. This would extend the FCNN's generalization capability and robustness to an even wider variety of eye and pupil appearances and avoid mis-segmentations that still do occur (cf. Fig. 7). An easy-to-use graphical user interface will also be a focus of development. To this end, it is possible to integrate our segmentation part into other existing frameworks where gaze inference is based on pupil information, since DeepVOG is modularised as two parts: pupil segmentation by FCNN and gaze estimation by Świrski et al. model. Especially Pupil Labs Research (Dierkes et al., 2018), with its more realistic Le Grand eye model (Le Grand, 1968) and its Python-based open-source user interface,<sup>2</sup> serves as an inspiration to our next step of improvement.

### Acknowledgements

The study was supported by the German Federal Ministry of Education and Research (BMBF) in connection with the foundation of the German Center for Vertigo and Balance Disorders (DSGZ) (grant number 01 EO 0901), and a stipend of the Graduate School of Systemic Neurosciences (DFG-GSC 82/3; TR: Oct. 2015–Jan. 2016; Mar. 2018–Sept. 2018).

### References

- Bednarik, T., Kinnunen, A., Mihaila, P., 2005. FrSnti: Eye-Movements as a Biometric, vol. 3540, pp. 780–789.
- Ben Slama, A., Mouelhi, A., Sahli, H., Manoubi, S., Mbarek, C., Trabelsi, H., Fnaiech, F., Sayadi, M., 2017. A new preprocessing parameter estimation based on geodesic active contour model for automatic vestibular neuritis diagnosis. *Artif. Intell. Med.* 80, 48–62. <https://doi.org/10.1016/j.artmed.2017.07.005>.
- Bradley, M.M., Miccoli, L., Escrig, M.A., Lang, P.J., 2008. The pupil as a measure of emotional arousal and autonomic activation. *Psychophysiology* 45 (4), 602–607. <https://doi.org/10.1111/j.1469-8986.2008.00654.x>.
- Chen, J., Ji, Q., 2008. 3d gaze estimation with a single camera without IR illumination. 2008 19th International Conference on Pattern Recognition 1–4. <https://doi.org/10.1109/ICPR.2008.4761343>.
- Chinsatit, W., Saitoh, T., 2017. CNN-based pupil center detection for wearable gaze estimation system. *Appl. Comput. Intell. Soft Comput.* <https://doi.org/10.1155/2017/2017/8718956>.
- Dierkes, K., Kassner, M., Bulling, A., 2018. A novel approach to single camera, glint-free 3d eye model fitting including corneal refraction. *Proceedings of the 2018 ACM Symposium on Eye Tracking Research Applications, ETRA'18* 9:1–9:9.
- Fuhl, W., Kübler, T., Sippel, K., Rosenstiel, W., Kasnecki, E., 2015a. Excuse: robust pupil detection in real-world scenarios. In: Azzopardi, G., Petkov, N. (Eds.), *Computer Analysis of Images and Patterns*. Springer International Publishing, Cham, pp. 39–51.
- Fuhl, W., Santini, T.C., Kübler, T.C., Kasnecki, E., 2015b. Else: Ellipse Selection for Robust Pupil Detection in Real-World Environments. *CoRR abs/1511.06575*.
- Fuhl, W., Santini, T., Kasnecki, G., Kasnecki, E., 2016. Pupilnet: Convolutional Neural Networks for Robust Pupil Detection. *CoRR abs/1601.04902*.
- Guerrin, E.D., Eizenman, M., 2006. General theory of remote gaze estimation using the pupil center and corneal reflections. *IEEE Trans. Biomed. Eng.* 53 (6), 1124–1133.
- Hornig, W.-B., Chen, C.-Y., Chang, Y., Fan, C.-H., 2004. Driver fatigue detection based on eye tracking and dynamic template matching. *IEEE International Conference on Networking, Sensing and Control*, 2004, vol. 1 7–12. <https://doi.org/10.1109/ICNSC.2004.1297400>.
- Ishikawa, T., Baker, S., Matthews, I., Kanade, T., 2004. Passive driver gaze tracking with active appearance models. *Tech. Rep. CMU-RI-TR-04-08*. Carnegie Mellon University, Pittsburgh, PA (February).
- Koo, T., Li, M.Y., 2016. A guideline of selecting and reporting intraclass correlation coefficients for reliability research. *J. Chiropr. Med.* 15 (03). <https://doi.org/10.1016/j.jcm.2016.02.012>.
- Krafka, K., Khosla, A., Kellnhofer, P., Kannan, H., Bhandarkar, S., Matusik, W., Torralba, A., 2016. Eye tracking for everyone. *IEEE Conference on Computer Vision and Pattern Recognition (CVPR)*.
- Kumar, A., Passi, A., 2010. Comparison and combination of iris matchers for reliable personal authentication. *Pattern Recogn.* 43 (3), 1016–1026.
- Kumar, N., Kohlbecher, S., Schneider, E., 2009. A novel approach to video-based pupil tracking. 2009 IEEE International Conference on Systems, Man and Cybernetics 1255–1262. <https://doi.org/10.1109/ICSMC.2009.5345909>.
- Le Grand, Y., 1968. *Light, Colour and Vision*, 1st ed. Chapman and Hall, London, UK.
- LeCun, Y., Bengio, Y., Hinton, G., 2015. Deep learning. *Nature* 521 (7553), 436–444. <https://doi.org/10.1038/nature14539>.
- Li, D., Winfield, D., Parkhurst, D.J., 2005. Starburst: a hybrid algorithm for video-based eye tracking combining feature-based and model-based approaches. 2005 IEEE Computer Society Conference on Computer Vision and Pattern Recognition (CVPR'05) – Workshops 79. <https://doi.org/10.1109/CVPR.2005.531>.
- Liang, Z., Tan, F., Chi, Z., 2012. Video-Based Biometric Identification Using Eye Tracking Technique. pp. 728–733.
- Litjens, G., Kooi, T., Bejnordi, B.E., Setio, A.A.A., Ciompi, F., Ghafoorian, M., van der Laak, J.A., van Ginneken, B., Sñchez, C.I., 2017. A survey on deep learning in medical image analysis. *Med. Image Anal.* 42, 60–88. <https://doi.org/10.1016/j.media.2017.07.005>.
- Lohse, G.L., 1997. Consumer eye movement patterns on yellow pages advertising. *J. Advert.* 26 (1), 61–73.
- Milletari, F., Navab, N., Ahmadi, S., 2016. V-net: Fully Convolutional Neural Networks for Volumetric Medical Image Segmentation. In 2016 Fourth International Conference on 3D Vision (3DV) 565–571 IEEE.
- Moschner, C., Crawford, T.J., Heide, W., Trillenber, P., Kömpf, D., Kennard, C., 1999. Deficits of smooth pursuit initiation in patients with degenerative cerebellar lesions. *Brain* 122 (11), 2147–2158. <https://doi.org/10.1093/brain/122.11.2147>.
- Multimedia-University, 2019. MMU Iris Dataset. (accessed 20.01.19). <http://www.cs.princeton.edu/andyz/irisrecognition>.
- Naqvi, R.A., Arsalan, M., Batchuluun, G., Yoon, H.S., Park, K.R., 2018. Deep learning-based gaze detection system for automobile drivers using a NIR camera sensor. *Sensors* 18 (2). <https://doi.org/10.3390/s18020456>.
- Noh, H., Hong, S., Han, B., 2015. Learning Deconvolution Network for Semantic Segmentation. *CoRR abs/1505.04366*.
- Rehder, B., Hoffman, A.B., 2005. Eyetracking and selective attention in category learning. *Cogn. Psychol.* 51 (1), 1–41.
- Reutskaia, E., Nagel, R., Camerer, C.F., Rangel, A., 2011. Search dynamics in consumer choice under time pressure: an eye-tracking study. *Am. Econ. Rev.* 101 (2), 900–926.
- Ronneberger, O., Fischer, P., Brox, T., 2015. U-net: Convolutional Networks for Biomedical Image Segmentation. *CoRR abs/1505.04597*.
- Safaei-Rad, R., Tchoukanov, I., Smith, K.C., Benhabib, B., 1992. Three-dimensional location estimation of circular features for machine vision. *IEEE Trans. Robot. Autom.* 8 (5), 624–640. <https://doi.org/10.1109/70.163786>.
- Santini, T., Fuhl, W., Geisler, D., Kasnecki, E., 2017. Eyerectoo: Open-Source Software for Real-Time Pervasive Head-Mounted Eye Tracking. pp. 96–101.
- Satriya, T., Wibirama, S., Ardiyanto, I., 2016. Robust pupil tracking algorithm based on ellipse fitting. 2016 International Symposium on Electronics and Smart Devices (ISESD) 253–257. <https://doi.org/10.1109/ISESD.2016.7886728>.
- Schnipke, S.K., Todd, M.W., 2000. Trials and tribulations of using an eye-tracking system. *CHI'00 Extended Abstracts on Human Factors in Computing Systems, CHI EA'00*. ACM, New York, NY, USA, pp. 273–274. <https://doi.org/10.1145/633292.633452>.
- Soille, P., 2003. *Morphological Image Analysis: Principles and Applications*, 2nd ed. Springer-Verlag, Berlin, Heidelberg.
- Springenberg, J.T., Dosovitskiy, A., Brox, T., Riedmiller, M.A., 2014. Striving for Simplicity: the All Convolutional Net. *CoRR abs/1412.6806*.
- Świrski, L., Dodgson, N.A., 2013. A fully-automatic, temporal approach to single camera, glint-free 3d eye model fitting. *Proceedings of ECCEM 2013*.
- Świrski, L., Dodgson, N.A., 2014. Rendering synthetic ground truth images for eye tracker evaluation. *Proceedings of ETRA 2014* 219–222.
- Świrski, L., Bulling, A., Dodgson, N., 2012. Robust real-time pupil tracking in highly off-axis images. *Proceedings of the Symposium on Eye Tracking Research and Applications, ETRA'12* 173–176.
- Tonsen, M., Zhang, X., Sugano, Y., Bulling, A., 2015. Labeled Pupils in the Wild: A Dataset for Studying Pupil Detection in Unconstrained Environments. *CoRR abs/1511.05768*.
- Yamazoe, H., Utsumi, A., Yonezawa, T., Abe, S., 2008. Remote gaze estimation with a single camera based on facial-feature tracking without special calibration actions. *Proceedings of the 2008 Symposium on Eye Tracking Research & Applications – ETRA'08*, 1 (212) 245. <https://doi.org/10.1145/1344471.1344527>.
- Yang, G., Saniie, J., 2016. Eye tracking using monocular camera for gaze estimation applications. 2016 IEEE International Conference on Electro Information Technology (EIT) 0292–0296. <https://doi.org/10.1109/EIT.2016.7535254>.

<sup>2</sup> <https://github.com/pupil-labs/pupil>.



### **3. General discussion**

#### **3.1 Summary of the main results**

Within the scope of this thesis four projects were presented. The following paragraphs will outline the main findings of each project independently. Subsequently, the findings will be discussed with respect to known literature in a broader range.

The first study titled “IE-Map: A human in-vivo atlas template of the inner ear” focused on the inner ear structures. The combination of three imaging sequences led to the inner ear atlas (IE-Map). The IE-Map represents the first in-vivo morphologically unbiased atlas for the human inner ear describing the labyrinth and its auditory and vestibular organs using data of the largest dedicated cohort to date. It is a validated atlas comprised of all known neuroanatomical dimensions used in neuroimaging. For validation, the anatomical measurements were compared to established measurements from the literature (Lee et al., 2013). The atlas represents a unique multi-sequence structural MR imaging approach (T1-weighted, T2-weighted and constructive interference in steady state (CISS)), achieving high-resolution (0.2 mm). The approach was completely non-invasive (hence without the use of a contrast agent or application of radiation). The IE-Map is further characterized by more accurate measurements of the substructures compared to any previously published work on the topic as we did not use simplifications of substructures.

The second study presented the first human corticocortical vestibular connectome (CVC). Through the advance of recently localized vestibular regions of interest (ROI), we (1) established structural and functional corticocortical vestibular connectomes, (2) investigated their modules and common network measures, and (3) compared the human structural connectome to the one previously reported in non-human primates (using gold standard tracer injections; see Guldin & Grüsser, 1989). Our results show that the modularity of the structural corticocortical vestibular connectome of humans is extremely stable. Modules of brain regions are formed by the algorithm if those regions are more highly connected to each other compared to the other regions. Comparisons with non-human primate data revealed substantial differences in the organization across the two species. The human structural vestibular corticocortical connectome is characterized by high intrahemispheric connectivity whereas the functional one

shows a substantial synchronicity for homotopic ROIs. Overall, a laterality preference in vestibular processing can be observed for the right hemisphere: (1) with larger anatomical ROIs, (2) stronger connectivity values both structurally and functionally, and (3) higher functional vulnerability.

The third project inspected whether cortical signal fluctuations correlate with the fluctuations observed in the magnetic vestibular stimulation (MVS). It further focused on cortical connectivity represented in functional resting state networks (RSN) during MVS effect. The project was based on the indirect measurement of the physiological MVS effect using video-oculography (VOG) in complete darkness. A stimulation of the peripheral vestibular organs leads to a nystagmus through the vestibulo-ocular reflex. The mechanism that leads to these eye-movements is explained in detail in the introduction. In short, slow and fast eye-movements can be observed, called nystagmus. Unexplained fluctuations in the slow phase velocity (SPV) have been previously observed during MVS. In line with previous results (Boegle et al., 2016; Roberts et al., 2011), we found that the strength of the MVS effect is dependent on the participants head position. For receiving the exact head position, we measured the orientation of the horizontal semicircular canal (hSCC) with the established IE-Map. Yet, the orientation of the hSCC did not explain all of the observed SPV variance across subjects. A major influencing factor was the varying intersubjective sensitivity with respect to vestibular stimulation measured with caloric irrigation in our cohort. Whether the underlying cause for the intersubjective variability is of anatomical nature remains unclear.

The fourth project focused on analyzing eye-tracking videos under specific circumstances. During offline analysis of the eye-tracking videos for the MVS project, we realized that eye-tracking is often very challenging due to dilated pupils, low-light conditions, or heterogeneous light conditions throughout the measurement. Existing methods failed to track the pupil with a high accuracy in our data. We therefore established DeepVOG, a tool for VOG data analyses based on deep learning methods. Its core consists of a fully convolutional neural network model that segments and tracks the pupil. DeepVOG tracks not only the pupil center, but also detects eyeblinks. In addition, the elliptical contour can be estimated, and given enough eye-movement, the data will be automatically calibrated to output eye-movements in degrees visual angle by estimating a model of the eye. The method has been validated with another clinical gold standard system. DeepVOG is accurate and robust and it can be applied to data sets it has not been trained for. For the MVS project the DeepVOG algorithm was used for VOG analyses.

With these four multimodal projects the vestibular system was described in a way not yet presented to this date. Through improved magnetic resonance imaging methods, detailed anatomical in-vivo and non-invasive measurements of the peripheral and central structures involved in vestibular processing were realized. Further the functional influence of the MRI machine could further be investigated, and a major confound of the MVS onto rsfMRI data could be ruled out. Still, a minor effect was present that is worth further investigations.

## **3.2 Main results in context**

Improved MRI imaging with a 3T magnetic field led to novel structural and functional findings outlined in the paragraph above. The vestibular sense was characterized in further detail with non-invasive structural imaging and the influence of the magnetic field onto RSN was ruled out as a potential critical confound. Additionally, DeepVOG as a novel eye-tracking analyses algorithm will help overcome major problems in VOG data analyses. DeepVOG will only be discussed briefly in the scope of this thesis as the main focus lies on the vestibular system. In the next passages, the findings will be put in comprehensive context of previous knowledge.

### **3.2.1 Structural insights into the human peripheral vestibular system**

The structural analyses in this thesis provide knowledge about the vestibular structural organization in the periphery (IE-Map) as well as in the cortex (with the CVC). Ex-vivo micro-CT imaging (Gerber et al., 2017; Lee et al., 2013) or ex-vivo ultra-high-field MRI (Thylur, Jacobs, Go, Toga, & Niparko, 2017) provided most of our present knowledge about the peripheral vestibular system. Most of these studies suffer from a low sample size and problems that can arise in post-mortem imaging. Published in-vivo imaging approaches on the other hand, also suffer from small sample sizes, and data are collected with the use of contrast agents (Nakashima et al., 2007). We collected data in-vivo from a sizeable cohort (> 60 normal participants) for a morphologically unbiased atlas of the inner ear (IE-Map). The IE-Map is the first inner ear atlas to date with more precise and more accurate measurements of the substructures than have been reported before. Buckingham and Valvassori (2001) simplified the ampullae as spheres or the cochlea as a cone. No geometrical simplifications were used in our template; the structures themselves were used for calculating the volume of the respective substructure. In direct

comparison to these previous published measurements, our template inner ear volume was slightly overestimated, the ampullae on the other hand were underestimated in volume (Buckingham & Valvassori, 2001). We believe that the measurements of the IE-Map substructures are more accurate and realistic than previously reported. Micro-CT measurements result in a resolution of the inner ear in the  $\mu\text{m}$  range (Gerber et al., 2017; Lee et al., 2013), compared to the sub-mm range in our template. However, those studies investigate specimens ex-vivo. The IE-Map has a high resolution of 2 mm for MRI methods. More importantly, it was acquired in-vivo with multiple MRI sequences. Image collection of the inner ear structures was non-invasive, i.e. without using contrast agents. This means that the template can be applied to new images from patients or healthy subjects and used for comparison purposes. Future pending additions to the IE-Map are already being considered.

Providing the IE-Map as well as its templates as a widely applicable tool, will help gain knowledge in neuroscientific as well as clinical applications, such as neurosurgery or neuro-otology for instance. For the MVS project, the IE-Map has already been used for detection of the orientation of the hSCC. This was a core input measurement for the analyses as the orientation of the hSCC with respect to the magnetic field was used in our model to explain the strength of the MVS effect. In general, the MVS effect scales with extension of the head with respect to the magnetic field. With a head tilt towards the chest the direction of the horizontal nystagmus reverses with a null position in between (see chapter *1.3.4.1 Influencing factors for the strength of the MVS effect*).

As structural dimensions of the inner ear segments were studied, influencing factors were considered. The total intracranial volume (TIV) was found to be significantly correlated with the labyrinth parameters. Typically, gender can be revealed through the size of the inner ear (Osipov et al., 2013). Therefore, we corrected for TIV in our analyses, which revealed no gender difference in our data. Hence, TIV can be used to rule out gender differences in future studies that are interested in other influencing parameters on the anatomy of the inner ear.

### 3.2.2 Organization of the human central corticocortical vestibular connectome

The corticocortical connectome (CVC) used diffusion-weighted MRI images to map the connectivity of the cortical vestibular system. Little is known to date about the cortical organization of vestibular processing regions, in comparison to other senses. In studies investigating different senses, the vestibular sense is frequently neglected (Karolis, Corbetta, & Thiebaut de Schotten, 2019).

Evidence suggests that there is no primary vestibular cortex in the human brain, but rather a network of several brain regions responsible for stimulus processing (Guldin & Grüsser, 1998; Kirsch et al., 2018). We used ten recently defined cortical areas per hemisphere involved in vestibular processing (zu Eulenburg et al., 2018) as ROIs in the analyses of chapter 2.2 The human corticocortical vestibular connectome (for human vestibular cortical areas see additionally chapter 1.1.2.4 *Cortical vestibular areas*). These ROIs were defined via galvanic vestibular stimulation (see 1.3.3 Galvanic vestibular stimulation for details). Our results represent the first established corticocortical connectome for the vestibular system.

One of the findings of CVC revealed that vestibular information is processed in a bottom-up manner without the use of commissural fibers. Information is sent via association and projection fibers to both cortical hemispheres resulting in a high synchronicity in homotopic brain areas. Information could thereby be either spread from the vestibular nuclei in the brainstem or thalamic regions. Remarkably, the structural and functional CVC in humans were fundamentally different. Structurally, we see an intrahemispheric integrity and not many connecting fibers between the hemispheres. Functionally, a high synchronicity is observed between left and right homotopic brain areas. Interpretations have to be made with caution as structure not always leads to function and vice versa. Yet, it is essential to combine the two modalities (Zimmermann, Griffiths, & McIntosh, 2018).

Functional resting state data were acquired with eyes open and a fixation task within the CVC project. It would be worth investigating how functional vestibular network connectivity and its modularity changes in response to differences in conditions (e. g. with eyes open in complete darkness) and what role the MVS effect plays in terms of connectivity.

### 3.2.3 The magnetic field of the MRI and whether it affects the brain

For the MVS study we did not restrict our functional analyses to only vestibular regions. Therefore, we did not perform a ROI-to-ROI analyses with the vestibular defined cortical areas of zu Eulenburg et al (2018) in this project. Hence, whether modularity changes significantly due to different rsfMRI conditions remains unclear.

In the MVS project we investigated the effect of the MVS on resting state connectivity of higher cognitive regions as well as correlations of the BOLD signal and horizontal eye-movements. According to Boegle et al. (2016) the default mode network (DMN) is modulated by the MVS effect. More specifically, it modulates activity in the cerebellar vermis, anterior cingulum and calcarine sulcus. In our cohort of the MVS project, we found the MVS effect to be present via nystagmus detection in 88% of participants. In direct comparison of the MVS effect in complete darkness with a rsfMRI condition with fixation task, no differences were found in functional connectivity. Investigating the DMN in greater detail, greater connectivity values were found in the precentral gyri in complete darkness (i.e. with MVS effect presented with nystagmus). Further, lower connectivity values were found in the left pre- and postcentral gyri in complete darkness. These results are not coherent with findings of Boegle et al. (2016) as we did not find an effect of MVS within anterior cingulum and calcarine sulcus. While Boegle et al. (2016) used a theoretical change in strength of the MVS effect, our results directly relate to the SPV and to the BOLD signal in each participant. Our cortical results might therefore depict the present eye-movements or nystagmus suppression, respectively. Still, our data suffer from a high inter-subject variability which might reduce the power of our results. Future studies should consider only including participants with a high vestibular sensitivity.

With increasing values for the horizontal slow phase velocity (horSPV), activation in the cerebellar vermis was found as well. This is in line with Boegle et al (2016). In contrast, when investigating the horSPV in a between subject design, the MVS effect modulated activation in additional cortical areas: premotor cortex, right frontalorbital cortex, bilateral lateral occipital cortex, superior frontal gyri, superior parietal lobules, pars opercularis of the inferior frontal gyrus (i.e. Broca44) and left cerebellar region VIIb. However, most of the regions, except the premotor cortex, are not part of the known vestibular cortical areas (zu Eulenburg et al., 2018). Cortical activation in the frontal, precentral and parietal lobules might be due to the eye-

movements whereas vestibular stimulation might end being processed on the cerebellar level (vermis and cerebellar region VIIb).

### **3.2.4 (Cortical) laterality effects**

Our results partly support previously reported right-sided dominance in the cortical organization of the vestibular system (Brandt, 1991; Dieterich et al., 1998; Fasold et al., 2002; Kirsch et al., 2018). It has been suggested, that in right-handed participants the right hemisphere is dominant in vestibular processing. In left-handers, the left hemisphere is reported to be dominant.

In comparison to cortical results, in the peripheral vestibular system, no laterality difference was detected with detailed measurements of the inner ear structures. Since there were no laterality differences in the peripheral anatomy of our balance organ, we could mirror the left inner ear structures onto the right and therefore double the sample size from 63 pairs to 126 inner ear structures. In the cortical organization however, a right sided dominance was observable in the right-handed participants: as mentioned already, we found significantly larger anatomical ROIs, stronger connectivity values (structurally and functionally) and a higher functional vulnerability in the right hemisphere. We corrected the CVC not only for streamline length but also for node volume, so the latter two results (stronger connectivity values and higher vulnerability) were not affected by the node size. We did not investigate left-handed participants, but according to results of Dieterich et al (2003) we would expect the opposite pattern for left-handers.

For the MVS project we did not investigate laterality effects. The polarity inside the MRI scanner and the orientation of the hSCC results in bilateral stimulation and therefore a nystagmus with a principle direction. On a descriptive level, we found bilateral activation patterns that correlated with the horSPV strength between subjects (i.e. lateral occipital cortices, superior frontal gyri, superior parietal lobules, pars opercularis of the inferior frontal gyri). Whether these bilateral regions were significantly different in size or intensity cannot be answered. The only unilateral activation pattern associated with higher horSPV was in the right premotor cortex, right frontal orbital cortex, and the left cerebellar region VIIb. This pattern could be due to the rightward SPV and leftward quick phase. Whether the opposite pattern would be visible in systems with opposite polarity (or same polarity but head tilt towards the chest) remains unclear.

From a clinical point of view, it is further of interest, whether laterality differences are visible in the occurrence of symptoms (due to the lesion side) or in rehabilitation time of vertigo patients after stroke for example.

### **3.2.5 Transient symptoms due to cortical lesions**

As was pointed out in the discussion of chapter 2.2 The human corticocortical vestibular connectome (CVC) there is no chronic vestibular central disorder. Within the CVC chapter it has been discussed why this might be the case. In about 5% of patients with dizziness, imbalance or vertigo symptoms, an acute ischemic stroke is diagnosed (Kim et al., 2018). With lesions in one node or one connection of the vestibular network patients can suffer from vertigo in the acute stage after stroke (see review Brandt & Dieterich, 2017). The locations of a stroke that cause vertigo show a highly variable anatomical localization: they can be found in the parietal cortex (Naganuma et al., 2006), insular regions (Papathanasiou et al., 2006), brainstem and cerebellar regions (Kim & Lee, 2013). In the course of vestibular central disorders the symptoms are typically transient (Brandt & Dieterich, 2017). Alternative paths in a network allow robust communication flow despite a damaged site in the network: single nodes or edges can be impaired through brain damage of different etiologies, but signals can compensatively still be delivered through alternative routes within the same network (Wook Yoo et al., 2015). The robustness of the CVC was investigated and measured through the vulnerability of each node. Communication is more likely to be sent through nodes with higher betweenness centrality. If a node with high betweenness centrality is damaged this leads to a lower global efficiency and higher vulnerability, both measures of graph theoretical approaches (see 2.2 The human corticocortical vestibular connectome). As expected, with high centrality values we observed higher vulnerability. For most nodes, global efficiency did not change when a node was simulated to be damaged. Vulnerability was accumulated around 0 for most nodes of the structural connectome (between -0.05 and 0.05), as well as for most nodes of the functional connectome (between -0.01 and 0.03). There was no laterality for the structural vulnerability. So, despite the structural laterality profile, vulnerability was the same for both hemispheres. However, functional vulnerability was significantly higher for right hemispheric nodes. Leading to the conclusion that there is a difference in the occurrence of symptoms depending on the side of lesion in stroke patients. This is in line with recent findings of Eguchi et al. (2019) who

report that right sided lesions cause vestibular symptoms more frequently than left sided lesions. Further, Abe and colleagues (2012) reported longer rehabilitation time in the Pusher Syndrome (a disorder of postural balance that manifests as a pushing away toward the contralesional side in unilateral stroke) following right hemispheric lesions. Whether there is a general difference in remission of vestibular symptoms depending on the lesion site needs to be further investigated by comparing vulnerability profiles of the nodes with lesion mapping and vestibular symptom status.

The high vulnerability values for premotor and supplementary motor area (SMA) in the structural connectome are noteworthy. These nodes are important for the structural connectome to keep the global efficiency high. Though, the functional vulnerability was the lowest for SMA and not exceptional high for premotor regions. In general, all vulnerability values were relatively low, and we cannot state whether lesions in specific nodes of the network are more likely to resolve in vertigo symptoms. But in the case of symptoms, the high intrahemispheric structural connectivity might help to overcome these symptoms generated from stroke or other etiologies. In the acute state, functional synchronicity might be reduced between homotopic regions leading to vertigo symptoms. Depending on which edge or node is damaged, this information flow can be rebuilt through an alternative route. The structural corticocortical network with the detected modules forms a good basis for this. We can only claim this for corticocortical vestibular connections. Whether the same holds true for corticothalamic, corticocerebellar and corticospinal connections is unclear.

### **3.2.6 Comparative neuroanatomy**

As mentioned in the introduction and the corticocortical vestibular connectome project (2.2 The human corticocortical vestibular connectome), comparative studies gain attention for answering basic research questions. Studies have compared the inner ear structures across different species (e.g. Gunz, Ramsier, Kuhrig, Hublin, & Spoor, 2012). As our established IE-Map of the human inner ear is freely available, it can easily be used for future comparative studies (see 3.5.4 Clinical and comparative studies for further discussion).

Comparing the cortical structures and vestibular connectome across species, was one of the goals of the CVC project. Besides the comparison of functional and structural connectomes in humans, we investigated differences between the structural connectomes of humans and

monkeys (Guldin & Grüsser, 1998). Outstanding was the structural difference in connections of the macaques' PIVC and the human pendant OP2. Whereas the PIVC was densely connected with other brain regions of the vestibular network, human area OP2 was only scarcely connected within the vestibular network. This would either mean (1) that human area OP2 is not the right pendant to PIVC, (2) that PIVC is a core region in monkeys and lost its importance in humans, or that (3) DW imaging is not able to depict the ground truth of fiber connections (as measured with tracer injections for instance). Functionally, however, human OP2 is well interconnected and shares more similarities with the monkeys' structural connectome. As already mentioned, structural connections not always resolve in functional synchronicity, so interpretations have to be made with caution. In general, the method of diffusion weighted imaging (DWI) needs to be seen in a critical light and results have to be interpreted with caution. Despite the big opportunity of streamline imaging, DWI faces some obstacles that will be addressed in the limitations section of the discussion.

Concerning the MVS effect, there are no studies directly comparing two or more species with each other. However animal studies have shown that the utricle plays a critical role in the MVS effect (Ward et al., 2018). Genetically modified mice with missing otoconia led to an absence of MVS effect with VOR-function remaining intact. At the current state, we did not include utricle measurements as regressors into the analyses of the MVS manuscript. Differences among participants onto the strength of the MVS effect could lie in the utricle but today's resolution of MRI imaging with a 3T machine is too poor to detect details about the otoconia.

### **3.3 Methodological considerations**

#### **3.3.1 Limitations due to spatial resolution and location precision**

Despite technical improvements in neuroimaging, visualizing structural data with non-invasive imaging methods remains approximate at best. Our and other in-vivo imaging approaches of the peripheral vestibular system lack the visualization of small membranous structures like the organ of Corti that lies inside the cochlea or the hair cells (see chapter 1.1.1 Peripheral vestibular system). Ultra-high field MRI already overcomes these obstacles in some sense with a resolution in the  $\mu\text{m}$  range (Thylur et al., 2017). The authors were able to visualize the ampullae and the maculae in clearer detail than ever before using a 11.7 T MRI. However, visualization of the hair cells in-vivo, for instance, is still far out of reach with today's imaging technologies. The same

holds true for the spatial resolution of DWI and its structural connectivity analyses. Fiber orientation can be estimated but the organization and orientations of the fibers cannot be directly measured with the in-vivo imaging techniques available for human experiments. We estimated fiber orientations through water diffusion at a resolution just below  $2\text{mm}^3$  and therefore results lack precision because the actual thickness of fibers is in the nanometer range. More research is needed comparing tracer studies with DWI studies within the same species and across species to determine whether biases exist in estimating fiber organization with DWI. Spatial dimension is also a limiting factor for the DeepVOG analysis method for video-oculography (VOG). With the well-established online and offline analyses methods, eye movement components can be measured in two dimensions. However, the eye can move in one additional dimension, i.e. torsion. Torsion is much more complicated to estimate. Common methods for determining torsional eye-movements involve temporary markers placed on the sclera, magnetic search coils worn on the eye, or matching the pattern of the iris to a template if high-resolution video information is available. Search coils can be painful to wear which increases the drop-out rate. Dilated pupils or heterogeneous lighting make extraction of torsional information with the other methods especially difficult. Scleral markers tend to vanish shortly after application due to blinking or physiological fluid in the eye. The focal range of the camera is another limitation as the iris or scleral markers must be in focus the entire time for accurate torsional measurements. Future methodological advancements are necessary to reliably detect the torsional component of the eyeball (see 3.5.1 The vestibular system and neighboring structures).

A number of assumptions are made for the DeepVOG network to successfully analyze the data. The DeepVOG algorithm estimates the direction of gaze by analyzing the ellipsoid of the pupil and estimating the center of rotation. This method assumes that the pupil is perfectly circular and that the eyeball is a sphere. Both are not always true. An analysis of the variability of eye shapes and the influence it has on the model would lead to a more accurate gaze direction estimation.

### 3.3.2 Other methodological limitations

Young healthy participants were exclusively recruited for all of the projects presented in this thesis. Therefore, important hypotheses that we would like to make about the diseased vestibular system or vertigo patients (as in 3.2.5 Transient symptoms due to cortical lesions), cannot be made. In healthy, young participants, vHIT does not seem to be a very good measurement of vestibular sensitivity, as ceiling effects occurs. In our cohort in the MVS project, gains in the vHIT ranged around 1. Gains below and above 1 have been observed in normal healthy subjects previously (Janky et al., 2017). The question remains why so many normal participants show gains above 1. Physiologically, a gain above 1 means that the velocity of the compensatory eye-movement after a head movement is greater than the head movement velocity during the head impulse test. Gains above 1 could be due to noise. Slippage of the head-mounted camera system could lead to gains above 1 during vHIT. In general, more studies on the variability of vestibular sensitivity in normal participants measured with the current vestibular diagnostic tests would be desirable as well as a reduction in measurement noise.

## 3.4 Technical strengths

### 3.4.1 MRI

It is worth emphasizing that the data quality of projects presented in this thesis is as high as we can currently acquire in terms of data collection, pre- and postprocessing at 3 Tesla. In all imaging studies, we minimized head motion via a dedicated head fixation device (<sup>®</sup>Pearltec Crania adult, Schlieren, Switzerland). We used physiological nuisance regressors (motion and cardiac parameters) as well as denoising steps to improve the fMRI data quality. Despite the mentioned limitations of DWI, it is the only available method for detecting fiber orientation in-vivo in the human brain so far. The quality of the acquired data was set to the highest standards available at the time of data collection with a 3T MRI machine. We chose multiple shells (i.e. 3), 10 non-diffusion and 150 direction encoding scans to improve sensitivity of the fiber orientation. Other very recently published DWI studies often use less shells, less b-values as well as less diffusion gradients: Horbruegger et al. (2019), for instance, used 2 shells with  $b_1=800$  s/mm<sup>2</sup>,  $b_2=1200$  s/mm<sup>2</sup> and 60 direction encoding scans. Additionally, in our data, a second inverted DWI sequence was collected to reduce susceptibility-induced distortions. We further increased

temporal and spatial resolution by using a multiband image acquisition method. Preprocessing involved selecting only high quality data using the MRI Quality Control tool (MRIQC, Version 0.9.6) across the projects (Esteban et al., 2017).

### **3.4.2 Eye-tracking improvements**

Within the presented DeepVOG paper (see chapter 2.4 Pupil segmentation and gaze estimation using deep learning (DeepVOG)), different methods for calibrating the eye-tracking analysis to degrees visual angle were compared and validated. The standard 5-point calibration (“narrow-ranged”) which involves providing set visual fixation points at a known visual angle, was compared to calibration with a stable head and wandering gaze (“free-looking”), and fixation of an object/dot while moving the head in a circular manner (“CalibMe” by Santini et al. (2017)). “CalibMe” outperformed the other methods and should be considered in future studies. It makes calibration of eye-tracking devices easier than ever before as no explicit visual presentation is necessary. The only prerequisite is that the participant or patient can move his or her head in a relatively large radius. The DeepVOG algorithm can be generalized to other datasets it has not been trained for and is publicly available.

The confidence values of the DeepVOG algorithm were used to detect sleep in the MVS project. In darkness on average a third of participants fall asleep after 4 minutes of rsfMRI (Tagliazucchi & Laufs, 2014). In the MVS project, only 20% of participants were asleep after 5 minutes of scanning (see section 2.3 Magnetic vestibular stimulation). It is of major interest to detect sleep in rsfMRI studies as resting state networks change between sleep and wakefulness (e.g. Fukunaga et al., 2006). With regular online eye-tracking methods sleep might not be captured. Algorithms typically search for the darkest spot and once eyes are closed this might be the eyelashes for example. With our method a confidence for the pupil center was received and blinks as well as closed eyes could therefore easily be detected.

### 3.4.3 Vestibular stimulation

MVS was introduced as the only pure vestibular stimulation in the introduction (see 1.3.4.2 *MVS as unimodal bilateral stimulation of the vestibular system*). Even though we were able to see the MVS effect in 88% of our participants, we could not detect significant differences in functional connectivity between rsfMRI measures with MVS and rsfMRI with nystagmus suppression through fixation. Either the MVS effect is too small with a 3 T MRI, or it is cancelled out in subcortical areas and therefore has no cortical effect. As the MVS effect did not lead to a sensory percept in participants, it is hypothesized that the effect is cancelled out in lower infratentorial brain areas. In the MVS project, painless GVS was used to descriptively compare activated brain regions between GVS and MVS. It would be interesting to see whether a GVS stimulus below threshold would result in the picture seen with MVS or whether the MVS effect in higher field strength MRIs results in a similar activation pattern as GVS. Whether magnetic fields of higher Tesla MRI scanners might be able to elicit stronger maybe even subjectively perceivable MVS effects via nystagmus needs to be clarified.

GVS, in contrast to MVS, stimulates the vestibular organ in the periphery with a perceptual outcome; participants have the feeling of being tilted or moved. Different stimuli can be chosen and can be varied in intensity without pain perception if anesthetics are used. Most published GVS studies, however, do not use topical anesthetics before the experiment (e.g. Fujimoto et al., 2019; Javaid, Chouhna, Varghese, Hammam, & Macefield, 2019). Yet, with the reduced skin discomfort through lidocaine for example a cleaner vestibular signal is received. GVS has evolved into a very important method for vestibular research (see review by Dlugaiczyk et al., 2019) and was directly and indirectly used within the projects in this thesis. GVS elicits a natural perception of head and/or body tilt, especially with sinusoidal stimuli (Dlugaiczyk et al., 2019). Zu Eulenburg and colleagues (2018) have defined a vestibular cortical atlas by means of GVS during fMRI. We used these regions as basis for the CVC project.

## **3.5 Future work**

### **3.5.1 The vestibular system and neighboring structures**

Future work should focus on the interaction of the visual and ocular-motor with the vestibular sense due to the mentioned convergence on the brain stem level (Boyle et al., 1996; Sekirnjak & du Lac, 2006; Waespe & Henn, 1977) and the visual activation and connectivity patterns seen in the MVS study.

With the vestibulo-ocular reflex a vestibular and ocular motor interaction is very nicely observable for instance (see chapter 1.2 Reflexive eye-movements as a window to the vestibular sense). Adding the eye-muscles to the IE-Map atlas could advance our understanding of this relationship. The orientation of the muscles together with the canal orientation might answer clinical and basic research questions. It might detect further insights in the relation of the two structures and might potentially answer variability in vestibular sensitivity.

Previous work already investigated coplanarity of the functional SCC pairs (Kim et al., 2015) and individual anatomical differences (Della Santina et al., 2005). Within the MVS project (that was using the IE-Map) a bigger variability in hSCC orientation with respect to Reid's plane was observable (see figure 3a of the MVS manuscript). The orientation angles of the functional SCC pairs were not added to the IE-Map yet but could be realized in parallel with including the eye-muscles. This augmentation could further increase clinical relevance and further address the variance of planarity of the functional SCC pairs across participants.

Besides adding the eye-muscles and canal orientations to the IE-Map, the afferent fibers of the vestibular system should further be added to it. This could have clinical relevance. Data could potentially reveal nerve compressions for instance when comparing it to the template. The facial nerve could be added along this step as it runs in close proximity.

Because of the strong interaction between visual and vestibular sensory modalities, it is of special interest how the visual and the vestibular corticocortical connectomes interact or change their interaction due to different tasks. Functional connectivity might change due to visual tasks or vestibular stimulation. Combining the two modalities should be focus of future research. With imaging, this can be realizable with specific vestibular stimulations (GVS for instance), visual stimulations and their combination.

### 3.5.2 Adding a third dimension to DeepVOG

When it comes to adding features to projects, another dimension can be added to the DeepVOG project. Besides the mentioned gaze direction estimation, the published DeepVOG algorithm (Yiu et al., 2019) results in horizontal and vertical components of the eye-movements. Future work will focus on implementing the third, torsional, dimension: DeepVOG-3D. With an iris recognition pattern, torsional eye-movements will be depictable without scleral markers. The pattern of the iris will be monitored and through the extracted band of the iris pattern and a neural network (training data has already been labelled), robust open-source torsional eye-tracking algorithm will be available in the near future. As no markers are needed to be placed onto the eye, this method is more tolerable for participants. Especially for GVS, torsional component is of major interest as mainly horizontal and torsional eye-movements are observed due to the stimulation (MacDougall et al., 2003).

### 3.5.3 Individual differences

For the peripheral vestibular system, an analysis of the individual differences in SCC orientation are desirable. Few studies have looked at these differences so far (Della Santina et al., 2005). The data of Roberts and colleagues (2011) and the presented MVS project (see chapter 1.3.4 Magnetic vestibular stimulation and 2.3 Magnetic vestibular stimulation and its effect on brain networks) suggest that the individual differences play a critical role in the MVS effect. In comparison to Della Santina et al. (2005) a bigger variability was detected in hSCC orientation with respect to Reid's plane in the MVS project. The angle between Reid's plane and hSCC ranged from  $-22^{\circ}$  to  $7^{\circ}$  with a mean of  $-8^{\circ} \pm 6^{\circ}$ . Della Santina et al. investigated patients (aged  $48 \pm 15$  years) that had taken a CT due to different indications and found the hSCC-Reid's plane difference to be  $19.9^{\circ} \pm 7.0^{\circ}$ . Our cohort however consisted of young healthy adults and structural MRI images were taken. The angle differences between their and our results most likely not result because of health status, age nor the imaging method used. Most likely the differences occur because of the manually labelling of the Reid's plane. Future studies should consider a larger number of raters when investigating individual differences.

Not only anatomically, but additionally in a functional perspective more studies are needed to investigate individual differences. Across healthy subjects an intersubjective variability onto vestibular testing was observed in the MVS project. Whereas some participants only respond

mildly to caloric irrigation, others responded strongly to the stimulation. We did not find significant correlations of the caloric irrigation with motion sickness scores nor general physical activity values (retrieved through questionnaires). What causes these functional differences is still up for debate. It has been suggested over half a decade ago that caloric response might be modulated by the otoliths (Coats & Smith, 1967). Interestingly, the utricle is also mentioned to be an influencing factor for the MVS effect (studied in genetically modified mice by Ward et al., 2018). The exact influence of the otoliths onto the VOR is still not resolved. Individual differences in sensitivity to vestibular cues could hypothetically also result from the orientation of the cupula inside of the ampullae, or even the hair cell orientation. Future work is required to shed light on this matter.

#### **3.5.4 Clinical and comparative studies**

From a clinical and evolutionary point of view, more studies on the vestibular system in health and disease are desirable, as well as cross-species comparisons. Future research on disease connectomics should, for instance, investigate the functional synchronicity in the acute and the post-acute stages of stroke patients with or without vanishing vertigo symptoms over time. In chapter 3.2.5 Transient symptoms due to cortical lesions, it was already hypothesized that most likely functional synchronicity is rehabilitated in chronic stages leaving no vestibular symptoms behind. This should be tested in a longitudinal disease connectomics study.

Further, with the CVC developed here, we can begin to address differences in the structural and functional CVC in vestibular patient populations (e.g. Menière's disease, functional dizziness). In functional dizziness patients, changes in functional connectivity of the insular cortex can be observed despite the absence of cerebral structural changes (Indovina et al., 2015). Whether and how the entire CVC changes in these patient populations should be addressed by future studies.

Cross-species comparisons with more evolutionarily similar animals to humans are wished for. Fundamental differences in hair cells between humans and fish or amphibians make comparisons difficult, although the information gleaned from these species is still highly important for understanding the vestibular system (see *1.1.1.2 Mechanoreceptive hair cells*). Reptiles, birds and mammals have both type I and type II hair cells, which may improve comparability. Birds, however, have a slightly different anatomy in the inner ear in comparison

to humans (lagena – another inner ear structure- instead of cochlea). Still both species have three SCC (Benson, Starmer-Jones, Close, & Walsh, 2017). Comparing species revealed fundamental differences about vestibular afferents between mice and monkeys as mice show lower sensitivities to head velocity (Cullen, Chen-Huang, & McCrea, 1993; Cullen & McCrea, 1993). Differences in head velocity and acceleration between bipeds and quadrupeds should not be neglected in future studies.

More studies that compare non-human primate research to human research would answer some important questions about cortical processing. Most of our knowledge considering subcortical vestibular processing is retrieved from animal studies with monkeys (Lang et al., 1979; Marlinski & McCrea, 2008; Meng et al., 2007). For translating the results of tracer studies onto the human organism, more insights are needed. Also, more within-species comparisons of tracer injection and DWI data are necessary to validate DWI study results (e.g. Schilling et al., 2019).

## 4. Conclusion

This work provides a broad and fundamental contribution to basic vestibular research. The openly available morphologically unbiased atlas of the inner ear that was established here has several clinical and scientific purposes. Similarly, we were able to improve offline eye-tracking analyses via deep-learning, that is versatile enough to track the pupil in various eye-position and lighting situations and that is also now open source. This has the potential to improve eye-tracking methods in low lighting situations or with reflections such as glasses. We characterized the first corticocortical vestibular connectome and show that structural and functional connectivity information are complementary and not completely overlapping. Finally, we show that the MVS effect is maintained during fMRI but that if there are any effects on resting state activity, they are likely to be small.

## References

- Abe, H., Kondo, T., Oouchida, Y., Suzukamo, Y., Fujiwara, S., & Izumi, S.-I. (2012). Prevalence and length of recovery of pusher syndrome based on cerebral hemispheric lesion side in patients with acute stroke. *Stroke*, *43*(6), 1654–1656.  
<https://doi.org/10.1161/STROKEAHA.111.638379>
- Ahmadi, S.-A., Raiser, T., Ruehl, R. M., Flanagan, V., & Eulenburg, P. zu. (2019). IE-Map: A novel in-vivo atlas template of the human inner ear. *MedRxiv Preprint*, 19011908.  
<https://doi.org/10.1101/19011908>
- Angelaki, D. E., & Dickman, J. D. (2000). Spatiotemporal processing of linear acceleration: Primary afferent and central vestibular neuron responses. *Journal of Neurophysiology*, *84*(4), 2113–2132. <https://doi.org/10.1152/jn.2000.84.4.2113>
- Angelaki, D. E., & Hess, B. J. (1994). The cerebellar nodulus and ventral uvula control the torsional vestibulo-ocular reflex. *Journal of Neurophysiology*, *72*(3), 1443–1447.  
<https://doi.org/10.1152/jn.1994.72.3.1443>
- Ango, F., & Dos Reis, R. (2019). Sensing how to balance. *ELife*, *8*, e46973.  
<https://doi.org/10.7554/eLife.46973>
- Aw, S. T., Todd, M. J., & Halmagyi, G. M. (2006). Latency and Initiation of the Human Vestibuloocular Reflex to Pulsed Galvanic Stimulation. *Journal of Neurophysiology*, *96*(2), 925–930. <https://doi.org/10.1152/jn.01250.2005>
- Babu, S., Schutt, C. A., & Bojrab, D. I. (2019). *Diagnosis and Treatment of Vestibular Disorders*. Springer.
- Balmer, T. S., & Trussell, L. O. (2019). Selective targeting of unipolar brush cell subtypes by cerebellar mossy fibers. *ELife*, *8*. <https://doi.org/10.7554/eLife.44964>
- Bárány, R. (1906). *Untersuchungen über den vom Vestibularapparat des Ohres reflektorisch ausgelösten rhythmischen Nystagmus und seine Begleiterscheinungen*. Coblentz: Oscar.
- Barmack, N. H. (2003). Central vestibular system: Vestibular nuclei and posterior cerebellum. *Brain Research Bulletin*, *60*(5–6), 511–541. [https://doi.org/10.1016/s0361-9230\(03\)00055-8](https://doi.org/10.1016/s0361-9230(03)00055-8)
- Barmack, N. H., & Yakhnitsa, V. (2013). Vestibulocerebellar Connections. In M. Manto, J. D. Schmähmann, F. Rossi, D. L. Gruol, & N. Koibuchi (Eds.), *Handbook of the Cerebellum and Cerebellar Disorders* (pp. 357–375). [https://doi.org/10.1007/978-94-007-1333-8\\_18](https://doi.org/10.1007/978-94-007-1333-8_18)
- Barrett, K. E., Barman, S. M., Boitano, S., & Brooks, H. L. (2012). Chapter 10: Hearing & Equilibrium. In *Ganong's review of medical physiology* (24th ed.). New York: McGraw-Hill.
- Behrman, W. (1942). Über Indifferenzlagen und Nystagmusgebiete.: II. Versuche mit horizontal liegenden, nach einseitiger kalorischer Reizung um ihre Längsachse rotierten Personen. *Acta Oto-Laryngologica*, *30*(4), 298–310.  
<https://doi.org/10.3109/00016484209124178>
- Bense, S., Stephan, T., Yousry, T. A., Brandt, T., & Dieterich, M. (2001). Multisensory Cortical Signal Increases and Decreases During Vestibular Galvanic Stimulation (fMRI). *Journal of Neurophysiology*, *85*(2), 886–899. <https://doi.org/10.1152/jn.2001.85.2.886>
- Benson, R. B. J., Starmer-Jones, E., Close, R. A., & Walsh, S. A. (2017). Comparative analysis of vestibular ecomorphology in birds. *Journal of Anatomy*, *231*(6), 990–1018.  
<https://doi.org/10.1111/joa.12726>

- Bent, L. R., Bolton, P. S., & Macefield, V. G. (2006). Modulation of muscle sympathetic bursts by sinusoidal galvanic vestibular stimulation in human subjects. *Experimental Brain Research*, 174(4), 701–711. <https://doi.org/10.1007/s00221-006-0515-6>
- Blair, E. A., & Erlanger, J. (1933). A comparison of the characteristics of axons through their individual electrical responses. *American Journal of Physiology-Legacy Content*, 106(3), 524–564. <https://doi.org/10.1152/ajplegacy.1933.106.3.524>
- Boegle, R., Stephan, T., Ertl, M., Glasauer, S., & Dieterich, M. (2016). Magnetic vestibular stimulation modulates default mode network fluctuations. *NeuroImage*, 127, 409–421. <https://doi.org/10.1016/j.neuroimage.2015.11.065>
- Boyle, R., Belton, T., & McCrea, R. A. (1996). Responses of identified vestibulospinal neurons to voluntary eye and head movements in the squirrel monkey. *Annals of the New York Academy of Sciences*, 781, 244–263. <https://doi.org/10.1111/j.1749-6632.1996.tb15704.x>
- Boyle, R., Büttner, U., & Markert, G. (1985). Vestibular nuclei activity and eye movements in the alert monkey during sinusoidal optokinetic stimulation. *Experimental Brain Research*, 57(2), 362–369. <https://doi.org/10.1007/BF00236542>
- Brandt, T. (1991). *Vertigo: Its Multisensory Syndromes*. <https://doi.org/10.1007/978-1-4471-3342-1>
- Brandt, T., Dieterich, M., & Danek, A. (1994). Vestibular cortex lesions affect the perception of verticality. *Annals of Neurology*, 35(4), 403–412. <https://doi.org/10.1002/ana.410350406>
- Brandt, Thomas, & Dieterich, M. (2017). The dizzy patient: Don't forget disorders of the central vestibular system. *Nature Reviews. Neurology*, 13(6), 352–362. <https://doi.org/10.1038/nrneurol.2017.58>
- Bremmer, F., Klam, F., Duhamel, J.-R., Ben Hamed, S., & Graf, W. (2002). Visual-vestibular interactive responses in the macaque ventral intraparietal area (VIP). *The European Journal of Neuroscience*, 16(8), 1569–1586. <https://doi.org/10.1046/j.1460-9568.2002.02206.x>
- Buckingham, R. A., & Valvassori, G. E. (2001). Inner ear fluid volumes and the resolving power of magnetic resonance imaging: Can it differentiate endolymphatic structures? *The Annals of Otolaryngology, Rhinology, and Laryngology*, 110(2), 113–117. <https://doi.org/10.1177/000348940111000204>
- Büttner, U., & Büttner, U. W. (1978). Parietal cortex (2v) neuronal activity in the alert monkey during natural vestibular and optokinetic stimulation. *Brain Research*, 153(2), 392–397. [https://doi.org/10.1016/0006-8993\(78\)90421-3](https://doi.org/10.1016/0006-8993(78)90421-3)
- Büttner-Ennever, J. A. (1999). A review of otolith pathways to brainstem and cerebellum. *Annals of the New York Academy of Sciences*, 871, 51–64. <https://doi.org/10.1111/j.1749-6632.1999.tb09175.x>
- Chen, A., DeAngelis, G. C., & Angelaki, D. E. (2010). Macaque Parieto-Insular Vestibular Cortex: Responses to Self-Motion and Optic Flow. *Journal of Neuroscience*, 30(8), 3022–3042. <https://doi.org/10.1523/JNEUROSCI.4029-09.2010>
- Chen-Huang, C., & McCrea, R. A. (1999). Effects of viewing distance on the responses of horizontal canal-related secondary vestibular neurons during angular head rotation. - PubMed—NCBI. *Journal of Neurophysiology*, 81(5), 2517–2537.
- Coats, A. C., & Smith, S. Y. (1967). Body position and the intensity of caloric nystagmus. *Acta Oto-Laryngologica*, 63(6), 515–532. <https://doi.org/10.3109/00016486709128785>
- Cohen, B., Martinelli, G. P., Ogorodnikov, D., Xiang, Y., Raphan, T., Holstein, G. R., & Yakushin, S. B. (2011). Sinusoidal galvanic vestibular stimulation (sGVS) induces a vasovagal

- response in the rat. *Experimental Brain Research*, 210(1), 45–55.  
<https://doi.org/10.1007/s00221-011-2604-4>
- Cohen, B., Martinelli, G. P., Xiang, Y., Raphan, T., & Yakushin, S. B. (2017). Vestibular Activation Habituates the Vasovagal Response in the Rat. *Frontiers in Neurology*, 8, 83.  
<https://doi.org/10.3389/fneur.2017.00083>
- Cullen, K. E., Chen-Huang, C., & McCrea, R. A. (1993). Firing behavior of brain stem neurons during voluntary cancellation of the horizontal vestibuloocular reflex. II. Eye movement related neurons. *Journal of Neurophysiology*, 70(2), 844–856.  
<https://doi.org/10.1152/jn.1993.70.2.844>
- Cullen, K. E., & McCrea, R. A. (1993). Firing behavior of brain stem neurons during voluntary cancellation of the horizontal vestibuloocular reflex. I. Secondary vestibular neurons. *Journal of Neurophysiology*, 70(2), 828–843. <https://doi.org/10.1152/jn.1993.70.2.828>
- Cullen, Kathleen E. (2008). Procedural learning: VOR. In *Memory Systems. Learning and Memory: A Comprehensive Reference* (Vol. 3, pp. 383–402). Oxford: Academic Press/Elsevier.
- Cullen, Kathleen E. (2012). The vestibular system: Multimodal integration and encoding of self-motion for motor control. *Trends in Neurosciences*, 35(3), 185–196.  
<https://doi.org/10.1016/j.tins.2011.12.001>
- Curthoys, I. S., & MacDougall, H. G. (2012). What Galvanic Vestibular Stimulation Actually Activates. *Frontiers in Neurology*, 3. <https://doi.org/10.3389/fneur.2012.00117>
- Della Santina, C. C., Potyagaylo, V., Migliaccio, A. A., Minor, L. B., & Carey, J. P. (2005). Orientation of Human Semicircular Canals Measured by Three-Dimensional Multiplanar CT Reconstruction. *Journal of the Association for Research in Otolaryngology*, 6(3), 191–206. <https://doi.org/10.1007/s10162-005-0003-x>
- Demer, J. L., Goldberg, J., Jenkins, H. A., & Porter, F. I. (1987). Vestibulo-ocular reflex during magnified vision: Adaptation to reduce visual-vestibular conflict. *Aviation, Space, and Environmental Medicine*, 58(9 Pt 2), A175-179.
- Dickman, J. D., & Angelaki, D. E. (2002). Vestibular convergence patterns in vestibular nuclei neurons of alert primates. *Journal of Neurophysiology*, 88(6), 3518–3533.  
<https://doi.org/10.1152/jn.00518.2002>
- Dieterich, M., Bense, S., Lutz, S., Drzezga, A., Stephan, T., Bartenstein, P., & Brandt, T. (2003). Dominance for Vestibular Cortical Function in the Non-dominant Hemisphere. *Cerebral Cortex*, 13(9), 994–1007. <https://doi.org/10.1093/cercor/13.9.994>
- Dieterich, M., Bucher, S. F., Seelos, K. C., & Brandt, T. (1998). Horizontal or vertical optokinetic stimulation activates visual motion-sensitive, ocular motor and vestibular cortex areas with right hemispheric dominance. An fMRI study. *Brain: A Journal of Neurology*, 121 (Pt 8), 1479–1495. <https://doi.org/10.1093/brain/121.8.1479>
- Dits, J., Houben, M. M. J., & van der Steen, J. (2013). Three Dimensional Vestibular Ocular Reflex Testing Using a Six Degrees of Freedom Motion Platform. *Journal of Visualized Experiments : JoVE*, (75). <https://doi.org/10.3791/4144>
- Dlugaiczek, J., Gensberger, K. D., & Straka, H. (2019). Galvanic vestibular stimulation: From basic concepts to clinical applications. *Journal of Neurophysiology*, 121(6), 2237–2255.  
<https://doi.org/10.1152/jn.00035.2019>
- Doeller, C. F., Barry, C., & Burgess, N. (2010). Evidence for grid cells in a human memory network. *Nature*, 463(7281), 657–661. <https://doi.org/10.1038/nature08704>
- Dow, R. S. (1936). The fiber connections of the posterior parts of the cerebellum in the rat and cat. *Journal of Comparative Neurology*, 63(3), 527–548.  
<https://doi.org/10.1002/cne.900630308>

- Eatock, R. A., & Hurley, K. M. (2003). Functional Development of Hair Cells. In *Current Topics in Developmental Biology* (Vol. 57, pp. 389–448). [https://doi.org/10.1016/S0070-2153\(03\)57013-2](https://doi.org/10.1016/S0070-2153(03)57013-2)
- Ebata, S., Sugiuchi, Y., Izawa, Y., Shinomiya, K., & Shinoda, Y. (2004). Vestibular projection to the periarculate cortex in the monkey. *Neuroscience Research*, *49*(1), 55–68. <https://doi.org/10.1016/j.neures.2004.01.012>
- Eguchi, S., Hirose, G., & Miaki, M. (2019). Vestibular symptoms in acute hemispheric strokes. *Journal of Neurology*, *266*(8), 1852–1858. <https://doi.org/10.1007/s00415-019-09342-9>
- Eichenbaum, H. (2017). The role of the hippocampus in navigation is memory. *Journal of Neurophysiology*, *117*(4), 1785–1796. <https://doi.org/10.1152/jn.00005.2017>
- Eickhoff, S. B., Weiss, P. H., Amunts, K., Fink, G. R., & Zilles, K. (2006). Identifying human parieto-insular vestibular cortex using fMRI and cytoarchitectonic mapping. *Human Brain Mapping*, *27*(7), 611–621. <https://doi.org/10.1002/hbm.20205>
- Ertl, M., Moser, M., Boegle, R., Conrad, J., Zu Eulenburg, P., & Dieterich, M. (2017). The cortical spatiotemporal correlate of otolith stimulation: Vestibular evoked potentials by body translations. *NeuroImage*, *155*, 50–59. <https://doi.org/10.1016/j.neuroimage.2017.02.044>
- Esteban, O., Birman, D., Schaer, M., Koyejo, O. O., Poldrack, R. A., & Gorgolewski, K. J. (2017). MRIQC: Advancing the automatic prediction of image quality in MRI from unseen sites. *PloS One*. <https://doi.org/10.1371/journal.pone.0184661>
- Ewald, J. (1882). *Physiologische Untersuchungen über das Endorgan des Nervus octavus*. Wiesbaden: Bergmann.
- Fasold, O., von Brevern, M., Kuhberg, M., Ploner, C. J., Villringer, A., Lempert, T., & Wenzel, R. (2002). Human Vestibular Cortex as Identified with Caloric Stimulation in Functional Magnetic Resonance Imaging. *NeuroImage*, *17*(3), 1384–1393. <https://doi.org/10.1006/nimg.2002.1241>
- Fedorov, A., Beichel, R., Kalpathy-Cramer, J., Finet, J., Fillion-Robin, J. C., Pujol, S., ... Kikinis, R. (2012). 3D Slicer as an image computing platform for the Quantitative Imaging Network. *Magnetic Resonance Imaging*, *30*(9), 1323–1341. <https://doi.org/10.1016/j.mri.2012.05.001>
- Fetsch, C. R., Wang, S., Gu, Y., Deangelis, G. C., & Angelaki, D. E. (2007). Spatial reference frames of visual, vestibular, and multimodal heading signals in the dorsal subdivision of the medial superior temporal area. *The Journal of Neuroscience: The Official Journal of the Society for Neuroscience*, *27*(3), 700–712. <https://doi.org/10.1523/JNEUROSCI.3553-06.2007>
- Finby, N., & Chynn, K.-Y. (1982). Cranial Computerized Tomography: Technique and Anatomy. In *Manual of Cranial Computerized Tomography* (pp. 15–29). <https://doi.org/10.1159/000406259>
- Frenzel, H. (1956). Practical methods of a systematic study of otorhinolaryngology. *Münchener medizinische Wochenschrift*, *98*(29), 972–975.
- Fujimoto, C., Kinoshita, M., Kamogashira, T., Egami, N., Kawahara, T., Uemura, Y., ... Iwasaki, S. (2019). Noisy galvanic vestibular stimulation has a greater ameliorating effect on posture in unstable subjects: A feasibility study. *Scientific Reports*, *9*(1), 17189. <https://doi.org/10.1038/s41598-019-53834-7>
- Fukunaga, M., Horovitz, S. G., van Gelderen, P., de Zwart, J. A., Jansma, J. M., Ikonomidou, V. N., ... Duyn, J. H. (2006). Large-amplitude, spatially correlated fluctuations in BOLD

- fMRI signals during extended rest and early sleep stages. *Magnetic Resonance Imaging*, 24(8), 979–992. <https://doi.org/10.1016/j.mri.2006.04.018>
- Gdowski, G. T., & McCrea, R. A. (2000). Neck proprioceptive inputs to primate vestibular nucleus neurons. *Experimental Brain Research*, 135(4), 511–526. <https://doi.org/10.1007/s002210000542>
- Gensberger, K. D., Kaufmann, A.-K., Dietrich, H., Branoner, F., Banchi, R., Chagnaud, B. P., & Straka, H. (2016). Galvanic Vestibular Stimulation: Cellular Substrates and Response Patterns of Neurons in the Vestibulo-Ocular Network. *The Journal of Neuroscience: The Official Journal of the Society for Neuroscience*, 36(35), 9097–9110. <https://doi.org/10.1523/JNEUROSCI.4239-15.2016>
- Gerber, N., Reyes, M., Barazzetti, L., Kjer, H. M., Vera, S., Stauber, M., ... Ballester, M. A. G. (2017). A multiscale imaging and modelling dataset of the human inner ear. *Scientific Data*, 4, 170132–170132. <https://doi.org/10.1038/sdata.2017.132>
- Goldberg, J. M. (2000). Afferent diversity and the organization of central vestibular pathways. *Experimental Brain Research*, 130(3), 277–297. <https://doi.org/10.1007/s002210050033>
- Goldberg, J. M., & Cullen, K. E. (2011). Vestibular control of the head: Possible functions of the vestibulocollic reflex. *Experimental Brain Research*, 210(3–4), 331–345. <https://doi.org/10.1007/s00221-011-2611-5>
- Goldberg, J. M., Wilson, V. J., Angelaki, D. E., Cullen, K. E., Buttner-Ennever, J., & Fukushima, K. (2012). *The Vestibular System: A Sixth Sense*. OUP USA.
- Gonshor, A., & Jones, G. M. (1976). Extreme vestibulo-ocular adaptation induced by prolonged optical reversal of vision. *The Journal of Physiology*, 256(2), 381–414. <https://doi.org/10.1113/jphysiol.1976.sp011330>
- Goodroe, S. C., Starnes, J., & Brown, T. I. (2018). The Complex Nature of Hippocampal-Striatal Interactions in Spatial Navigation. *Frontiers in Human Neuroscience*, 12. <https://doi.org/10.3389/fnhum.2018.00250>
- Gu, Y., Watkins, P. V., Angelaki, D. E., & DeAngelis, G. C. (2006). Visual and Nonvisual Contributions to Three-Dimensional Heading Selectivity in the Medial Superior Temporal Area. *Journal of Neuroscience*, 26(1), 73–85. <https://doi.org/10.1523/JNEUROSCI.2356-05.2006>
- Guldin, W. O., Akbarian, S., & Grüsser, O.-J. (1992). Cortico-cortical connections and cytoarchitectonics of the primate vestibular cortex: A study in squirrel monkeys (*Saimiri sciureus*). *Journal of Comparative Neurology*, 326(3), 375–401. <https://doi.org/10.1002/cne.903260306>
- Guldin, W. O., & Grüsser, O. J. (1998). Is there a vestibular cortex? *Trends in Neurosciences*, 21(6), 254–259.
- Gunz, P., Ramsier, M., Kuhrig, M., Hublin, J.-J., & Spoor, F. (2012). The mammalian bony labyrinth reconsidered, introducing a comprehensive geometric morphometric approach. *Journal of Anatomy*, 220(6), 529–543. <https://doi.org/10.1111/j.1469-7580.2012.01493.x>
- Hain, T. C. (2007). Chapter 12 - Cranial Nerve VIII: Vestibulocochlear System. In C. G. Goetz (Ed.), *Textbook of Clinical Neurology (Third Edition)* (pp. 199–215). <https://doi.org/10.1016/B978-141603618-0.10012-8>
- Hain, T., & Helminski, J. (2007). Chapter 1 Anatomy and Physiology of the Normal Vestibular System. In *Vestibular Rehabilitation*. Philadelphia: Davos Company.
- Hallgren, E., Kornilova, L., Fransen, E., Glukhikh, D., Moore, S. T., Clément, G., ... Wuyts, F. L. (2016). Decreased otolith-mediated vestibular response in 25 astronauts induced by

- long-duration spaceflight. *Journal of Neurophysiology*, 115(6), 3045–3051.  
<https://doi.org/10.1152/jn.00065.2016>
- Halmagyi, G. M., & Curthoys, I. S. (1988). A clinical sign of canal paresis. *Archives of Neurology*, 45(7), 737–739.
- Halmagyi, G. M., Curthoys, I. S., Cremer, P. D., Henderson, C. J., Todd, M. J., Staples, M. J., & D’Cruz, D. M. (1990). The human horizontal vestibulo-ocular reflex in response to high-acceleration stimulation before and after unilateral vestibular neurectomy. *Experimental Brain Research*, 81(3), 479–490. <https://doi.org/10.1007/bf02423496>
- Hamid, M. (2005). More than a 50% canal paresis is needed for the head impulse test to be positive. *Otology & Neurotology: Official Publication of the American Otological Society, American Neurotology Society [and] European Academy of Otology and Neurotology*, 26(2), 318–319.
- Hashimoto, S., Naganuma, H., Tokumasu, K., Itoh, A., & Okamoto, M. (2005). Three-Dimensional Reconstruction of the Human Semicircular Canals and Measurement of Each Membranous Canal Plane Defined by Reid’s Stereotactic Coordinates. *Annals of Otology, Rhinology & Laryngology*, 114(12), 934–938.  
<https://doi.org/10.1177/000348940511401207>
- Helmchen, C., Rother, M., Spliethoff, P., & Sprenger, A. (2019). Increased brain responsivity to galvanic vestibular stimulation in bilateral vestibular failure. *NeuroImage: Clinical*, 24, 101942. <https://doi.org/10.1016/j.nicl.2019.101942>
- Highstein, S. M., & Holstein, G. R. (2006). Chapter 6 The Anatomy of the vestibular nuclei. In *Progress in Brain Research* (Vol. 151, pp. 157–203). [https://doi.org/10.1016/S0079-6123\(05\)51006-9](https://doi.org/10.1016/S0079-6123(05)51006-9)
- Hitier, M., Besnard, S., & Smith, P. F. (2014). Vestibular pathways involved in cognition. *Frontiers in Integrative Neuroscience*, 8, 59. <https://doi.org/10.3389/fnint.2014.00059>
- Horbruegger, M., Loewe, K., Kaufmann, J., Wagner, M., Schippling, S., Pawlitzki, M., & Schoenfeld, M. A. (2019). Anatomically constrained tractography facilitates biologically plausible fiber reconstruction of the optic radiation in multiple sclerosis. *NeuroImage: Clinical*, 22. <https://doi.org/10.1016/j.nicl.2019.101740>
- Horner, A. J., Bisby, J. A., Zotow, E., Bush, D., & Burgess, N. (2016). Grid-like Processing of Imagined Navigation. *Current Biology*, 26(6), 842–847.  
<https://doi.org/10.1016/j.cub.2016.01.042>
- Hubel, D. H., & Wiesel, T. N. (1959). Receptive fields of single neurones in the cat’s striate cortex. *The Journal of Physiology*, 148(3), 574–591.
- Huterer, M., & Cullen, K. E. (2002). Vestibuloocular reflex dynamics during high-frequency and high-acceleration rotations of the head on body in rhesus monkey. *Journal of Neurophysiology*, 88(1), 13–28. <https://doi.org/10.1152/jn.2002.88.1.13>
- Imagawa, M., Graf, W., Sato, H., Suwa, H., Isu, N., Izumi, R., & Uchino, Y. (1998). Morphology of single afferents of the saccular macula in cats. *Neuroscience Letters*, 240(3), 127–130.  
[https://doi.org/10.1016/s0304-3940\(97\)00944-0](https://doi.org/10.1016/s0304-3940(97)00944-0)
- Imagawa, M., Isu, N., Sasaki, M., Endo, K., Ikegami, H., & Uchino, Y. (1995). Axonal projections of utricular afferents to the vestibular nuclei and the abducens nucleus in cats. *Neuroscience Letters*, 186(2–3), 87–90. [https://doi.org/10.1016/0304-3940\(95\)11288-8](https://doi.org/10.1016/0304-3940(95)11288-8)
- Indovina, I., Riccelli, R., Chiarella, G., Petrolo, C., Augimeri, A., Giofrè, L., ... Passamonti, L. (2015). Role of the Insula and Vestibular System in Patients with Chronic Subjective Dizziness: An fMRI Study Using Sound-Evoked Vestibular Stimulation. *Frontiers in Behavioral Neuroscience*, 9, 334. <https://doi.org/10.3389/fnbeh.2015.00334>

- Jacobs, J., Weidemann, C. T., Miller, J. F., Solway, A., Burke, J. F., Wei, X.-X., ... Kahana, M. J. (2013). Direct recordings of grid-like neuronal activity in human spatial navigation. *Nature Neuroscience*, *16*(9), 1188–1190. <https://doi.org/10.1038/nn.3466>
- Janky, K. L., Patterson, J. N., Shepard, N. T., Thomas, M. L., & Honaker, J. A. (2017). Effects of device on video head impulse test (vHIT) gain. *Journal of the American Academy of Audiology*, *28*(9), 778–785. <https://doi.org/10.3766/jaaa.16138>
- Jareonsettasin, P., Otero-Millan, J., Ward, B. K., Roberts, D. C., Schubert, M. C., & Zee, D. S. (2016). Multiple Time Courses of Vestibular Set-Point Adaptation Revealed by Sustained Magnetic Field Stimulation of the Labyrinth. *Current Biology*, *26*(10), 1359–1366. <https://doi.org/10.1016/j.cub.2016.03.066>
- Javaid, A., Chouhna, H., Varghese, B., Hammam, E., & Macefield, V. G. (2019). Changes in skin blood flow, respiration and blood pressure in participants reporting motion sickness during sinusoidal galvanic vestibular stimulation. *Experimental Physiology*, *104*(11), 1622–1629. <https://doi.org/10.1113/EP087385>
- Jones, G. M. (1974). The Functional Significance of Semicircular Canal Size. In D. Bagger-Sjöbäck, A. Brodal, B. Cohen, G. F. Dohlman, J. M. Fredrickson, R. R. Gacek, ... H. H. Kornhuber (Eds.), *Vestibular System Part 1: Basic Mechanisms* (pp. 171–184). [https://doi.org/10.1007/978-3-642-65942-3\\_5](https://doi.org/10.1007/978-3-642-65942-3_5)
- Karolis, V. R., Corbetta, M., & Thiebaut de Schotten, M. (2019). The architecture of functional lateralisation and its relationship to callosal connectivity in the human brain. *Nature Communications*, *10*(1), 1417. <https://doi.org/10.1038/s41467-019-09344-1>
- Khan, S., & Chang, R. (2013). Anatomy of the vestibular system: A review. *NeuroRehabilitation*, *3*(3), 437–443. <https://doi.org/10.3233/NRE-130866>
- Kheradmand, A., & Zee, D. S. (2012). The bedside examination of the vestibulo-ocular reflex (VOR): An update. *Revue Neurologique*, *168*(10), 710–719. <https://doi.org/10.1016/j.neurol.2012.07.011>
- Kim, D.-K., Kim, D.-R., Jeong, S. H., Kim, G. J., Chang, K.-H., & Jun, B.-C. (2015). Analysis of the coplanarity of functional pairs of semicircular canals using three-dimensional images reconstructed from temporal bone magnetic resonance imaging. *The Journal of Laryngology & Otology*, *129*(5), 430–434. <https://doi.org/10.1017/S0022215115000201>
- Kim, J. (2013). Tonic eye movements induced by bilateral and unilateral galvanic vestibular stimulation (GVS) in guinea pigs. *Brain Research Bulletin*, *90*, 72–78. <https://doi.org/10.1016/j.brainresbull.2012.09.010>
- Kim, J. S., & Lee, H. (2013). Vertigo due to posterior circulation stroke. *Seminars in Neurology*, *33*(3), 179–184. <https://doi.org/10.1055/s-0033-1354600>
- Kim, Y., Faysel, M., Balucani, C., Yu, D., Gilles, N., & Levine, S. R. (2018). Ischemic Stroke Predictors in Patients Presenting with Dizziness, Imbalance, and Vertigo. *Journal of Stroke and Cerebrovascular Diseases: The Official Journal of National Stroke Association*, *27*(12), 3419–3424. <https://doi.org/10.1016/j.jstrokecerebrovasdis.2018.08.002>
- Kirsch, V., Boegle, R., Keeser, D., Kierig, E., Ertl-Wagner, B., Brandt, T., & Dieterich, M. (2018). Handedness-dependent functional organizational patterns within the bilateral vestibular cortical network revealed by fMRI connectivity based parcellation. *NeuroImage*, *178*, 224–237. <https://doi.org/10.1016/j.neuroimage.2018.05.018>
- Klingner, C. M., Volk, G. F., Brodoehl, S., Witte, O. W., & Guntinas-Lichius, O. (2014). Disrupted functional connectivity of the default mode network due to acute vestibular deficit. *NeuroImage: Clinical*, *6*, 109–114. <https://doi.org/10.1016/j.nicl.2014.08.022>

- Lang, W., Büttner-Ennever, J. A., & Büttner, U. (1979). Vestibular projections to the monkey thalamus: An autoradiographic study. *Brain Research*, *177*(1), 3–17.  
[https://doi.org/10.1016/0006-8993\(79\)90914-4](https://doi.org/10.1016/0006-8993(79)90914-4)
- Langer, T., Fuchs, A. F., Scudder, C. A., & Chubb, M. C. (1985). Afferents to the flocculus of the cerebellum in the rhesus macaque as revealed by retrograde transport of horseradish peroxidase. *The Journal of Comparative Neurology*, *235*(1), 1–25.  
<https://doi.org/10.1002/cne.902350102>
- Lee, J. Y., Shin, K. J., Kim, J. N., Yoo, J. Y., Song, W. C., & Koh, K. S. (2013). A Morphometric Study of the Semicircular Canals Using Micro-CT Images in Three-Dimensional Reconstruction. *Anatomical Record*. <https://doi.org/10.1002/ar.22664>
- Liu, X.-P., Koehler, K. R., Mikosz, A. M., Hashino, E., & Holt, J. R. (2016). Functional development of mechanosensitive hair cells in stem cell-derived organoids parallels native vestibular hair cells. *Nature Communications*, *7*(1), 1–11.  
<https://doi.org/10.1038/ncomms11508>
- Lobel, E., Kleine, J. F., Bihan, D. L., Leroy-Willig, A., & Berthoz, A. (1998). Functional MRI of Galvanic Vestibular Stimulation. *Journal of Neurophysiology*, *80*(5), 2699–2709.  
<https://doi.org/10.1152/jn.1998.80.5.2699>
- MacDougall, H. G., Brizuela, A. E., & Curthoys, I. S. (2003). Linearity, symmetry and additivity of the human eye-movement response to maintained unilateral and bilateral surface galvanic (DC) vestibular stimulation. *Experimental Brain Research*, *148*(2), 166–175.  
<https://doi.org/10.1007/s00221-002-1289-0>
- MacDougall, H. G., Weber, K. P., McGarvie, L. A., Halmagyi, G. M., & Curthoys, I. S. (2009). The video head impulse test: Diagnostic accuracy in peripheral vestibulopathy. *Neurology*, *73*(14), 1134–1141. <https://doi.org/10.1212/WNL.0b013e3181bacf85>
- Manzoni, D. (2005). The cerebellum may implement the appropriate coupling of sensory inputs and motor responses: Evidence from vestibular physiology. *The Cerebellum*, *4*(3), 178. <https://doi.org/10.1080/14734220500193493>
- Marianelli, P., Bassi Luciani, L., & Micera, S. (2012). Electrical potential distribution within the inner ear: A preliminary study for vestibular prosthesis design. *Conference Proceedings: ... Annual International Conference of the IEEE Engineering in Medicine and Biology Society. IEEE Engineering in Medicine and Biology Society. Annual Conference, 2012*, 3017–3020. <https://doi.org/10.1109/EMBC.2012.6346599>
- Marlinski, V., & McCrea, R. A. (2008). Activity of ventroposterior thalamus neurons during rotation and translation in the horizontal plane in the alert squirrel monkey. *Journal of Neurophysiology*, *99*(5), 2533–2545. <https://doi.org/10.1152/jn.00761.2007>
- Meng, H., May, P. J., Dickman, J. D., & Angelaki, D. E. (2007). Vestibular signals in primate thalamus: Properties and origins. *The Journal of Neuroscience: The Official Journal of the Society for Neuroscience*, *27*(50), 13590–13602.  
<https://doi.org/10.1523/JNEUROSCI.3931-07.2007>
- Minor, L. B. (1998). Physiological principles of vestibular function on earth and in space. *Otolaryngology--Head and Neck Surgery: Official Journal of American Academy of Otolaryngology-Head and Neck Surgery*, *118*(3 Pt 2), S5-15.  
<https://doi.org/10.1016/S0194-59989870002-6>
- Moser, E. I., Kropff, E., & Moser, M.-B. (2008). Place cells, grid cells, and the brain's spatial representation system. *Annual Review of Neuroscience*, *31*, 69–89.  
<https://doi.org/10.1146/annurev.neuro.31.061307.090723>

- Munro, K. J., & Higson, J. M. (1996). The test-retest variability of the caloric test: A comparison of a modified air irrigation with the conventional water technique. *British Journal of Audiology*, 30(5), 303–306. <https://doi.org/10.3109/03005369609076777>
- Naganuma, M., Inatomi, Y., Yonehara, T., Fujioka, S., Hashimoto, Y., Hirano, T., & Uchino, M. (2006). Rotational vertigo associated with parietal cortical infarction. *Journal of the Neurological Sciences*, 246(1–2), 159–161. <https://doi.org/10.1016/j.jns.2006.02.012>
- Nakashima, T., Naganawa, S., Sugiura, M., Teranishi, M., Sone, M., Hayashi, H., ... Ishida, I. M. (2007). Visualization of endolymphatic hydrops in patients with Meniere's disease. *The Laryngoscope*, 117(3), 415–420. <https://doi.org/10.1097/MLG.0b013e31802c300c>
- Nó, R. L. de. (1933). Vestibulo-ocular reflex arc. *Archives of Neurology & Psychiatry*, 30(2), 245–291. <https://doi.org/10.1001/archneurpsyc.1933.02240140009001>
- Noaksson, Schulin, Kovacsovics, & Ledin. (1998). Temperature Order Effects in the Caloric Reaction. *The International Tinnitus Journal*, 4(1), 71–73.
- Osipov, B., Harvati, K., Nathena, D., Spanakis, K., Karantanas, A., & Kranioti, E. F. (2013). Sexual dimorphism of the bony labyrinth: A new age-independent method. *American Journal of Physical Anthropology*, 151(2), 290–301. <https://doi.org/10.1002/ajpa.22279>
- Otero-Millan, J., Zee, D. S., Schubert, M. C., Roberts, D. C., & Ward, B. K. (2017). Three-dimensional eye movement recordings during magnetic vestibular stimulation. *Journal of Neurology*, 1–6. <https://doi.org/10.1007/s00415-017-8420-4>
- Paige, G. D. (1985). Caloric responses after horizontal canal inactivation. *Acta Oto-Laryngologica*, 100(5–6), 321–327. <https://doi.org/10.3109/00016488509126555>
- Papathanasiou, E. S., Papacostas, S. S., Charalambous, M., Eracleous, E., Thodi, C., & Pantzaris, M. (2006). Vertigo and imbalance caused by a small lesion in the anterior insula. *Electromyography and Clinical Neurophysiology*, 46(3), 185–192.
- Pawlak-Osinska, K., Wypych, A., Osinski, S., Kazmierczak, H., Marzec, M., Matulewski, J., & Serafin, Z. (2019). Vestibular Stimulation in Humans by Static Magnetic Fields of A 3T MRI Scanner – A Pilot Study. *NeuroQuantology*, 17(4). <https://doi.org/10.14704/nq.2019.17.4.2043>
- Perez, N., & Rama-Lopez, J. (2003). Head-impulse and caloric tests in patients with dizziness. *Otology & Neurotology: Official Publication of the American Otological Society, American Neurotology Society [and] European Academy of Otology and Neurotology*, 24(6), 913–917.
- Peterson, B. W., Bilotto, G., Goldberg, J., & Wilson, V. J. (1981). Dynamics of Vestibulo-Ocular, Vestibulo-Collic, and Cervicocollic Reflexes\*. *Annals of the New York Academy of Sciences*, 374(1), 395–402. <https://doi.org/10.1111/j.1749-6632.1981.tb30885.x>
- Petit, L., & Beauchamp, M. S. (2003). Neural basis of visually guided head movements studied with fMRI. *Journal of Neurophysiology*, 89(5), 2516–2527. <https://doi.org/10.1152/jn.00988.2002>
- Phillips, J. O., Ling, L., Nie, K., Jameyson, E., Phillips, C. M., Nowack, A. L., ... Rubinstein, J. T. (2015). Vestibular implantation and longitudinal electrical stimulation of the semicircular canal afferents in human subjects. *Journal of Neurophysiology*, 113(10), 3866–3892. <https://doi.org/10.1152/jn.00171.2013>
- Ramos, B. F., Cal, R., Carmona, S., Weber, K. P., & Zuma E Maia, F. (2019). Corrective Saccades in Unilateral and Bilateral Vestibular Hypofunction During Slow Rotation Expressed by Visually Enhanced VOR and VOR Suppression: Role of the Cerebellum. *Cerebellum (London, England)*. <https://doi.org/10.1007/s12311-019-01066-w>

- Rinaudo, C. N., Schubert, M. C., Figtree, W. V. C., Todd, C. J., & Migliaccio, A. A. (2019). Human vestibulo-ocular reflex adaptation is frequency selective. *Journal of Neurophysiology*, *122*(3), 984–993. <https://doi.org/10.1152/jn.00162.2019>
- Roberts, D. C., Marcelli, V., Gillen, J. S., Carey, J. P., Della Santina, C. C., & Zee, D. S. (2011). MRI Magnetic Field Stimulates Rotational Sensors of the Brain. *Current Biology*, *21*(19), 1635–1640. <https://doi.org/10.1016/j.cub.2011.08.029>
- Ropper, A. H., & Samuels, M. A. (2009). Chapter 15: Deafness, Dizziness, and Disorders of Equilibrium. In *Adams and Victor's Principles of Neurology* (9th ed.). McGraw-Hill Education Ltd.
- Rosengren, S. M., Colebatch, J. G., Young, A. S., Govender, S., & Welgampola, M. S. (2019). Vestibular evoked myogenic potentials in practice: Methods, pitfalls and clinical applications. *Clinical Neurophysiology Practice*, *4*, 47–68. <https://doi.org/10.1016/j.cnp.2019.01.005>
- Rowland, D. C., Roudi, Y., Moser, M.-B., & Moser, E. I. (2016). Ten Years of Grid Cells. *Annual Review of Neuroscience*, *39*, 19–40. <https://doi.org/10.1146/annurev-neuro-070815-013824>
- Sadeghi, S. G., Chacron, M. J., Taylor, M. C., & Cullen, K. E. (2007). Neural variability, detection thresholds, and information transmission in the vestibular system. *The Journal of Neuroscience: The Official Journal of the Society for Neuroscience*, *27*(4), 771–781. <https://doi.org/10.1523/JNEUROSCI.4690-06.2007>
- Sadeghi, S. G., Minor, L. B., & Cullen, K. E. (2007). Response of vestibular-nerve afferents to active and passive rotations under normal conditions and after unilateral labyrinthectomy. *Journal of Neurophysiology*, *97*(2), 1503–1514. <https://doi.org/10.1152/jn.00829.2006>
- Sailesh, K. S., Archana, R., & Mukkadan, J. K. (2015). Vestibular stimulation: A simple but effective intervention in diabetes care. *Journal of Natural Science, Biology, and Medicine*, *6*(2), 321–323. <https://doi.org/10.4103/0976-9668.159991>
- Sailesh, K. S., & Mukkadan, J. K. (2014). Vestibular Modulation of Endocrine Secretions – A Review. *International Journal of Research in Health Sciences*, *2*(1), 68–78.
- Santini, T., Fuhl, W., & Kasneci, E. (2017). CalibMe: Fast and Unsupervised Eye Tracker Calibration for Gaze-Based Pervasive Human-Computer Interaction. *Proceedings of the 2017 CHI Conference on Human Factors in Computing Systems*, 2594–2605. <https://doi.org/10.1145/3025453.3025950>
- Sato, H., Endo, K., Ikegami, H., Imagawa, M., Sasaki, M., & Uchino, Y. (1996). Properties of utricular nerve-activated vestibulospinal neurons in cats. *Experimental Brain Research*, *112*(2), 197–202. <https://doi.org/10.1007/bf00227638>
- Sato, H., Imagawa, M., Kushiro, K., Zakir, M., & Uchino, Y. (2000). Convergence of posterior semicircular canal and saccular inputs in single vestibular nuclei neurons in cats. *Experimental Brain Research*, *131*(3), 253–261. <https://doi.org/10.1007/s002219900309>
- Schenck, J. F. (1992). Health and Physiological Effects of Human Exposure to Whole-Body Four-Tesla Magnetic Fields during MRI. *Annals of the New York Academy of Sciences*, *649*(1), 285–301. <https://doi.org/10.1111/j.1749-6632.1992.tb49617.x>
- Schilling, K. G., Gao, Y., Christian, M., Janve, V., Stepniewska, I., Landman, B. A., & Anderson, A. W. (2019). A Web-Based Atlas Combining MRI and Histology of the Squirrel Monkey Brain. *Neuroinformatics*, *17*(1), 131–145. <https://doi.org/10.1007/s12021-018-9391-z>

- Schneider, E., Glasauer, S., & Dieterich, M. (2002). Comparison of human ocular torsion patterns during natural and galvanic vestibular stimulation. *Journal of Neurophysiology*, *87*(4), 2064–2073. <https://doi.org/10.1152/jn.00558.2001>
- Schnipke, S. K., & Todd, M. W. (2000). Trials and Tribulations of Using an Eye-tracking System. *CHI'00 Extended Abstracts on Human Factors in Computing Systems, CHI EA'00*. ACM, New York, NY, USA, 273–274. <https://doi.org/10.1145/633292.633452>
- Schubert, M. C., & Migliaccio, A. A. (2019). New advances regarding adaptation of the vestibulo-ocular reflex. *Journal of Neurophysiology*, *122*(2), 644–658. <https://doi.org/10.1152/jn.00729.2018>
- Sekirnjak, C., & du Lac, S. (2006). Physiological and Anatomical Properties of Mouse Medial Vestibular Nucleus Neurons Projecting to the Oculomotor Nucleus. *Journal of Neurophysiology*, *95*(5), 3012–3023. <https://doi.org/10.1152/jn.00796.2005>
- Shaikh, A. G., Ghasia, F. F., Dickman, J. D., & Angelaki, D. E. (2005). Properties of Cerebellar Fastigial Neurons During Translation, Rotation, and Eye Movements. *Journal of Neurophysiology*, *93*(2), 853–863. <https://doi.org/10.1152/jn.00879.2004>
- Sherman, S. M. (2005). Thalamic relays and cortical functioning. In *Cortical Function: A View from the Thalamus: Vol. 149. Progress in Brain Research* (pp. 107–126). [https://doi.org/10.1016/S0079-6123\(05\)49009-3](https://doi.org/10.1016/S0079-6123(05)49009-3)
- Shinder, M. E., & Taube, J. S. (2010). Differentiating ascending vestibular pathways to the cortex involved in spatial cognition. *Journal of Vestibular Research: Equilibrium & Orientation*, *20*(1), 3–23. <https://doi.org/10.3233/VES-2010-0344>
- Shine, J. P., Valdés-Herrera, J. P., Hegarty, M., & Wolbers, T. (2016). The Human Retrosplenial Cortex and Thalamus Code Head Direction in a Global Reference Frame. *The Journal of Neuroscience: The Official Journal of the Society for Neuroscience*, *36*(24), 6371–6381. <https://doi.org/10.1523/JNEUROSCI.1268-15.2016>
- Smith, A. T., Wall, M. B., & Thilo, K. V. (2012). Vestibular Inputs to Human Motion-Sensitive Visual Cortex. *Cerebral Cortex*, *22*(5), 1068–1077. <https://doi.org/10.1093/cercor/bhr179>
- Tagliazucchi, E., & Laufs, H. (2014). Decoding wakefulness levels from typical fMRI resting-state data reveals reliable drifts between wakefulness and sleep. *Neuron*, *82*(3), 695–708. <https://doi.org/10.1016/j.neuron.2014.03.020>
- Takimoto, Y., Imai, T., Okumura, T., Takeda, N., & Inohara, H. (2016). Three-dimensional analysis of otolith-ocular reflex during eccentric rotation in humans. *Neuroscience Research*, *111*, 34–40. <https://doi.org/10.1016/j.neures.2016.04.006>
- Tascioglu, A. B. (2005). *Brief review of vestibular system anatomy and its higher order projections*.
- Taube, J. S. (2007). The head direction signal: Origins and sensory-motor integration. *Annual Review of Neuroscience*, *30*, 181–207. <https://doi.org/10.1146/annurev.neuro.29.051605.112854>
- Terem, I., Ni, W. W., Goubran, M., Rahimi, M. S., Zaharchuk, G., Yeom, K. W., ... Holdsworth, S. J. (2018). Revealing sub-voxel motions of brain tissue using phase-based amplified MRI (aMRI). *Magnetic Resonance in Medicine*, *80*(6), 2549–2559. <https://doi.org/10.1002/mrm.27236>
- Thylur, D. S., Jacobs, R. E., Go, J. L., Toga, A. W., & Niparko, J. K. (2017). Ultra-High-Field Magnetic Resonance Imaging of the Human Inner Ear at 11.7 Tesla. *Otology & Neurotology: Official Publication of the American Otological Society, American Neurotology Society [and] European Academy of Otology and Neurotology*, *38*(1), 133–138. <https://doi.org/10.1097/MAO.0000000000001242>

- Ueda, H., Suga, M., Yagi, T., Kusumoto-Yoshida, I., Kashiwadani, H., Kuwaki, T., & Miyawaki, S. (2016). Vagal afferent activation induces salivation and swallowing-like events in anesthetized rats. *American Journal of Physiology. Regulatory, Integrative and Comparative Physiology*, 311(5), R964–R970. <https://doi.org/10.1152/ajpregu.00292.2016>
- Waespe, W., & Henn, V. (1977). Neuronal activity in the vestibular nuclei of the alert monkey during vestibular and optokinetic stimulation. *Experimental Brain Research*, 27(5), 523–538. <https://doi.org/10.1007/BF00239041>
- Ward, B. K., Lee, Y. H., Roberts, D. C., Naylor, E., Migliaccio, A. A., & Della Santina, C. C. (2018). Mouse Magnetic-field Nystagmus in Strong Static Magnetic Fields Is Dependent on the Presence of Nox3. *Otology & Neurotology: Official Publication of the American Otological Society, American Neurotology Society [and] European Academy of Otology and Neurotology*, 39(10), e1150–e1159. <https://doi.org/10.1097/MAO.0000000000002024>
- Ward, B. K., Otero-Millan, J., Jareonsettasin, P., Schubert, M. C., Roberts, D. C., & Zee, D. S. (2017). Magnetic Vestibular Stimulation (MVS) As a Technique for Understanding the Normal and Diseased Labyrinth. *Frontiers in Neurology*, 8. <https://doi.org/10.3389/fneur.2017.00122>
- Ward, B. K., Roberts, D. C., Della Santina, C. C., Carey, J. P., & Zee, D. S. (2014). Magnetic Vestibular Stimulation in Subjects with Unilateral Labyrinthine Disorders. *Frontiers in Neurology*, 5. <https://doi.org/10.3389/fneur.2014.00028>
- Wardman, D. L., Day, B. L., & Fitzpatrick, R. C. (2003). Position and velocity responses to galvanic vestibular stimulation in human subjects during standing. *The Journal of Physiology*, 547(Pt 1), 293–299. <https://doi.org/10.1113/jphysiol.2002.030767>
- Weintraub, M. I., Khoury, A., & Cole, S. P. (2007). Biologic effects of 3 Tesla (T) MR imaging comparing traditional 1.5 T and 0.6 T in 1023 consecutive outpatients. *Journal of Neuroimaging: Official Journal of the American Society of Neuroimaging*, 17(3), 241–245. <https://doi.org/10.1111/j.1552-6569.2007.00118.x>
- Wijesinghe, R., Protti, D. A., & Camp, A. J. (2015). Vestibular Interactions in the Thalamus. *Frontiers in Neural Circuits*, 9. <https://doi.org/10.3389/fncir.2015.00079>
- Wilkinson, D., Zubko, O., & Sakel, M. (2009). Safety of repeated sessions of galvanic vestibular stimulation following stroke: A single-case study. *Brain Injury*, 23(10), 841–845. <https://doi.org/10.1080/02699050903232541>
- Wilson, V. J., Boyle, R., Fukushima, K., Rose, P. K., Shinoda, Y., Sugiuchi, Y., & Uchino, Y. (1995). The vestibulocollic reflex. *Journal of Vestibular Research: Equilibrium & Orientation*, 5(3), 147–170.
- Wit, H. P., Spoelstra, H. A., & Segenhout, J. M. (1990). Bárány's theory is right, but incomplete. An experimental study in pigeons. *Acta Oto-Laryngologica*, 110(1–2), 1–6. <https://doi.org/10.3109/00016489009122507>
- Wook Yoo, S., Han, C. E., Shin, J. S., Won Seo, S., Na, D. L., Kaiser, M., ... Seong, J.-K. (2015). A Network Flow-based Analysis of Cognitive Reserve in Normal Ageing and Alzheimer's Disease. *Scientific Reports*, 5, 10057. <https://doi.org/10.1038/srep10057>
- Wuehr, M., Boerner, J. C., Pradhan, C., Decker, J., Jahn, K., Brandt, T., & Schniepp, R. (2018). Stochastic resonance in the human vestibular system – Noise-induced facilitation of vestibulospinal reflexes. *Brain Stimulation: Basic, Translational, and Clinical Research in Neuromodulation*, 11(2), 261–263. <https://doi.org/10.1016/j.brs.2017.10.016>
- Yakusheva, T. A., Shaikh, A. G., Green, A. M., Blazquez, P. M., Dickman, J. D., & Angelaki, D. E. (2007). Purkinje cells in posterior cerebellar vermis encode motion in an inertial

- reference frame. *Neuron*, 54(6), 973–985.  
<https://doi.org/10.1016/j.neuron.2007.06.003>
- Yakushin, S. B., Raphan, T., & Cohen, B. (2017). Coding of Velocity Storage in the Vestibular Nuclei. *Frontiers in Neurology*, 8. <https://doi.org/10.3389/fneur.2017.00386>
- Yiu, Y.-H., Aboulatta, M., Raiser, T., Ophey, L., Flanagan, V. L., zu Eulenburg, P., & Ahmadi, S.-A. (2019). DeepVOG: Open-source pupil segmentation and gaze estimation in neuroscience using deep learning. *Journal of Neuroscience Methods*, 324, 108307. <https://doi.org/10.1016/j.jneumeth.2019.05.016>
- Yoder, R. M., & Taube, J. S. (2014). The vestibular contribution to the head direction signal and navigation. *Frontiers in Integrative Neuroscience*, 8. <https://doi.org/10.3389/fnint.2014.00032>
- Zimmermann, J., Griffiths, J. D., & McIntosh, A. R. (2018). Unique Mapping of Structural and Functional Connectivity on Cognition. *Journal of Neuroscience*, 38(45), 9658–9667. <https://doi.org/10.1523/JNEUROSCI.0900-18.2018>
- zu Eulenburg, P., Caspers, S., Roski, C., & Eickhoff, S. B. (2012). Meta-analytical definition and functional connectivity of the human vestibular cortex. *NeuroImage*, 60(1), 162–169. <https://doi.org/10.1016/j.neuroimage.2011.12.032>
- zu Eulenburg, P., Stephan, T., Dieterich, M., & Ruehl, R. M. (2018, June 10). *The human vestibular cortex*. Presented at the 30th Bárány Society meeting, Uppsala, Sweden.

## Acknowledgements

This work would not have been possible without the support of some people that I'd like to mention in the following paragraphs.

The first "Thank you" goes to Dr. Virginia Flanagin for supervising this work and being open minded about letting me join her group as an 'exotic' speech pathologist. I am grateful for her input during the last four years, her help with coding, and the feedback sessions. She offered me a lot of freedom and we could learn a lot from each other during the past years. She taught me so much about MR imaging, how to program, and being patient in science.

I thank Prof. Dr. Peter zu Eulenburg for being so enthusiastic and critical at the same time. He kept my motivation high and pushed me to step outside of my comfort zone. His attitude helped me with developing further, believing in my skills and from time to time leaving aside my self-diagnosed imposter syndrome.

Thanks to my TAC committee for all the feedback you supported me with during our meetings: Dr. Virginia Flanagin, Prof. Dr. Klaus Jahn, Prof. Dr. Paul Taylor and Prof. Dr. Peter zu Eulenburg! Further, I thank my several funding sources during my PhD. Virginia, Peter, the GSN which provided a stipend: even though times might have been difficult I stuck to the PhD, and I am very proud that I was able to finish this work with your financial support!

I'd like to thank Virginia, Paul and Dr. Christopher Bockisch for reviewing this thesis!

MRI data collection was time consuming but so much fun with Matthias Hübner who is always caring and has an eye for the little details. Thanks as well for all the coffee that kept us going!

Thanks to Dr. Ahmad Ahmadi and his students - my experts when it comes to the deep learning analyses! Tagging eye-tracking pictures during Halloween was a fun experience and I enjoyed listening to the Serial podcast with you guys! I am grateful of having worked with Ahmad. I enjoyed writing papers with him, learned about abstract deep learning algorithms and latex formatting especially during the second half of my PhD.

Further I'd like to thank Dr. Thomas Eggert for sharing his expertise in the field of eye-tracking. His input was essential for wrapping our heads around the eye-tracking analyses.

I am further thankful to Prof. Dr. Adrian Danek. He suggested me to apply to GSN in the first place and gave me the opportunity to learn about neurological, especially neurodegenerative diseases. Working with him just before my PhD prepared me for several situations. Standing up for myself, being critical and loyal – some of the skills I could further develop in the past years during my PhD.

I thank Prof. Dr. Benedikt Grothe for putting trust in me and being so supportive right at the beginning of my PhD when it was needed most. Further, I would like to say my special thanks addressing the GSN staff: Lena, Julia, Raluca, Renate, Stefanie, Catherine, Birgit, Nadine – always there and great just the way you are!

Life is better with friends.

Everyone who was lucky to spend time in Forschungshaus, aka "FoHa", knows that this building and the people that worked inside are very special and unique. I am so thankful for this time

(including all the BBQs, Healthy Fridays, birthday and defense celebrations) and to have gained many friends over the past years! Thanks to “Room 6”: my office mates Josh and Alex – thank you for all the help whenever I felt stuck with Matlab, for Krapfen-Wednesday, for sharing the mindfulness-calendar-wisdoms, for fruitful discussions, and for all the fun! Thanks to Matthias who joined our office for almost a year for his kind distractions and his ability to provide (mostly) good music! I’ll always look back to the “FoHa”-times with a smile upon my face! Thanks to: Lina, Angela, Michaela, James, Matthias E., Matthias T., Josh, Alex, Rainer, Sarah, Judita, Kathrin, Isi, Cecilia, Nadine, Christopher, Nisha, Steffi, Dian, Mehrdad, Conny, Johanna, Katharina, Virginia, Hans, Sabine, Thommi, Peter, Maxine, Ahmad, Frau Hauser, Katie, Bernadette, and Elisabeth! Thanks to all the GSN - friendships that developed through retreats, soft skill courses and social events!

Thanks as well to my close friends who supported me and decreased my stress level during busy times: special thanks to Lilli, Claudi, Hannah, Roland and Dominik!

I’d like to thank my mum and dad: thank you for letting me explore the world. You have never been judgmental and always support me in every possible way. You stand by my side without reservation. Sofie, thank you for so much laughter, for being the proof that distance doesn’t matter and the fact that we got the same “interior design”. You are the best family one could wish for!

Anselm, thank you for being on my side throughout this period of my life, for understanding, caring, and loving. For teaching and reminding me to never forget the essentials in life, the positive things and the art of living in the moment. (And thanks for proof-reading this work ☺)

I am grateful for so many experiences and emotions during the past years!

## List of publications

- Yiu, YH, Aboulatta, M., **Raiser, T.**, Ophey, L., Flanagan, V.L., zu Eulenburg, P., Ahmadi, S.A (2019). DeepVOG: Open-source Pupil Segmentation and Gaze Estimation in Neuroscience using Deep Learning. *Journal of Neuroscience Methods*, 324.
- Croot, K., **Raiser, T.**, Taylor-Rubin, C., Ruggero, L., Ackl, N., Wlasich, E., ... Nickels, L. (2019). Lexical retrieval treatment in primary progressive aphasia: An investigation of treatment duration in a heterogeneous case series. *Cortex; a Journal Devoted to the Study of the Nervous System and Behavior*, 115, 133–158.
- Schönecker, S., Prix, C., **Raiser, T.**, Ackl, N., Wlasich, E. Stenglein-Krapf, G., Oestreicher, D., Brendel, M., Levin, J., Rominger, A., Danek, A. (2017). Amyloid-Positronenemissionstomographie mit Florbetaben (FBB-PET) in der Demenzdiagnostik. *Der Nervenarzt*, 88 (2), 156-161.
- Teipel, S., **Raiser T.**, Grothe, M., Schroeter, M., Otto, M., Danek, A. (2016). Atrophy and structural connectivity of the cholinergic basal forebrain in primary progressive aphasia. *Brain*, 83, 124-135.
- **Raiser, T.**, Croot, K., Nickels, L., Taylor, C. & Danek, A. (2014). Telemedicine in Primary Progressive Aphasia. *Aphasie und verwandte Gebiete*, 3, 37-40.

## List of poster presentations

- **Raiser, T.**, Ruehl, R.M., Ophey, L., Ertl, M., Flanagan, V., zu Eulenburg, P. Human Area MST – a cortical visual motion, ocular motor, or vestibular module? OHBM, 9-13 June 2019, Rome, Italy
- **Raiser, T.**, Flanagan, V. Magnetic vestibular stimulation during resting-state imaging. OHBM, 9-13 June 2019, Rome, Italy
- Danek, A., Seckin, M., Ricard, I., **Raiser, T.**, Ebert, A., Heitkamp, N., Ackl, N., Bader, B., Prix, C., Loosli, S., Deschner, M., Wlasich, E., Levin, J., & German FTLD consortium. Utility of the Repeat and Point Test in Primary Progressive Aphasia. Language in Mind and Brain, 10-11 December 2018, Munich, Germany
- Croot, K., **Raiser, T.**, Taylor-Rubin, C., Ruggero, L., Ackl, N., Wlasich, E., Stenglein-Krapf, G., Rominger, A., Danek, A., Scharfenberg, A., Foxe, D., Hodges, J.R., Piguet, O., Kochan, N.A. & Nickels, L. Long-term treatment of word retrieval in Primary Progressive Aphasia. Australian Psychological Society College of Clinical Neuropsychologists Annual Conference, 9-11 November 2017, Perth, Australia
- Croot, K., **Raiser, T.**, Taylor-Rubin, C., Ruggero, L., Ackl, N., Wlasich, E., Stenglein-Krapf, G., Rominger, A., Danek, A., & Nickels, L. Long-term treatment of lexical retrieval in Primary Progressive Aphasia. Science of Aphasia Conference (SoA 2017), Geneva, Switzerland
- Croot, K., Taylor, C., Abel, S., Ruggero, L., **Raiser, T.**, Savage, S., Hodges, J.R. & Nickels, L. (2015). Lexical retrieval treatment for functionally-relevant vocabulary in primary

progressive aphasia: Investigating generalisation to a structured interview. 12th Conference of the Neuropsychological Special Interest Group of the World Federation for NeuroRehabilitation, 6.-07. July 2015, Daydream Island, Australia

- **Raiser, T.**, Croot, K., Nickels, L., Taylor, C., Ackl, N., Wlasich, E., Stenglein-Krapf, G., Rominger, A., & Danek, A. (2014). Naming Treatment in Three Cases of Primary Progressive Aphasia. 9th International Conference on Frontotemporal Dementias (ICFTD), Vancouver, 22.-25. Oktober, 2014
- **Raiser, T.**, Croot, K., Nickels, L., Taylor, C., Ackl, N., Wlasich, E., Stenglein-Krapf, G., Rominger, A., & Danek, A. (2014). Word Retrieval in Primary Progressive Aphasia following language therapy. Alzheimer s Association International Conference, Kopenhagen, 12.–17. Juli 2014.
- Mueller-Sarnowski, F., Meißner, J., Laub, C., **Raiser, T.**, Wlasich, E., Rominger, A., Biskup, S., Danek, A. (2014). First proven observation of a de novo PSEN1 mutation from Germany. Alzheimer s Association International Conference, Kopenhagen, 12.–17. Juli 2014.
- Mueller-Sarnowski, F., Meißner, J., Laub, C., Wlasich, E., **Raiser, T.**, Prix, C., Rominger, A., Biskup, S., & Danek, A. (2014). Alzheimer de novo Mutation Erste Beobachtung aus dem deutschsprachigen Raum. Neurowoche 2014, München, 15.-19.09. 2014
- Mueller-Sarnowski, F., Meißner, J., Laub, C., **Raiser, T.**, Wlasich, E., Rominger, A., Biskup, S., Danek, A. (2014). PSEN1 de novo mutation first proven observation from German speaking countries. Eibsee Meeting, Eibsee, 05.-07. November 2014.